SURFACE SENSITIZATION AND MODIFICATION IN HYBRID ORGANIC-INORGANIC PHOTOVOLTAICS

A Dissertation
Presented to
The Academic Faculty

by

Rebecca B. M. Hill

In Partial Fulfillment
of the Requirements for the Degree
Doctor of Philosophy in the
School of Chemistry

Georgia Institute of Technology
May 2018

SURFACE SENSITIZATION AND MODIFICATION IN HYBRID ORGANIC-INORGANIC PHOTOVOLTAICS

Approved by:

Dr. Seth R. Marder, Advisor
School of Chemistry and Biochemistry
Georgia Institute of Technology

Dr. Zhiqun Lin
School of Materials Science and Engineering
Georgia Institute of Technology

Dr. Veaceslav Coropceanu
School of Chemistry and Biochemistry
Georgia Institute of Technology

Dr. John R. Reynolds
School of Chemistry and Biochemistry
Georgia Institute of Technology

Dr. Stefan France
School of Chemistry and Biochemistry
Georgia Institute of Technology

Date Approved: January 9, 2018

To my husband, my parents, and our family

soli Deo gloria

ACKNOWLEDGEMENTS

I would like to thank the individuals who I have been fortunate to work with and learn from during the course of my Ph.D. Whether or not your names are listed here, I am grateful. First and foremost, I would like to thank my advisor Prof. Seth Marder. I will always be grateful to him for welcoming me into his group and working so hard to provide me and other group members with research and development opportunities. I am grateful for the guidance and for the freedom he has provided along the way to allow me to grow as a scientist. He has changed the way I analyze and understand the world around me. I am grateful for invaluable discussions and assistance from members of the Marder group including Dr. Stephen Barlow, Dr. Junxiang Zhang, and Dr. Tim Parker, with special thanks to Steve for all his time spent in thesis edits. Caleb Ackermann, Daniel Morales-Salazar, Jay Patel, and Thomas Dellaert were wonderful to work with and aided in the synthesis of squaraine sensitizers. I am grateful to Dr. Yadong Zhang, Dr. Iryna Davydenko, and Dr. Fadi Jradi for intermediates and insightful discussions. I would like to thank Dr. Anthony Giordano, Dr. Sergio Paniagua-Barrantes, Dr. O'Neil Smith, Dr. Lauren (Hayden) Scholz, and many others who were excellent mentors when I joined the Marder group. I would like to thank Dr. Karttikay Moudgil, Dr. Marcel Said, Dr. Yeli Fang, Hye Kyung Kim, János Simon, Matthew Cooper, Federico Pulvirenti, Dr. Elena Longhi, Theo Hicks, Marie-Hélène Tremblay, those previously listed, and many others for their support and kindness.

I would like to thank Dr. Xiongwu Kang of Prof. Mostafa El-Sayed's group for his early work on DSSC device fabrication and sensitizer characterization and for

insightful discussions, along with the assistance of Dr. Daniel O'Neil and Dr. Paul Szymanski.

From my second home in the group of Prof. Jean-Luc Brédas, I am grateful for assistance from Dr. Stephen Shiring and Dr. Paul Winget, with thanks to many others for their advice and support, including Dr. Zilong Zheng, Dr. Alex Hyla, Dr. Junghyun Noh, Dr. Rebecca Gieseking, Dr. Hong Li, and Dr. Veaceslav Coropceanu.

I am very grateful to Prof. Henry Snaith for the formative time I spent in his group and the many welcoming and helpful group members and affiliates, including Dr. Nakita Noel, Dr. Maximillian Hörantner, Dr. Konrad Wojciechowski, Dr. Severin Habisreutinger, Dr. Jacob Wang, and Dr. Juan Manuel Bermudez Garcia. I am grateful to Dr. Seulki Song and Kyoungwon Choi in the group of Dr. Taiho Park for device fabrication and characterization and for their kind continuation and diligence in collaboration.

I am grateful to Prof. Anders Hagfeldt and his group at EPFL for opening their doors to me and to be able to work with Parnian Ferdowsi for DSSC device fabrication and characterization. The DSSC projects would not have progressed without valuable discussions with Dr. Kazuteru Nonomura, Dr. M. K. Zakeeruddin, Dr. Jun Ho Yum of the group of Dr. Kevin Sivula, Dr. Nick Vlachopoulos, and Weiwei Zhang. I am very grateful to Dr. Juan-Pablo Baena-Correa, Dr. Silver-Hamill Turren-Cruz, and Dr. Wolfgang Tress for perovskite device fabrication and characterization and insightful discussions. I am also grateful to Dr. Michael Graetzel and all the members of his group who started me on this Ph.D. journey, with special thanks to Dr. Jun Ho Yum, Dr.

Etienne Baranoff, Francine Duriaux, Dr. Sandy Pham Trang, and Dr. Magdalena Marszałek.

From Utah State University, I would like to thank all the Greaves and Reeder friends, especially Heather Sagers and Dr. Asti Bhatt. I would like to thank Asti for her friendship and for making me promise to do a Ph.D. if at all possible. I would like to thank Dr. John Hubbard for making freshman chemistry fun, and Frank (Yifei) Zhang for his friendship and for believing I could win a Nobel Prize someday, which helped me to believe in myself too. I would like to say a huge thank you to Dr. Alvan Hengge, Dr. Tim Humphreys, Dr. Amy Fuller, and all of the Hengge lab crew who made research what I wanted to do on a Friday night.

I would like to thank my parents Dr. Alan and Elizabeth Mitchell, who taught me to dream big crazy dreams, then work to make them happen, sometimes succeed, and love the journey either way. I would like to thank my grandmother Elaine Mitchell for teaching me to love materials synthesis at a very young age. I would like to thank my siblings Karma Sue and Tallon Boles, Sam and Sara Mitchell, Rex Colin and Johnita Mitchell, Frost Mitchell, Forrest Hill, Thomas and Shelby Hill, and Ben Hill for their support. I would like to thank all of the Hill family, especially David Hill and Robin Hill, for their patience and support. I would like to thank Britta Franceschi for her help in fixing English errors in the document and for providing kind encouragement.

Last and most of all, I would like to thank my husband Max, who encouraged me to begin this crazy graduate journey. He didn't let me quit when I failed, encouraged me to start again, and again didn't let me quit the many times I lost hope. He has been there

in all the good and, more importantly, the bad times and he has always believed in us and in me. I cannot put into words what he means to me.

TABLE OF CONTENTS

LIST OF TABLES

LIST OF FIGURES

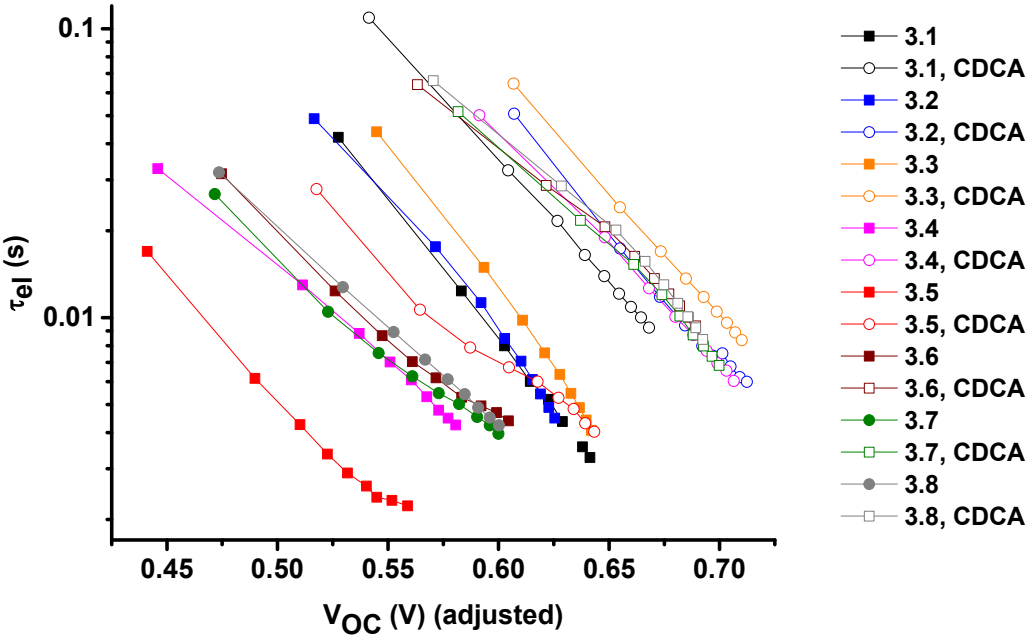

LIST OF ABBREVIATIONS

HOMO	Highest occupied molecular orbital
LUMO	Lowest unoccupied molecular orbital
Vis.	Visible
near-IR	Near-infrared
UV	Ultra-violet
DSSC	Dye-sensitized solar cell
OPV	Organic photovoltaic
PSC	Perovskite solar cell
PCE	Power conversion efficiency
IPCE	Incident photon-to-current conversion efficiency
J-V	Current-voltage
NMR	Nuclear magnetic resonance
HRMS	High resolution mass spectrometry
EA	Electron Affinity
IE	Ionization Energy
CV	Cyclic Voltammetry
Calc.	Calculated
HPLC	High-performance liquid chromatography
d	Days
h	Hours
min	Minutes
sec	Seconds
et al.	*Et alia*
kcal	Kilocalorie
mol	Mole
mmol	Millimole
g	Gram
mg	Milligram
Sq	Squaraine
PL	Photoluminescence
Abs.	Absorbance
a.u.	Arbitrary units
equiv.	Equivalents
rt	Room temperature
eV	Electronvolts
cm	Centimeters
cm^{-1}	Wavenumbers
nm	nanometers
^{o}C	Degrees Celsius
K	Kelvin
dmby	6,6′-dimethyl-2,2′-bipyridine
tmby	4,4′,6,6′-tetramethyl-2,2′-bipyridine
dmp	bis(2,9-dimethyl-1,10-phenanthroline)
bpy	2,2’-bipyridine

TiO_2	Titanium dioxide
ITO	Indium-tin oxide
FTO	Fluorine-doped tin oxide
ZnO	Zinc oxide
Al_2O_3	Alumina
CA	Carboxylic acid
PA	Phosphonic acid
Gen	Generation
NHE	Normal hydrogen electrode
SCE	Saturated calomel electrode
vs.	versus
LDA	Lithium diisopropylamide
^{i}Pr	isopropyl
tert-, t-	tertiary
CDCA	Chenodeoxycholic acid
M	mol/L
L	Liter
mL	Milliliter
DTS	Dithienosilole
CPDT	Cyclopentadithiophene
BTD	Benzothiadiazole
EtOAc	Ethyl acetate
CH_2Cl_2	Dichloromethane
DMF	N,N-Dimethylformamide
THF	Tetrahydrofuran
DMSO	Dimethyl sulfoxide
MeOH	MeOH
$CHCl_3$	Chloroform
$CDCl_3$	Deuterated chloroform
NBS	N-Bromosuccinimide
BuLi	Butyl lithium
ps	picosecond
FF	Fill factor
Hz	Hertz
ca.	Circa
FeC_{p2}	Ferrocene
FeC_{p2}^{*}	Decamethylferrocene
CBM	Conduction band minimum
VBM	Valence band maximum
TLC	Thin layer chromatography
V	Volts
A	Amperes
W	Watt
C	Coulombs

Other abbreviations are explained in the text.

LIST OF SYMBOLS

P_{in}	Incident power
P_{max}	Maximum power point
V_{OC}	Open-circuit voltage
J_{SC}	Short-circuit current
ε_{max}	Extinction coefficient at maximum absorption
λ	Wavelength
λ_{max}	Wavelength at maximum absorption
λ_{onset}	Wavelength at the onset of absorption
$E_{0\text{-}0}^{opt}$	Optical gap
$E_{0\text{-}0}^{elec}$	Electrochemical gap
$E_{(S+/S^*)}$	Excited-state oxidation potential
$E_{(S+/S)}$	Ground-state oxidation potential
k_{ei}	Charge injection rate constant
Å	Angstrom
η_{inj}	Efficiency of charge injection
η_{reg}	Efficiency of regeneration
η_{cc}	Efficiency of charge collection
f	Oscillator strength
$-\Delta G_{ei}^0$	Driving force for electron injection
$-\Delta G_{reg}^0$	Driving force for dye regeneration
E_F	Fermi level energy
E_{CB} *or* E_{CBM}	Conduction band minimum energy
E_{VB} *or* E_{VBM}	Valence band maximum energy
E_{redox}	Redox potential
ΔG_{diss}^0	Driving force for exciton dissociation
q	Elementary charge
Φ_p	Photon flux
μ	Dipole moment
τ_{obs}	The average lifetime of the excited state
τ_e	Electron lifetime in TiO_2
τ_{tr}	Electron transport time in TiO_2
Q_{OC}	Charge extraction
δ	Chemical shift
α_λ	Dye absorptance
n_0	Electron density in conduction band in the dark
τ_0	Recombination in the dark
n_c	Electron density in the conduction band
n_s	Electron density at the semiconductor surface
N_C	Electron density in the bulk conduction band states

SUMMARY

Interface optimization is key to the development of next-generation photovoltaic systems such as dye-sensitized and perovskite solar cells.[1–3] In dye-sensitized solar cells, sensitizers have a pivotal role in light absorption, charge generation, and prevention of recombination at an interface.[4] A power conversion efficiency of 20% can theoretically be obtained in dye-sensitized solar cells with a near-IR absorption onset of 940 nm (top certified efficiency currently at 12%).[5,6] Squaraine sensitizers are a promising class of near-IR absorbing materials, and the investigation of out-of-plane groups and extended π-conjugation yielded promising results in red-shifting the absorption maxima, preventing dye aggregation, and increasing current. For donor-π-acceptor dyes, a direct comparison of rhodanine-based acceptors with carboxylic acids vs. phosphonic acids as anchors demonstrated the stability of strongly binding phosphonic acids to dye desorption in the electrolyte.

In an n-i-p architecture lead organo-halide perovskite solar cell device, the formation of the perovskite crystal is greatly affected by the electron transport layer's surface energy and solvent resistance. Fullerene electron transport layers have the advantage of low temperature processing for flexible substrates, but suffer from pinholes during perovskite layer deposition in an n-i-p device architecture.[7] Covalently linking C_{60} with poly(allylamine) resulted in optimized surface energy for perovskite crystal formation, decreased work function for optimal electron transfer, increased solvent resistance for a pinhole-free fullerene layer, increased power conversion efficiency, and increased retention of device performance relative to the control after 600 bending cycles

on a flexible substrate. Tin oxide electron transport layers are of interest due to their UV stability relative to titania, but decreases in device performance have been observed for ALD-deposited tin oxide layers stored under inert atmosphere. Phosphonic acid surface modification of ALD-deposited tin oxide electron transport layers yielded modified devices that retained 86% of their initial efficiency under inert atmosphere while the control retained 65%, making phosphonic acid surface modification of interest for the stability of perovskite solar cells under encapsulation.

CHAPTER 1. INTRODUCTION

1.1 Introduction to Photovoltaics

First generation solar cell technology was developed in the 1940's, with rapid development achieved through the use of silicon at Bell Labs.[8–10] The progress was based on the p-n junction, an electric field created by the junction of an n-doped and a p-doped semiconductor. When electron and hole pairs, or excitons, are created by light in the vicinity of a p-n junction, minority carriers are transported across the electric field and flow through the semiconductor to the electrode where they are then collected.

Reductions in manufacturing costs of silicon have facilitated a robust photovoltaics market, but technologies that have either a higher power conversion efficiency (PCE), lower production costs, or advantageous properties (flexible, lightweight, semitransparent) for niche applications have opportunities for growth. Various technologies are currently in the market and under development, including thin film silicon, GaAs, CdTe, $CuIn_xGa_{(1-x)}Se_2$ (CIGS),[11] and organic (OPV), dye-sensitized (DSSC), and perovskite (PSC) solar cells.[11]

Table 1-1. Independently confirmed record solar cell efficiencies by device type.[12]

Solar cell	PCE (%)
Silicon (single crystal)	26.7 ± 0.5
Silicon (multicrystalline)	21.9 ± 0.4
Silicon (thin transfer submodule)	21.2 ± 0.4
GaAs (thin film)	28.8 ± 0.9
CIGS	21.7 ± 0.5
OPV	11.2 ± 0.3
DSSC	11.9 ± 0.4
PSC	19.7 ± 0.6*

*22.1 ± 0.7% PCE reported & confirmed, not classified as a record

This thesis discusses developments related to surface sensitization in DSSCs and surface modification in perovskite solar cells. In 1991, Brian O'Regan and Michael Graetzel presented substantial progress in the power conversion efficiency of dye-sensitized solar cells by using a nanocrystalline photoanode,[13] building upon previous research on nanocrystalline TiO_2[14,15] and the sensitization of photoanodes.[16–19] Efficiencies as high as 12-14% have been reported,[20–23] with a record independently certified efficiency of 11.9%.[12]

In 2012, Lee *et al*. published the first example of using a solution-processable hybrid organic-inorganic perovskite material ($CH_3NH_3PbI_2Cl$) as a thick active layer on top of a nanocrystalline TiO_2 layer,[24] building upon previous research on lead organo-halide perovskites[25] in transistors, LEDs,[26] and quantum dot-sensitized solar cells.[27,28] Efficiencies as high as 22.1% have been reported for perovskite solar cells, with a certified record PCE of 19.7% achieved to date.[12,29]

1.1.1 Solar cell characterization

The power conversion efficiency, PCE or η, is the ratio of the maximum electrical power output, P_{max}, to the power input from the incident light, P_{in}, and reflects the overall conversion of light into electricity (Equation 1-1).

$$\eta = \frac{P_{max}}{P_{in}} \qquad 1\text{-}1$$

At a standard intensity and spectrum of light, the maximum electrical power output is measured by applying a voltage (V) bias and measuring the corresponding change in current per unit area (J) to produce a J-V curve (Figure 1-1). The standard light spectrum for solar cell certification is global AM1.5 irradiance. AM1.5 corresponds to measurements at 25 °C with an intensity of 1000 W/m^2 and a spectrum representative of that of sunlight at 48.19° solar zenith angle at sea level, which is representative of the mid-latitudes where many large population centers are located.

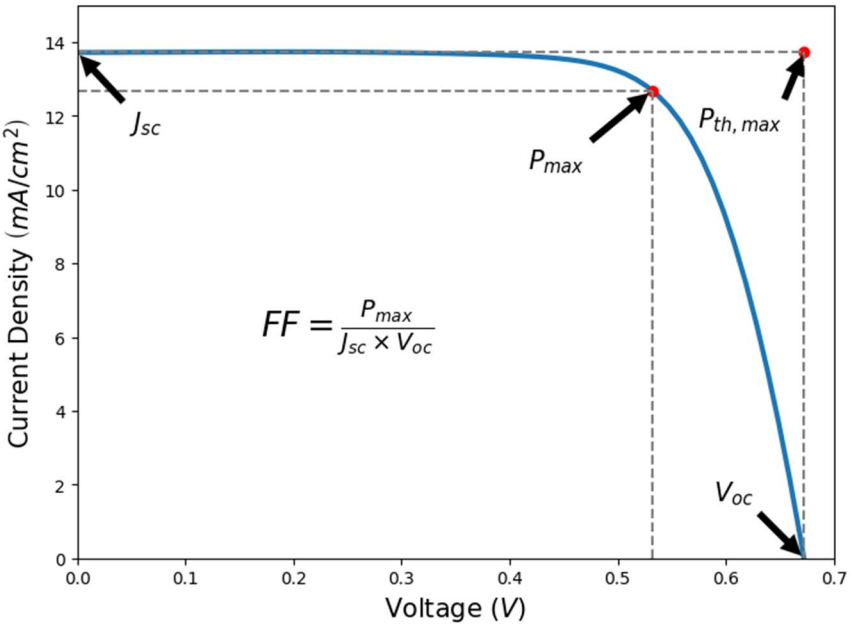

Figure 1-1. *J-V* curve highlighting the parameters V_{OC}, J_{SC}, FF, $P_{th,max}$, and P_{max} discussed additionally in the following section.

When the current is equal to zero, the voltage measured is termed the open-circuit voltage V_{OC}. When the voltage is equal to zero, the current measured is referred to as the short circuit current and is expressed per unit area as the short-circuit current density J_{SC}. The P_{max} is the product of the photocurrent density and the voltage at the maximum power point, J_{max} and V_{max}, respectively (Equation 1-2).

$$\eta = \frac{P_{max}}{P_{in}} = \frac{J_{max} \cdot V_{max}}{P_{in}} = \frac{J_{SC} \cdot V_{OC} \cdot FF}{P_{in}} \qquad 1\text{-}2$$

P_{max} can also be expressed as the product of the short circuit current, J_{SC}, the open circuit voltage, V_{OC}, and the fill factor, FF (Equation 1-2). The fill factor is defined as the ratio of P_{max} versus $P_{max,th}$, which is equal to the product of V_{OC} and J_{SC} (Equation 1-3)

$$FF = \frac{P_{max}}{P_{th,max}} = \frac{J_{max} \cdot V_{max}}{J_{SC} \cdot V_{OC}} \quad 1\text{-}3$$

The incident photon-to-current efficiency is measured using monochromatic light to obtain the quantum yield for the charge-injection process, or yield of electrons generated per photon. The IPCE is measured by scanning each wavelength to obtain the J_{SC} produced for the P_{in} at that wavelength (Equation 1-4),

$$IPCE = \frac{Jsc(\lambda)}{q \cdot \Phi_p(\lambda)} = 1240 \frac{Jsc(\lambda)[Acm^{-2}]}{\lambda[nm] P_{in}(\lambda)[Wc^{-2}]} \quad 1\text{-}4$$

where q is the elementary charge and Φ_p is the photon flux. Therefore, the J_{SC} of the device under polychromatic light is approximately equal to the integrated sum of the IPCE over the spectrum of light irradiated. The IPCE spectrum may resemble the absorption spectra of the sensitizer, with the spectral shape changing depending on the collection efficiency (Figure 1-2).

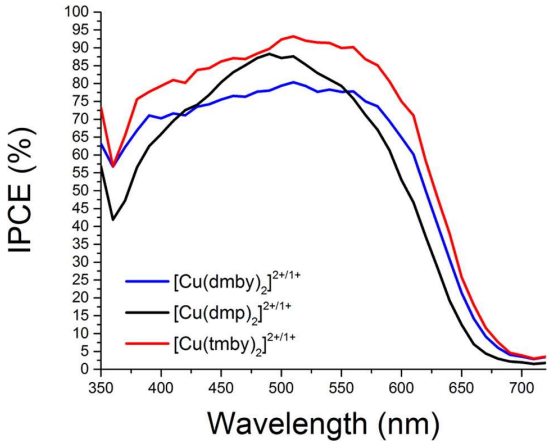

Figure 1-2. Representative IPCE spectra of DSSC devices sensitized with the Y123 sensitizer (see Figure 1-10 for structure). Ligands: dmby = 6,6′-dimethyl-2,2′-bipyridine, tmby = 4,4′,6,6′-tetramethyl-2,2′-bipyridine, and dmp = bis(2,9-dimethyl-1,10-phenanthroline). Reproduced from Saygili *et al.*[30] with permission. Copyright 2016 American Chemical Society.

1.2 Dye-Sensitized Solar Cells

1.2.1 DSSC architecture and theory

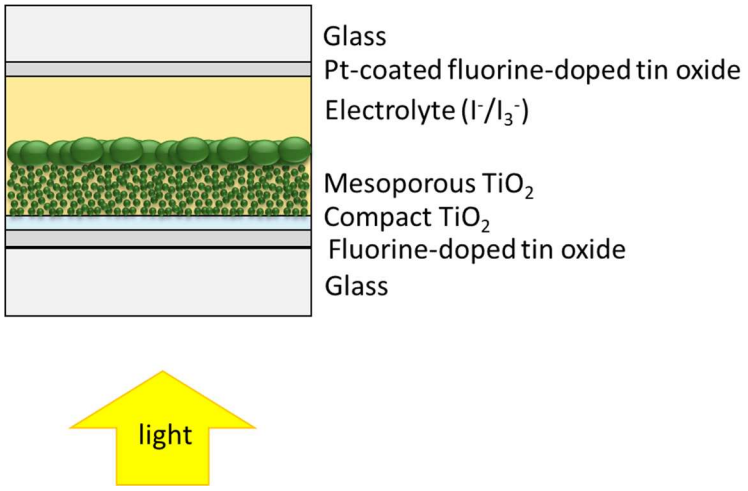

Figure 1-3. Dye-sensitized solar cell device architecture, with light passing through the glass, FTO anode, a compact TiO_2 blocking layer, a "transparent" layer of sintered 18-30 nm diameter TiO_2 particles sensitized with a green dye, a "scattering" layer of ~100 nm diameter particles, an electrolyte, a Pt-coated FTO counter electrode, and glass.

In a dye-sensitized solar cell (Figure 1-3), a dye sensitizer is grafted onto the surface of a semiconducting oxide. After excitation of the dye with light, the dye may transfer, or inject, electrons into the conduction band of the semiconducting oxide (Figure 1-4). The injected electrons will in turn be transferred to a photoanode that is in contact with the semiconducting oxide. The photoanode is spatially separated from a photocathode, creating directional flow of electrons in the circuit and allowing power to be produced by the cell. After photoexcitation and electron transfer, a redox couple in the electrolyte, which is in contact with the dye, transfers an electron to the oxidized dye, regenerating the dye for continued light excitation. The redox couple, once oxidized,

diffuses less than 50 μm to the photocathode or counter electrode, which is typically a thin layer of platinum deposited onto a fluorine-doped tin oxide (FTO) glass substrate, where the oxidized redox couple is reduced.

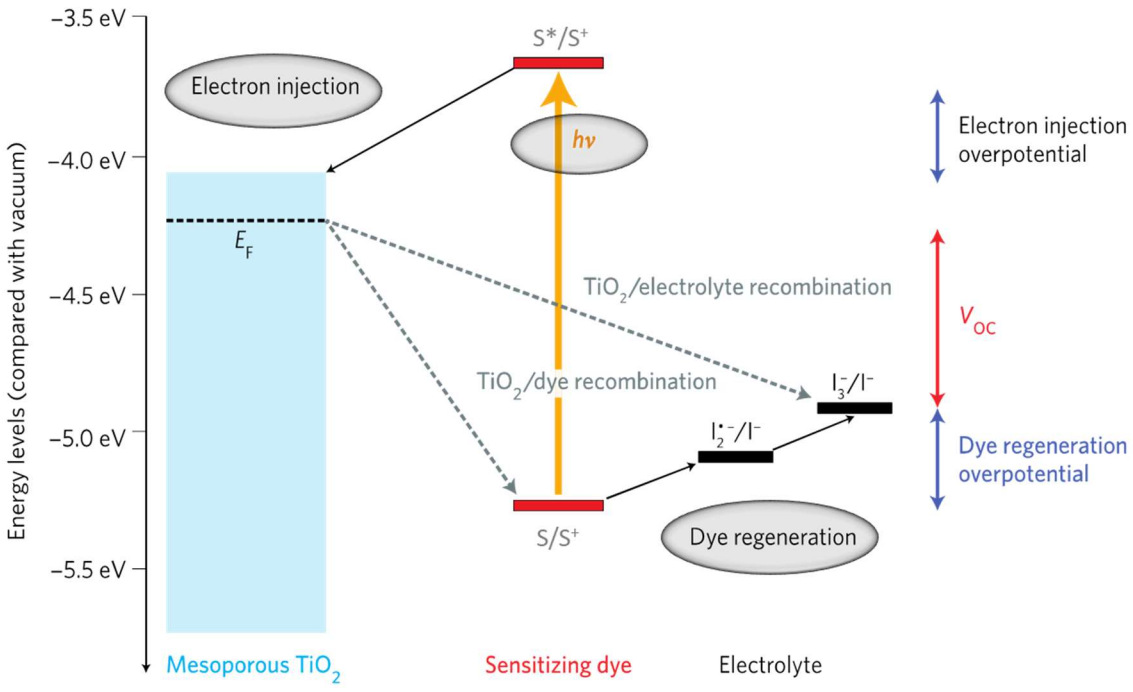

Figure 1-4. Electron transfer processes in the DSSC system employing TiO_2 and the I^-/I_3^- redox couple. Blue region indicates the band gap of TiO_2. Adapted from Hardin *et al.*[31] with permission from The Royal Society of Chemistry.

Possible competing back electron transfer reactions include recombination from TiO_2 to the oxidized dye and recombination from TiO_2 to the oxidized form of the redox couple (Figure 1-4).[32,33] It is important to note that the excited state oxidation potential should have sufficient driving force, or overpotential, for electron injection, while the ground state oxidation potential must have sufficient driving force for regeneration. The

instances of electron transfer are detailed below, where S is the dye or sensitizer, RC is the reduced form of the redox couple, CE is the counter electrode, and SC is the semiconducting oxide.

Forward reactions

$S \mid SC + h\nu \rightarrow S^* \mid SC$	Photoexcitation
$S^* \mid SC \rightarrow e^-_{cb}\,(SC) + S^+ \mid SC$	Electron injection
$S^+ \mid SC + RC \rightarrow S \mid SC + RC^+$	Dye regeneration
$RC^+ + e^-\,(CE) \rightarrow RC$	Regeneration at counter electrode

Back reactions

$S^* \mid SC \rightarrow S \mid SC + h\nu + \nabla$	Excited state deactivation (∇=heat)
$S^+ \mid SC + e^-_{cb}\,(SC) \rightarrow S \mid SC$	Recombination to oxidized dye
$RC^+ + e^-_{cb}\,(SC) \rightarrow RC$	Recombination to oxidized RC

Electron transfer between neighboring dye molecules may be possible when there is aggregation of the dye instead of a monolayer on TiO_2. A monolayer of dye allows each dye molecule to be bound to TiO_2 via anchoring groups that facilitate electron transfer through coupling of electronic orbitals. A multilayer or partially anchored

aggregate allows light to be absorbed by unanchored dyes that may not efficiently transfer electrons to the photoanode.

Electron transfer from the dye to the TiO_2 will only occur if the excited electron has energy above that of the TiO_2 conduction band with enough driving force, or overpotential, to drive injection. The high surface area mesoporous TiO_2 facilitates electron injection due to the large number of adsorbed dyes, and a light scattering layer of larger nanoparticles (~100 nm diameter) is used to increase absorption of light passing through the cell. Metal oxides such as ZnO[34–36] and SnO_2[37–39] have been tested in hopes of improving transport mobility and UV-stability of the electron acceptor, though TiO_2 is the most widely used.

Regeneration of the oxidized dye will only occur if the potential of the oxidized dye is sufficiently more oxidizing than that of the oxidized redox couple. The iodine/iodide redox couple in an acetonitrile-based electrolyte was historically widely used due to its low viscosity and appropriate redox potentials. However, alternative redox couples have also been explored,[40] including copper complexes (Cu^{II}/Cu^{I}),[30,41–43] cobalt complexes (Co^{III}/Co^{II}),[20,44–49] a disulfide/thiolate (T_2/T^-) couple,[50] 2,2,6,6-tetramethyl-1-piperidinyloxy ($TEMPO^+$/TEMPO),[51] the solid state redox mediator Spiro-OMeTAD (Figure 1-5)[52] , and other arylamines.[53]

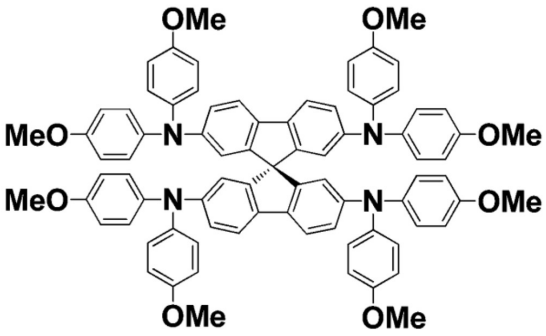

Figure 1-5. Molecular structure of Spiro-OMeTAD.

Due to the relatively large oxidizing potentials and lower required driving force for regeneration, high efficiency DSSCs have been obtained using cobalt and copper complexes as redox mediators for improved V_{OC}.[20,41] Copper complexes provide a tunable oxidation potential as low as 0.97 V vs. SHE (Figure 1-6), and have been reported to require as little as 0.2 eV in overpotential.[30,42]

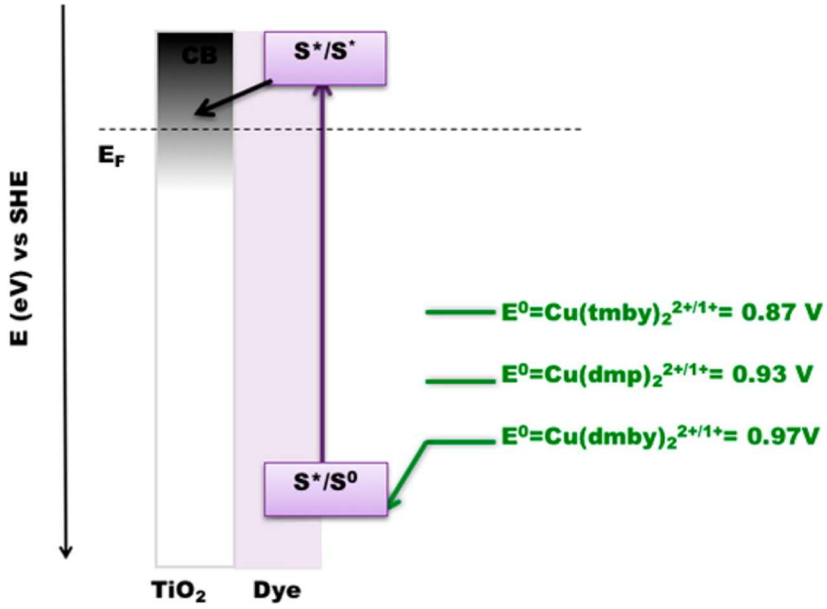

Figure 1-6. Oxidation potentials of copper complexes used as redox mediators in DSSCs. Ligands: dmby = 6,6′-dimethyl-2,2′-bipyridine, tmby = 4,4′,6,6′-tetramethyl-2,2′-bipyridine, and dmp = bis(2,9-dimethyl-1,10-phenanthroline). Adapted from Saygili *et al.*[30] with permission. Copyright 2016 American Chemical Society.

1.2.2 DSSC development

1.2.2.1 A path to 20% PCE

Capturing a large range of the solar spectrum down to an energy of 1.1 eV was calculated by Shockley and Queisser[54] to lead to a maximum PCE of 30% for an ideal single junction solar cell. This calculation was for an ideal device, where no driving force is required for charge separation and the only recombination mechanism of hole-electron pairs is radiative. Therefore, efficiencies attainable in a realistic device with nonradiative recombination and losses in overpotential are lower than this 30% limit, pushing the optimal onset of absorption to a higher energy. Snaith examined the maximum efficiencies that may be attainable specifically for the DSSC system under various assumptions (Figure 1-7), and estimated that a maximum efficiency of 20% would be possible with an optical bandgap of 1.31 eV (940 nm) and a loss-in-potential of 0.4 eV.[5,55] In DSSCs, developing near-infrared sensitizers which maintain panchromatic absorption across the visible spectrum and redox couples requiring low overpotentials has therefore been pursued as a route to improving J_{SC} and overall PCE.

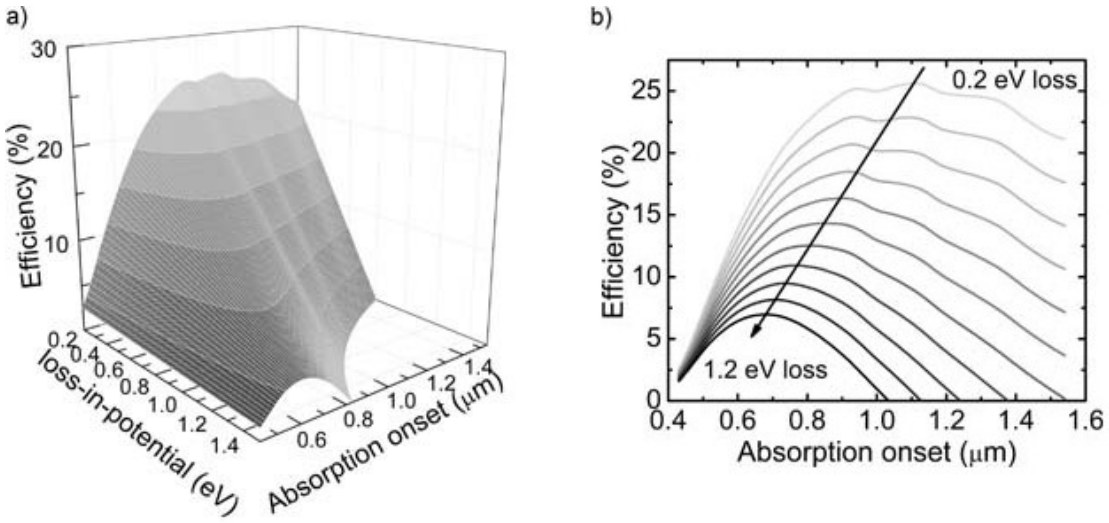

Figure 1-7. a) Three-dimensional plot of the estimated PCE of a sensitized solar cell exposed to AM 1.5 illumination of 100 mW cm^{-2}, as a function of the absorption onset and the loss-in-potential, going from the optical bandgap of the sensitizer to the V_{OC} under full sun illumination. For all calculations, the fill factor is set at 0.73. The J_{SC} over the range of absorption onsets is as calculated by integrating the hypothetical spectral response curves over the AM 1.5 solar spectrum. The V_{OC} is the absorption onset energy – the loss-in-potential. b) Slices of the same dataset at constant loss-in-potential, going from 0.2 to 1.2 eV losses with increments of 0.1 eV. The arrow indicates increasing loss-in-potential and a corresponding blueshift of the peak efficiency absorption onset. Reproduced from Snaith[5] with permission from John Wiley and Sons, Ltd.

1.2.2.2 Sensitizer development

As the light-harvesting component, the sensitizer's electrochemical, photophysical, and ground- and excited-state properties influence its ability to effectively transfer an electron into the TiO_2 conduction band and to be regenerated by the redox couple. In general, the ideal sensitizer should exhibit the properties of strong panchromatic absorption across the visible and near-infrared (near-IR), a suitable anchoring group, appropriate ground and excited state redox potentials, appropriate interaction with the electrolyte, and photochemical and thermal stability.

Both inorganic complexes and organic dyes have been pursued as sensitizers for DSSCs. The ruthenium complex sensitizer **N3** and its doubly deprotonated analog **N719** (Figure 1-8) held the record for DSSCs for many years at 9-10% PCE. The ruthenium complex sensitizer **N-749** increased J_{SC} relative to **N-719** by shifting absorption by over 100 nm further into the near-infrared while maintaining panchromatic absorption across the visible spectrum. **N-749** yielded a J_{SC} of over 20 mA/cm^2 with a similar PCE of 10% as **N-719** due to a lower V_{OC}.[56]

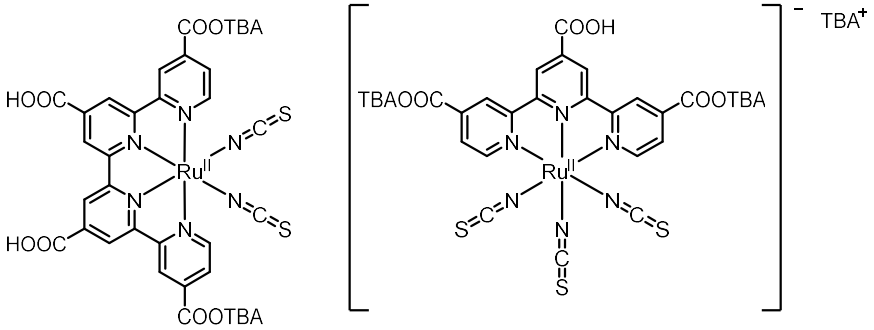

Figure 1-8. Molecular structures of sensitizers **N719** and **N749**.

Sensitizers incorporating non-precious metals have also reached record efficiencies due to significant near-IR absorption and due to employing cobalt redox couples such as $[Co(bpy)_3]^{2+/3+}$ (bpy = bipyridine) with more oxidizing potentials than the traditional iodine/triiodide electrolyte. The porphyrin sensitizer **SM315** (Figure 1-9) produced the highest performing singly-sensitized dye-sensitized solar cell at a PCE of 13%. **SM315** improved PCE relative to **SM371** (similar to **YD-2-*o*-C8**[20]) by using benzothiadiazole to bathochromically shift the absorption onset to near 750 nm without a

significant compromise of the absorption in any particular region to yield a J_{SC} of 18.1 mA/cm^2 and an overall PCE of 13.0% with a V_{OC} of 0.91 V.[21] **SM371** and **SM315** also utilized alkoxy groups *ortho*- and *para*-substitued onto out-of-plane phenyl rings. The alkoxy groups on the non-anchoring side of the molecule are hypothesized to prevent close interactions with the $[Co(bpy)_3]^{2+/3+}$ redox couple in the electrolyte for improved overall PCE.

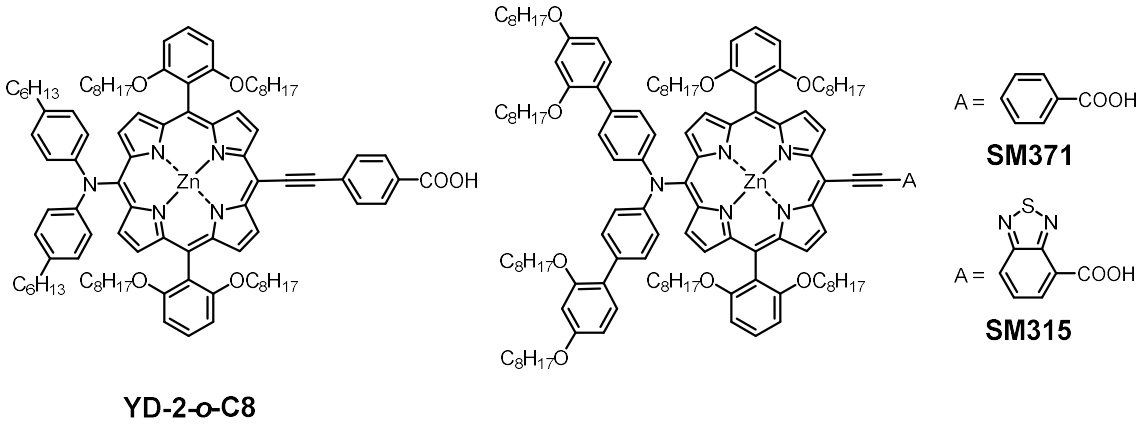

Figure 1-9. Molecular structures of sensitizers **YD-2-*o*-C8**, **SM371** and **SM315**.

The alkoxy groups *ortho*- and *para*-substituted onto out-of-plane phenyl rings were originally employed in the sensitizer **D35**,[46] (Figure 1-10) then later in **Y123**[44,45] and **LEG4**,[57] which were shown to perform well with the $[Co(bpy)_3]^{2+/3+}$, $[Cu(dmp)_2]^{1+/2+}$,[42] $[Cu(tmpy)_2]^{2+/1+}$, and $[Cu(dmpy)_2]^{2+/1+}$ redox couples (dmby = 6,6′-dimethyl-2,2′-bipyridine, tmby = 4,4′,6,6′-tetramethyl-2,2′-bipyridine, and dmp = bis(2,9-dimethyl-1,10-phenanthroline).[30]

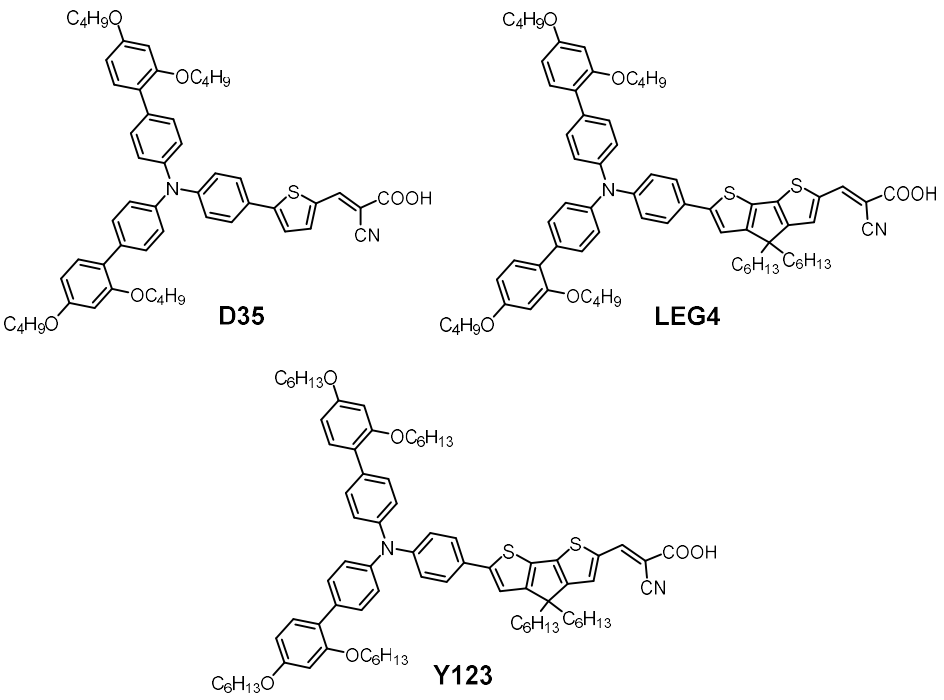

Figure 1-10. Molecular structures of sensitizers **D35**, **LEG4** and **Y123**.

The highest reported PCE in dye-sensitized solar cells is based on a co-sensitized device employing sensitizers **ADEKA-1** (Figure 1-11) and **LEG4** to achieve a PCE of 14.3%. Rather than the cyanoacrylic acid anchoring group, **ADEKA-1** employs a silyl anchoring group, known for its ability to form stable, robust monolayers.

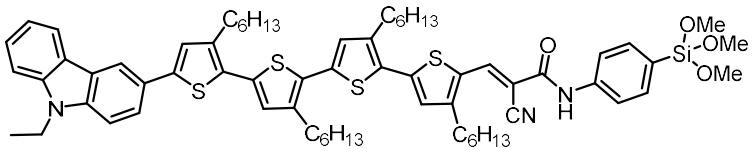

Figure 1-11. Molecular structure of sensitizer **ADEKA-1**.

Although the calculated LUMO distribution makes it clear that electronic coupling with the metal oxide is unlikely to pass through the silane anchor,[23] **ADEKA-1** is an example of the performance that could be achieved with a very strongly bound stable monolayer. Strongly bound sensitizers can promote a fuller coverage of the TiO_2 surface either through increased dye-loading of sensitizers or through strongly bound co-adsorbents.[58,59] A tightly packed monolayer will theoretically result in an increased V_{OC} due to decreased TiO_2-electrolyte recombination.[60] Jradi *et al*. used cyanovinylphosphonic acid as strongly binding alternative to the cyanoacetic acid anchoring group.[61,62] Although a decreased performance and electron injection efficiency (η_{inj}) was observed with use of the cyanovinylphosphonic acid in sensitizer **DTS-PA** relative to the use of cyanoacetic acid in **DTS-CA** (Figure 1-12), promising PCEs of up to 5.0% (unmasked) for the cyanovinylphosphonic acid-anchored **DTS-PA** were achieved.

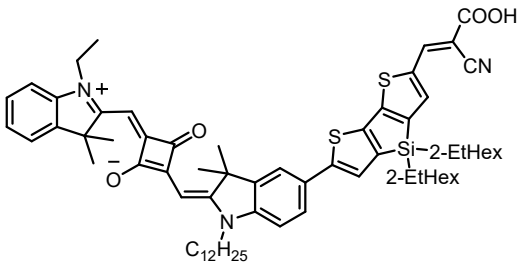

DTS-CA

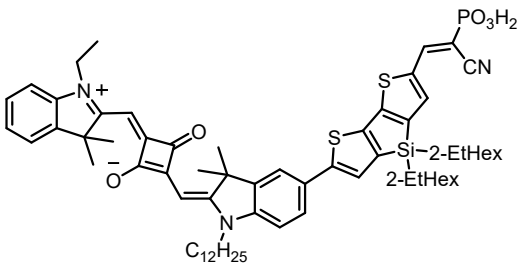

DTS-PA

Figure 1-12. Molecular structures of sensitizers **DTS-CA and DTS-PA**.

1.2.2.3 Photovoltaic characterization of dye-sensitized solar cells

A deeper understanding of what contributes to J_{SC} and V_{OC} is necessary for drawing meaningful conclusions from photovoltaic results. The following discussion draws from reviews by Hamann and Ondersma,[63] Hagfeldt,[32] and Graetzel.[60]

The J_{SC} depends on processes occurring at the TiO_2/dye/electrolyte interface as well as the diffusion of the redox couple to and from the counter electrode. In the case of efficient electrolyte diffusion, the J_{SC} essentially depends on processes occurring at the TiO_2/dye/electrolyte interface. The J_{SC} (Equation 1-5) will be a function of the photon flux (Φ_p) over the λ's of interest of the dye and TiO_2, of the dye absorptance (α_λ), and of the charge injection, dye regeneration, and charge collection efficiencies (η_{inj}, η_{reg}, η_{cc}, respectively).

$$J_{SC} = q\left(\int_{\lambda_{TiO_2}}^{\lambda_{dye}} \Phi_p(\lambda)\alpha_\lambda d\lambda\right)\eta_{inj}\eta_{reg}\eta_{cc} \qquad 1\text{-}5$$

where q is the elementary charge. The η_{inj} is the kinetic competition between electron injection and deactivation of the excited state dye, η_{reg} is the kinetic competition between dye regeneration and recombination with the oxidized dye, and η_{cc} is the kinetic competition between electron transport in TiO_2 and recombination with the redox couple. J_{SC} therefore describes a complex race, the start of which is light absorption.

Taking a closer look at open-circuit voltage (V_{OC}), one notes that when the current is zero, the previous photocurrent density (J_{SC}) is completely offset by recombination. Recombination can be from TiO_2 to the oxidized dye, or from TiO_2 to the oxidized form of the redox couple in the electrolyte. If dye regeneration is efficient, then recombination

to the dye can be considered negligible, and the V_{OC} will mainly be affected by recombination to the oxidized redox couple.[63] If one assumes that the concentration of electrons at the semiconductor surface (n_s) is in rapid equilibrium with the number of electrons in the bulk TiO_2, (N_C), and that recombination with n_s is first order, one can obtain an expression for V_{OC} (Equation 1-6),

$$V_{OC} = \frac{kT}{q} \ln\left(\frac{J_{SC}\tau_0}{q\zeta n_0}\right) \qquad 1\text{-}6$$

where n_0 is the electron concentration in the conduction band in the dark and τ_0 is the recombination in the dark.

Therefore, V_{OC} and J_{SC} are not separable quantities, and, to some extent, an increase in V_{OC} can be achieved by increasing J_{SC}. Increasing electron lifetime (τ_0) through decreased recombination will also improve V_{OC}, and a tightly packed monolayer blocking dark current is a strategy for doing so.[60] Significant changes in V_{OC} can be achieved by making the solution potential more positive via the redox couple potential, as a more positive redox couple potential will decrease n_0. The potential of the electrolyte will also affect electron injection, influencing η_{inj} and therefore J_{SC}.[32]

Fill factor depends mainly on the diode quality and the V_{OC}. For the diode quality, series and shunt resistance are considered. In DSSCs, shunt resistance can generally be avoided through use of a compact TiO_2 blocking layer, so after the V_{OC}, series resistance has the largest effect on FF, and can be caused by a variety of processes such as recombination from TiO_2 to the electrolyte. Charge transfer resistance at the counter electrode can also affect the FF.

1.2.3 Photoelectrochemical characterization of dye-sensitized solar cells

Photoelectrochemical methods are advantageous for the study of DSSCs under actual operating conditions.[32] Photovoltage and photocurrent transients examine the electron's behavior in the semiconducting oxide, which provides a deeper understanding of the electron movement in the semiconducting film, including the presence of electron traps and presence of recombination processes, which are influenced by the electrolyte. Impedance spectroscopy is another method that can be used to distinguish the interfacial capacitance from the charge-transfer resistance and can be used to understand components of electrolyte diffusion.[32,33,64]

This introduction will focus on the use of small light modulation techniques in DSSC devices employing an iodide/triiodide electrolyte. Boschloo *et al*. provide an in-depth description of the use of small light modulation techniques for extracting information about the origin of changes in device performance due to addition of 4-*tert*-butylpyridine, and their work is featured as an example analysis in the following sections.[65]

1.2.3.1 Charge extraction

The Fermi level (E_F, section 0) of the electrons in a semiconductor is determined by the density of conduction band electrons and states (Equation 1-7)

$$E_F = E_{CBM} + kTln(\frac{n_c}{N_C}) \qquad 1\text{-}7$$

where kT is the thermal energy, E_{CBM} is the conduction band minimum energy, n_c is the density of conduction band electrons, and N_C is the effective density of conduction band states.[65]

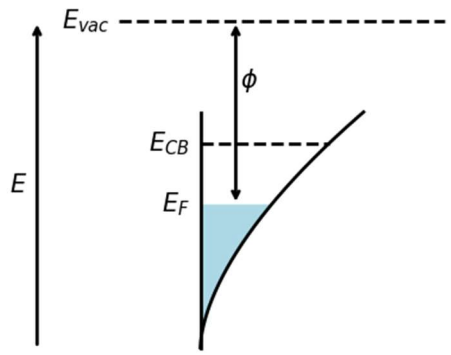

Figure 1-13. Work function (ϕ) illustrated for the TiO_2 semiconductor with surface trap states below the conduction band minimum.

The difference between E_F at the TiO_2 surface and the redox potential of the electrolyte determines in large part the measured potential in the device. Following Equation 1-7, an increase or decrease in E_F and therefore V_{OC} can be ascribed to either 1) a shift of E_{CBM} to a higher or lower energy, 2) an increase or decrease in conduction band electron concentration (n_c/N_C) under open-circuit conditions, or 3) a combination of a shift of E_{CBM} and a change in n_c/N_C (Figure 1-14).

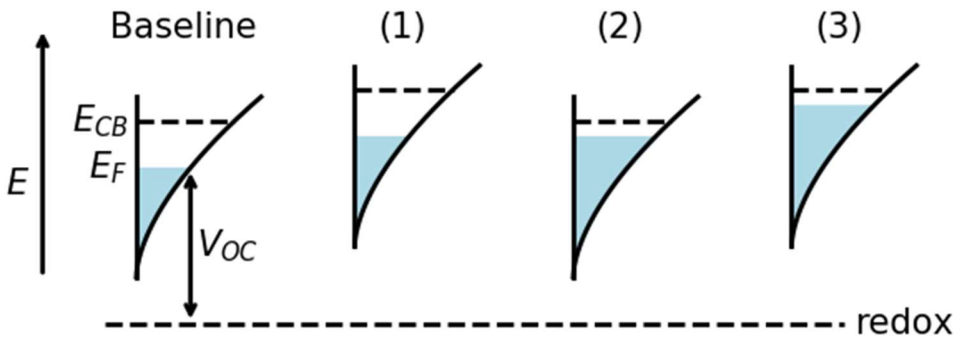

Figure 1-14. Possible causes of an increase in V_{OC}: 1) E_{CBM} increase, 2) n_c/N_C increase, or 3) E_{CBM} and n_c/N_C increase.

The purpose of the charge extraction measurement is to quantify the total shift in V_{OC} (Figure 1-14, part 3) and elucidate the origin of the V_{OC} (Figure 1-14, parts 1 and 2) for a series of devices. An assembled device is held in the dark, then a fixed light intensity is turned on and the device is held at open circuit. The V_{OC} is observed, then the light is turned off and the device is switched to short circuit, where the current is monitored over time and the extracted charge (Q_{OC}) is calculated. Charge extraction measures the number of electrons filling the conduction band at a certain V_{OC}.

A plot of the V_{OC} obtained vs. light intensity (Figure 1-15) may be examined to first quantify the shift in V_{OC} for the series of devices. For example, Boschloo *et al.*[65] noted a change of 260 mV in the V_{OC} when 0 vs. 500 mM 4-*tert*-butylpyridine (4TBP) was employed (Figure 1-15).

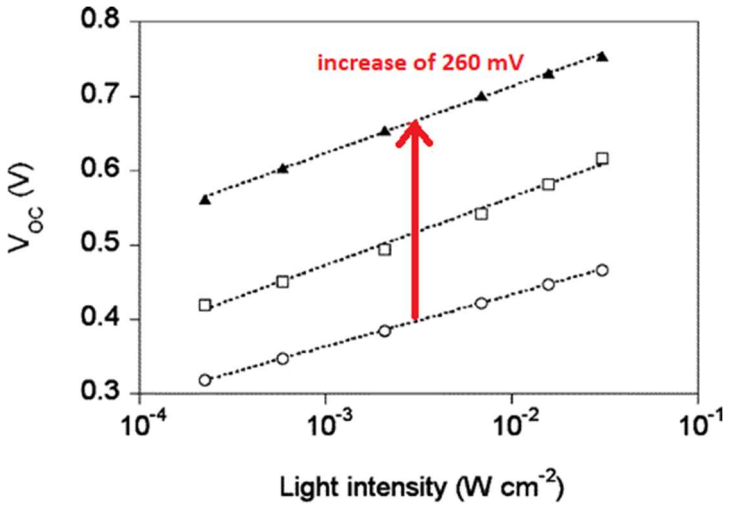

Figure 1-15. Light intensity dependence of the V_{OC} of dye-sensitized TiO_2 solar cells with 4TBP concentrations in the electrolyte of: 0 mM (circles), 55 mM (squares), 500 mM (triangles). The red arrow shows the increase in V_{OC} from 0 to 500 mM 4TBP. Adapted with permission from Boschloo *et al*.[65] Copyright 2006 American Chemical Society.

Next, a plot of charge extraction under open circuit conditions (Q_{OC}) vs. V_{OC} (Figure 1-16) can be examined to elucidate the origin of the changes in V_{OC}, since the change in V_{OC} can be compared at identical levels of extracted charge, or approximately identical concentrations of conduction band electrons (n_c/N_C).

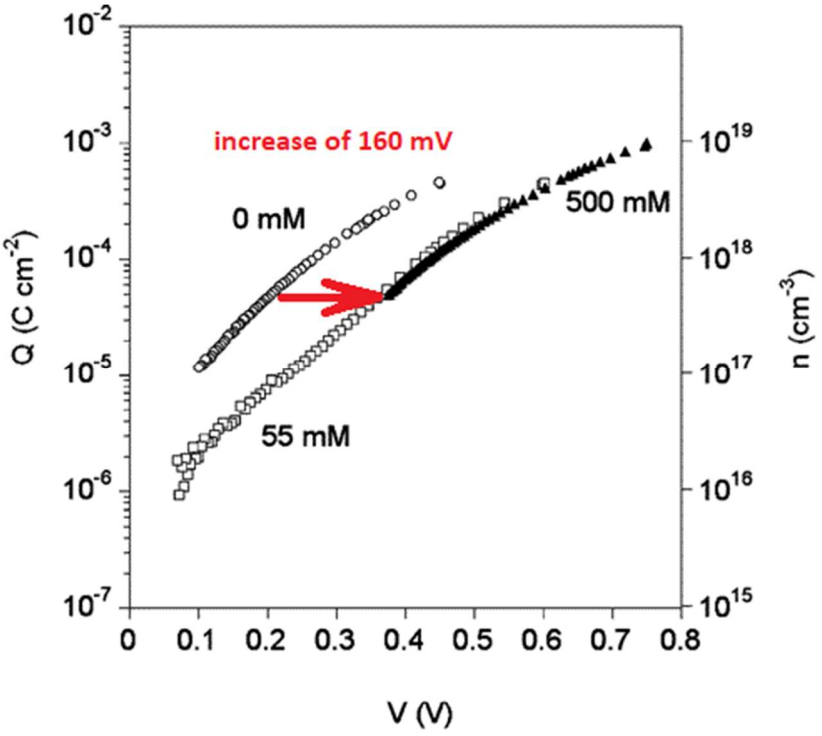

Figure 1-16. Extracted charge and electron density as a function of the open-circuit potential in dye-sensitized TiO_2 solar cells. The 4TBP concentration in the electrolyte is indicated. The red arrow indicates the increase in V_{OC} from 0 to 500 mM 4TBP. Adapted with permission from Boschloo *et al.*[65] Copyright 2006 American Chemical Society.

The ΔV_{OC} seen at constant extracted charge, approximating constant n_c/N_C, is the portion of the total ΔV_{OC} that is due to a shift of the E_{CBM} (Figure 1-14, part 1). From this quantity and the total ΔV_{OC} seen in a plot of V_{OC} vs. light intensity, one can calculate the portion of the total ΔV_{OC} that is due to a higher concentration of conduction band electrons under open-circuit conditions (due to increased $(n_c/N_C)_{OC}$) (Figure 1-14, part 2) (Equation 1-8), which in the referenced Boschloo *et al.* article[65] was 100 mV.

$$\Delta V_{OC}\ (from\ \Delta(n_c/N_C)_{OC}) = \text{total}\ \Delta V_{OC} - \Delta V_{OC}(from\ \Delta E_{CBM}) \qquad 1\text{-}8$$

1.2.3.2 Electron lifetime and electron transport time

Additional information can be obtained from plots of electron lifetime and electron transport time. The electron lifetime (τ_e) describes the kinetics of recombination of electrons in the TiO_2 film with acceptors in the electrolyte.[32] The electron transport time (τ_e) describes the kinetics of electrons transported through the the TiO_2 film to the anode. The electron transport time (τ_{tr}) and electron lifetime (τ_e) can be derived from time-resolved small modulation techniques.[32] Small square wave light intensity modulations are applied over a larger constant light intensity, and a time constant is obtained from fitting the photocurrent response (Figure 1-17). A large baseline light intensity is used so that the E_F remains high and relatively constant under all measurement conditions.

A time constant for the photocurrent response to the light intensity modulation (τ_{pc}) will depend on the electron transport time (τ_{tr}) and the electron lifetime (τ_e) according to Equation 1-9:

$$(\tau_{pc})^{-1} = (\tau_{tr})^{-1} + (\tau_e)^{-1} \qquad 1\text{-}9$$

For the measurement of electron transport, a device is held under a fixed light intensity at short circuit, then the light intensity is increased by a small amount of the total light intensity. The J_{SC} is observed, then the small modulation is ended, and the decay of the photocurrent is fitted to a time constant. Since the device is held at short circuit, the electrons will mainly be transported through the TiO_2 and will largely not recombine with the electrolyte or dyes. Therefore, a high electron transport equals efficient transport of the electrons in the TiO_2 film to the anode. In other words, under

short circuit conditions, the electron lifetime is generally significantly longer than the electron transport time, so the photocurrent decay (Figure 1-17) will be derived almost exclusively from electron transport, and the time constant fitted to the photocurrent decay will therefore be approximately equal to the electron transport time. The electron transport time will be affected by film thickness and by charges at the TiO_2 surface or surface states that may affect electron transport.

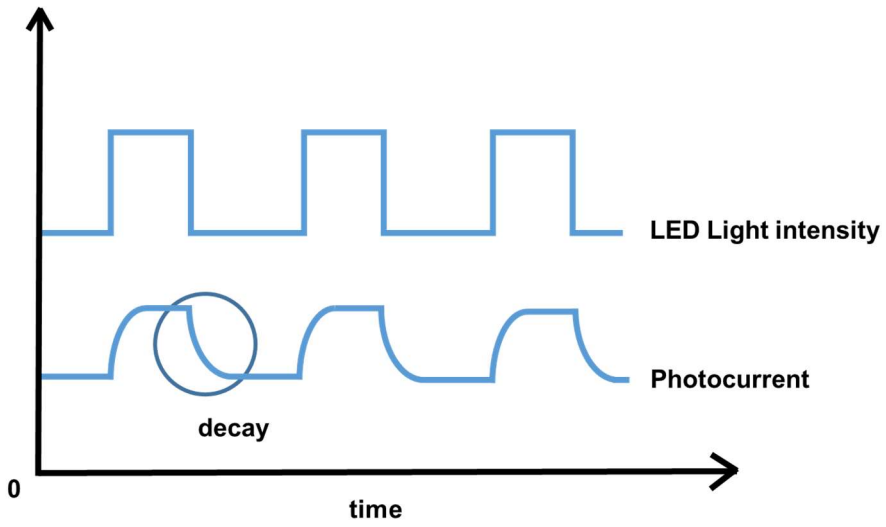

Figure 1-17. Schematic representation of electron transport measurement, with photocurrent response to small modulations of light intensity and time constants extracted from a circled "decay" portion of the spectrum.

For the measurement of electron lifetime, a device is held under a fixed light intensity at open circuit, then the light intensity is increased by a small amount of the total light intensity (Figure 1-18). The potential (V_{OC}) is observed, then the light intensity increase is ended. The decay of the photovoltage is observed and fitted to a time constant. Under open-circuit conditions, the photogenerated electrons in the TiO_2 will largely

recombine with the electrolyte to reduce the potential, rather than being extracted at the counter electrode. This makes the photovoltage decay time constant depend on TiO_2-electrolyte recombination in the device, with the time constant approximately equal to τ_e, the electron lifetime. A high electron lifetime (τ_e) indicates low recombination of electrons in the TiO_2 film with acceptors in the electrolyte, and an increase in the recombination rate of electrons in TiO_2 with triiodide in the electrolyte will decrease the electron lifetime in TiO_2. A dye may increase the electron lifetime by making the TiO_2 surface less accessible to triiodide ions in the electrolyte.

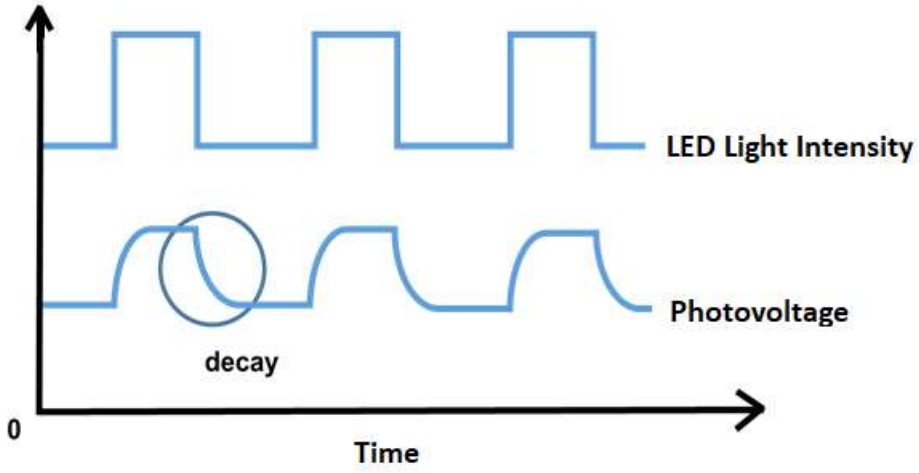

Figure 1-18. Schematic representation of electron lifetime measurement, with photovoltage response to small modulations of light intensity and time constants extracted from a circled "decay" portion of the spectrum.

Electron lifetime may be plotted vs. light intensity and compared to the transport lifetime (Figure 1-19). From this plot, the differences in how electron transport time changes vs. electron lifetime are apparent. Often a difference of approximately 1 order of magnitude is seen between τ_{tr} and τ_e.

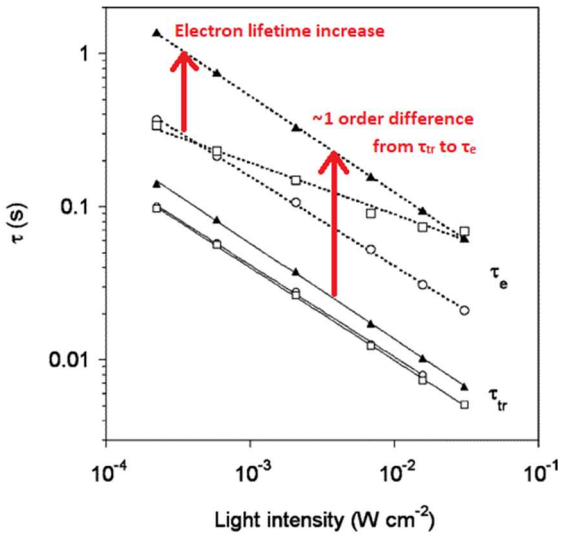

Figure 1-19. Electron transport times τ_{tr} and lifetimes τ_e as functions of the light intensity. Time constants were determined using time-resolved small light modulation techniques. The dotted lines correspond to power-law fits. 4TBP concentration: 0 mM (circles), 55 mM (squares), 500 mM (triangles). Adapted with permission from Boschloo *et al.*[65] Copyright 2006 American Chemical Society.

Electron lifetime also may be plotted vs. V_{OC} (Figure 1-20) or vs. Q_{OC} (Figure 1-21). From the plot of τ_e vs. V_{OC}, one can examine whether the plot shows an exponential decrease of τ_e with V_{OC}, and the change in V_{OC} can be seen. The plot of τ_e vs. Q_{OC} shows the dependence of τ_e on the total electron concentration in the mesoporous TiO_2. The slope can be noted, along with quantitative increases in τ_e at identical levels of Q_{OC}.

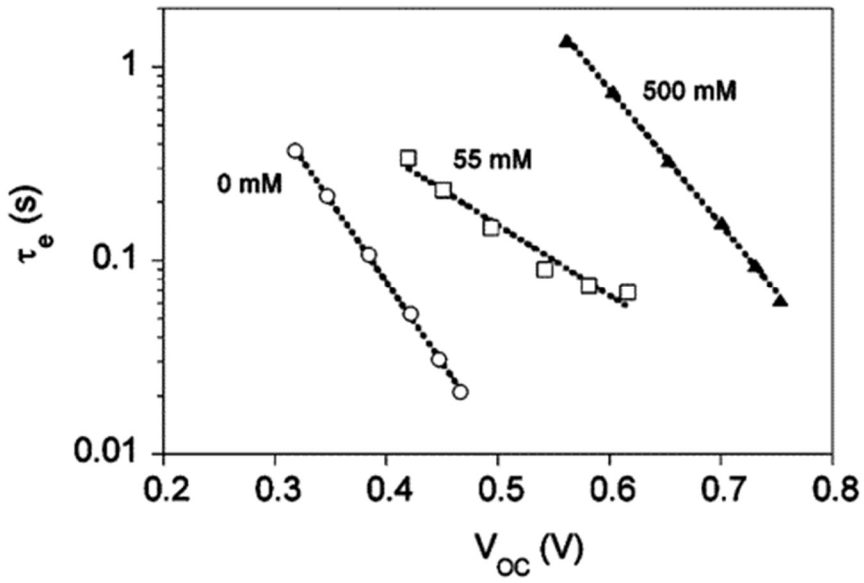

Figure 1-20. Electron lifetime τ_e as a function of V_{OC}. Time constants were determined using time-resolved small light modulation techniques. The dotted lines correspond to power-law fits. 4TBP concentration: 0 mM (circles), 55 mM (squares), 500 mM (triangles). Adapted with permission from Boschloo *et al*.[65] Copyright 2006 American Chemical Society.

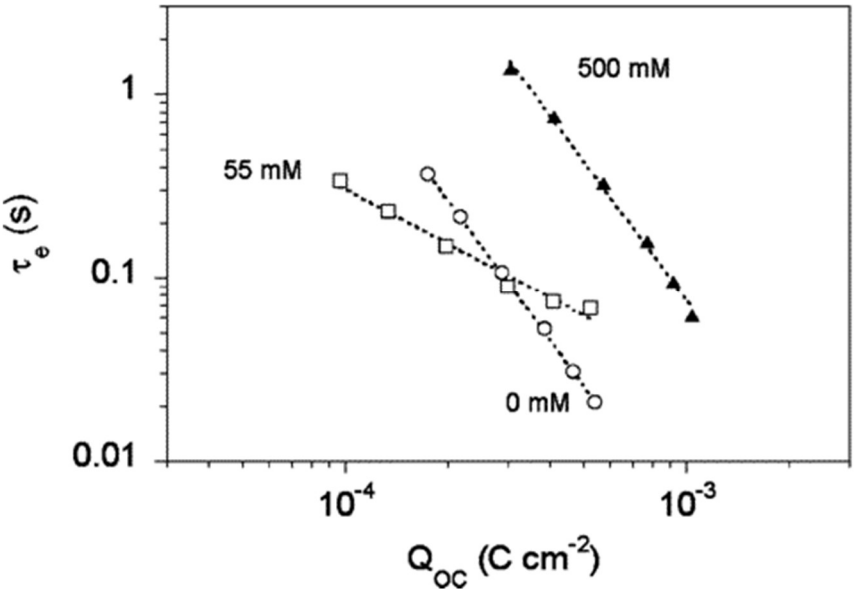

Figure 1-21. Electron lifetime τ_e as a function of Q_{OC}. Time constants were determined using time-resolved small light modulation techniques. The dotted lines correspond to power-law fits. 4TBP concentration: 0 mM (circles), 55 mM (squares), 500 mM (triangles). Adapted with permission from Boschloo *et al*.[65] Copyright 2006 American Chemical Society.

1.3 Perovskite Solar Cells *(*PSCs*)*

Organic-inorganic perovskites are emerging as ideal materials for photovoltaic, photonics, and optoelectronic applications due to their large absorption coefficients,[66,67] bipolar charge transport,[68–70] low bandgaps,[70] long carrier diffusion lengths,[71] and small exciton binding energies.[72,73] The power conversion efficiency (PCE) of perovskite solar cells has increased rapidly and has reached efficiencies of 21-23% over a few years.[6,24,27,74,75]

1.3.1 PSC architecture

Perovskite materials are a broad class of materials of the ideal formula ABX_3 of the structure type shown in Figure 1-22. Of relevance to solar cells are those where A = methylammonium, ethylammonium, formamidinium, or Cs; B = Pb or Sn, and X = I, Br, or Cl. Perovskites of this type are of interest for photovoltaics due to their outstanding electronic properties as both hole and electron conductors (intrinsic semiconductors) with long diffusion lengths,[71] their relatively low band gaps in the range of 1.3-1.8 eV,[76] and their ability to be solution-processed at relatively low temperatures.[77]

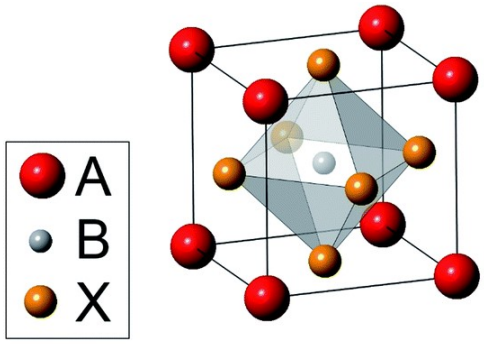

Figure 1-22. Generic perovskite crystal structure. Reproduced from Eperon *et al*.[76] with permission from The Royal Society of Chemistry.

Lead organohalides were investigated for use in transistors[25] and LEDs[26] before their use in quantum dot-sensitized solar cells by Miyasaka *et al*.[27] The ground-breaking report by Lee *et al*. published the first example of using a solution-processable hybrid organic-inorganic perovskite material as a thick active layer on top of a nanocrystalline TiO_2 layer.[24] Various architectures have since been developed (Figure 1-23).

The current record-holding PSCs are formamidinium lead iodide ($FAPbI_3$) -based perovskites first introduced by Eperon *et al*.[76] with broadly tuneable band gaps compared to methyl ammonium lead iodide-based perovskites.[75] Dense and uniform $FAPbI_3$ films were achieved by Yang *et al*. through the use of DMSO in film processing, with the direct exchange of DMSO molecules for formamidinium ions during perovskite film formation hypothesized.[78]

Currently, the highest efficiency perovskite solar cells employ a mesosporous electron transport layer (ETL). However, perovskite incorporation into the mesoporous layer is not necessary for sufficient light absorption and charge generation in the device,

and alternative architectures with nonporous ETLs, called "planar" devices, have been introduced.[79,80]

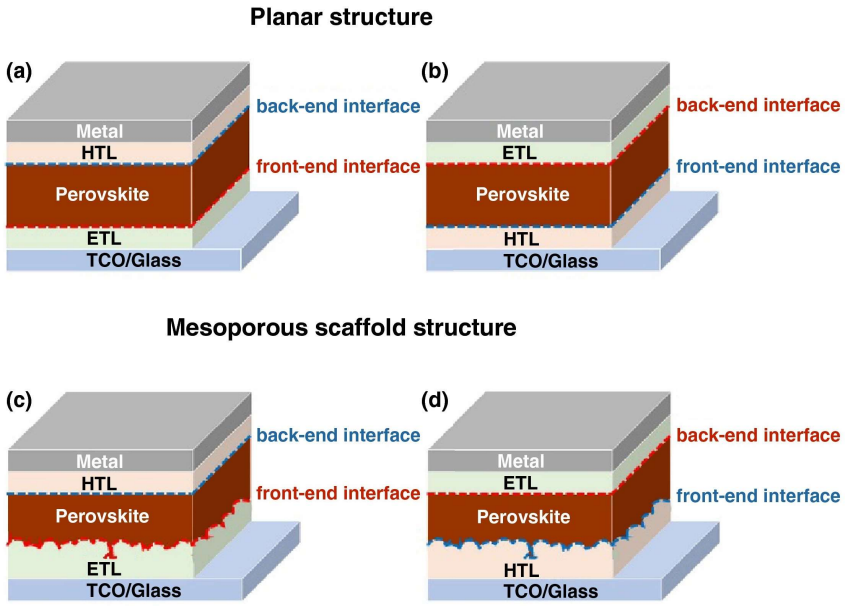

Figure 1-23. Perovskite solar cell device structures with four different types of interfaces: (a) planar n-i-p, (b) planar p-i-n, (c) mesoscopic n-i-p, and (d) mesoscopic p-i-n. Reproduced from Manspeaker *et al.* [81] with permission from Elsevier.

1.3.2 Current areas of research

1.3.2.1 Hysteresis

Snaith et al. were the first to discuss in depth the occurrence of hysteresis in the current-voltage curves of perovskite solar cells, a phenomenon not observed in other photovoltaic technologies.[82] The term hysteresis here describes a change in the photovoltaic response for a *J-V* scan done from forward to reverse bias vs. from reverse

to forward bias, resulting in non-superimposable *J-V* curves. Even high-performing devices exhibit a moderate level of hysteresis, as shown in Figure 1-24.

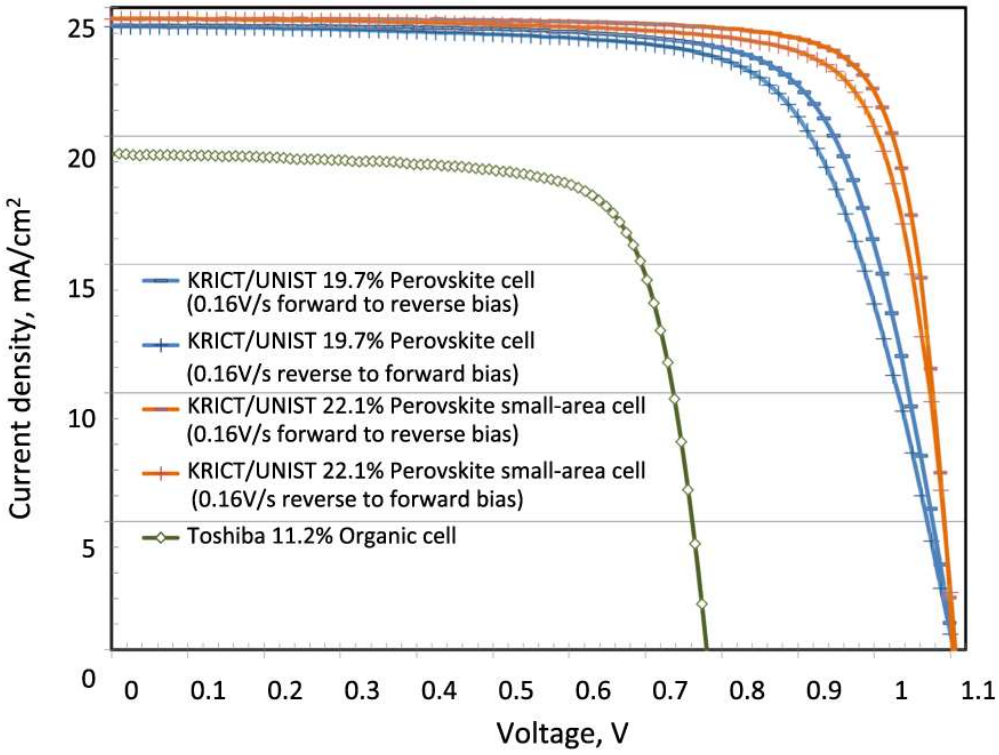

Figure 1-24. Current-voltage (*J-V*) curves for high efficiency perovskite and organic solar cells. Reproduced from Green *et al*.[83] with permission from John Wiley & Sons, Ltd.

Kim and Park noted a larger crystal size tended to diminish hysteresis.[84] The presence of fullerene electron transport layers in n-i-p[85] or p-i-n[86] architectures with diffusion into the perovskite was also seen to decrease hysteresis, with surface and grain boundary charge trap states seen to be a major cause of hysteresis. Hysteresis was found to be related to ion migration and interfacial states in the perovskite, with reduction of the density of mobile ionic species or reduction of carrier trapping at the interface as proposed solutions.[87]

1.3.2.2 Stability

With their low-cost fabrication methods and record efficiencies reaching 22% PCE, perovskite solar cells are advancing toward commercialization, but increases in PSC stability are imperative. Ion migration and current-voltage hysteresis have been demonstrated to be related to the stability of perovskite solar cells. Moisture, light, and heat can be sources of decomposition, with device stability depending on the interfaces and contacts as well as the perovskite material itself.[88]

1.3.2.3 Interfacial engineering

Optimized interfaces play a significant role in device stability and are essential for perovskite solar cell commercialization. The choice of electrode and treatments at the interface can impact interface and device stability. The stability of a charge transport layer-perovskite interface can also be affected by its configuration in the device.[81]

Kaltenbrunner *et al*. reported an increase in device stability with a chromium oxide-chromium interlayer that protects the metal top contacts from reactions with the perovskite for increased device stability.[89] Cao *et al*. saw an increase in the stability of PSCs using a pentafluorobenzenethiol at the perovskite-HTL interface.[90] Rong *et al*. provide a more extensive review of possible degradation mechanisms and progress in stability due to interfacial engineering.[91]

1.3.2.4 Flexible and lightweight devices

Lightweight solar technologies can extend the flight time of unmanned aerial vehicles. Consumer electronics applications are another application of lightweight,

flexible solar cells. Technologies are needed that are highly efficient, lightweight, low cost, and stable during operation.[92] Based on their PCE per weight and low cost processing methods, perovskite solar cells can potentially compete with other thin film solar technologies (Figure 1-25).[89]

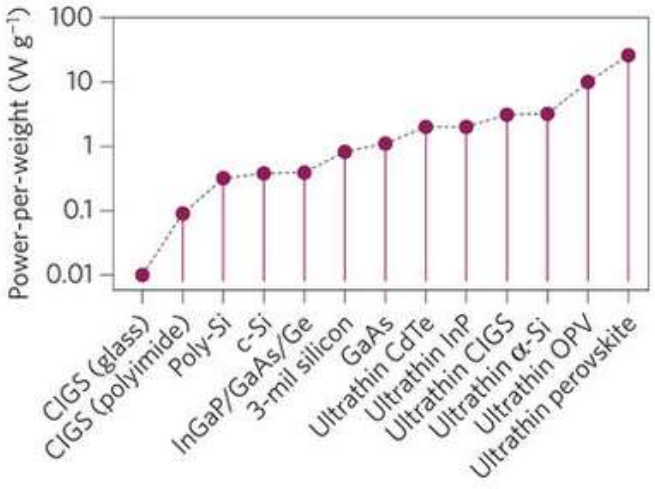

Figure 1-25. Comparison of power-per-weight of ultrathin (3 μm) perovskite solar cells using data compared from published academic results of leading lightweight solar cells. Reproduced from Kaltenbrunner *et al*.[89] with permission from Springer Nature.

Kaltenbrunner et al. described ultrathin (3 μm), flexible, and lightweight PSCs on a PET support that powered model airplanes for hours.[89] Li et al. replaced the PET support with a Ag-mesh/transparent conducting polymer (FEAM/PH1000) support for flexible PSCs with 14% PCE.[93] Advances continue to be made in hole and electron transport layers that facilitate flexibility.[94–97]

1.3.2.5 Hole transport layers

2,21,7,71-tetrakis-(N,N-di-4-methoxyphenylamino)-9,91-spirobifluorene, or Spiro-OMeTAD, is widely used as a hole transport material in n-i-p perovskite architectures. Spiro-OMeTAD was developed as a redox mediator for solid-state dye sensitized solar cells, and is a widely used HTL because of its appropriate redox potential for most perovskites (Figure 1-26), its lack of strong absorption in the visible range, and its ability to be spin-coated from solution. Spiro-OMeTAD must be doped to improve its mobility and the presence of the additives has been hypothesized to contribute to low device stability.[98]

PEDOT:PSS is a commonly used HTL for p-i-n perovskite architectures. PEDOT:PSS allows for low-temperature processing on flexible substrates, but is relatively acidic. PEDOT:PSS is also very conductive, which can cause difficulty in defining active area and can lead to overestimation of the device PCE.[99]

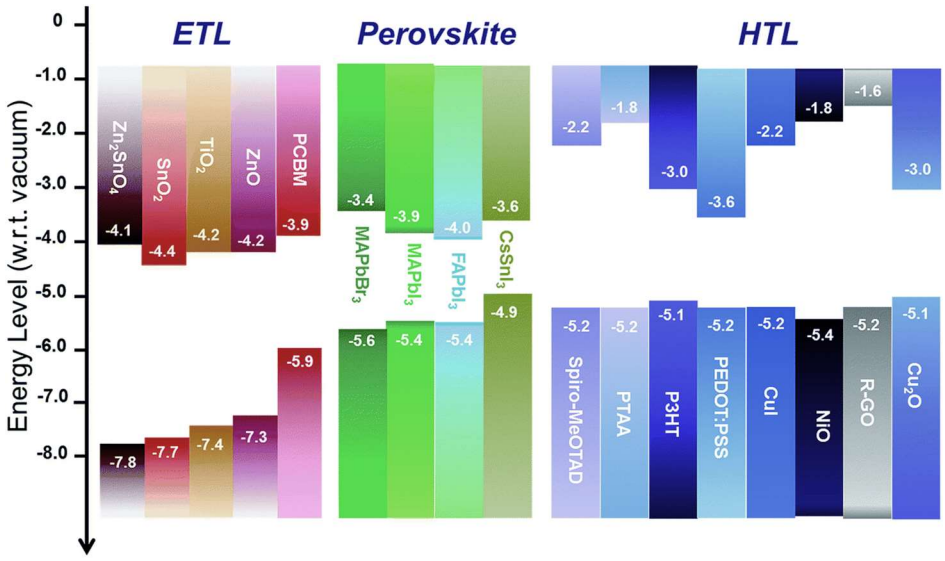

Figure 1-26. Illustration of literature values for energy levels with respect to the vacuum level of electron-selective (left), perovskite absorber, and hole-selective (right) layers in perovskite solar cells. These are the most commonly reported literature values, though values are spread over a wide range and may change according to deposition methods and post-deposition treatments. Adapted from Zardetto *et al.*[100] with permission from The Royal Society of Chemistry.

1.3.2.6 Electron transport layers for low-temperature processing

Inorganic TiO_2 (processed at >450 °C)[74,75] has been widely used as an electron-transporting layer (ETL) in planar solar-cell devices. However, the brittle nature and the high processing temperatures needed are incompatible with widely used flexible substrates, such as PEN and PET.

SnO_2 is an ETL that can be processed at moderate temperatures (≥180 °C).[101] SnO_2 was used as an ETL in perovskite solar cells following the original report of Baena *et al.* on the use of an ALD-deposited SnO_2 layer,[102] and spin-coated tin oxide ETLs have also

been developed.[103] SnO_2 ETLs improve PCE compared to TiO_2, and have the advantage of being able to be processed at lower temperatures (below 150 °C).

ZnO is an ETL with an order higher mobility than TiO_2 that can be processed at moderate temperatures. Im *et al*. demonstrated spin-coated ZnO as an ETL material processed at approximately 150 °C with PCE values of 10.3%–15.6%.[97] The Zn_2SnO_4 ETL reported by Seok *et al*. employed a preheated process (200 °C) and resulted in a PCE of 16.5%.[96] However, ZnO is known to promote hysteresis and to degrade the perovskite film.[104]

C_{60} and other fullerene derivatives have been widely used as ETLs in p-i-n-type perovskite devices.[105–110,110] Wojciechowski *et al*. spin-coated a C_{60} ETL layer in an n-i-p-type device based on a glass substrate and obtained a stabilized PCE of 13.9%.[7] However, the C_{60} layer was dissolved by dimethylformamide (DMF) and chlorobenzene, used in the depositions of perovskite and hole-transport layers, respectively. Wojciechowski *et al*. employed reactive C_{60} derivatives to increase the solvent resistance of the fullerene layer. The resulting glass-substrate-based devices exhibited stabilized PCEs of approximately 15%–16%.[111] To enhance the attraction between C_{60} molecules and flexible substrates, Yoo *et al*. employed ethoxylated polyethylenimine (PEIE) as an interfacial treatment to enhance the adhesion of thermally evaporated C_{60} molecules to a ITO–PEN layer, resulting in a PCE of 13.8% for the flexible substrate-based device.[94]

1.4 Organization of Thesis and General Overview

This thesis examines the surface sensitization of nanocrystalline, mesoporous TiO_2 for dye-sensitized solar cells and the surface modification of ALD-desposited SnO_2 and spin-coated fullerene electron transport layers for hybrid organic-inorganic perovskite solar cells. The surface sensitization and modification studies vary in their focus, but all strive to develop an understanding of the surface phenomena that influence charge generation and charge transport at interfaces in hybrid organic-inorganic photovoltaics.

In Chapter 2, entitled "Asymmetric Squaraine Sensitizers for Near-IR Sensitization of Dye-Sensitized Solar Cells: Donors and Acceptors", the influence of various electron donating and electron accepting groups on optical properties and device performance is investigated.

In Chapter 3, entitled "Asymmetric Squaraine Sensitizers for Near-IR Sensitization of Dye-Sensitized Solar Cells: The Role of Out-of-Plane Substituents", the effects of out-of-plane alkyl chains in various regions of the squaraine sensitizer structure are examined for their influence on dye-dye aggregation at the semiconductor surface and resulting device performance.

A comparison of phosphonic acids versus carboxylic acids in rhodanine acceptors on donor-π-acceptor dyes is made in Chapter 4, entitled "Exploring the Role of Phosphonic Acids in Rhodanine Acceptor Anchors for Dye-Sensitized Solar Cells". This chapter focuses on the effects of phosphonic acid incorporation upon device efficiency and film stability for dye-sensitized solar cell applications.

Chapter 5, “Surface Modification of Electron Transport Layers for Lead Organo-Halide Perovskite Solar Cells” focuses on the surface modification of SnO_2 and fullerene electron transport layers. The effects upon work function, surface energy, perovskite film morphology, and device stability were examined for the amine-modified fullerene ETL and phosphonic acid modified ALD-depostited SnO_2 for perovskite solar cells. These studies were accomplished in conjunction with the groups of Anders Hagfeldt at EFPL, Henry Snaith at the University of Oxford, and Taiho Park at KAIST.

For Chapters 2-4, the synthesis and characterization were accomplished in the Seth Marder group at Georgia Tech. The computational modeling for Chapters 2-4 was accomplished in the group of Jean-Luc Brédas at Georgia Tech. The device fabrication and characterization was accomplished in the group of Anders Hagfeldt at EPFL. Specific contributors and contributions are referenced in the Acknowledgements section and at the start of each chapter.

Chapter 6, “Conclusions”, summarizes the work presented in this dissertation and the relevant conclusions that can inform future work. The chapter describes potential next steps in each area of research on surface sensitization and modification.

CHAPTER 2. ASYMMETRIC SQUARAINE SENSITIZERS FOR NEAR-IR SENSITIZATION OF DYE-SENSITIZED SOLAR CELLS: DONORS AND ACCEPTORS

This work was accomplished in collaboration with Parnian Ferdowsi in the group of Prof. Anders Hagfeldt. Training and assistance were provided by Dr. M. D. Zakeeruddin, Dr. Kazuteru Nonomura, Dr. Nick Vlachopoulos, and Dr. Stephen Shiring in the group of Prof. Jean-Luc Brédas. Dr. Xiongwu Kang of Prof. Mostafa El-Sayed's group performed initial DSSC device fabrication and transient absorption spectroscopy studies, with the assistance of Dr. Daniel O'Neil and Dr. Paul Szymanski. The author performed the synthesis, materials characterization, UV-Vis, fluorescence, cyclic voltammetry, and computational modeling, along with some device fabrication, optimization, and photoelectrochemical characterization.

2.1 Introduction

In DSSCs, developing near-infrared sensitizers which maintain panchromatic absorption across the visible spectrum has been pursued as a route to improving J_{SC} and overall PCE (see section 1.2.2.1). The sensitizer should be both panchromatic and absorb in the near-IR in order to increase the overall integrated absorption. For example, the ruthenium complex sensitizer **N-749** (Figure 2-1) increased J_{SC} relative to **N-719** by shifting absorption by over 100 nm further into the near-infrared while maintaining panchromatic absorption across the visible spectrum to yield a J_{SC} of over 20 mA/cm^2. However, a similar PCE as **N-719** was obtained due to a lower V_{OC}.[56] The high-

performing porphyrin sensitizer **SM315** (Figure 2-1) improved PCE relative to **SM371** by using benzothiadiazole to bathochromically shift the absorption onset to near 750 nm without a significant compromise of the absorption in any particular region to yield a J_{SC} of 18.1 mA/cm^2 and overall PCE of 13.0% with a V_{OC} of 0.91 V.[21]

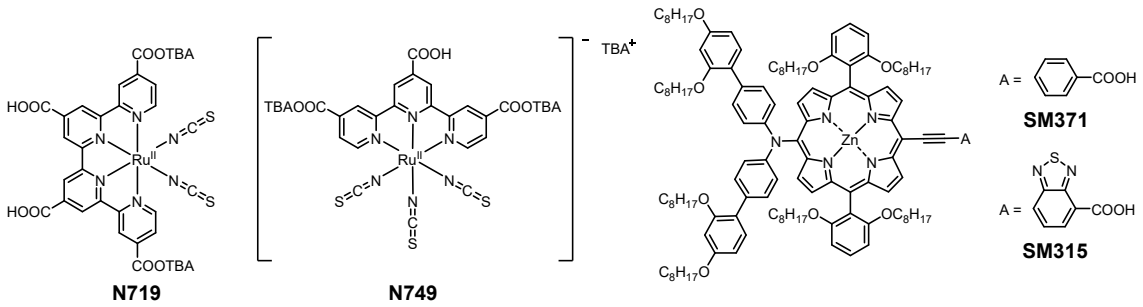

Figure 2-1. Molecular structures of sensitizers **N719**, **N749**, **SM371**, and **SM315**.

With a near-infrared onset of 940 nm, an overall PCE of 20% could theoretically be obtained by producing a J_{SC} of 30 mA/cm^2 via an IPCE of 90% (assuming a FF of 0.73 and a V_{OC} of 920 mV).[5] Depending on the substituents attached, the class of squaraine sensitizers has the potential to absorb into the near-IR while maintaining appropriate overpotentials for electron injection and dye regeneration, and, if appropriately designed, will still have strong absorption throughout the visible region of the spectrum. In early investigations, symmetric and asymmetric squaraines were shown to produce moderate PCE in the DSSC system; however, low V_{OC} and J_{SC} were observed.[34,112] Squaraines were generally bound via a carboxylic acid on an alkyl chain until the use of conjugation between the anchor and the squaraine π-system in the

asymmetric squaraine **SQ01** (Figure 2-2). **SQ01** utilized a carboxylic acid anchor in conjugation with the squaraine π-system and exhibited an absorption peak at 647 nm to achieve a PCE of 4.5%.[9] Squaraine **SQ02** further red-shifted absorption to 662 nm due to a benzo[*e*]indole functionality to obtain a PCE of 5.4%.[10]

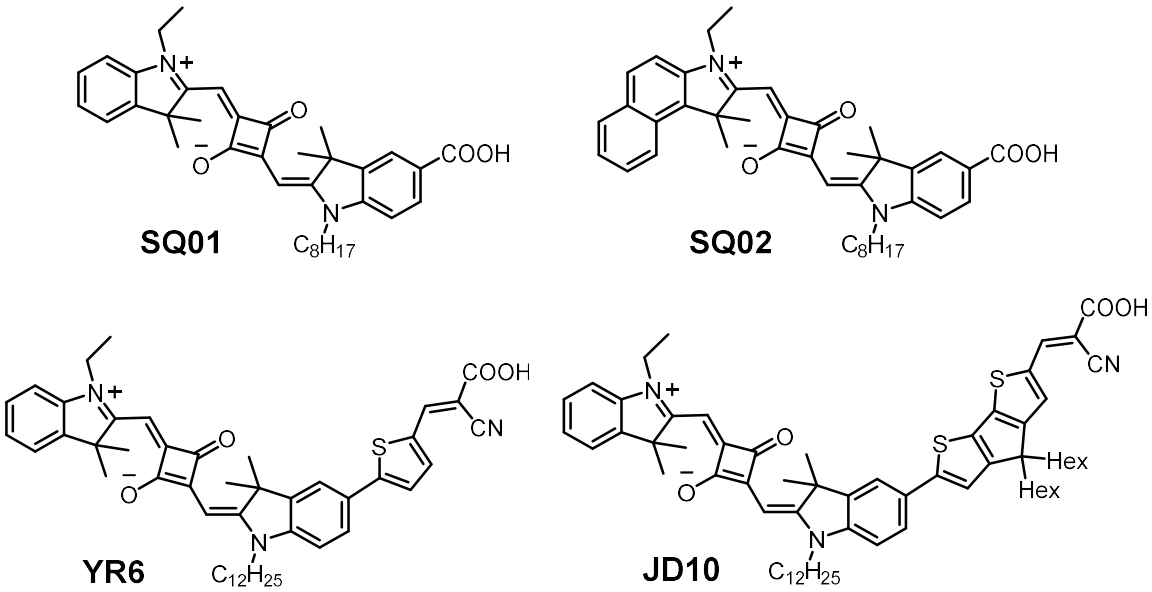

Figure 2-2. Squaraine sensitizer structures **SQ01**, **SQ02**, **YR6**, and **JD10**.

In 2011, the sensitizer **YR6** (Figure 2-2) lead to an increased J_{SC} of 14.8 mA/cm^2 by incorporating a thiophene π-bridge and carboxycyanovinyl anchoring group.[11] These additions resulted in a red-shifted absorption maximum (659 nm) and additional absorption across much of the high-energy visible spectrum for a PCE of 6.7%. Subsequently, aggregation was investigated as a cause of the decreased IPCE.[113] In 2013, Delcamp *et al*. reported the squaraine sensitizer **JD10,** which red-shifted the absorption

maximum using a cyclopentadithiophene π-bridge and increased J_{SC} to 16.4 mA/cm^2 to obtain a PCE of 7.3%.[12] The increased J_{SC} was attributed to the *gem*-di-*n*-hexyl substituents incorporated, the red-shifted absorption maximum (680 nm), and the increased absorption in the high-energy visible spectrum. Utilizing a similar structure, Jradi *et al*. developed the sensitizer **DTS-CA** with a *gem*-di-2-ethylhexyl substituted dithienosilole π-bridge to obtain a J_{SC} of 19.1 mA/cm^2 and an overall PCE of 8.9%. The increase in efficiency may have been due to the branched 2-ethylhexyl alkyl chains, or may have been due to the use of Si in the dithienosilole π-bridge of **DTS-CA** rather than the C in the cyclopentadithiophene π-bridge of **JD10**. Additionally, the devices were not masked, so a portion of the increase in J_{SC} and PCE may have been due to the lack of mask. Without a mask, an increase of ~10-15% is often seen relative to the masked sample; however, depending on the sensitizer and device structure, increases in J_{SC} of up to 40% and increases in PCE of up to 36% have been reported without the use of a mask.[114,115]

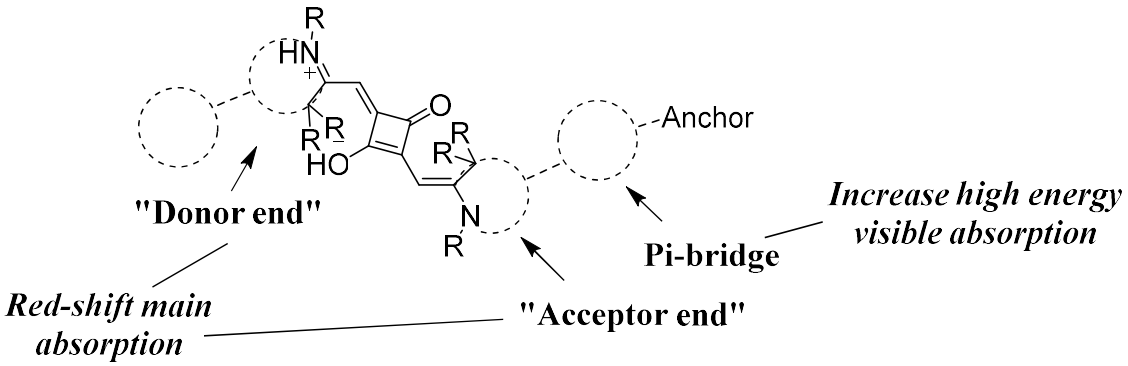

Figure 2-3. Areas of squaraine sensitizer modification.

This chapter explores further red-shifting of absorption maxima and increasing absorbance across the high-energy part of the visible spectrum through substitution of functionalities on the squaraine core and π-bridge (Figure 2-3). The absorption maximum is bathochromically shifted using benzo[*e*]indole, benzo[*g*]indole, and bis(4-butoxyphenyl)amino-indole functionalities (Figure 2-4) on the "donor end" of the squaraine core. The benzo[*e*]indole donor was used previously on sensitizer **SQ02** (Figure 2-2), and here it is interesting to see the effect of this group combined with thiophene and cyclopentadithiophene (CPDT) π-bridges, along with the differences when compared to the benzo[*g*]indole isomer. Compared to previously reported strong donor-substituted squaraines,[116–119] the bis(4-butoxyphenyl)amino-indole donor is of interest to clarify the role of a strong donor directly substituted onto the indole in a sensitizer employing a π-bridge. The π-bridges thiophene, CPDT, benzothiadiazole-CPDT (BTD-CPDT), and cyclopentadithiophene-benzothiadiazole-cyclopentadithiophene (CPDT-BTD-CPDT) (Figure 2-4) are utilized primarily for increasing absorption in the high-energy portion of the visible spectrum, while also potentially red-shifting the absorption maxima. Benzothiadiazole has been employed successfully in high-performing donor-π-acceptor[120–122] and porphyrin[21] sensitizers, where the absorption maxima are red-shifted and absorption in the visible region is obtained. Groups with out-of-plane alkyl functionalities are included in various structures, with the effect of out-of-plane groups on aggregation examined explicitly in Chapter 3.

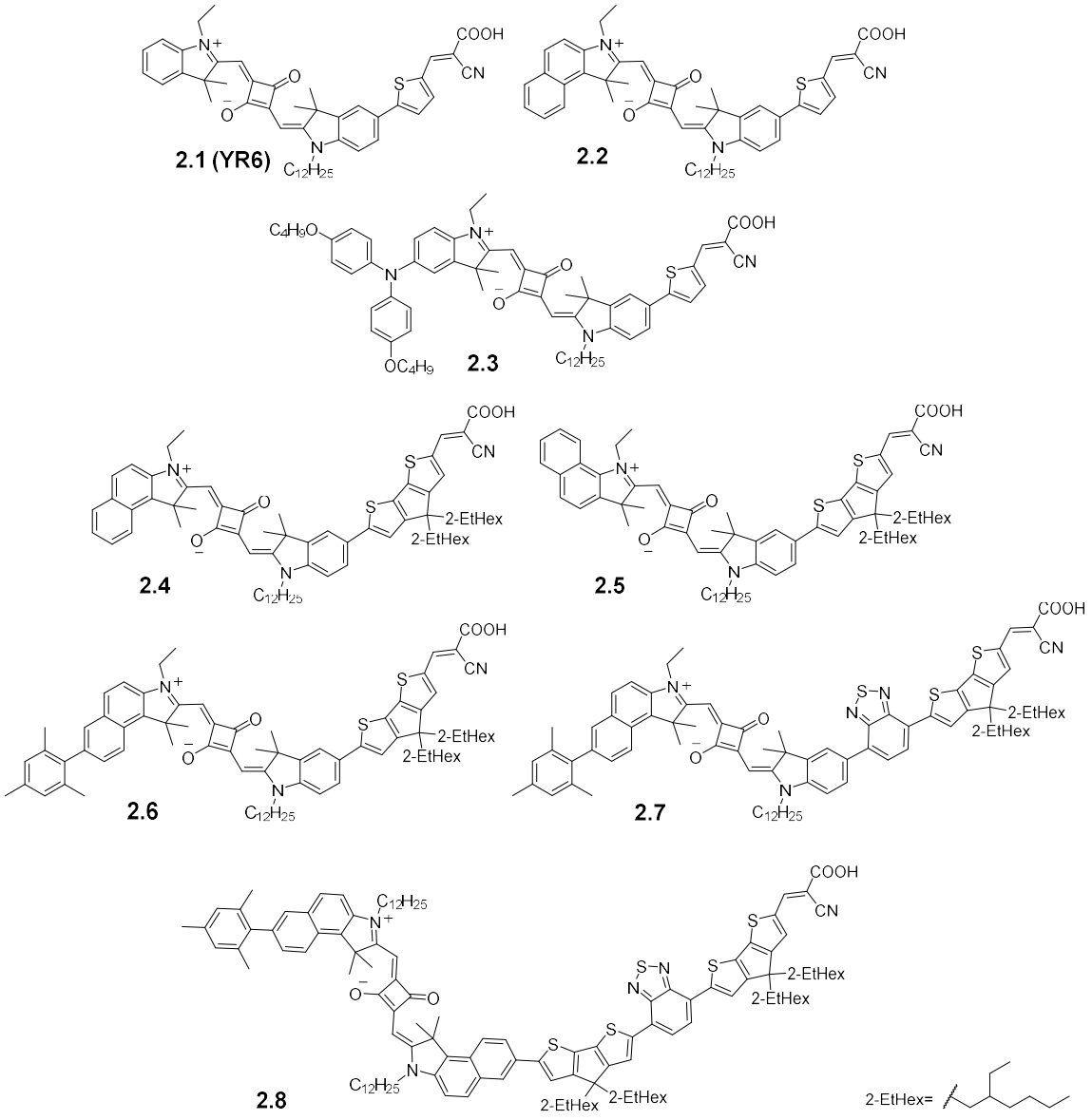

Figure 2-4. Molecular structures of squaraines **2.1**-**2.8** investigated in this chapter including literature sensitizer **YR6**.

2.2 Sensitizer Synthesis

The target squaraine sensitizers **2.2-2.8** were synthesized following an asymmetric strategy, as reported for sensitizer **2.1**,[123] beginning with a Fischer indole condensation of the appropriate aryl-hydrazine and ketone and passing through a

hydrazone intermediate.[124,125] For sensitizers **2.6** and **2.7**, a Suzuki coupling to the mesityl boronic acid then formed the mesityl indole.[126] For sensitizer **2.3**, a Buchwald-Hartwig cross coupling was performed to obtain the bis(4-butoxyphenyl)amino-indole in 46% yield.[127] For all sensitizers, *N*-alkylation using an alkyl iodide was then performed to obtain the indolinium salt.[128]

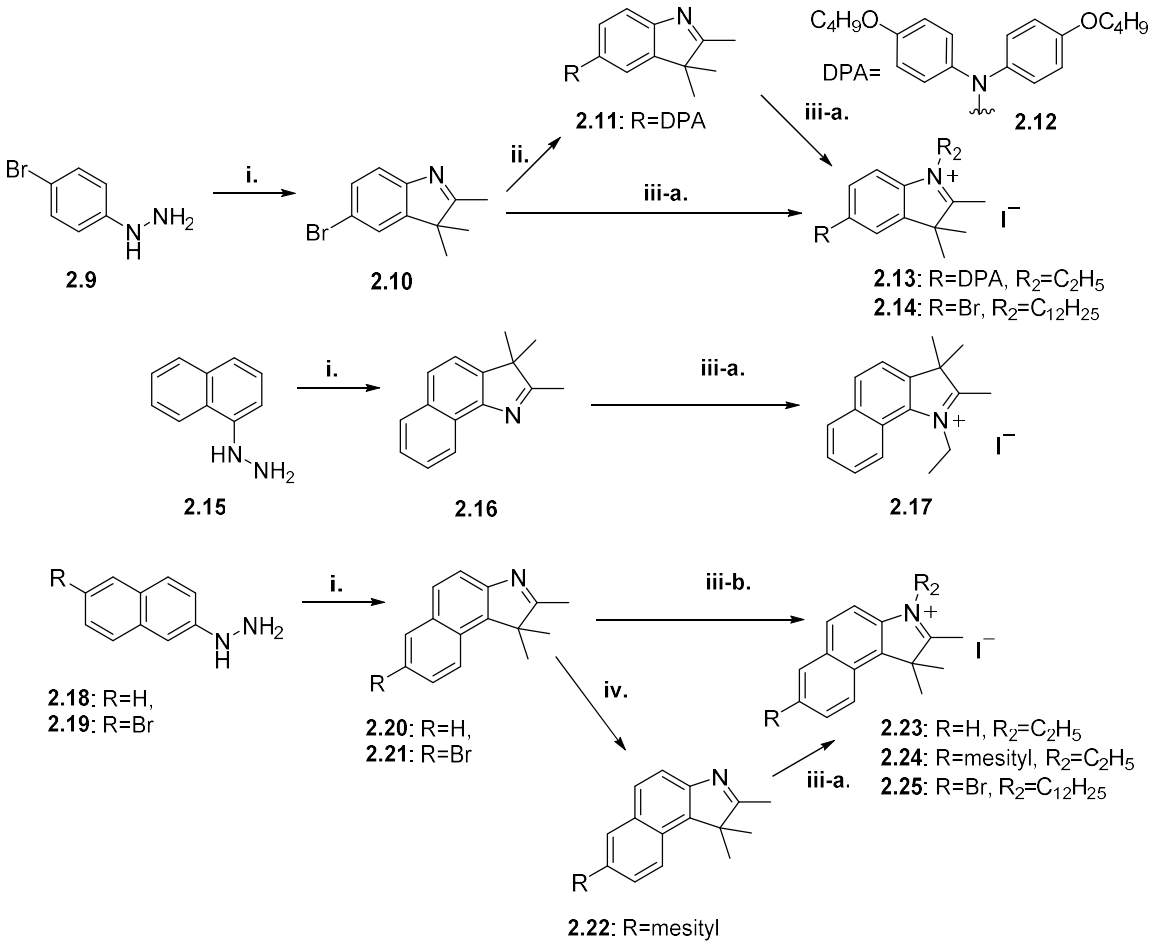

Scheme 2-1. Synthesis of indolinium salts. **i**. 3-methylbutan-2-one, acetic acid, 100 °C, 23 h, 95%+. **ii**. $Pd_2(dba)_3$, P(*t*-Bu)$_3$, *t*-BuONa, toluene, reflux, 48 h, 46%. **iii**. a) iodoethane, acetonitrile, reflux, 6-7 d., 35-75%. b) iodoethane, microwave vial, 85 °C, overnight, 86%. **iv**. mesitylene-2-boronic acid, $Pd(PPh_3)_4$, potassium carbonate, toluene, MeOH, water, 85 °C, 26%.

A semi-squaraine was formed by condensation of compound **2.14** with ethyl squarate, which was then refluxed under basic conditions to form the common intermediate semi-squaric acid **2.28**. The desired indolinium salt (compounds **2.13**, **2.14**, **2.17**, **2.23**, and **2.24**) and semi-squaric acid **2.28** were condensed to form the full squaraine under basic conditions, removing water using a Dean-Stark trap.

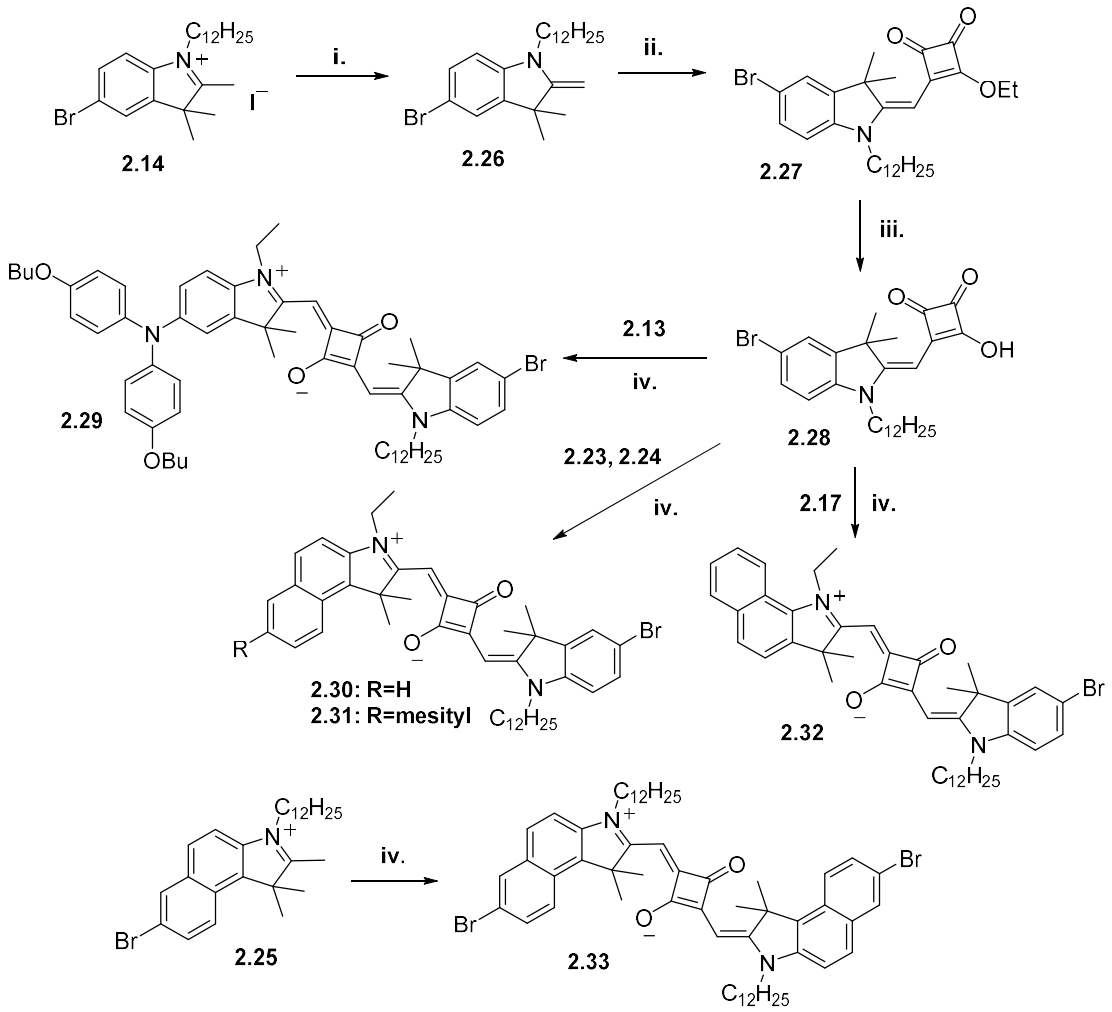

Scheme 2-2. Condensation to form full squaraine. **i**. 1 M NaOH, diethyl ether,15 min, quantitative. **ii**. ethyl squarate, triethylamine, ethanol, reflux, 18 h, 23%. **iii**. ethanol, 40 wt% NaOH, reflux, 30 min, 94%. **iv**. *n*-butanol, toluene, Dean-Stark apparatus for water removal, 18 h, 20-81%.

The (5-formylthiophen-2-yl)boronic acid was purchased commercially, while the cyclopentadithiophene, dithienosilole, benzothiadiazole-cyclopentadithiophene, and cyclopentadithiophene-benzothiadiazole-cyclopentadithiophene π-bridges were synthesized starting from dibromo derivatives of bithiophene or benzothiadiazole. The synthesis of cyclopentadithiophene **2.34** with *gem*-di-2-ethylhexyl substituents was accomplished according to literature procedures,[129–131] and a Vilsmeier-Haack reaction was performed to obtain compound **2.35**. Compound **2.35** was then coupled to dibromobenzothiadiazole using a C-H activation cross-coupling reaction,[132] to obtain a mixture of mono- and di-substituted benzothiadiazole with a yield of 66% for the desired compound **2.36**. A further C-H activation cross-coupling reaction was performed to yield the extended π-bridge **2.37**.

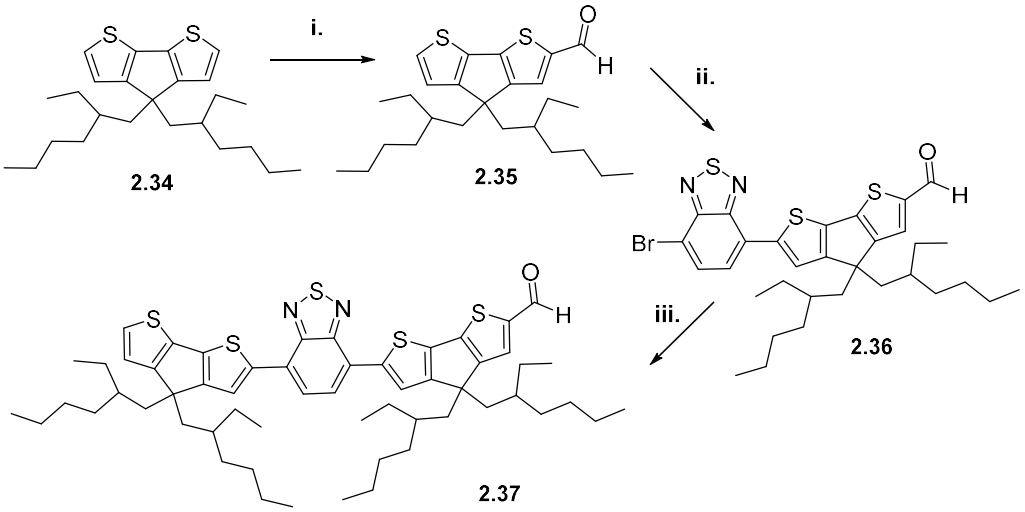

Scheme 2-3. Synthesis of π-bridges **2.35**, **2.36**, and **2.37**. **i.** DMF, 1,2-dichloroethane, $POCl_3$, 0 °C, 4 h; NaOAc, water, 2-4 h. **ii**. 4,7-dibromobenzo[*c*][1,2,5]thiadiazole, palladium(II) acetate, $(t\text{-Bu})_2PMeHBF_4$, pivalic acid, potassium acetate, dimethylacetamide, 120 °C, 11 h, 66%. **iii**. **2.34**, palladium(II) acetate, $(t\text{-Bu})_2PMeHBF_4$, pivalic acid, potassium acetate, dimethylacetamide, 120 °C, 12 h, 32%.

The π-bridges were coupled to the bromo-squaraines **2.29**-**2.33** using Suzuki cross-coupling or C-H activation conditions. For the coupling of **2.30** and **2.35**, a cleaner reaction product was observed when using dimethylacetamide as compared to toluene, and these conditions were used for subsequent reactions. A Knoevenagel condensation of the respective aldehydes with cyanoacetic acid yielded the final sensitizers **2.2-2.8**.

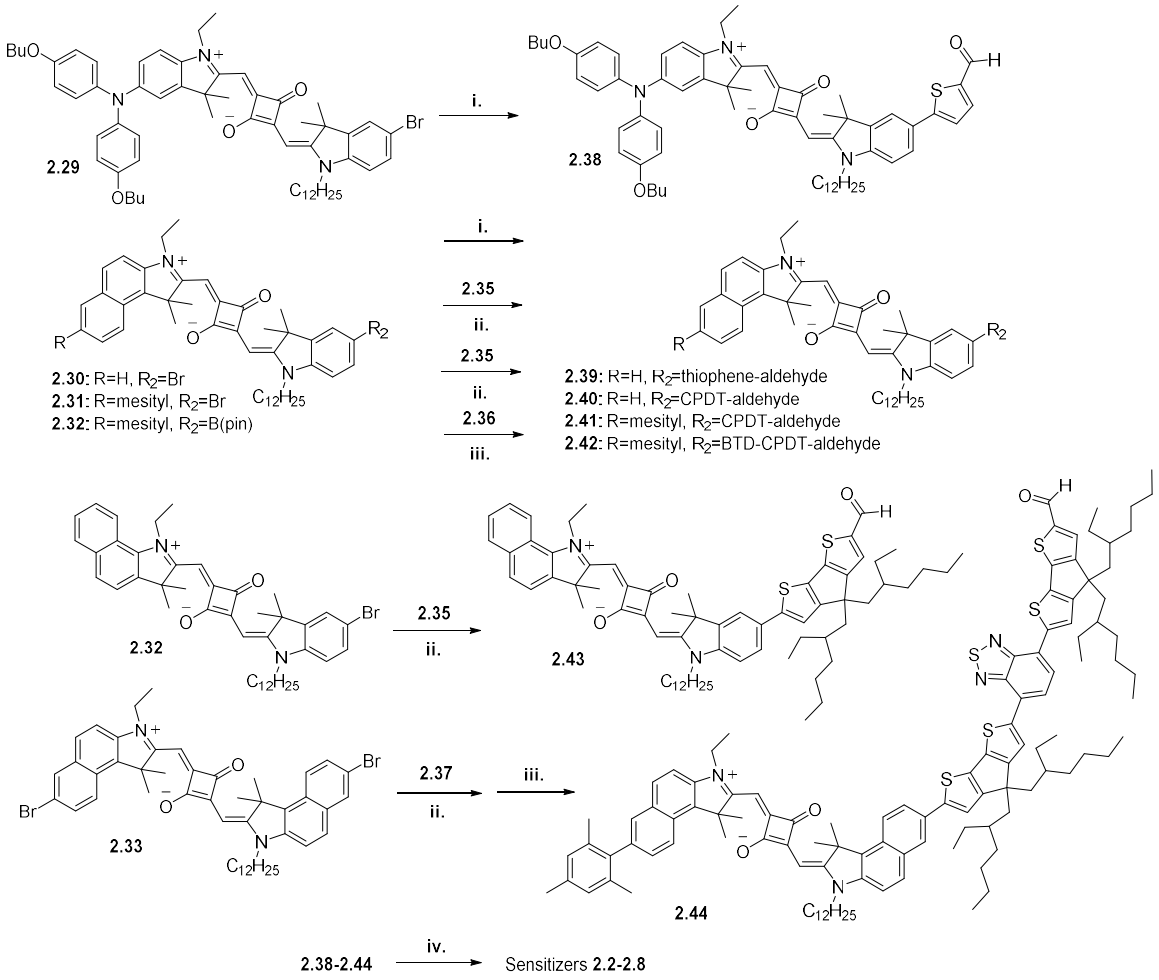

Scheme 2-4. Cross-coupling, C-H activation cross coupling reaction, and Knoevenegal condensations to yield the final sensitizers **2.2-2.8**. **i**. 5-formylthiophen-2-ylboronic acid, $PdCl_2(dppf)\cdot CH_2Cl_2$, potassium carbonate, toluene, MeOH, 70 °C, microwave for 15 min, 61-81%. **ii**. palladium(II) acetate, $(t\text{-Bu})_2PMeHBF_4$, pivalic acid, potassium acetate, dimethylacetamide, 120 °C, 12 h, 22-45%. **iii**. mesitylene-2-boronic acid, $PdCl_2(dppf)\cdot CH_2Cl_2$, potassium carbonate, toluene, MeOH, 70 °C, 18 h, 59%. **iv**. $(NH_4)_2CO_3$, cyanoacetic acid, propanoic acid, toluene, 100 °C, overnight, 7-62%.

2.3 Optical and Electrochemical Properties

The absorption maxima of sensitizers **2.1**-**2.8** in chloroform spanned from 670 to 717 nm. As expected, the extended conjugation of the benzo[*e*]indole-based sensitizer **2.2** led to a red-shift relative to the indole-based sensitizer **2.1**.[133] The strongly electron-donating bis(4-butoxyphenyl)amino-indole of sensitizer **2.3** led not only to a bathochromic shift of over 978 cm^{-1} relative to sensitizer **2.1**, but also to a large broadening of the main absorption band peak width at half maximum from 945 cm^{-1} in sensitizer **2.1** to 2063 cm^{-1} in sensitizer **2.3**.[134] The extended π-bridge on sensitizer **2.4** led to a very slight red-shift in the absorption maximum and to an increase in the high-energy absorption in the visible spectrum (Figure 2-5). Relative to sensitizer **2.6** without BTD in the π-bridge, sensitizers **2.7** and **2.8** shared increased absorption across the visible spectrum, with sensitizer **2.8** leading to more significant panchromatic absorption. The molar extinction coefficients vary among the series, with a lower molar extinction coefficient (ε_{max}) observed for sensitizers **2.3** and **2.8,** which exhibited broad absorption, than for sensitizers such as **2.1** (Table 2-1).

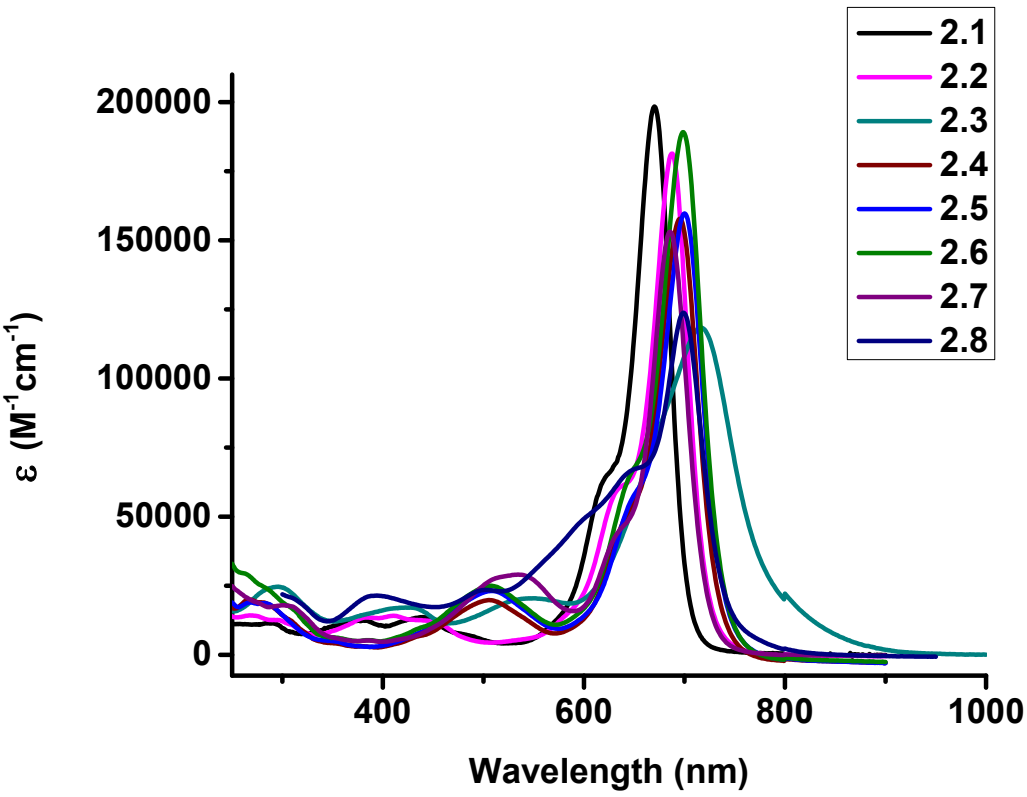

Figure 2-5. Molar absorptivity in chloroform for sensitizers **2.1**-**2.8**.

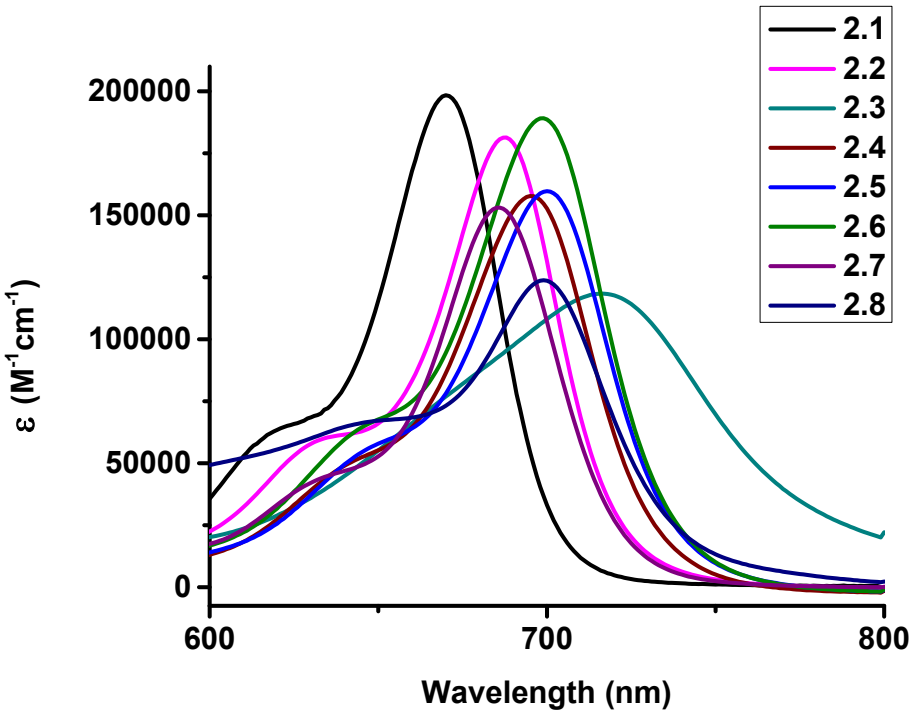

Figure 2-6. Absorption maxima in chloroform for sensitizers **2.1**-**2.8**.

To obtain the oxidation potential of the adsorbed dye,[135,136] the squaraine dyes were adsorbed onto TiO_2 films without $TiCl_4$ pretreatment that were dipped for 4 h in a 0.05 mM dye solution in ethanol (1:4 chloroform:ethanol for sensitizer **2.8**). Cyclic voltammetry was performed using the sensitized films in a solution of acetonitrile with a Ag/AgCl reference electrode calibrated to ferrocenium/ferrocene (0.63 V vs. NHE)[137] to yield the ground-state oxidation potential of the adsorbed dye. The ground-state oxidation potentials left at least 0.4 V of driving force for dye regeneration by the I_3^-/I^- redox couple (at ~0.35 V vs. NHE),[138] which for similar systems has been shown to be sufficient,[61,123,139] although as much as 0.5 V may be optimal depending on the sensitizer.[32]

Table 2-1. Optical and electrochemical properties of the squaraine sensitizers **2.1**-**2.8**.

Dyes	λ_{max} [nm][a)]	ε [10^5 $M^{-1}cm^{-1}$][a)]	E_{0-0}^{opt} [eV][b)]	$E_{(S^+/S)}$ [V][c)]	$E_{(S^+/S^*)}$ [V][d)]
2.1	670	2.0	1.82	+0.80	−1.02
2.2	688	1.8	1.79	+0.82	−0.97
2.3	717	1.2	1.62	+0.72	−0.90
2.4	695	1.6	1.72	+0.79	−0.93
2.5	700	1.6	1.72	+0.77	−0.95
2.6	699	1.9	1.72	+0.78	−0.94
2.7	686	1.5	1.79	+0.80	−0.99
2.8	699	1.2	1.74	+0.77	−0.97

[a)] Measured in chloroform; [b)] Determined from the intersection of the normalized absorption and emission spectra in chloroform. [c)] Half-wave ground state oxidation potentials vs. NHE determined via cyclic voltammetry on TiO_2 films in 0.1 M lithium bistrifluoromethanesulfonimidate (LiTFSI) in MeCN. [d)] Excited state oxidation potentials were calculated according to the following equation $E_{(S^+/S^*)} = E_{(S^+/S)} - E_{0-0}$.

2.3.1 Absorption and emission

To gain insight into the extent of charge redistribution in the lowest-energy transitions of the dyes, the absorption and emission of sensitizers **2.1**-**2.8** were compared in ethanol and chloroform. A relatively large Stokes shift was observed for sensitizer **2.3** in both ethanol and chloroform. The Stokes shift will reflect the relaxation of the excited

state before fluorescence, and can indicate how different the ground and excited state geometries may be. Molecules with a large Stokes shift may be moving away from a cyanine-like transition, where the ground state and excited state geometries are very similar, to a more charge transfer-like transition, where the ground and excited state geometries can be quite different.

Table 2-2. Differences between absorption and emission maxima in ethanol and chloroform for sensitizers **2.1**-**2.8**. *Low, broad emission observed

Dyes	λ_{abs} **[nm]** **(EtOH)**	λ_{emiss} **[nm]** **(EtOH)**	$\nu_{emiss} - \nu_{abs}$ **[cm^{-1}]** **(EtOH)**	λ_{abs} **[nm]** **($CHCl_3$)**	λ_{emiss} **[nm]** **($CHCl_3$)**	$\nu_{emiss} - \nu_{abs}$ **[cm^{-1}]** **($CHCl_3$)**
2.1	660	675	337	670	689	412
2.2	675	684	195	688	696	167
2.3	701	736	678	717	790*	1289
2.4	685	710	514	695	736	802
2.5	690	714	487	700	734	662
2.6	688	712	490	699	740	793
2.7	680	704	501	686	706	413
2.8	695	714	383	699	753*	1026

2.4 Absorption Spectra of Dyes Adsorbed on TiO_2 Films

The UV-vis absorption spectra for the dyes adsorbed on TiO_2 films are significantly broadened and include the appearance of a peak on the high-energy side of the main absorption (Figure 2-7), which has previously been ascribed to H-type aggregation on the TiO_2 surface for squaraine sensitizers.[113] As its origin may not necessarily be due to well-defined H-aggregates for this specific group of sensitizers, this peak will be referred to as the "aggregate" peak. In the presence of CDCA, the peak absorbance for the sensitizers **2.1**-**2.8** adsorbed on TiO_2 decreases by 0-70%. Most sensitizers' peak absorbance decreased by ~40-70% in the presence of CDCA, while the peak absorbance of sensitizer **2.3** increased slightly in the presence of CDCA. The decrease may be due to co-adsorption of CDCA which may decrease the total amount of squaraine sensitizers and squaraine aggregates at the TiO_2 surface.

Sensitizers **2.1**-**2.3** are squaraines with varied groups on the "donor end" and a thiophene π-bridge. Sensitizer **2.1** employs an indoline on the donor end, while sensitizer **2.2** extends conjugation using a benzo[*e*]indoline. Sensitizer **2.3** employs the more strongly donating bis(4-butoxyphenyl)amino-indoline. Without CDCA, the absorption of sensitizers **2.1** and **2.2** have similar aggregate to main absorption peak ratios (Figure 2-7), with the absorption red-shifted for sensitizer **2.2**. In the presence of CDCA, the benzo[*e*]indole-substitued sensitizer **2.2** has a slightly more pronounced aggregate peak than sensitizer **2.1**. Without CDCA, the aggregate peak of sensitizer **2.3** is more pronounced than the main absorption peak. In the presence of CDCA, the aggregate peak

decreases to be near the same height as the main absorption peak. Although increased aggregation was not originally expected for sensitizer **2.3**, aggregation appears to potentially play a role. Tailing absorption above 800 nm was also observed for sensitizer **2.3**, which may provide photocurrent response in this region.

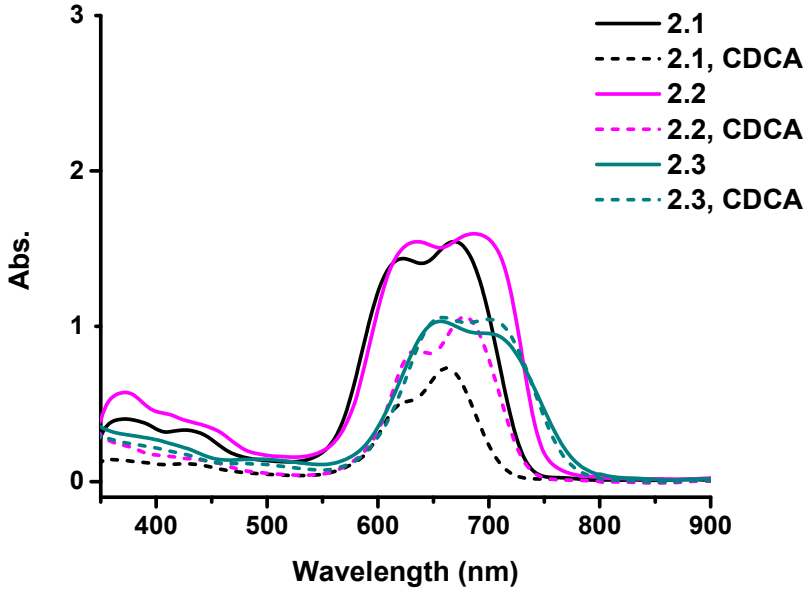

Figure 2-7. Absorption spectra of sensitizers **2.1**-**2.3** adsorbed on TiO_2 films.

Figure 2-8 compares the absorption on TiO_2 for sensitizers **2.2**, **2.4**, and **2.5** whose structures are based on benzoindoline donors with thiophene or CPDT π-bridges. Sensitizer **2.2** employs a benzo[*e*]indole-substituted squaraine and a thiophene π-bridge, while sensitizer **2.4** employs a benzo[*e*]indole-substituted squaraine and a CPDT π-bridge. Sensitizer **2.5** employs a benzo[*g*]indole-substituted squaraine, again with a

CPDT π-bridge. Sensitizers **2.4** and **2.5** show the presence of a high-energy visible absorption band near 450 nm from the CPDT, as seen previously by Delcamp *et al.*[139] The cyclopentadithiophene π-bridge-based benzo[*e*]indole-substituted sensitizer **2.4** has a larger aggregate than main absorption peak without the presence of CDCA than the thiophene π-bridge-based benzo[*e*]indoline sensitizer **2.2**. This may indicate that in the absence of CDCA, CPDT promotes aggregation. The benzo[*g*]indole sensitizer **2.5** has a very slightly higher ratio of aggregate peak to main absorption peak compared to the benzo[*e*]indole sensitizer **2.4**., which may indicate that benzo[*g*]indole aggregates more easily than benzo[*e*]indole.

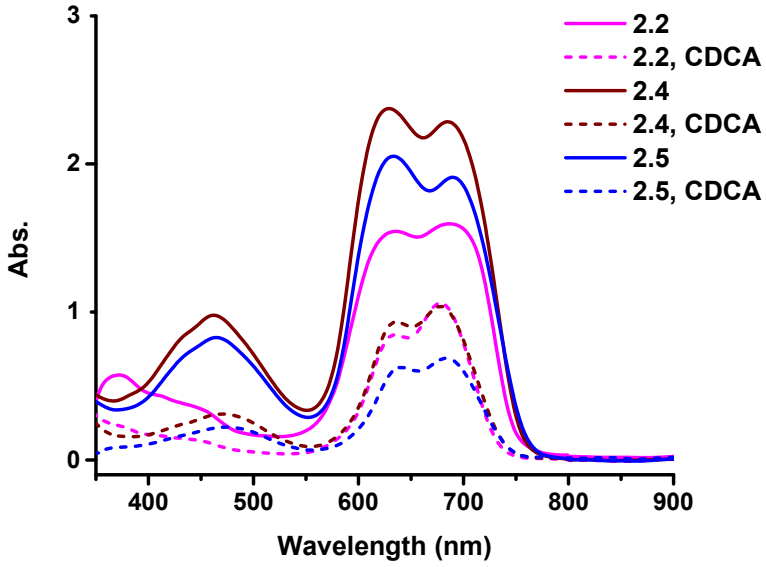

Figure 2-8. Absorption spectra of sensitizers **2.2**, **2.4**, and **2.5** adsorbed on TiO_2 films.

In Figure 2-9, the mesityl-benzo[*e*]indole-substituted sensitizers **2.6**-**2.8** are compared to highlight the effects of BTD and extended conjugation. Sensitizer **2.6** employs a CPDT π-bridge, while sensitizer **2.7** is based on a BTD-CPDT π-bridge. Sensitizer 2.8 both employs a benzo[*e*]indole on the squaraine near the π-bridge and a CPDT-BTD-CPDT π-bridge. Without CDCA, sensitizer **2.7** incorporating BTD exhibits a decreased aggregate peak compared to sensitizer **2.6** without BTD, while the aggregrate to main absorption peak ration is similar in the presence of CDCA. Sensitizer **2.8** with a benzo[*e*]indole-substitution and CPDT-BTD-CPDT π-bridge has a lower aggregate to main absorption peak ratio than the BTD-CPDT π-bridge-based sensitizer **2.7**, indicating that the additional benzo[*e*]indole and CPDT may be beneficial for preventing aggregation. Sensitizer **2.8** also exhibits panchromatic and red-shifted absorption, which is more intense in the presence of CDCA relative to sensitizers **2.6** and **2.7**.

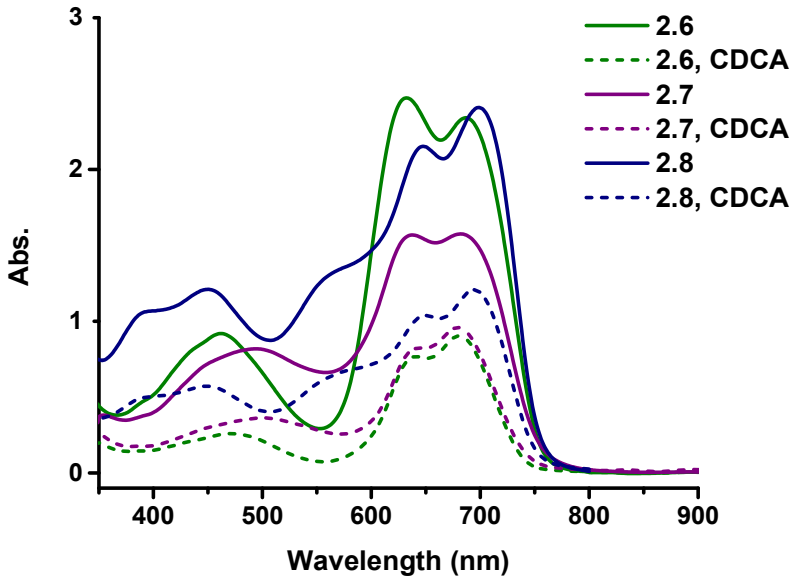

Figure 2-9. Absorption spectra of sensitizers **2.6**-**2.8** adsorbed on TiO_2 films.

2.5 Computational Investigation

2.5.1 Computational methods

Ground-state geometries of the squaraine sensitizers were optimized at the Density Functional (DFT) level using the Gaussian 09 package (revision D.01).[140] Since the long alkyl chains are not expected to contribute significantly to the electronic structure of the core, these chains were replaced with methyl groups for computational efficiency. The conductor-like polarizable continuum model, C-PCM, was used to account for the effect of solvation;[141] ethanol ($\varepsilon = 24.8$, for ground- and excited-state optimization and Natural Transition Orbitals) and acetonitrile ($\varepsilon = 35.7$, for ground-state neutral, cation, and anion optimization for ionization potential and electron affinity) were selected for implicit dielectric mediums as these solvents were used for photo- and electrochemical measurements empirically. The M06-2X hybrid functional[142] and 6-31G(d) basis set were used following the report of Alberto *et al*. that for squaraines this functional more reliably reproduced the maximum absorption energy compared to long-range corrected hybrid functionals.[143] The excitation energies and oscillator strengths for the 15 lowest singlet states were calculated using Time-Dependent DFT with the M06-2X functional and the TZVP basis set[144,145] in ethanol using C-PCM. Calculations to determine the Natural Transition Orbitals (NTOs) were performed for the first excited state. The first excited-state energies calculated were within 0.5 eV of the experimental maximum absorption values, with a similar range of values to those observed experimentally (within 0.8 eV).

2.5.2 Molecular orbitals

For each dye examined, the ground-state electronic structure at the DFT level showed the highest occupied molecular orbital (HOMO) centered on the squaraine core and delocalized throughout the backbone (Table 2-3). The lowest unoccupied molecular orbital (LUMO) is also delocalized throughout the backbone, but is more significantly toward the cyanoacrylic acid anchor. For sensitizer **2.3**, the HOMO extends across the bis(4-butoxyphenyl)amino group, while no electron density is present on the bis(4-butoxyphenyl)amino group in the LUMO.

Table 2-3. HOMO and LUMO for sensitizers **2.1**-**2.8** for ground state structures optimized in ethanol at the m06-2X/6-31G(d) level.

MO	HOMO	LUMO
2.1	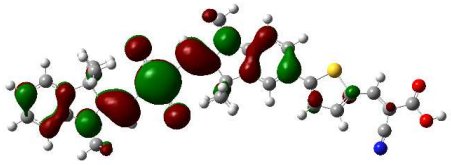	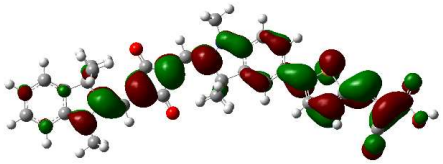
2.2	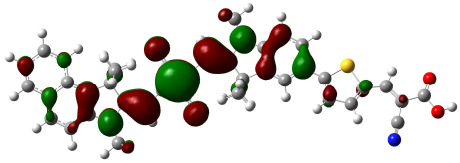	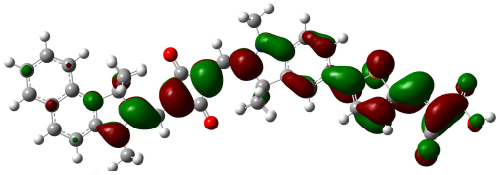
2.3	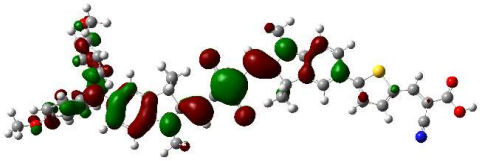	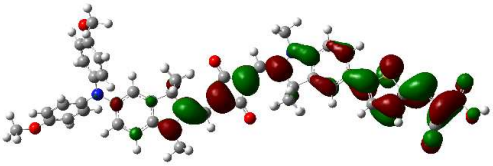
2.4	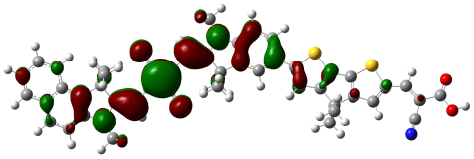	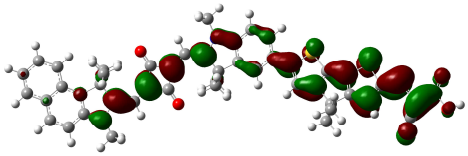
2.5	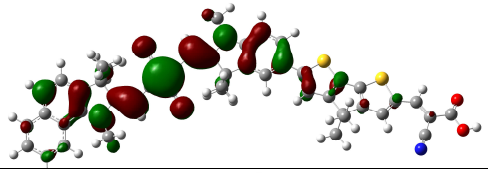	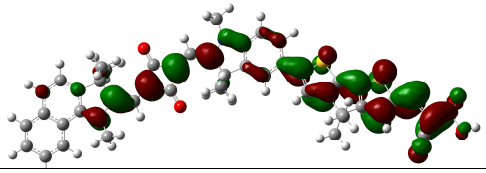
2.6	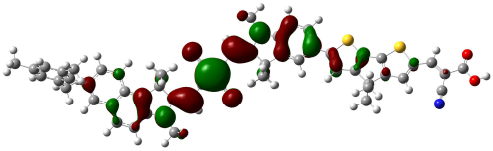	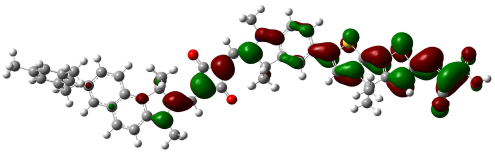
2.7	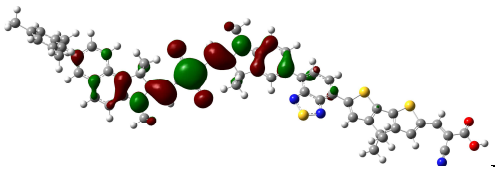	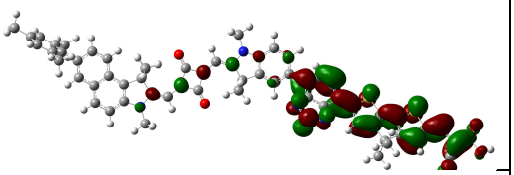
2.8	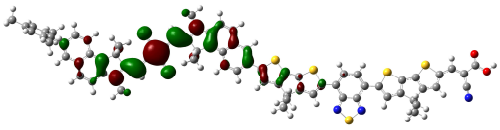	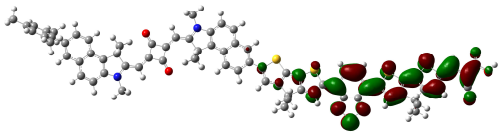

The calculated energy gap between the HOMO and LUMO (Table 2-4) can be seen to be much larger than the absorption maximum seen experimentally, as has been seen previously for DFT calculations on squaraine systems.[146]

Table 2-4. HOMO and LUMO energies and energy gap for sensitizers **2.1**-**2.8** for ground state structures optimized in ethanol at the M06-2X/6-31G(d) level compared to the empirical absorption maximum in chloroform.

Sensitizer	**E_{HOMO} (eV)**	**E_{LUMO} (eV)**	**$E_{HOMO-LUMO}$ (eV)**	**E_{abs} ($CHCl_3$) (eV)**
2.1	-5.77	-2.10	3.67	1.85
2.2	-5.74	-2.09	3.64	1.80
2.3	-5.60	-2.07	3.53	1.73
2.4	-5.69	-2.08	3.61	1.78
2.5	-5.69	-2.08	3.61	1.77
2.6	-5.69	-2.08	3.61	1.77
2.7	-5.69	-2.23	3.47	1.81
2.8	-5.62	-2.27	3.35	1.77

2.5.3 Natural transition orbitals

Time-dependent density functional theory (TD-DFT) calculations were performed for the first 15 excited states. The NTO analysis of the first transition of each dye reveals that the hole, *i.e.*, the absence of an electron due to the transition, is centered on the squaraine core and delocalized over the backbone, similar to the HOMO (Table 2-5). The electron NTO, however, shows less of a shift towards the anchor than would be expected for a pure HOMO → LUMO excitation. For example, on the hole NTO of sensitizer **2.3**, very little electron density extends across the bis(4-butoxyphenyl)amino group, and the electron NTO is also centered about the squaraine core, with the electron density only partially delocalized to the anchor. The electron NTO for the first transition of sensitizer **2.1** is also largely similar to the hole NTO, being localized across the squaraine backbone, with little-to-no electron density localized on the cyanoacrylic acid anchor. These very localized hole and electron NTOs are consistent with the relatively minor perturbations seen in the absorption spectra of the series of sensitizers. It is worthwhile to note that a different picture of the NTOs may be observed for the dyes bound to TiO_2, where the electron NTO may be more likely to extend to the TiO_2 surface. Modeling the sensitizers on a TiO_2 slab[147] or cluster[148] could clarify a hole and electron distribution that may be more relevant in the device.

Table 2-5. First excited-state hole and electron natural transition orbitals for sensitizers **2.1**-**2.8** from TD-DFT calculations in ethanol at the m06-2X/TZVP level.

NTO	Hole NTO	Electron NTO
2.1	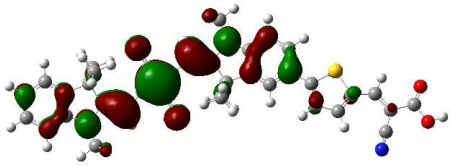	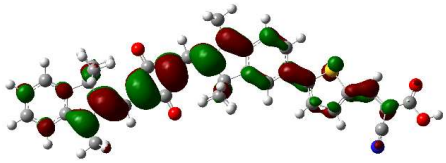
2.2	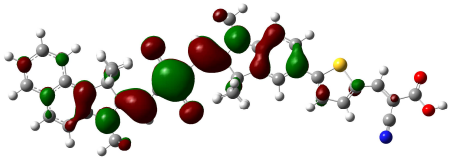	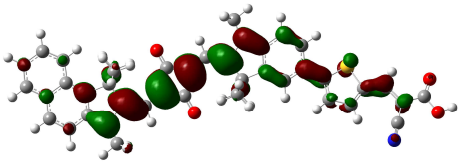
2.3	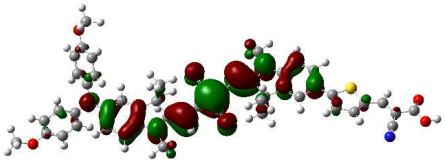	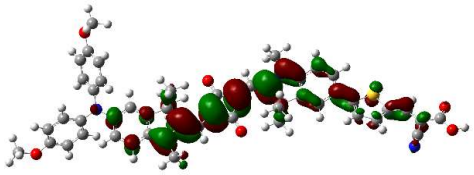
2.4	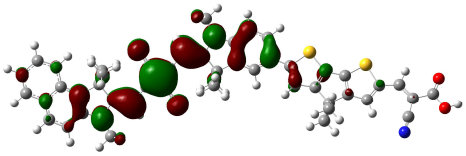	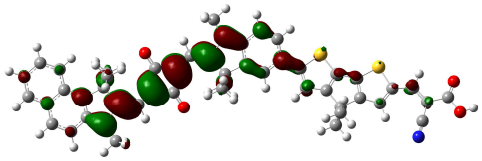
2.5	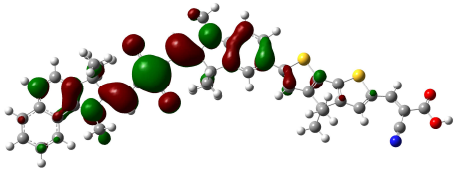	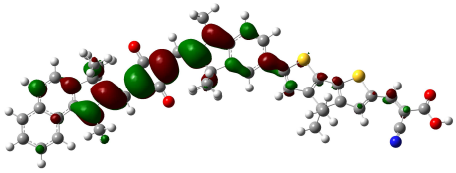
2.6	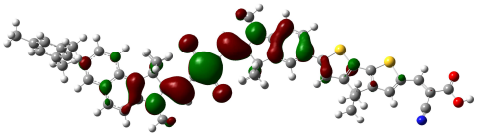	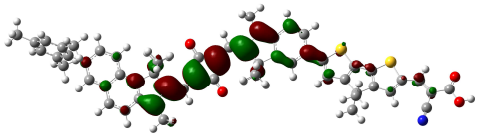
2.7	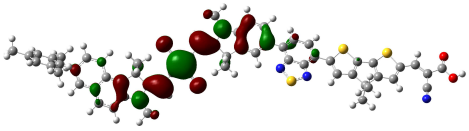	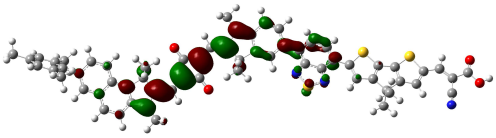

Table 2-5, continued.

NTO	Hole NTO	Electron NTO
2.8	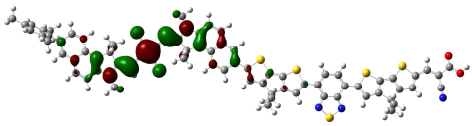	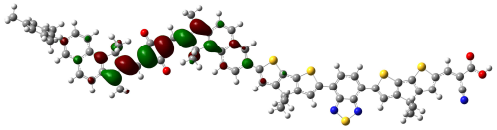

The differences between the NTO hole and electron distributions are minor among sensitizers **2.1**-**2.6**, with a small amount of electron density seen on the π-bridge and anchor for each sensitizer (Table 2-5). For sensitizers **2.7** and **2.8**, however, negligible electron density is distributed on the π-bridge, and no electron density is seen on the anchor. This is interesting, as sensitizer **2.7** will be seen to produce a relatively low IPCE, while sensitizer **2.8** will demonstrate an increased IPCE relative to sensitizer **2.7**, but an IPCE lower than several other sensitizers. This may indicate that the NTOs give a more accurate picture of electron injection than the molecular orbitals for these sensitizers.

The TD-DFT excitation energies are compared to the energy of the empirical absorption maximum in chloroform measured. The energy of the first excitation was at a slightly higher energy than the empirical absorption maximum in chloroform.

Table 2-6. First and second state excitation energies with their corresponding oscillator strength from TD-DFT calculations at the M06-2X/TZVP level in ethanol, compared to the energy of the empirical absorption maximum in chloroform.

Dyes	$S_0 \rightarrow S_1$		$S_0 \rightarrow S_2$		$E_{abs\ (CHCl_3)}$ (eV)
	E [eV]	f	E [eV]	f	
2.1	2.18	2.32	2.95	0.28	1.85
2.2	2.14	2.36	2.93	0.25	1.80
2.3	2.10	2.58	2.87	0.19	1.73
2.4	2.13	2.69	2.72	0.68	1.78
2.5	2.12	2.70	2.73	0.75	1.77
2.6	2.12	2.80	2.72	0.67	1.77
2.7	2.13	2.90	2.56	0.79	1.81
2.8	2.11	3.56	2.32	0.90	1.77

2.5.4 Ionization potential and electron affinity

The ionization potential and electron affinity were calculated based on the ground state cation, neutral, and anion species (Table 2-7). Theoretically, the optical gap, $E_{0\text{-}0}$, should be substantially lower in energy than the fundamental gap, $E_{IP\text{-}EA}$, due to the electron-hole pair binding energy. However, the values are similar, and there may be an underestimation of the fundamental gap.

Table 2-7. Calculated adiabatic ionization potential and electron affinity for sensitizers **2.1**-**2.8** in acetonitrile, compared to empirical $E_{0\text{-}0}$. Calculated from differences in SCF energy from a) ground state to cation, b) ground state to anion, c) cation to anion.

Dyes	IP [eV][a)]	EA [eV][b)]	E_{IP-EA} [eV][c)]	E_{0-0}^{opt} [eV][b)]
2.1	4.76	2.94	1.83	1.82
2.2	4.75	2.93	1.81	1.79
2.3	4.68	2.91	1.77	1.62
2.4	4.72	3.06	1.66	1.72
2.5	4.74	3.06	1.68	1.72
2.6	4.72	3.06	1.66	1.72
2.7	4.71	3.17	1.54	1.79
2.8	4.67	3.22	1.46	1.74

2.5.5 Ground vs. excited state geometries

The change in the dihedral angle ϕ^4 (Figure 2-10) from the optimized ground to optimized excited state is an indicator of the degree of delocalization between the squaraine and the π-bridge in the excited state. For all sensitizers, the dihedral angle ϕ^4 is decreased in the excited state. For sensitizers **2.1** and **2.2** with a thiophene π-bridge, the dihedral angle ϕ^4 is reduced from near 25° to 8-9° upon excitation. For sensitizer **2.3**, also employing a thiophene π-bridge, but with a bis(4-butoxyphenyl)amino-indole, the dihedral angle ϕ^4 is reduced to a lesser degree, from 25° to 14° upon excitation. The

benzo[*e*]indole- and benzo[*g*]indole-substituted sensitizers **2.4** and **2.5** both employing a CPDT π-bridge see a reduction of the dihedral angle ϕ^4 to an even lesser degree, from 25° to 19° and 25° to 17°, respectively, upon excitation. For sensitizer **2.7**, with a BTD-CPDT π-bridge, the dihedral angle ϕ^A, analogous to ϕ^4, is relatively large at 40° and only decreases to 34° upon excitation, which is consistent with the low electron density seen in the electron NTO for sensitizer **2.7**. Sensitizer **2.8**, with a CPDT-BTD-CPDT π-bridge, is able to achieve a lower dihedral angle ϕ^4 of 20° from the squaraine to the π-bridge, closer to that of sensitizers **2.1-2.6**, that decreases to 17° upon excitation.

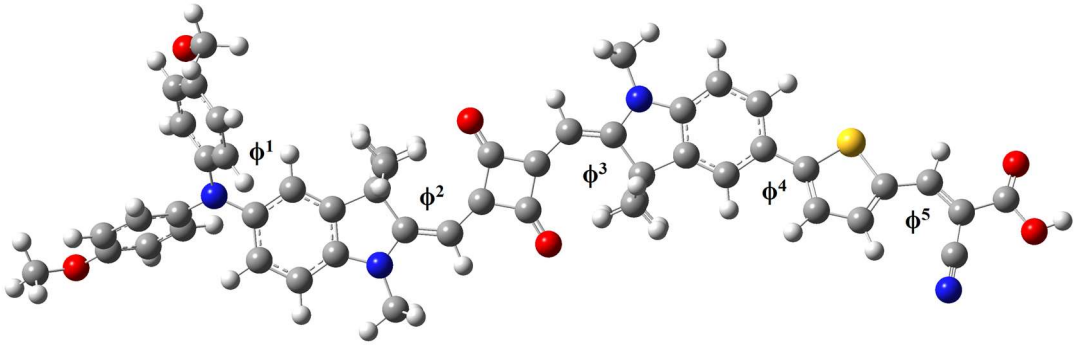

Figure 2-10. Dihedral angles of interest labeled on sensitizer **2.3**.

Table 2-8. Dihedral angles for sensitizers **2.1**-**2.5** optimized in ethanol at M06-2X/6-31G(d) at the ground and first excited state.

Sensitizer	S_0 / S_1	ϕ^1 (°)	ϕ^2 (°)	ϕ^3 (°)	ϕ^4 (°)	ϕ^5 (°)
2.1	S_0	—	0.46	0.97	25.15	1.76
2.1	S_1	—	0.21	0.31	9.03	1.02
2.2	S_0	—	0.19	0.85	25.13	1.55
2.2	S_1	—	0.75	0.94	8.52	1.45
2.3	S_0	35.80	0.07	0.94	24.72	2.36
2.3	S_1	31.98	0.10	0.70	13.80	1.24
2.4	S_0	—	0.18	0.27	24.86	0.06
2.4	S_1	—	0.13	0.33	19.21	0.44
2.5	S_0	—	2.08	0.21	27.44	0.48
2.5	S_1	—	3.48	0.26	17.33	0.68

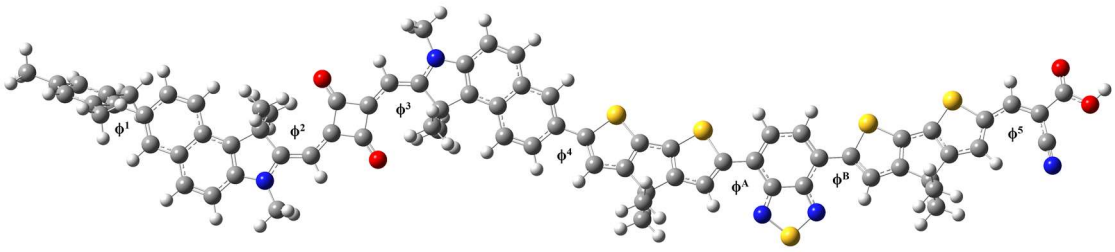

Figure 2-11. Dihedral angles of interest labeled on sensitizer **2.8**.

Table 2-9. Dihedral angles for sensitizers **2.6-2.8** optimized in ethanol at M06-2X/6-31G(d) at the ground and first excited state obtained from TD-DFT calculations at the M06-2X/6-31G(d) level.

Dye	S_0 / S_1	ϕ^1 (°)	ϕ^2 (°)	ϕ^3 (°)	ϕ^4 (°)	ϕ^A (°)	ϕ^B (°)	ϕ^5 (°)
2.6	S_0	72.89	0.87	0.34	24.79	—	—	0.32
2.6	S_1	71.41	0.53	1.28	19.83	—	—	0.19
2.7	S_0	75.10	0.27	0.31	—	39.99	10.43	0.62
2.7	S_1	69.36	0.45	0.11	—	33.66	0.92	0.35
2.8	S_0	76.15	0.12	0.16	20.37	19.27	17.71	0.60
2.8	S_1	72.82	0.39	0.58	17.05	18.49	19.14	0.73

2.5.6 Ground vs. excited state dipole moments

Examination of the ground-state dipole moment (Table 2-10) shows that, as expected, electron-donating functionalities increase the dipole moment in the ground state. For example, the bis(4-butoxyphenyl)amino-indole functionality (sensitizer **2.3**) and, to a lesser extent, the CPDT π-bridge (sensitizer **2.4**), increase the dipole moment in the ground state relative to sensitizer **2.1**.

The change of dipole moment from the ground to excited state can indicate the degree of charge-transfer character in the absorption. Changes in dipole moment were projected along the C-COOH bond to approximate the dipole in the direction of TiO_2 for sensitizers bound on TiO_2. Sensitizer **2.3** exhibits the largest change of dipole moment of

3.84 Debye from ground to excited state (Table 2-10), indicating a large change in geometry in the optimized excited state. This correlates well with the large Stokes shifts seen for sensitizer **2.3** in ethanol and chloroform, since the Stokes shift will reflect the relaxation of the excited state before fluorescence. Sensitizer **2.8** showed a small change in dipole moment of 0.30 Debye from ground to excited state. This correlates to the small Stokes shift seen empirically for sensitizer **2.8** in ethanol, or less geometry relaxation in the excited state, and does not correlate to the large Stokes shift seen empirically in chloroform.

Table 2-10. For sensitizers **2.1**-**2.8**, magnitude of the ground-state dipole moment and geometry optimized first-excited-state dipole moment, then the magnitude projected along the anchoring group C-COOH bond.

Sensitizer	**μ of S_0 (Debye)**	**μ of S_1 (Debye)**	**μ_{proj} of S_0 (Debye)**	**μ_{proj} of S_1 (Debye)**
2.1	20.61	19.82	16.12	15.02
2.2	22.29	20.46	17.98	16.00
2.3	28.02	25.74	24.89	21.05
2.4	24.51	22.03	22.47	19.86
2.5	22.09	21.64	19.68	19.30
2.6	22.84	21.76	21.22	19.55
2.7	20.45	19.66	15.89	14.95
2.8	21.10	20.69	18.54	18.14

2.6 Photovoltaic Characterization

2.6.1 DSSC device fabrication

Double-layer TiO_2 films with an 8 μm transparent and a 4μm scattering layer were prepared by screen-printing (DyeSol 30 NR-T) and treating with a 0.05 M titanium tetrachloride solution as previously reported by Nazeeruddin *et al*.[149] The films were heated to 500 °C in air for 30 min before use, then dipped in 0.1mM dye solutions in either ethanol or chloroform:ethanol (1:4) with 0, 10, or 20 mM 3α,7α-dihydroxy-5β-cholic acid (chenodeoxycholic acid or CDCA) for 4 h at room temperature. The sensitized films were rinsed briefly with acetonitrile before solar cell fabrication, which was done using procedures, testing conditions, and equipment previously reported.[150] The liquid electrolyte consisted of 0.6 M 1,3-dimethylimidazolium iodide, 0.03 M iodine, 0.05 M LiI, 0.05 M guanidinium thiocyanate, and 0.5 M 4-*tert*-butylpyridine in a 15/85 (v/v) mixture of valeronitrile and acetonitrile.

2.6.2 J-V measurements

The sensitizers were first compared under common conditions of 0.05 mM dye and either 0 or 20 mM CDCA, and the cell area was restricted to 0.16 cm^2 using a metal mask. V_{OC} values remained in a range common to squaraine sensitizers from 620 to 667 mV,[151,152] while the J_{SC} values ranged from 9.79-13.50 mA/cm^2 (Table 2-11). Of note is the PCE for sensitizer **2.1**, or **YR6**, which is slightly lower than previously reported.[123,139] Shi *et al*. had previously reported 6.7% PCE for a 0.1 mM dye with 10 mM CDCA, and Delcamp *et al*. had reported 6.5% PCE for 0.05 mM dye and 20 mM CDCA. A 4.5%

PCE for 0.05 mM dye and 20 mM CDCA, and a 5.0 % PCE for 0.05 mM dye and 10 mM CDCA were observed.

Table 2-11. Photovoltaic performance of the squaraine-based DSSCs under uniform conditions. [a,b,c]

	V_{OC} [mV]	J_{SC} [mA/cm^2]	FF [%]	PCE [%]
2.1	643 ± 5	10.81 ± 0.25	64.1 ± 5.0	4.46 ± 0.48
2.2	667 ± 6	11.58 ± 0.01	71.5 ± 0.5	5.52 ± 0.01
2.3	632 ± 4	12.24 ± 0.22	64.6 ± 0.6	5.00 ± 0.17
2.4	658 ± 5	13.43 ± 0.34	70.3 ± 3.7	6.22 ± 0.40
2.5	632 ± 1	12.69 ± 0.23	72.6 ± 0.3	5.82 ± 0.10
2.6	658 ± 6	13.50 ± 0.13	71.9 ± 0.8	6.38 ± 0.20
2.7	647 ± 7	9.79 ± 1.63	69.9 ± 6.6	4.47 ± 1.20
2.8	620 ± 2	13.10 ± 0.23	65.1 ± 5.4	5.29 ± 0.55

[a]Based on measurements of 2-4 devices for all dyes with the standard deviation shown. [b]The photovoltaic measurements were conducted using a mask to restrict the cell active area to 0.16 cm^2. The dye solutions were 0.05 mM dye and 20 mM CDCA in ethanol with a dipping time of 4 h, except compound for compound 2.8 which was dipped in 1:4 chloroform:ethanol. [c]YR6 was also tested at optimal literature conditions with 10 mM CDCA to yield the following: V_{OC}=654 ± 4 mV, J_{SC}=11.30 ± 0.16 mA/cm2, FF=67.9 ± 1.4 (%), PCE=5.02 ± 0.1 %

For sensitizers **2.1**-**2.3**, the J_{SC} increases moving from indole (**2.1**) to benzo[*e*]indole (**2.2**) to bis(4-butoxyphenyl)amino-indole (**2.3**). The V_{OC} increases

moving from indole (**2.1**) to benzo[*e*]indole (**2.2**), but slightly decreases for the bis(4-butoxyphenyl)amino-indole-substituted sensitizer **2.3** (Figure 2-12, Figure 2-13). This decrease in V_{OC} for sensitizer **2.3** could be related to increased recombination from unfavorable dye-dye or dye-electrolyte interactions.

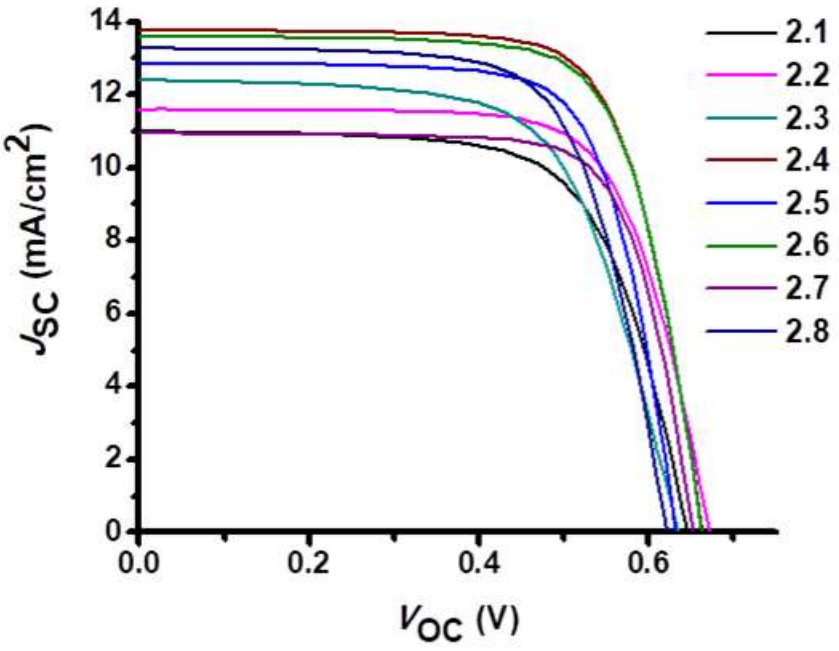

Figure 2-12. *J-V* curves with maximum PCE for each sensitizer under dipping conditions of 0.05 mM dye and 20 mM CDCA in ethanol.

For sensitizers **2.2**, **2.4** and **2.5** (Figure 2-12, Figure 2-13), the J_{SC} increases moving from the benzo[*e*]indole-substituted sensitizer **2.2** with a thiophene π-bridge to the benzo[*e*]indole-substituted sensitizer **2.4** with a CPDT π-bridge, with both sensitizers having similar V_{OC}. This suggests that the main effect of the CPDT π-bridge is an increase in current, potentially due to additional high-energy visible absorption. Comparing the benzo[*e*]indole-substituted sensitizer **2.4** and benzo[*g*]indole-substituted sensitizer **2.5**, there is a decrease in both J_{SC} and V_{OC} for the benzo[*g*]indole-substituted sensitizer, suggesting possible decreases in both electron injection and recombination.

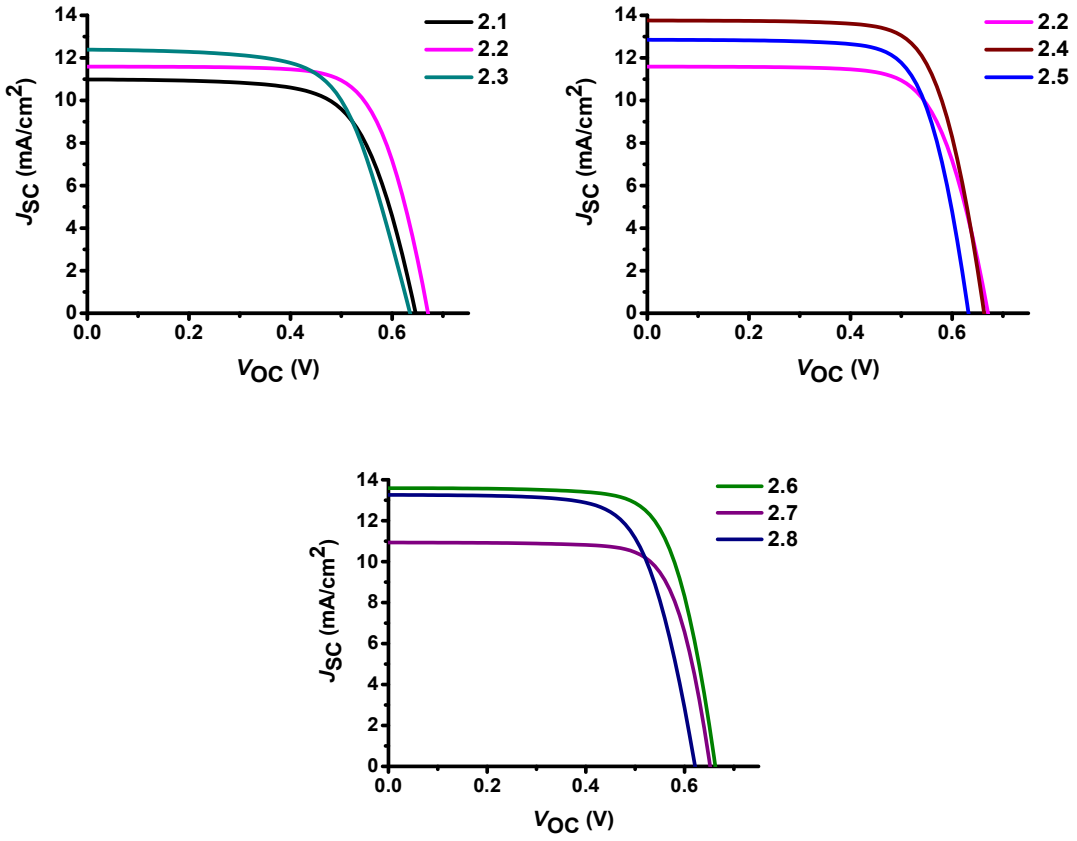

Figure 2-13. *J-V* curves grouped by structure.

For sensitizers **2.6**-**2.8**, there is a sharp decrease in J_{SC} moving from the mesityl- and benzo[*e*]indole-substituted sensitizer **2.6** with a CPDT π-bridge to the similar sensitizer **2.7** incorporating benzothiadiazole prior to the CPDT in the π-bridge, with a minor decrease in the V_{OC} also observed (Figure 2-12, Figure 2-13). This suggests that there are significant problems with either electron injection or recombination created by the inclusion of BTD. When an additional benzo[*e*]indole and CPDT are employed with a BTD, further extending the π-conjugation, a more favorable J_{SC} is observed, similar to that of sensitizer 2.6, but an additional decrease in the V_{OC} is also observed.

2.6.3 IPCE spectra

Examining the IPCE spectra for sensitizers **2.1**-**2.3** (Figure 2-14), a slight bathochromic shift is observed when incorporating the benzo[*e*]indole-based sensitizer **2.2** over the indole-based sensitizer **2.1**, with a larger shift observed for sensitizer **2.3** incorporating the bis(4-butoxyphenyl)amino-indole functionality. Sensitizer **2.3** has a panchromatic IPCE remaining over 40% from 350 to near 800 nm. However, at its maximum, the IPCE is under 52%, indicating problems with electron injection or recombination.

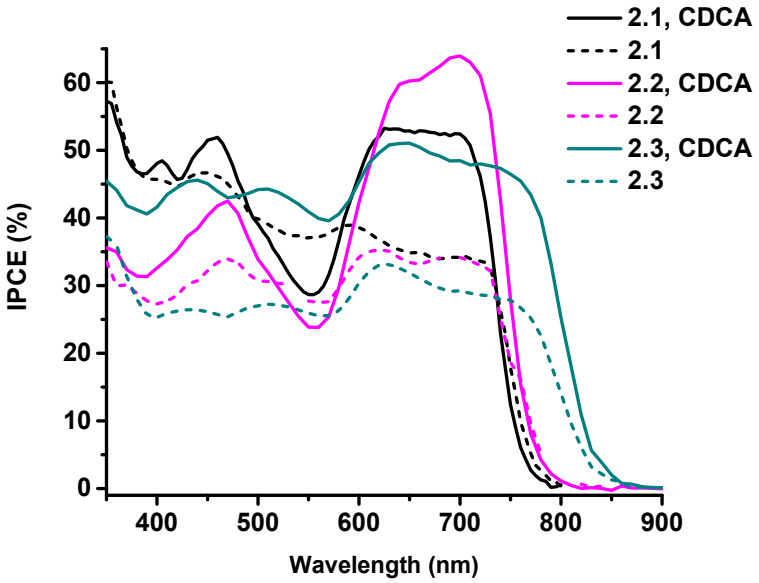

Figure 2-14. IPCE spectra of sensitizers **2.1**, **2.2**, and **2.3**

.

Holding the benzo[*e*]indole "donor" end of the squaraine constant and comparing the thiophene π-bridge (dye **2.2**) with the extended CPDT π-bridge (dye **2.4**), the CPDT promotes a much higher IPCE in the 400-600 nm wavelength range (Figure 2-15).

Examining the benzo[*e*]indole-based sensitizer **2.4** vs. benzo[*g*]indole-based sensitizer **2.5**, the benzo[*g*]indole-based sensitizer has a lower IPCE both with and without CDCA. The trend is consistent with the lower absorption seen for the dye-sensitized TiO_2 film of sensitizer **2.5**.

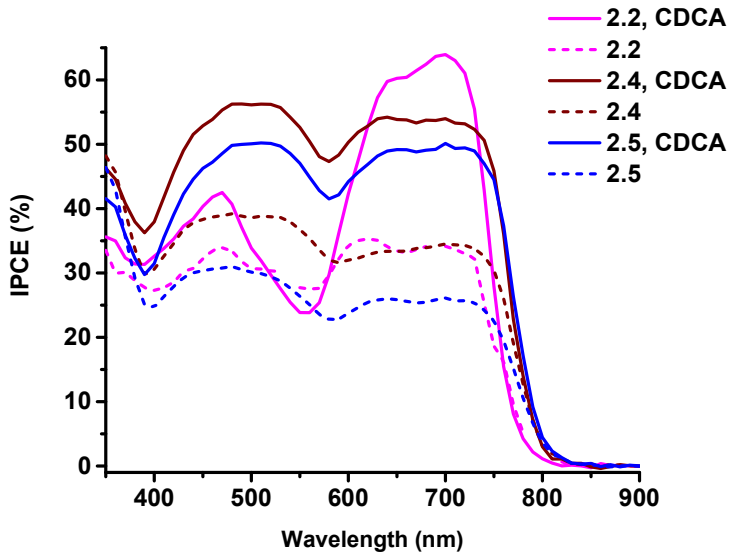

Figure 2-15. IPCE spectra of sensitizers **2.2**, **2.4**, and **2.5**.

Moving from the simple CPDT π-bridge-based sensitizer **2.6** to the BTD-CPDT π-bridge-based sensitizer **2.7** and the extended benzo[*e*]indole and CPDT-BTD-CPDT π-bridge-based sensitizer **2.8**, a slightly red-shifted IPCE onset is seen (Figure 2-16). The IPCE spectra remain consistently at ~40% (sensitizer **2.7**) and ~50% (sensitizer **2.8**) over the visible and near-IR spectrum for the dyes including a BTD, while the simple CPDT π-bridge (sensitizer **2.6**) allows an IPCE reaching near 60%, but with a dip at around 580 nm.

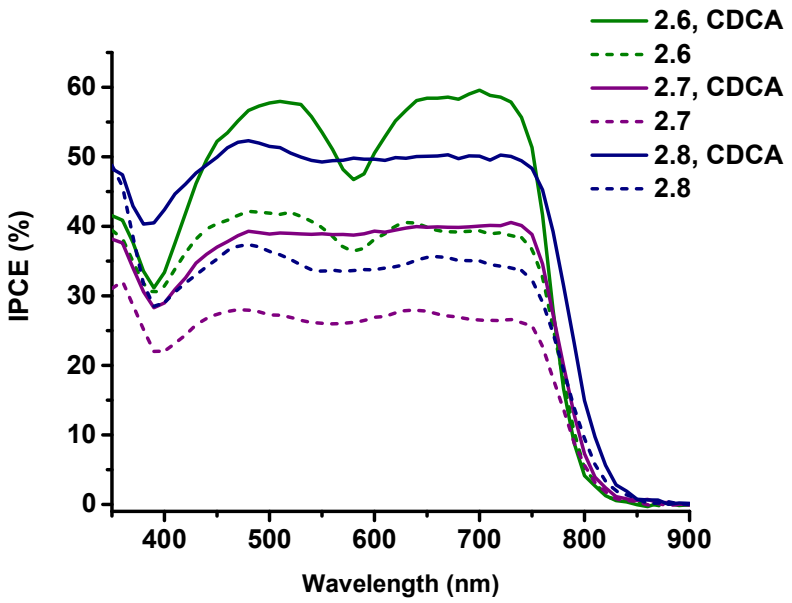

Figure 2-16. IPCE spectra of sensitizers **2.6**, **2.7**, and **2.8**.

2.7 Photoelectrochemical Characterization

2.7.1 Charge-injection measurements

Selected squaraines were examined by transient absorption spectroscopy and had electron-injection efficiencies over 70% (Table 2-12). Differences between the charge-injection rate constants or electron-injection efficiencies did not correlate directly with the J_{SC} or IPCE observed for the sensitizers under device operating conditions. For example, sensitizers **2.1** and **2.3** exhibited the fastest electron injection rate constants, k_{ei}, of 52.4×10^{-10} and 98.8×10^{-10} s^{-1}, respectively, almost 10 times greater than that of the equally well-performing sensitizer **2.2** at 5.5×10^{-10} s^{-1}. Sensitizer **2.3** has a relatively high

charge-injection yield, but a lower IPCE % than many other sensitizers. This may indicate that other factors play a greater role in governing the photocurrent for these devices.

Table 2-12. Charge-injection dynamics of **2.1**, **2.2**, and **2.3** on the TiO_2 films; the sensitized films were pumped near their ground state absorption maxima and probed around 500 nm. All data were fit with stretched exponentials. Based on the characteristic time (τ) and stretched exponential (β), the average time constant is derived and tabulated. The charge-injection rate constant and efficiency (η_{inj}) were calculated from these average values.

Dye	**τ_{obs}(ps)/TiO_2**	**τ_{obs}(ps)/ Al_2O_3**	**τ_{obs}(ps)/sol**	**k_{ei} (10^{-10} s^{-1})**	**ΔG_{ei}^0(eV)**	**η_{inj}(%)**
2.1	1.8	123.9	192	52.4	0.46	98.5
2.2	13.3	49.5	1973	5.5	0.45	73.3
2.3	1.0	85.2	292	98.8	0.51	98.8

*where τ_{obs} is the observed lifetime, ΔG_{ei}^0 is the driving force for electron injection, and k_{ei} is the electron injection rate constant

2.7.2 Charge transport lifetime

Electron transport measurements describe how photoinduced excess charge moves in a concentration gradient; essentially how charges move through the device. The electron transport time (τ_{tr}) was derived from time-resolved small modulation techniques using standard short-circuit conditions on a Dyenamo Toolbox. Under short-circuit conditions, the electron lifetime is generally significantly larger than the electron

transport time, making the measured photocurrent response time approximately equal to the electron transport time.

The electron transport lifetime exhibited a narrow distribution (Figure 2-17), with a slight increase in electron transport on average with the use of CDCA. Sensitizer **2.5**, which employed the benzo[*g*]indole moiety, exhibited lower electron transport than other squaraine sensitizers. This is could relate to the low V_{OC} observed for sensitizer **2.5**, at an average of 616 mV compared to the averages for other sensitizers which ranged from 643 to 669 mV.

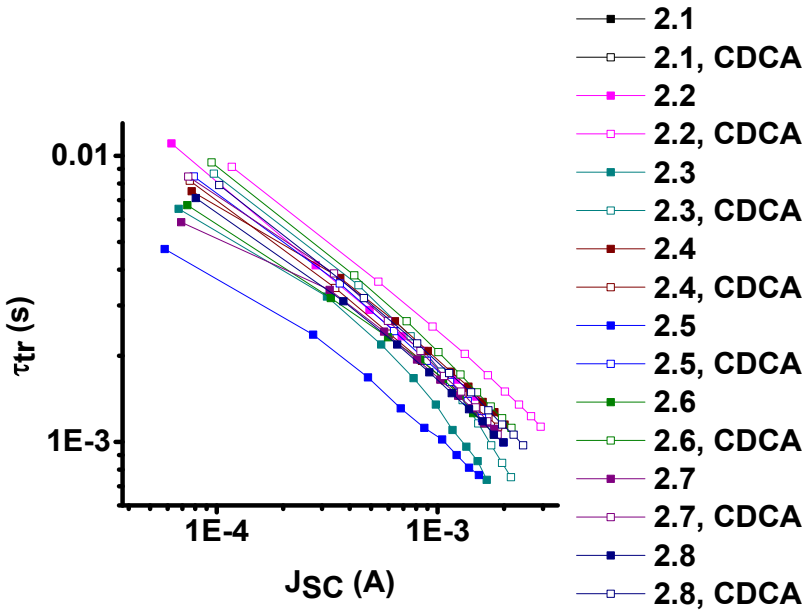

Figure 2-17. The electron transport lifetime as a function of short-circuit current for all sensitizers.

2.7.3 Charge extraction measurements

Charge extraction measurements can provide an understanding of the relative shifts in the TiO_2 conduction band for different sensitizers or amounts of coadsorbent. In the presence of CDCA, the charge extraction of all sensitizers is within a similar range (Figure 2-18). Without CDCA, the sensitizers **2.1** and **2.8** show a slight increase and the sensitizer **2.7** shows a slight decrease in charge extraction relative to sensitizers **2.2**-**2.6**. The sensitizer **2.7** incorporating BTD-CPDT shows a decrease while the sensitizer **2.8** incorporating CPDT-BTD-CPDT shows an increase in charge extraction, which could indicate there are significant differences in the molecular dipoles or how the sensitizers assemble at the surface.

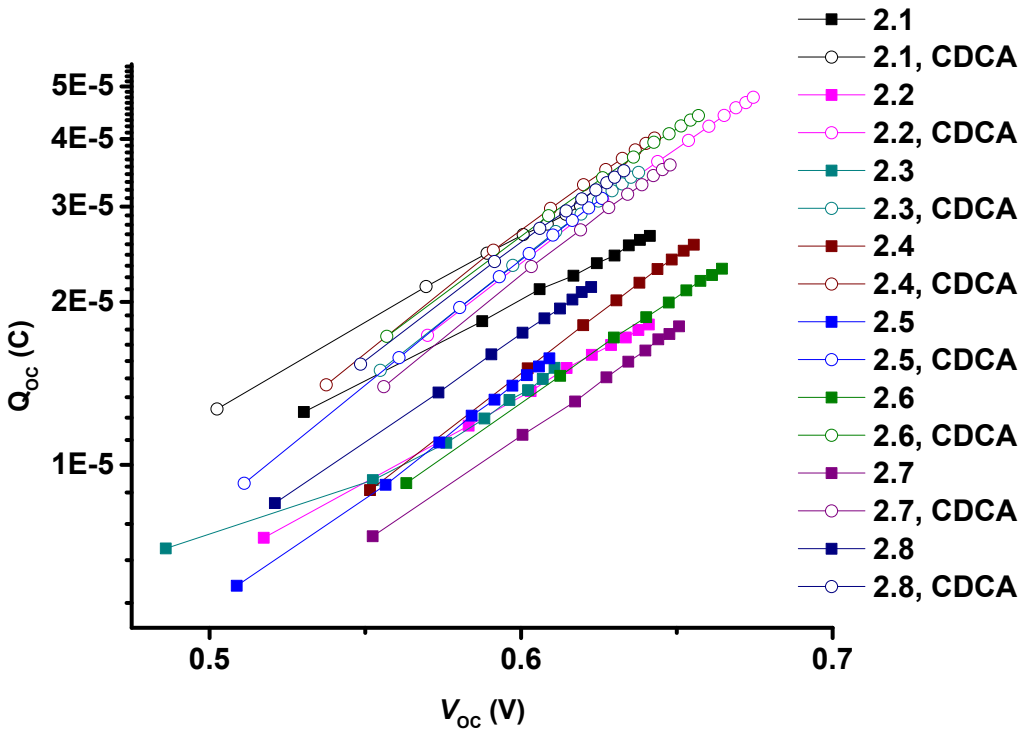

Figure 2-18. The charge extraction as a function of open-circuit voltage for all sensitizers.

2.7.4 Electron lifetime

Electron lifetime (τ_n) was obtained using small-modulation techniques under constant current conditions that allow electrons in the TiO_2 to recombine with acceptors in the electrolyte rather than extracting the electrons at the counter electrode. Under these conditions, the response time of the photovoltage is nearly equal to the lifetime of the electron in the TiO_2. Electron lifetime measurements can provide an understanding of the relative amounts of recombination that may decrease the electron lifetime in TiO_2. To focus on differences in electron recombination, shifts in the TiO_2 conduction band position are accounted for using the change in V_{OC} from charge extraction measurements.

In the presence of CDCA, the electron lifetime increases for each sensitizer. Without CDCA, sensitizers **2.2**, **2.3**, **2.4**, **2.6**, and **2.8** have similar electron lifetimes, while sensitizer **2.1** has an increased electron lifetime relative to this group, and sensitizers **2.5** and **2.7** exhibit minor decreases in electron lifetime relative to this group. This is consistent with the minor decreases in V_{OC} and decreases in J_{SC} observed for sensitizers **2.5** and **2.7** incorporating benzo[*g*]indole and BTD moieties. Despite incorporating a BTD, sensitizer **2.8**, with its additional benzo[e]indole and CPDT-BTD-CPDT π-bridge, exhibited a higher J_{SC} than sensitizer **2.7**, and the trends in electron lifetime are consistent with this.

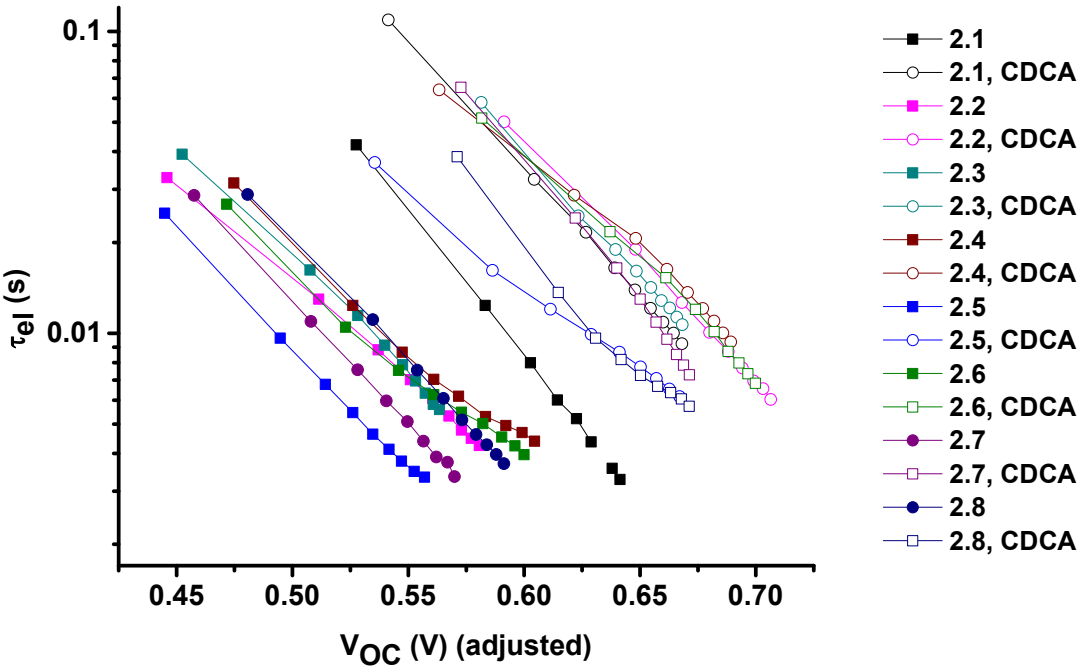

Figure 2-19. Electron lifetime vs. open circuit voltage for sensitizers **2.1**-**2.8**.

2.8 Conclusion

This work developed squaraine sensitizers with absorption maxima bathochromically shifted into the near-infrared and panchromatic absorption across the high-energy part of the visible spectrum. When employing the benzo[*e*]indole moiety in place of an indole (sensitizer **2.2** vs **2.1**), the absorption red-shifted by 18 nm to 688 nm. The V_{OC}, J_{SC}, and FF were all improved, for a PCE of 5.5% for sensitizer **2.2** compared to a PCE of 4.5% for sensitizer **2.1**. The electron lifetime was also slightly higher, indicating slightly lower TiO_2-electrolyte recombination for sensitizer **2.2**. When the benzo[*g*]indole group was utilized in place of the benzo[*e*]indole while employing the CPDT (sensitizer

2.5 vs **2.4**), the absorption maximum red-shifted 5 nm from 695 nm for the benzo[*e*]indole to 700 nm for the benzo[*g*]indole. The V_{OC} and J_{SC} decreased, though the FF improved slightly, resulting in a PCE of 5.8% for the benzo[*g*]indole-substituted sensitizer **2.5** compared to a PCE of 6.2% for the benzo[*e*]indole sensitizer **2.4**. The electron lifetime for the sensitizer **2.5** was also much lower than for sensitizer **2.4**, indicating increased TiO_2-electrolyte recombination for the benzo[*g*]indole-substituted sensitizer which contributed to the lowered V_{OC} and J_{SC}.

When the bis(4-butoxyphenyl)amino-indole group was employed in place of the indole (sensitizer **2.3** vs **2.1**), the bis(4-butoxyphenyl)amino-indole-substituted sensitizer exhibited a significant red-shift, with a promising IPCE onset of over 850 nm. Calculated ground and excited state dipoles predicted a large Stokes shift, which was observed experimentally, indicating a more charge transfer-type absorption. In devices, the bis(4-butoxyphenyl)amino-substituted sensitizer **2.3** saw decreased IPCE % at maximum absorption, resulting in a J_{SC} only slightly above that of the benzo[*e*]indole despite significant near-IR absorption for the amino-substituted sensitizer. The V_{OC} and FF values were similar between the two sensitizers, with a slight decrease in V_{OC} and incremental increase in FF for the amino-substituted sensitizer **2.3**, resulting in a PCE of 5.0%, which was an increase in PCE relative to the indole-based sensitizer **2.1** at 4.5%, but a decrease relative to the benzo[*e*]indole sensitizer **2.3** at 5.5%. The electron lifetime for sensitizer **2.3** was similar to, or slightly higher than that of sensitizer **2.1**, indicating that increased TiO_2-electrolyte recombination was not the cause of the slightly lower V_{OC} observed. The lower performance of sensitizer **2.3** may be related to the increased aggregation seen in the absorption when adsorbed on TiO_2.

Examining CPDT vs. thiophene on the π-bridge (sensitizer **2.4** vs. **2.2**), the CPDT-substituted sensitizer **2.4** red-shifted the absorption maximum by 7 nm from 688 to 695 nm and increased absorption near 300 and 500 nm. The improved IPCE response near 500 nm aided in improving the J_{SC} by almost 2 mA/cm^2, though the IPCE % did decrease near the absorption maximum from ~63% to ~53%. The improved J_{SC} and slightly decreased V_{OC} and FF resulted in a PCE of 6.2% for the CPDT-substituted sensitizer **2.4** vs. 5.5% for the thiophene-substituted sensitizer **2.2**. The electron lifetime for sensitizer **2.4** was similar to, but very slightly higher than for sensitizer **2.2**, indicating similar, but slightly decreased TiO_2-electrolyte recombination for the CPDT π-bridge relative to thiophene.

Relative to the mesityl- and CPDT-substituted sensitizer **2.6**, the inclusion of the BTD-CPDT π-bridge on sensitizer **2.7** results in a sharp decrease in J_{SC} and a PCE of 4.5% for the BTD-CPDT sensitizer **2.7** relative to 6.4% for the CPDT analogue sensitizer **2.6**. The BTD-CPDT-substituted sensitizer **2.7** also exhibited a slight decrease in electron lifetime. Computationally, the dihedral angle between the squaraine core and the BTD was relatively large at 40° in the ground state and 34° in the excited state, compared to angles of 25° and 20° for the squaraine-CPDT dihedral angle seen for sensitizer **2.6**. The absorption maximum was also blue-shifted by 13 nm from 699 nm with the CPDT-substituted sensitizer **2.6** to 686 nm for the BTD-CPDT π-bridge on sensitizer **2.7**.

On sensitizer **2.8**, an additional benzo[e]indole and CPDT are included, resulting in a red-shift of 13 nm relative to the BTD-CPDT sensitizer **2.7**, returning to the same absorption maximum as the CPDT-substituted sensitizer **2.6**. For the CPDT-BTD-CPDT-substituted sensitizer **2.8**, there was as an increase in J_{SC} relative to sensitizer **2.7**, with an

IPCE onset near 840 nm. However, the J_{SC} seen in the CPDT-BTD-CPDT-substituted sensitizer **2.8** is still less than that seen in the CPDT-substituted sensitizer **2.6**, and is accompanied by decreases in V_{OC} and FF relative to both sensitizer **2.6** and sensitizer **2.7**. A comparative lack of electron density on the CPDT and anchor is seen for sensitizers **2.7** and **2.8** in the natural transition orbitals calculated by TD-DFT, which could relate to the lower J_{SC} seen for sensitizer **2.7**, but does not explain the higher J_{SC} and lower V_{OC} of sensitizer **2.8**. The increased TiO_2-electrolyte recombination observed for sensitizer **2.8** through its low electron lifetime appears to be a larger factor contributing to its low performance.

In conclusion, promising photocurrent response in the 800-850 nm wavelength range was seen through the use of various functionalities including bis(4-butoxyphenyl)amino-indole, with the importance of considering the effects of recombination seen. Further studies could examine modifications to the squaraine termination using a variety of donors with alkoxy chains that could prevent close interaction with cobalt or copper electrolytes, as seen for literature sensitizers **LEG4** or **Y123**.[30,42] This may facilitate lower TiO_2-electrolyte recombination and a lower driving force for regeneration, which can promote a higher V_{OC} and allow for an optical gap closer to the calculated ideal of 1.3 eV.

2.9 Experimental Methods

The synthesis of sensitizer **2.1** was previously described.[123]

2.9.1 Synthesis of sensitizer 2.2

2.9.1.1 Synthesis of 5-bromo-2,3,3-trimethyl-3*H*-indole

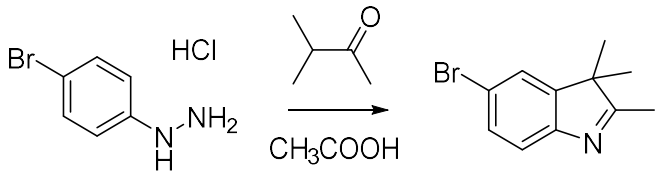

4-Bromophenyl hydrazine hydrochloride (21.2 g, 94.9 mmol) and 3-methyl-2-butanone (10.2 mL, 94.9 mmol) were added to a round-bottom flask fitted with a reflux condenser. Glacial acetic acid was added while filling with nitrogen. Slowing the flow of nitrogen, the reaction mixture was heated to 100 °C and stirred overnight (15 h). The reaction solution was red-brown with a white precipitate. Additional butanone was added (20 mL) and the reaction was left another 8 h. After cooling to room temperature, the solvent was removed under reduced pressure and the product was dissolved in CH_2Cl_2 and rinsed with H_2O. The solvent was removed under reduced pressure to yield a brown oil (22.6 g, 94.9 mmol, quantitative yield), which was used without further purification. The ^1H NMR spectrum was consistent with that previously reported in the literature.[153]

2.9.1.2 Synthesis of 5-bromo-1-dodecyl-2,3,3-trimethyl-3*H*-indol-1-ium iodide

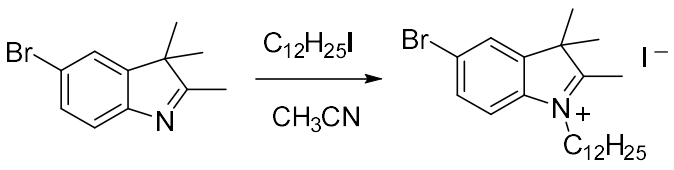

5-Bromo-2,3,3-trimethyl-3*H*-indole (23.5 g, 98.9 mmol) and 1-iodododecane (29 mL, 120 mmol) were refluxed in CH_3CN for 7 d. After cooling to room temperature, the solution was concentrated to 20 mL *in vacuo*. Ether was added, and the solution was stored at -10 °C for 3 h. After letting the solution warm to room temperature, the solid was removed by vacuum filtration, washed 4 times with ether and let dry on the vacuum filtration apparatus to yield an off-white solid (40. g, 74 mmol, 75% yield). The ^{1}H NMR spectrum was consistent with that previously reported in the literature.[123]

2.9.1.3 Synthesis of 5-bromo-1-dodecyl-3,3-dimethyl-2-methyleneindoline

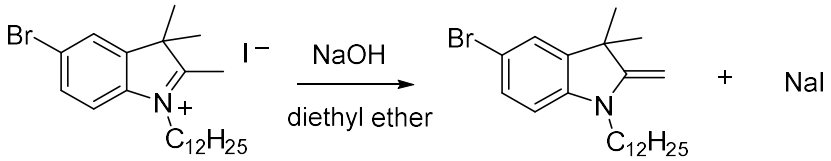

5-Bromo-1-dodecyl-2,3,3-trimethyl-3*H*-indol-1-ium iodide (7.2 g, 13 mmol) was stirred in a mixture of 1 M NaOH aqueous solution (125 mL) and diethyl ether (125 mL) for 15 min. The product was extracted by diethyl ether (3x) and dried over $MgSO_4$. The solvent was removed under reduced pressure to give a yellow oil (5.5 g, quantitative yield).

2.9.1.4 Synthesis of (*E*)-3-((5-bromo-1-dodecyl-3,3-dimethylindolin-2-ylidene)methyl)-4-ethoxycyclobut-3-ene-1,2-dione

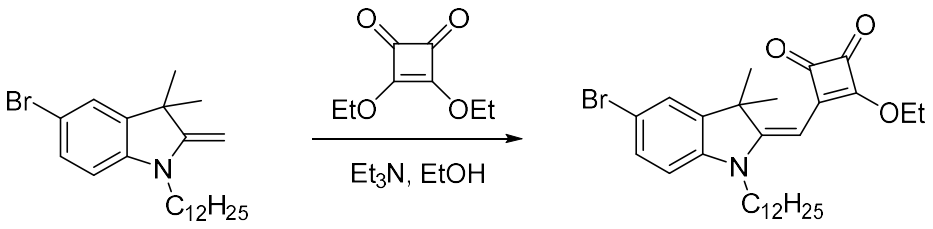

5-Bromo-1-dodecyl-3,3-dimethyl-2-methyleneindoline (13.18 g, 32.4 mmol) and ethyl squarate (4.80 mL, 32.4 mmol) were dissolved in 40 mL EtOH. Et_3N (4.52 mL, 32.4 mmol) was added and the mixture was heated at reflux under nitrogen overnight (18 h). The solvent was removed under reduced pressure. The residue was purified by flash column chromatography using CH_2Cl_2, then CH_2Cl_2: EtOAc 30:1. The product was collected and solvent removed to yield an orange solid (3.87 g, 23%). ^{1}H NMR (400 MHz, $CDCl_3$): δ (ppm) = 7.40-7.32 (m, 2H), 6.72 (d, *J* = 8.2 Hz, 1H), 5.37 (s, 1H), 4.88 (q, *J* = 7.1 Hz, 2H), 3.76 (t, *J* = 7.5 Hz, 2H), 1.71 (quin, *J* = 7.3 Hz, 2H), 1.60 (s, 6H), 1.52 (t, *J* = 7.1 Hz, 3H), 1.43-1.28 (m, 4H), 1.24 (s (br), 14H), 0.86 (t, *J* = 6.8 Hz, 3H). $^{13}C\{^1H\}$ NMR (101 MHz, $CDCl_3$) δ (ppm) = 192.29, 188, 187.76, 173.63, 167.34, 142.93, 141.88, 130.57, 125.35, 115.07, 109.65, 81.82, 70.05, 47.91, 43.08, 31.90, 29.59, 29.52, 29.44, 29.32, 29.27, 26.97, 26.24, 22.67, 15.92, 14.12. HRMS (ESI): m/z 520.2254 $[M+H]^+$ (calcd for $C_{29}H_{41}BrNO_3$: 520.2264). Anal. Calcd for $C_{29}H_{40}BrNO_3$: C, 65.65; H, 7.60; N, 2.64. Found: C, 65.63; H, 7.52; N, 2.68.

2.9.1.5 Synthesis of (*E*)-3-((5-bromo-1-dodecyl-3,3-dimethylindolin-2-ylidene)methyl)-4-hydroxycyclobut-3-ene-1,2-dione

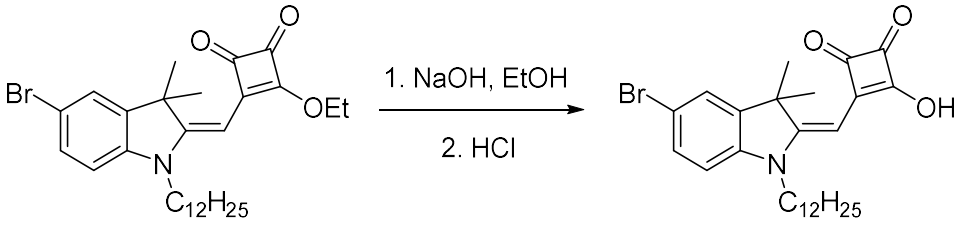

(*E*)-3-((5-Bromo-1-dodecyl-3,3-dimethylindolin-2-ylidene)methyl)-4-ethoxycyclobut-3-ene-1,2-dione (2.0 g, 3.8 mmol) was refluxed in EtOH (40 mL). 40% wt NaOH (5 mL) was added and refluxed for another 30 min. The solution was then cooled to room temperature and 2 N HCl (18

mL) was added to adjust the pH to approximately 3. The ethanol was removed and the residue was extracted with CH_2Cl_2 (3x), which was dried over $MgSO_4$. The solvent was removed under reduced pressure to yield an orange-brown solid (1.8 g, 94%).

2.9.1.6 Synthesis of 1,1,2-trimethyl-1*H*-benzo[*e*]indole

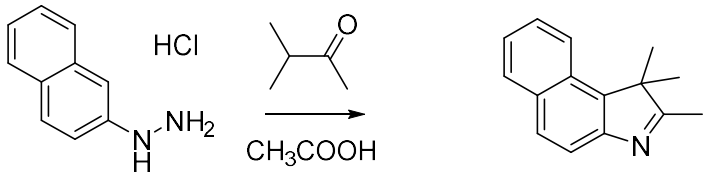

Naphthalen-2-ylhydrazine hydrochloride (6.1 g, 31 mmol) and 3-methyl-2-butanone (3.4 mL, 31 mmol) were added to a round-bottom flask fitted with a reflux condenser. Glacial acetic acid (100 mL) was added while filling with nitrogen. The mixture was heated to 100 °C under nitrogen and monitored. Additional 3-methyl-2-butanone was added after 19 h, as starting material remained. After completion (24 h) and cooling to room temperature, the solvent was removed under reduced pressure. The product was dissolved in CH_2Cl_2, and the combined organics were washed with H_2O and dried with $MgSO_4$. The solvent was removed under reduced pressure to yield a purple solid (6.2 g, 30 mmol, 95% yield). The ^{1}H NMR spectrum was consistent with that previously reported in the literature.[154]

2.9.1.7 Synthesis of 3-ethyl-1,1,2-trimethyl-1*H*-benzo[*e*]indol-3-ium iodide

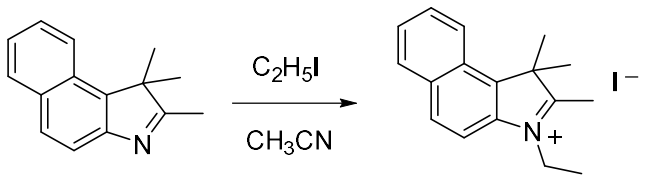

1,1,2-Trimethyl-1*H*-benzo[*e*]indole (6.1 g, 29 mmol) and iodoethane (3.5 mL, 44 mmol) were refluxed in CH_3CN for 6 d. After cooling to room temperature, ether was added, and the solution was stored at -10 °C for 3 h. The solid was then removed by vacuum filtration, washed with ether, and let dry on the vacuum filtration apparatus to yield a gray solid (7.7 g, 21 mmol, 68%). The ^{1}H NMR spectrum was consistent with that previously reported in the literature.[155]

2.9.1.8 Synthesis of (*E*)-2-((*Z*)-(5-bromo-1-dodecyl-3,3-dimethylindolin-2-ylidene)methyl)-4-((3-ethyl-1,1-dimethyl-1*H*-benzo[*e*]indol-3-ium-2-yl)methylene)-3-oxocyclobut-1-enolate

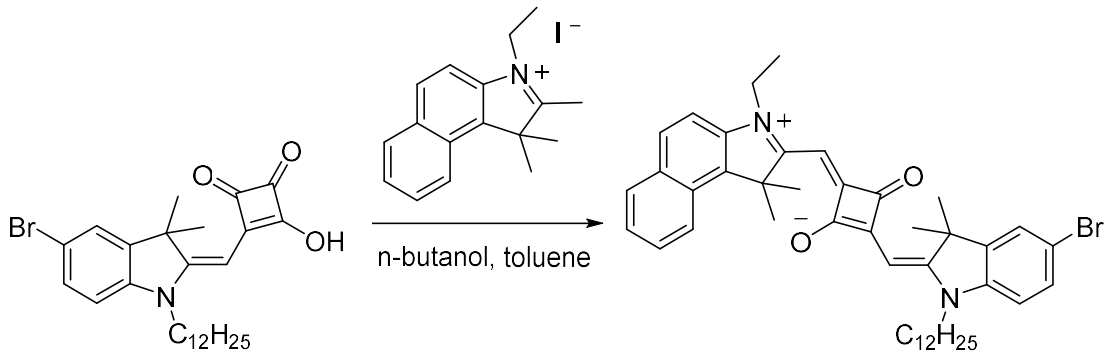

(*E*)-3-((5-Bromo-1-dodecyl-3,3-dimethylindolin-2-ylidene)methyl)-4-hydroxycyclobut-3-ene-1,2-dione (1.89 g, 3.76 mmol) and 3-ethyl-1,1,2-trimethyl-1*H*-benzo[*e*]indol-3-ium iodide (1.37 g, 3.76 mmol) were dissolved in a solution of 12 mL toluene and 12 mL *n*-butanol. The reaction was fitted with a Dean-Stark water separator and refluxed. After 15 min the solution turned green, then blue-green after an hour. The reaction was complete after 18 h. The solvent was removed under reduced pressure and the product was purified by column chromatography (CH_2Cl_2:MeOH = 97:3) to yield a blue/red solid (2.12 g, 78%). ^{1}H NMR (500 MHz, $CDCl_3$): δ (ppm) = 8.19 (d, J = 8.5 Hz, 1H), 7.89 (t, J = 12.2

Hz, 2H), 7.58 (ddd, *J* = 8.3, 7.1, 1.2 Hz, 1H), 7.43 (ddd, *J* = 8.2, 6.7, 0.8 Hz, 2H), 7.40 (dd, *J* = 8.3, 1.9 Hz, 1H), 7.32 (d, *J* = 8.8 Hz, 1H), 6.81 (d, *J* = 8.4 Hz, 1H), 6.05 (s, 1H), 5.94 (s, 1H), 4.23 (d, *J* = 5.6 Hz, 2H), 3.9 (s, br, 2H), 2.07 (s, 6H), 1.80 (s, br, 8H), 1.45 (t, *J* = 7.3 Hz, 3H), 1.41 (m, 2H), 1.35 (m, 2H), 1.26 (s, br, 14H), 0.88 (t, *J* = 6.8 Hz, 3H). $^{13}C\{^{1}H\}$ NMR (126 MHz, $CDCl_3$) δ (ppm) = 182.42, 180.24, 177.67, 172.29, 168.10, 144.18, 141.80, 138.90, 134.89, 131.45, 130.55, 129.83, 129.73, 128.67, 127.41, 125.62, 124.55, 122.59, 115.93, 110.29, 109.97, 86.80, 86.38, 51.52, 49.02, 43.68, 38.81, 31.90, 29.69, 29.65, 29.59, 29.52, 29.48, 29.37, 29.32, 27.18, 27.07, 26.89, 26.61, 22.68, 14.13, 12.44. HRMS (ESI): m/z 720.3278 $[M]^+$ (calcd for $C_{44}H_{53}BrN_2O_2$: 720.3285). Anal. Calcd for $C_{44}H_{53}BrN_2O_2(H_2O)_{0.5}$: C, 72.31; H, 7.45; Br, 10.93; N, 3.83. Found: C, 72.33; H, 7.52; Br, 10.81; N, 3.82.

2.9.1.9 Synthesis of 2-((*E*)-(1-dodecyl-5-(5-formylthiophen-2-yl)-3,3-dimethylindolin-2-ylidene)methyl)-4-((3-ethyl-1,1-dimethyl-1*H*-benzo[*e*]indol-3-ium-2-yl)methylene)-3-oxocyclobut-1-enolate

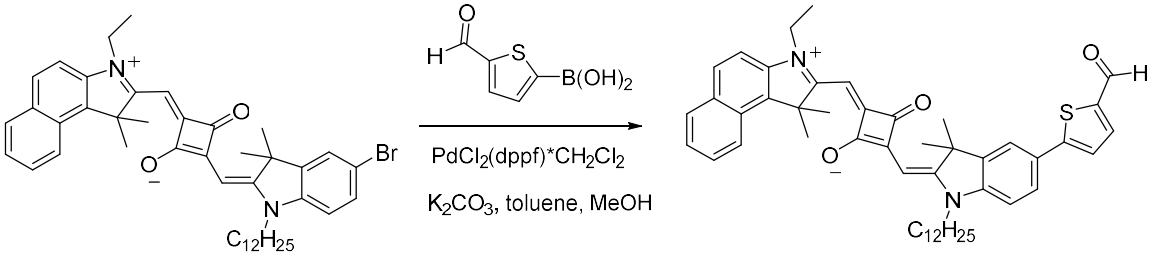

(*E*)-2-((*E*)-(5-Bromo-1-dodecyl-3,3-dimethylindolin-2-ylidene)methyl)-4-((3-ethyl-1,1-dimethyl-1*H*-benzo[*e*]indol-3-ium-2-yl)methylene)-3-oxocyclobut-1-enolate (100 mg, 0.139 mmol) and 5-formylthiophen-2-ylboronic acid (65 mg, 0.416 mmol), $PdCl_2(dppf)\cdot CH_2Cl_2$ (11 mg, 0.014 mmol), and potassium carbonate (96 mg, 0.69 mmol)

were combined in an oven-dried microwave tube. After filling with nitrogen in a glove box for 30 min, toluene (2 mL) and MeOH (2 mL) were added and the tube was capped before removal from the glove box. The microwave reactor (Biotage, Initiator 2.5) was set to 70 °C with a hold time of 15 min. Nine batches of the reaction mixture were combined and passed through a silica gel plug (CH_2Cl_2:EtOAc = 9:1, then 8:1). Further purification by size exclusion column (S-X1, Biobeads, THF) yielded a blue-green solid (760 mg, 81%). ^{1}H NMR (500 MHz, $CDCl_3$): δ (ppm) = 9.88 (s, 1H), 8.2 (d, *J* = 8.5 Hz, 1H), 7.91 (t, *J* = 7.6 Hz, 2H), 7.75 (d, *J* = 3.9 Hz, 1H), 7.65-7.57 (m, 3H), 7.45 (t, *J* = 7.5 Hz, 1H), 7.40 (d, *J* = 3.9 Hz, 1H), 7.34 (d, *J* = 8.8 Hz, 1H), 6.98 (d, *J* = 8.2 Hz, 1H), 6.09 (s, 1H), 6.00 (s, 1H), 4.25 (d, *J* = 6.4 Hz, 2H), 3.96 (s, 2H), 2.08 (s, 6H), 1.86 (s, br, 6H), 1.82 (quin, *J* = 6.9 Hz, 2H), 1.48 (t, *J* = 7.3 Hz, 3H), 1.44 (quin, *J* = 6.8 Hz, 2H), 1.37 (quin, *J* = 6.2 Hz, 2H), 1.26 (s, br, 14H), 0.87 (t, *J* = 6.8 Hz, 3H). ^{13}C{^{1}H} NMR (126 MHz, $CDCl_3$) δ (ppm) = 182.6, 180.88, 177.23, 172.67, 167.79, 154.33, 143.91, 143.14, 141.73, 138.82, 137.66, 135.06, 131.52, 129.9, 129.75, 128.63, 128.08, 127.47, 126.55, 124.67, 123.41, 122.62, 120.19, 110.01, 109.36, 87.37, 86.57, 51.64, 48.73, 43.71, 38.91, 31.9, 29.69, 29.6, 29.53, 29.5, 29.38, 29.33, 27.31, 27.1, 27, 26.57, 22.68, 14.13, 12.5. HRMS (ESI): m/z 752.3996 $[M]^+$ (calcd for $C_{49}H_{56}N_2O_3S$: 752.4006). Anal. Calcd for $C_{49}H_{56}N_2O_3S$ (%): C, 78.15; H, 7.50; N, 3.72; S, 4.26. Found: C, 77.97; H, 7.56; N, 3.66; S, 4.12.

2.9.1.10 Synthesis of (*E*)-2-((*E*)-(5-(5-((*E*)-2-carboxy-2-cyanovinyl)thiophen-2-yl)-1-dodecyl-3,3-dimethylindolin-2-ylidene)methyl)-4-((3-ethyl-1,1-dimethyl-1*H*-benzo[*e*]indol-3-ium-2-yl)methylene)-3-oxocyclobut-1-enolate

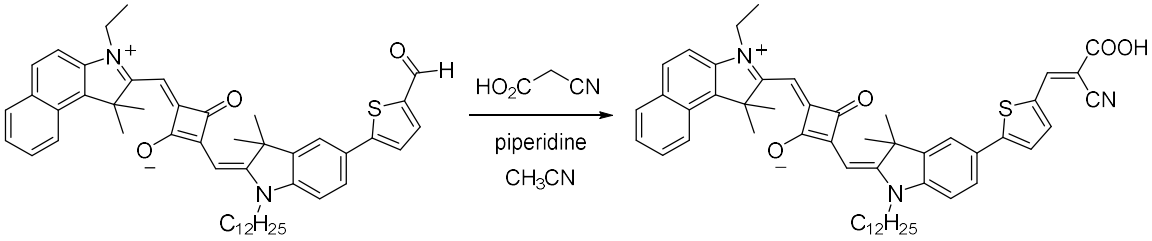

2-((*E*)-(1-Dodecyl-5-(5-formylthiophen-2-yl)-3,3-dimethylindolin-2-ylidene)methyl)-4-((3-ethyl-1,1-dimethyl-1*H*-benzo[*e*]indol-3-ium-2-yl)methylene)-3-oxocyclobut-1-enolate (390 mg, 0.518 mmol) and cyanoacetic acid (93 mg, 1.1 mmol) were added to an oven-dried round-bottom flask, then evacuated and filled with nitrogen three times before anhydrous acetonitrile (30 mL) was added. Piperidine (30 µL) was added, and the reaction mixture was refluxed for 4 h. This reaction was performed again, starting with 289 mg of the squaraine starting material and proportional amounts of other reactants. The two reactions were combined, and the solvent was removed under reduced pressure. The residue was passed through a size exclusion column (S-X1, Biobeads, THF). The crude product, obtained from the major fraction, was purified by column chromatography (CH_2Cl_2:MeOH:acetic acid = 98.5:0.5:1, then 98:1:1, then 89:10:1). The solvent was removed slowly under reduced pressure until minimal solvent remained. The product crystallized in the residual solvent (acetic acid) overnight, then the solvent was removed under reduced pressure and the residue was dried under high vacuum overnight (380 mg, 51%). ^{1}H NMR (500 MHz, $CDCl_3$): δ (ppm) = 8.30 (s, 1H), 8.21 (d, J = 8.5 Hz, 1H), 7.93 (d, J = 8.6 Hz, 2H), 7.77 (d, J = 3.9 Hz, 1H), 7.68 (d, J = 8.2 Hz, 1H), 7.65 (d, J = 1.2 Hz,

1H), 7.60 (t, *J* = 7.6 Hz, 1H), 7.52-7.34 (m, 3H), 7.03 (d, *J* = 8.3 Hz, 1H), 6.10 (s, 1H), 5.99 (s, 1H), 4.31 (d, *J* = 6.8 Hz, 2H), 4.05 (s, 2H), 2.06 (s, 6H), 1.83 (s, br, 8H), 1.50 (t, *J* = 7.1 Hz, 3H), 1.48-1.43 (m, 2H), 1.39 (quin, *J* = 6.7 Hz, 2H), 1.27 (s, 14H), 0.87 (t, *J* = 6.7 Hz, 3H) (COOH resonance not observed). $^{13}C\{^{1}H\}$ NMR (126 MHz, $CDCl_3$) δ (ppm) = 183.53, 178.65, 174.82, 173.71, 168.6, 164.9, 154.8, 146.93, 144.38, 143.42, 139.66, 139.09, 135.56, 134.78, 132.11, 130.36, 130.07, 128.9, 128.46, 127.77, 127.13, 125.12, 124.17, 122.9, 120.47, 116.86, 110.51, 110.08, 98.21, 87.42, 86.82, 51.99, 44.07, 39.40, 32.14, 29.82, 29.75, 29.65, 29.54, 27.41, 27.34, 27.26, 26.64, 22.87, 14.14, 12.56. HRMS (ESI): m/z 819.4058 $[M]^+$ (calcd for $C_{52}H_{57}N_3O_4S$: 819.4070). Anal. Calcd for $C_{52}H_{57}N_3O_4S$ (%): C, 76.16; H, 7.01; N, 5.12; S, 3.91. Found: C, 75.89; H, 7.15; N, 5.09; S, 3.86.

2.9.2 Synthesis of sensitizer 2.3

2.9.2.1 Synthesis of N,N-bis(4-butoxyphenyl)-2,3,3-trimethyl-3*H*-indol-5-amine

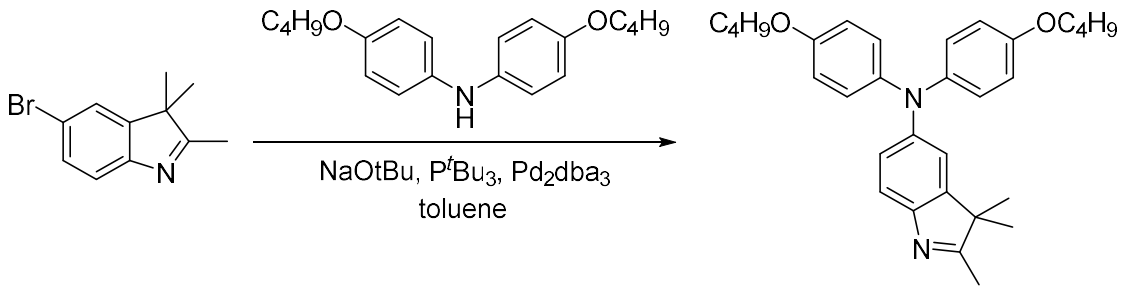

5-Bromo-2,3,3-trimethyl-3*H*-indole (1.00 g, 4.20 mmol), bis(4-methoxyphenyl)amine (1.38 g, 4.41 mmol), tri-*tert*-butylphosphine (51 mg, 0.25 mmol), and sodium *tert*-butoxide (0.61 g, 6.3 mmol) were dissolved in toluene under a nitrogen atmosphere and degassed with nitrogen for 15 min. Upon addition of $Pd_2(dba)_3$, the mixture was refluxed

for 48 h. The solvent was removed under reduced pressure and the residue was initially purified by passing through a silica gel plug (CH_2Cl_2, then CH_2Cl_2:EtOAc from 2-20%). The solvent from the main band fraction was removed under reduced pressure and the residue was further purified by flash chromatography (Biotage Isolera system, 50 g silica gel). The eluents were as follows: 100% CH_2Cl_2, followed by 9:1 CH_2Cl_2:EtOAc, with the product collected as the main fraction after several smaller bands exited the column. The main band fractions were combined, and the solvent was removed under reduced pressure to yield an orange oil (0.91 g, 46%). ^{1}H NMR (700 MHz, $CDCl_3$): δ (ppm) = 7.30 (d, *J* = 8.3 Hz, 1H), 7.01 (d, *J* = 9.0 Hz, 4H), 6.92 (d, *J* = 2.2 Hz, 1H), 6.85 (d, *J* = 8.3 Hz, 1H), 6.80 (d, *J* = 9.0 Hz, 4H), 3.93 (t, *J* = 6.5 Hz, 4H), 2.23 (s, 3H), 1.78-1.73 (m, 4H), 1.53-1.46 (m, 4H), 1.22 (s, 6H), 0.97 (t, *J* = 7.4 Hz, 6H). ^{13}C{^{1}H} NMR (176 MHz, $CDCl_3$): δ (ppm) = 185.7, 154.97, 147.73, 146.72, 146.59, 141.42, 125.86, 120.88, 119.79, 115.2, 115.12, 67.89, 53.57, 31.41, 23.11, 19.25, 15.28, 13.86. HRMS (ESI): m/z 470.2925 $[M]^+$ (calcd for $C_{31}H_{38}O_2N_2$: 470.2933). Anal. Calcd for $C_{31}H_{38}O_2N_2$ (%): C, 79.11; H, 8.14; N, 5.95. Found: C, 78.88; H, 8.34; N, 5.84.

2.9.2.2 Synthesis of 5-(bis(4-butoxyphenyl)amino)-1-ethyl-2,3,3-trimethyl-3*H*-indol-1-ium iodide

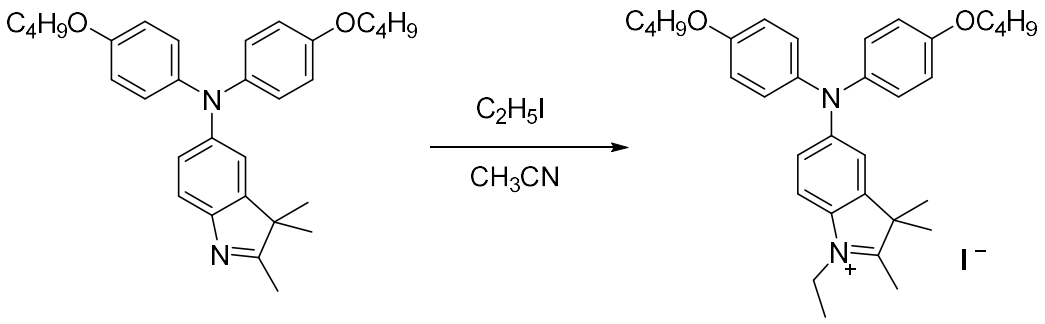

N,*N*-Bis(4-butoxyphenyl)-2,3,3-trimethyl-3*H*-indol-5-amine (0.57 g, 1.2 mmol) and iodoethane (0.19 g, 1.2 mmol) were refluxed in CH_3CN for 1.5 d. The solution was cooled to room temperature, after which ether was added. The solution was stored at -10 °C for a time. The solid was then removed by vacuum filtration and washed with ether to obtain an off-white brownish solid, which was then dried under high vacuum (0.268 g, 35%). ^{1}H NMR (700 MHz, $CDCl_3$): δ (ppm) = 7.34 (d, *J* = 8.9 Hz, 1H), 7.08 (d, *J* = 9.0 Hz, 4H), 6.91-6.89 (m, 2H), 6.88 (d, *J* = 9.0 Hz, 4H), 4.66 (q, *J* = 7.4 Hz, 2H), 3.96 (t, *J* = 6.5 Hz, 4H), 3.02 (s, 3H), 1.80-1.75 (m, 4H), 1.59 (t, *J* = 7.5 Hz, 3H), 1.54-1.47 (m, 4H), 1.51 (s, 6H), 0.99 (t, *J* = 7.4 Hz, 6H). ^{13}C{^{1}H} NMR (176 MHz, $CDCl_3$): δ (ppm) = 189.26, 156.79, 151.3, 143.3, 138.96, 132.14, 127.6, 118.18, 115.71, 115.54, 111.93, 67.97, 53.89, 45.23, 31.33, 23.23, 19.26, 16.14, 13.87, 13.62. HRMS (ESI): m/z 499.3310 $[M]^+$ (calcd for $C_{33}H_{43}O_2N_2$ (no I^-): 499.3319). Anal. Calcd for $C_{33}H_{43}O_2N_2$ (%): C, 63.25; H, 6.92; I, 20.25; N, 4.47. Found: C, 62.97; H, 6.86; I, 19.95; N, 4.61.

2.9.2.3 Synthesis of (*E*)-4-((5-(bis(4-butoxyphenyl)amino)-1-ethyl-3,3-dimethyl-3*H*-indol-1-ium-2-yl)methylene)-2-((*E*)-(5-bromo-1-dodecyl-3,3-dimethylindolin-2-ylidene)methyl)-3-oxocyclobut-1-enolate

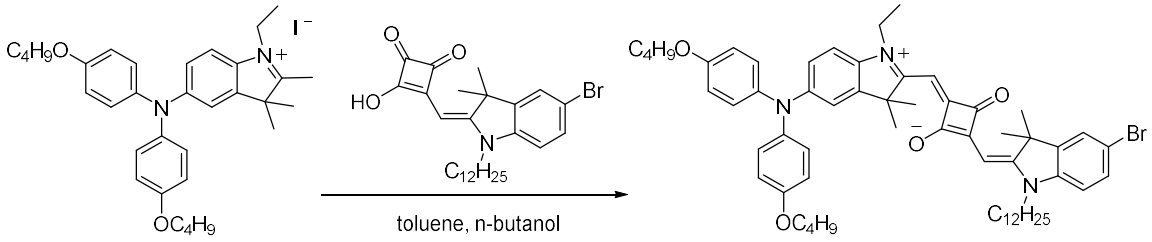

5-(Bis(4-butoxyphenyl)amino)-1-ethyl-2,3,3-trimethyl-3*H*-indol-1-ium iodide (1.25 g, 1.99 mmol) and (*Z*)-3-((5-bromo-1-dodecyl-3,3-dimethylindolin-2-ylidene)methyl)-4-

hydroxycyclobut-3-ene-1,2-dione (1.00 g, 1.99 mmol) were dissolved in a solution of 6 mL toluene and 6 mL *n*-butanol. The reaction was fitted with a Dean-Stark water separator and refluxed for 18 h. The solvent was removed under reduced pressure then high vacuum overnight. The product was purified by column chromatography twice (CH_2Cl_2:MeOH = 99:1, then CH_2Cl_2:MeOH = 99.5:0.5, 500 mL silica gel) to yield a blue/red solid (0.862 g, 44%). ^{1}H NMR (500 MHz, $CDCl_3$): δ (ppm) = 7.41 (s, 1H), 7.37 (dd, *J* = 8.3, 1.8 Hz, 1H), 7.02 (d, *J* = 2.1 Hz, 1H), 7.01 (d, *J* = 9.0 Hz, 4H), 6.87 (dd, *J* = 8.6, 2.1 Hz, 1H), 6.83 (d, *J* = 9.0 Hz, 5H), 6.77 (d, *J* = 8.4 Hz, 1H), 5.95 (s, 1H), 5.87 (s, 1H), 4.08 (q, *J* = 6.6 Hz, 2H), 3.95 (t, *J* = 6.5 Hz, 4H), 3.86 (t, *J* = 6.6 Hz, 2H), 1.81-1.73 (m, 10H), 1.71 (s, 6H), 1.55-1.46 (m, 4H), 1.41 (t, *J* = 7.2 Hz, 3H), 1.38-1.26 (m, 6H), 0.98 (t, *J* = 7.4 Hz, 6H), 0.87 (t, *J* = 6.9 Hz, 3H). ^{13}C{^{1}H} NMR (126 MHz, $CDCl_3$) δ (ppm) = 182.48, 180.20, 176.07, 170.19, 167.03, 155.38, 146.49, 144.08, 143.74, 141.92, 140.81, 135.30, 130.43, 126.00, 125.53, 120.69, 115.81, 115.47, 115.30, 109.99, 86.52, 86.45, 67.92, 49.82, 48.75, 43.50, 38.81, 31.88, 31.40, 29.68, 29.57, 29.50, 29.46, 29.36, 29.30, 27.19, 27.05, 26.81, 26.66, 22.67, 19.26, 14.12, 13.88, 12.25. HRMS (MALDI): m/z 981.5051 $[M]^+$ (calcd for $C_{60}H_{76}N_3O_4Br$: 981.5019). Anal. Calcd for $C_{60}H_{76}N_3O_4Br$: C, 73.30; H, 7.79; Br, 8.13; N, 4.27. Found: C, 73.27; H, 7.69; Br, 8.00; S, 4.22.

2.9.2.4 Synthesis of (*E*)-4-((5-(bis(4-butoxyphenyl)amino)-1-ethyl-3,3-dimethyl-3*H*-indol-1-ium-2-yl)methylene)-2-((*E*)-(1-dodecyl-5-(5-formylthiophen-2-yl)-3,3-dimethylindolin-2-ylidene)methyl)-3-oxocyclobut-1-enolate

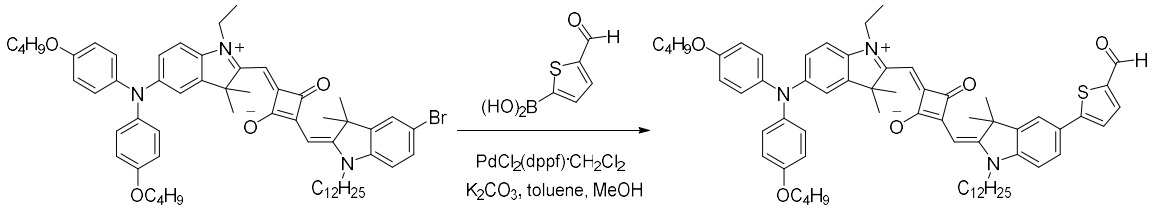

(*E*)-4-((5-(Bis(4-butoxyphenyl)amino)-1-ethyl-3,3-dimethyl-3*H*-indol-1-ium-2-yl)methylene)-2-((*E*)-(5-bromo-1-dodecyl-3,3-dimethylindolin-2-ylidene)methyl)-3-oxocyclobut-1-enolate (250 mg, 0.254 mmol) and 5-formylthiophen-2-ylboronic acid (119 mg, 0.763 mmol), $PdCl_2(dppf)\cdot CH_2Cl_2$ (21 mg, 0.025 mmol), and potassium carbonate (176 mg, 1.27 mmol) were combined in an oven-dried microwave tube. After filling with nitrogen in a glove box for 30 min, toluene (4 mL) and MeOH (4 mL) were added and the tube was capped before removal from the glove box. The microwave reactor (Biotage, Initiator 2.5) was set to 70 °C with a hold time of 15 min. The reaction mixture was passed through a silica gel plug (CH_2Cl_2:EtOAc = 9:1, then 8:1), then was further purified by size exclusion column (S-X1, Biobeads, THF) to yield a blue-green solid (191 mg, 74%). The reaction was repeated on a larger scale (300 mg enolate) with quantitative yield of crude product; 52 mg was purified to yield an analytically pure sample (32 mg, 61%). ^{1}H NMR (500 MHz, $CDCl_3$): δ (ppm) = 9.87 (s, 1H), 7.74 (d, *J* = 4.0 Hz, 1H), 7.6 (dd, *J* = 8.2, 1.8 Hz, 1H), 7.58 (s, 1H), 7.38 (d, *J* = 4.0 Hz, 1H), 7.05-6.99 (m, 5H), 6.93 (d, *J* = 8.2 Hz, 1H), 6.89-6.80 (m, 6H), 5.98 (s, 1H), 5.92 (s, 1H), 4.1 (d, *J* = 7.0 Hz, 2H), 3.95 (t, *J* = 6.5 Hz, 4H), 3.90 (d, *J* = 7.1 Hz, 2H), 1.82 (s, 6H), 1.81-

1.73 (m, 6H), 1.72 (s, 6H), 1.56-1.45 (m, 3H), 1.42 (t, J = 7.2 Hz, 3H), 1.25 (s, 14H), 0.99 (t, J = 7.4 Hz, 6H), 0.86 (t, J = 7.0 Hz, 3H). $^{13}C\{^{1}H\}$ NMR (126 MHz, $CDCl_3$): δ (ppm) = 182.56, 180.76, 175.48, 170.56, 166.7, 155.47, 154.51, 146.73, 144.11, 143.86, 143.06, 141.61, 140.77, 137.64, 135.15, 127.7, 126.5, 126.1, 123.26, 120.59, 120.14, 115.67, 115.34, 110.16, 109.06, 87.17, 86.7, 77.24, 67.95, 49.97, 48.48, 43.57, 38.94, 31.9, 31.41, 29.7, 29.59, 29.53, 29.49, 29.39, 29.32, 27.34, 27.1, 26.95, 26.62, 22.68, 19.28, 14.13, 13.89, 12.32. HRMS (ESI): m/z 1013.5726 $[M]^+$ (calcd for $C_{65}H_{79}N_3O_5S$: 1013.5735). Anal. Calcd for $C_{65}H_{79}N_3O_5S$ (%): C, 76.96; H, 7.85; N, 4.14; S, 3.16. Found: C, 76.73; H, 8.02; N, 3.95; S, 3.00.

2.9.2.5 Synthesis of (*E*)-4-((5-(bis(4-butoxyphenyl)amino)-1-ethyl-3,3-dimethyl-3*H*-indol-1-ium-2-yl)methylene)-2-(((*E*)-5-(5-((*E*)-2-carboxy-2-cyanovinyl)thiophen-2-yl)-1-dodecyl-3,3-dimethylindolin-2-ylidene)methyl)-3-oxocyclobut-1-en-1-olate

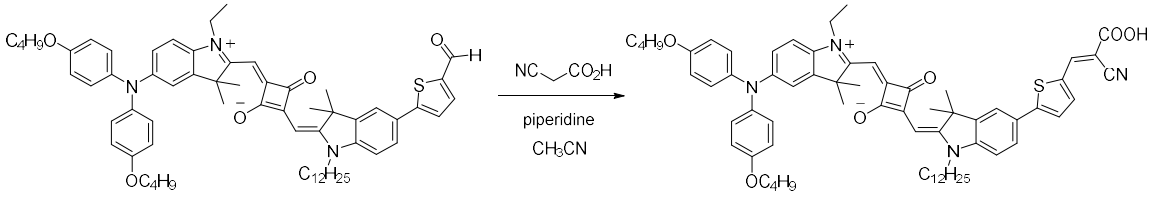

(*E*)-4-((5-(Bis(4-butoxyphenyl)amino)-1-ethyl-3,3-dimethyl-3*H*-indol-1-ium-2-yl)methylene)-2-((*E*)-(1-dodecyl-5-(5-formylthiophen-2-yl)-3,3-dimethylindolin-2-ylidene)methyl)-3-oxocyclobut-1-enolate (258 mg, 0.254 mmol) and cyanoacetic acid (45 mg, 0.534 mmol) were added to an oven-dried round-bottom flask, then evacuated and filled with nitrogen three times before anhydrous acetonitrile (20 mL) was added. Piperidine (40 μL) was added, and the reaction mixture refluxed overnight. The solution

was then cooled, and the solvent was removed under reduced pressure. The crude product was purified by column chromatography (starting with CH_2Cl_2, then moving to CH_2Cl_2:MeOH:acetic acid = 97:2:1). The main band was collected and the solvent was removed under reduced pressure. The product crystallized from warm acetic acid overnight, but very few crystals formed. The product was precipitated from CH_2Cl_2 using MeCN, then the precipitate was crystallized from CH_2Cl_2 and MeCN overnight. The fine precipitate was filtered, then recrystallized an additional time from CH_2Cl_2 and MeCN overnight. The fine, dark red precipitate was then collected by vacuum filtration (118 mg, 43%). ^{1}H NMR (500 MHz, $CDCl_3$): δ (ppm) = 8.36 (s, 1H), 7.76 (s, 1H), 7.65 (d, *J* = 8.4 Hz, 1H), 7.60 (s, 1H), 7.39 (s, 1H), 7.05-7.01 (m, 4H), 7.00 (s, 1H), 6.94 (d, *J* = 8.4 Hz, 1H), 6.87 (s, 2H), 6.85-6.81 (m, 4H), 6.07 (s, 1H), 5.95 (s, 1H), 4.15 (d, 2H), 3.95 (t, *J* = 6.5 Hz, 7H), 1.83 (s, 6H), 1.81-1.74 (m, 7H), 1.72 (s, 6H), 1.55-1.47 (m, 5H), 1.44 (t, *J* = 7.2 Hz, 3H), 1.42-1.38 (m, 2H), 1.37-1.30 (m, 2H), 1.30-1.24 (m, 5H), 1.22 (s, 12H), 0.99 (t, *J* = 7.4 Hz, 6H), 0.85 (t, *J* = 7.0 Hz, 3H) (CO_2H resonance not observed). $^{13}C\{^1H\}$ NMR (126 MHz, $CDCl_3$): δ (ppm) = 182.39, 178.04, 172.64, 171.08, 167.09, 164.93, 155.58, 154.62, 147.01, 146.5, 144.25, 144.07, 143.21, 140.66, 139.03, 134.93, 134.37, 127.58, 126.68, 126.25, 123.6, 120.3, 120.11, 116.69, 115.38, 110.43, 109.29, 97.98, 87.17, 67.97, 50.06, 48.55, 43.65, 39.22, 31.9, 31.42, 29.61, 29.45, 29.33, 27.32, 27.08, 27.03, 26.5, 22.68, 19.29, 14.13, 13.89, 12.42. HRMS (ESI): m/z 1080.5781 $[M]^+$ (calcd for $C_{68}H_{80}N_4O_6S$: 1080.5793). Anal. Calcd for $C_{68}H_{80}N_4O_6S$ (%): C, 75.52; H, 7.46; N, 5.18; S, 2.96. Found: C, 75.13; H, 7.32; N, 5.11; S, 2.98.

2.9.3 Synthesis of sensitizer 2.4

The synthesis of (*E*)-2-((*Z*)-(5-Bromo-1-dodecyl-3,3-dimethylindolin-2-ylidene)methyl)-4-((3-ethyl-1,1-dimethyl-1*H*-benzo[*e*]indol-3-ium-2-yl)methylene)-3-oxocyclobut-1-enolate (or Bz[*e*]IndSq-Br) was previously described in section 2.9.1.8. The synthesis of 4,4-bis(2-ethylhexyl)-4*H*-cyclopenta[2,1-*b*:3,4-*b'*]dithiophene-2-carbaldehyde was previously described in section 2.9.4.3.

2.9.3.1 Synthesis of (*E*)-2-(((*E*)-5-(4,4-bis(2-ethylhexyl)-6-formyl-4*H*-cyclopenta[2,1-*b*:3,4-*b'*]dithiophen-2-yl)-1-dodecyl-3,3-dimethylindolin-2-ylidene)methyl)-4-((3-ethyl-1,1-dimethyl-1*H*-benzo[*e*]indol-3-ium-2-yl)methylene)-3-oxocyclobut-1-en-1-olate

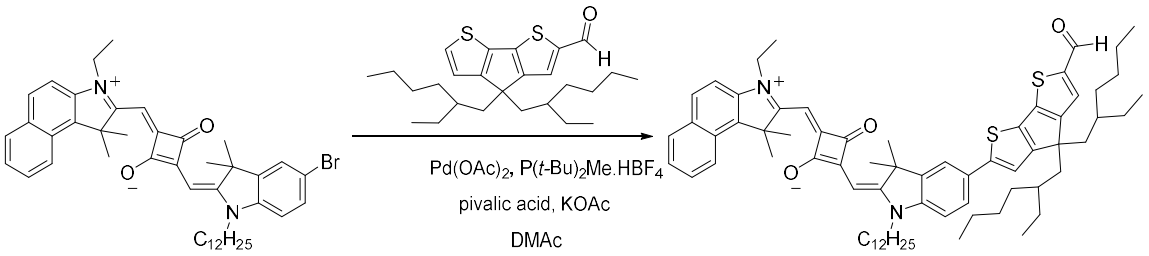

To a 20 mL oven-dried microwave vial cooled under nitrogen charged with a stir bar was added (*E*)-2-((*E*)-(5-bromo-1-dodecyl-3,3-dimethylindolin-2-ylidene)methyl)-4-((3-ethyl-1,1-dimethyl-1*H*-benzo[*e*]indol-3-ium-2-yl)methylene)-3-oxocyclobut-1-enolate (75 mg, 0.104 mmol), 4,4-bis(2-ethylhexyl)-4*H*-cyclopenta[1,2-*b*:5,4-*b'*]dithiophene-2-carbaldehyde (81 mg, 0.189 mmol), palladium(II) acetate (2 mg, 0.009 mmol), di-*tert*-butyl(methyl)phosphonium tetrafluoroborate (5 mg, 0.019 mmol), pivalic acid (10 mg, 0.095 mmol), and potassium acetate (28 mg, 0.283 mmol), and the vial was sealed. After three cycles of high vacuum, then filling with nitrogen, anhydrous degassed dimethylacetamide (1.7 mL) was added. The flask was filled with nitrogen, then the

solution was heated to 120 °C overnight. The reaction was worked up by dilution with CH_2Cl_2 (200 mL) and extraction with water (200 mL). The organic layer was dried over Na_2SO_4, then the solvent was removed under reduced pressure followed by high vacuum. The residue was purified by flash column chromatography (Biotage Isolera system, 10 g silica gel), dry-loading and using hexane:EtOAc, moving from 0-60% EtOAc slowly. Impurities exited the column early, then the main green band exited at higher polarity. The main band was collected and the solvent was removed under reduced pressure. The residue was dissolved in THF and purified by size exclusion column chromatography (SEC) (S-X1 Biobeads in THF (THF was HPLC grade or from a solvent purification system), one-foot column of one-inch diameter). The main green band was collected and the solvent removed under reduced pressure. The sample was then dissolved in distilled CH_2Cl_2, filtered through a 0.2 um PTFE filter, and the solvent removed under reduced pressure followed by high vacuum to yield the product as a dark green solid (49 mg, 45%). ^{1}H NMR (500 MHz, $CDCl_3$): δ (ppm) = 9.84 (s, 1H), 8.2 (d, *J* = 8.5 Hz, 1H), 7.9 (t, *J* = 7.9 Hz, 2H), 7.62-7.52 (m, 4H), 7.44 (t, *J* = 7.3 Hz, 1H), 7.33 (d, *J* = 8.8 Hz, 1H), 7.22 (s, 1H), 6.98 (d, *J* = 8.1 Hz, 1H), 6.07 (s, 1H), 6.00 (s, 1H), 4.24 (s, 2H), 3.98 (s, 2H), 2.08 (s, 6H), 2.03-1.92 (m, 4H), 1.92-1.79 (m, 8H), 1.47 (t, *J* = 7.3 Hz, 3H), 1.45-1.41 (m, 2H), 1.38 (quin, *J* = 6.6 Hz, 2H), 1.30 (quin, *J* = 7.2 Hz, 2H), 1.27 (s, 14H), 1.08-0.96 (m, 12H), 0.96-0.90 (m, 4H), 0.88 (t, *J* = 6.9 Hz, 3H), 0.76 (t, *J* = 6.9 Hz, 3H), 0.73 (t, *J* = 6.8 Hz, 3H), 0.65 (t, *J* = 7.3 Hz, 3H), 0.63 (td, *J* = 7.4, 1.8 Hz, 3H). ^{13}C{^{1}H} NMR (126 MHz, $CDCl_3$): δ (ppm) = 182.48, 182.41, 182.34, 179.97, 177.56, 172.07, 168.19, 163.18, 163.16, 157.19, 157.11, 157.03, 148.81, 148.18, 148.14, 148.10, 143.18, 142.82, 142.65, 138.92, 134.83, 134.70, 134.68, 131.42, 130.68, 130.00, 129.98, 129.83,

129.73, 128.67, 127.40, 125.52, 124.51, 122.58, 119.45, 118.05, 117.88, 117.72, 109.96, 109.48, 87.12, 86.35, 54.16, 54.15, 51.48, 48.93, 43.76, 43.17, 43.14, 43.09, 43.05, 38.78, 35.29, 35.24, 34.22, 34.18, 34.08, 31.90, 29.69, 29.59, 29.53, 29.49, 29.38, 29.32, 28.54, 28.52, 27.55, 27.51, 27.29, 27.1, 27.05, 26.62, 22.78, 22.74, 22.68, 14.13, 14.12, 14.07, 12.45, 10.73, 10.71, 10.60. HRMS (ESI): m/z 1070.6385 $[M]^+$ (calcd for $C_{70}H_{90}O_3N_2S_2$: 1070.6387). Anal. Calcd for $C_{70}H_{90}O_3N_2S_2$ (%): C, 78.46; H, 8.47; N, 2.61; S, 5.98. Found: C, 78.12; H, 8.57; N, 2.60; S, 5.90.

2.9.3.2 Synthesis of Synthesis of (*E*)-2-(((*E*)-5-(6-((*E*)-2-carboxy-2-cyanovinyl)-4,4-bis(2-ethylhexyl)-4*H*-cyclopenta[2,1-*b*:3,4-*b'*]dithiophen-2-yl)-1-dodecyl-3,3-dimethylindolin-2-ylidene)methyl)-4-((3-ethyl-1,1-dimethyl-1*H*-benzo[*e*]indol-3-ium-2-yl)methylene)-3-oxocyclobut-1-en-1-olate

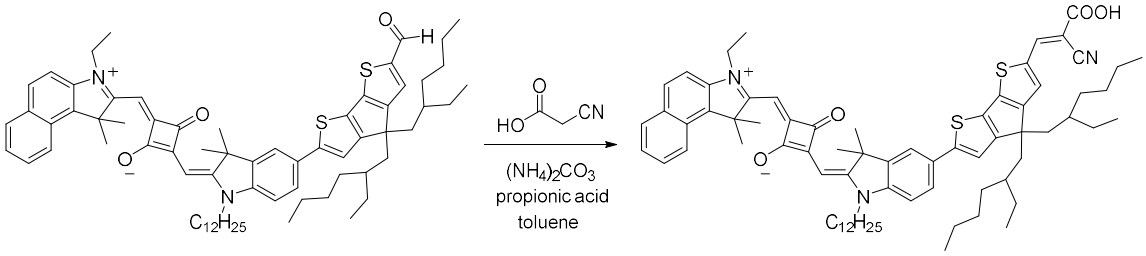

(*E*)-2-(((*E*)-5-(4,4-Bis(2-ethylhexyl)-6-formyl-4*H*-cyclopenta[2,1-*b*:3,4-*b'*]dithiophen-2-yl)-1-dodecyl-3,3-dimethylindolin-2-ylidene)methyl)-4-((3-ethyl-1,1-dimethyl-1*H*-benzo[*e*]indol-3-ium-2-yl)methylene)-3-oxocyclobut-1-en-1-olate (25 mg, 0.043 mmol) was placed in an oven-dried round-bottom flask with reflux condenser and the capped system was filled with nitrogen. Anhydrous toluene (4 mL) was added and stirred under nitrogen for 5 min. Ammonium carbonate (17 mg, 0.18 mmol) and cyanoacetic acid (8 mg, 0.09 mmol) were added and the solution was stirred under nitrogen for 5 min.

Propanoic acid (0.08 mL, 1.1 mmol) was added and the solution was stirred overnight under nitrogen at 100 °C. The solution was cooled and the solvent was removed slowly under reduced pressure. The residue was dissolved in CH_2Cl_2, extracted three times with water, dried over Na_2SO_4, and filtered. The solvent was removed under reduced pressure followed by high vacuum. The product was purified by silica gel column chromatography using 10-15 g of silica gel (Sorbtech). The eluents were as follows: 100% CH_2Cl_2, then 98:2 CH_2Cl_2:MeOH for several column volumes, then the ratio was changed to 96:2:2 CH_2Cl_2:MeOH:acetic acid (dark green main band quickly exited the column). The main band fractions were combined, and the solvent was removed under reduced pressure followed by high vacuum to yield a dark green solid. The main band fraction was dissolved in THF and purified by size exclusion column chromatography (SEC) (S-X1 Biobeads in THF (THF was HPLC grade or from a solvent purification system)). First, a one-foot column of one- inch diameter was run, and the main green band was collected and the solvent removed under reduced pressure. A three-foot column of 1.5-inch diameter SEC was then run, and again the main green band was collected and the solvent removed under reduced pressure followed by high vacuum. The sample was then dissolved in distilled CH_2Cl_2, filtered through a 0.2 um PTFE filter, and the solvent removed under reduced pressure followed by high vacuum (29.5 mg, 62% yield). ^{1}H NMR (400 MHz, $CDCl_3$): δ (ppm) = 8.39 (s, 1H), 8.23 (d, *J* = 8.6 Hz, 1H), 7.92 (d, *J* = 6.2 Hz, 1H), 7.91 (d, *J* = 7.2 Hz, 1H), 7.72-7.53 (m, 4H), 7.45 (t, *J* = 7.6 Hz, 1H), 7.35 (d, *J* = 8.9 Hz, 1H), 7.24 (s, 1H), 7.00 (d, *J* = 8.3 Hz, 1H), 6.15 (s, 1H), 6.05 (s, 1H), 4.31 (s, 2H), 4.05 (s, 2H), 2.09 (s, 5H), 2.06-1.93 (m, 4H), 1.88 (s, 7H), 1.50 (t, *J* = 7.1 Hz, 3H), 1.48-1.27 (m, 8H), 1.26 (s, 9H), 1.12-0.90 (m, 14H), 0.87 (t, *J* = 6.9 Hz, 3H), 0.78 (t, *J* =

6.9 Hz, 3H), 0.74 (t, *J* = 6.9 Hz, 4H), 0.71-0.63 (m, 6H) (COOH resonance not observed). $^{13}C\{^{1}H\}$ NMR (101 MHz, $CDCl_3$) δ (ppm) = 183.17, 177.39, 174.80, 172.72, 168.67, 165.93, 163.74, 157.98, 157.81, 149.79, 149.55, 147.08, 143.29, 142.82, 138.87, 135.94, 135.15, 134.84, 131.53, 131.22, 129.98, 129.90, 129.74, 128.62, 127.44, 125.67, 124.65, 122.69, 119.45, 118.17, 118.00, 117.84, 117.65, 110.09, 109.71, 94.68, 87.29, 86.72, 67.96, 54.20, 51.57, 49.00, 43.85, 43.12, 39.08, 35.36, 34.18, 31.92, 29.63, 29.58, 29.51, 29.44, 29.35, 28.58, 28.49, 27.49, 27.46, 27.36, 27.23, 27.13, 27.09, 26.54, 25.59, 22.80, 22.70, 14.13, 14.08, 12.50, 10.72, 10.70, 10.65. HRMS (ESI): m/z 1137.6432 $[M]^+$ (calcd for $C_{73}H_{91}O_4N_3S_2$: 1137.6446). Anal. Calcd for $C_{73}H_{91}N_3O_4S_2(H_2O)_{0.5}$: C, 76.40; H, 8.08; N, 3.66. Found: C, 76.43; H, 8.08; N, 3.66.

2.9.4 Synthesis of sensitizer 2.5

2.9.4.1 Synthesis of 1-ethyl-2,3,3-trimethyl-3*H*-benzo[*g*]indol-1-ium iodide

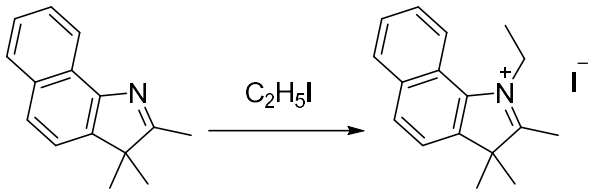

2,3,3-Trimethyl-3*H*-benzo[*g*]indole (1.00 g, 4.78 mmol) was dissolved in ethyl iodide (7.68 mL, 95.56 mmol). The reaction solution was heated at 90 °C for 12-48 h in a sealed microwave vial. The product was collected by vacuum filtration after precipitation from the reaction mixture using hexanes (1.109 g, 64%). ^{1}H NMR (400 MHz, $CDCl_3$) δ (ppm) = 8.32 (d, *J* = 8.7 Hz, 1H), 8.11 (d, *J* = 8.4 Hz, 1H), 8.05 (d, *J* = 8.1 Hz, 1H), 7.79 (ddd, *J* = 8.7, 7.0, 1.2 Hz, 1H), 7.67 (d, *J* = 8.4 Hz, 1H), 7.65 (ddd, *J* = 8.1, 7.1, 0.6 Hz, 1H), 5.15 (q, *J* = 7.4 Hz, 2H), 3.23 (s, 3H), 1.82 (t, *J* = 7.4 Hz, 3H), 1.70 (s, 6H). $^{13}C\{^{1}H\}$ NMR

(101 MHz, $CDCl_3$) δ (ppm) = 195.72, 142.3, 135.15, 134.69, 132.39, 130.35, 129.69, 126.98, 122.27, 119.99, 119.28, 54.26, 48.44, 22.79, 17.33, 14.04. HRMS (ESI) : m/z 238.1586 $[M]^+$ (calcd for $C_{17}H_{20}N$: 238.1590). Anal. Calcd for $C_{17}H_{20}IN$: C, 55.90; H, 5.52; N, 3.83. Found: C, 55.66; H, 5.66; N, 3.88.

2.9.4.2 Synthesis of (*E*)-2-(((*E*)-5-bromo-1-dodecyl-3,3-dimethylindolin-2-ylidene)methyl)-4-((1-ethyl-3,3-dimethyl-3*H*-benzo[*g*]indol-1-ium-2-yl)methylene)-3-oxocyclobut-1-en-1-olate

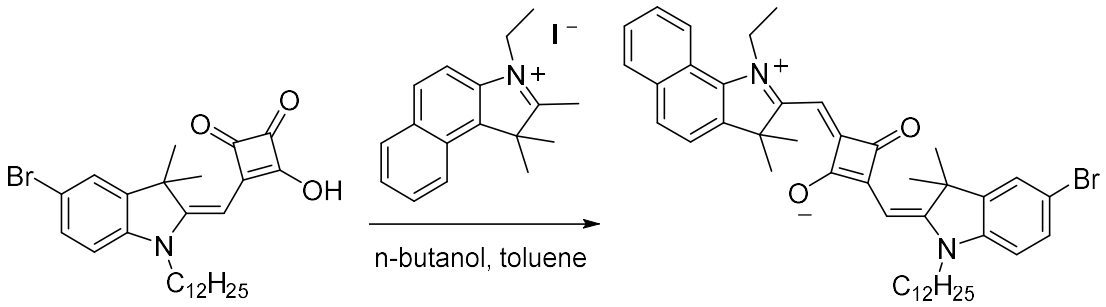

(*E*)-3-((5-bromo-1-dodecyl-3,3-dimethylindolin-2-ylidene)methyl)-4-hydroxycyclobut-3-ene-1,2-dione (0.450 g, 0.896 mmol) and 1-ethyl-2,3,3-trimethyl-3H-benzo[*g*]indol-1-ium iodide (0.372 g, 0.896 mmol) were dissolved in a solution of toluene (5 mL) and *n*-butanol (5 mL). The reaction was fitted with a Dean-Stark water separator and refluxed for 18 h. The solvent was removed under reduced pressure then high vacuum overnight. The residue was purified by column chromatography (CH_2Cl_2:MeOH = 99:1). The solvent was removed and the residue was further purified by column chromatography (hexanes:EtOAc = 100:0, then gradually moving to 30:70). The main band was collected and the solvent removed under reduced pressure. The residue was then purified by size exclusion column (SEC) chromatography (S-X1 Biobeads in THF (without stabilizers, HPLC grade or from a solvent purification system)), first on a one-foot column of one-

inch diameter, then on a three-foot column of 1.5-inch diameter. The main blue band was collected and the solvent was removed under reduced pressure. The purified product was then dissolved in distilled CH_2Cl_2 and filtered through a 0.2 um PFTE filter to yield a blue/red solid (153 mg, 20%). ^{1}H NMR (500 MHz, $CDCl_3$) δ (ppm) = 8.28 (d, *J* = 8.8 Hz, 1H), 7.94 (d, *J* = 8.1 Hz, 1H), 7.72 (d, *J* = 8.3 Hz, 1H), 7.58 (t, *J* = 7.4 Hz, 1H), 7.52 (d, *J* = 7.9 Hz, 1H), 7.50 (t, *J* = 7.2 Hz, 1H), 7.44 (d, *J* = 1.5 Hz, 1H), 7.40 (dd, *J* = 8.3, 1.8 Hz, 1H), 6.82 (d, *J* = 8.4 Hz, 1H), 6.17 (s, 1H), 5.95 (s, 1H), 4.63 (d, *J* = 6.6 Hz, 2H), 3.91 (s, 2H), 1.83 (s, 6H), 1.80 (s, 6H), 1.79-1.74 (m, 2H), 1.71 (t, *J* = 7.1 Hz, 3H), 1.45-1.37 (m, 2H), 1.37-1.32 (m, 2H), 1.32-1.27 (m, 2H), 1.26 (s, 12H), 0.88 (t, *J* = 6.9 Hz, 3H). ^{13}C{^{1}H} NMR (126 MHz, $CDCl_3$) δ (ppm) = 182.42, 180.64, 178.45, 172.30, 168.41, 144.19, 141.72, 140.14, 136.30, 134.65, 130.58, 129.99, 126.90, 125.64, 125.62, 125.41, 121.12, 120.87, 119.87, 116.10, 110.40, 86.98, 86.87, 49.13, 43.74, 42.22, 34.65, 31.90, 29.59, 29.52, 29.48, 29.36, 29.32, 27.14, 27.06, 27.01, 26.91, 25.27, 22.68, 20.70, 14.13, 13.80. HRMS (ESI) : m/z 721.3351 $[M+H]^+$ (calcd for $C_{44}H_{54}BrN_2O_2$: 721.3363). Anal. Calcd for $C_{44}H_{53}BrN_2O_2$: C, 73.21; H, 7.40; N, 3.88. Found: C, 72.97; H, 7.64; N, 3.84.

2.9.4.3 Synthesis of 4,4-bis(2-ethylhexyl)-4*H*-cyclopenta[2,1-*b*:3,4-*b'*]dithiophene-2-carbaldehyde

To a cold solution of 4,4-bis(2-ethylhexyl)-4*H*-cyclopenta[2,1-*b*:3,4-*b'*]dithiophene (3.00 g, 7.45 mmol) and N,N-dimethylformide (0.653 g, 8.94 mmol) in 1,2-dichloroethane (24

mL) at 0 °C was added phosphoryl trichloride (1.371 g, 8.94 mmol) under nitrogen. The reaction solution was stirred at 0 °C for 4 h. Saturated sodium acetate aqueous solution (50 mL) was added. The mixture was further stirred at room temperature for 2-4 h. The crude product was extracted into CH_2Cl_2, which was then washed with brine and water and dried over anhydrous sodium sulfate. After removing solvent under reduced pressure, the residue was purified by silica gel column chromatography (hexanes/ CH_2Cl_2, 9:1, v/v). The band was seen to have slight differences in ^{1}H NMR data at the front of the band than at the end, which was likely due to R_f differences of the possible diastereomers. All bands containing the diastereomers were combined to yield a yellow oil (2.99 g, 93% yield). Upon sitting, a small amount of material crystallized, and the crystals were submitted for elemental analysis. ^{1}H NMR (500 MHz, $CDCl_3$): δ (ppm) = 9.83 (s, 1H), 7.57 (t, J = 4.5 Hz, 1H), 7.38 (d, J = 4.9 Hz, 1H), 7.00 (dt, J = 4.9, 3.1 Hz, 1H), 1.98-1.86 (m, 4H), 1.08-0.80 (m, 16H), 0.75 (t, J = 7.0 Hz, 3H), 0.74 (t, J = 7.0 Hz, 3H), 0.63-0.54 (m, 8H). ^{13}C{^{1}H} NMR (126 MHz, $CDCl_3$) δ (ppm) = 182.67, 182.60, 162.05, 161.99, 157.73, 157.69, 147.98, 142.85, 135.93, 130.81, 129.12, 122.61, 122.57, 53.76, 43.11, 43.07, 35.15, 34.25, 34.04, 28.51, 27.36, 27.22, 22.69, 14.03, 10.60. HRMS (ESI): m/z 431.2430 $[M]^+$ (calcd for $C_{26}H_{39}OS_2$: 431.2437). Anal. Calcd. for $C_{26}H_{38}OS_2$ (%): C, 72.50; H, 8.89; S, 14.89. Found: C, 72.77; H, 9.05; S, 15.15.

2.9.4.4 Synthesis of (*E*)-2-(((*E*)-5-(4,4-bis(2-ethylhexyl)-6-formyl-4*H*-cyclopenta[2,1-*b*:3,4-*b*']dithiophen-2-yl)-1-dodecyl-3,3-dimethylindolin-2-ylidene)methyl)-4-((1-ethyl-3,3-dimethyl-3*H*-benzo[*g*]indol-1-ium-2-yl)methylene)-3-oxocyclobut-1-en-1-olate

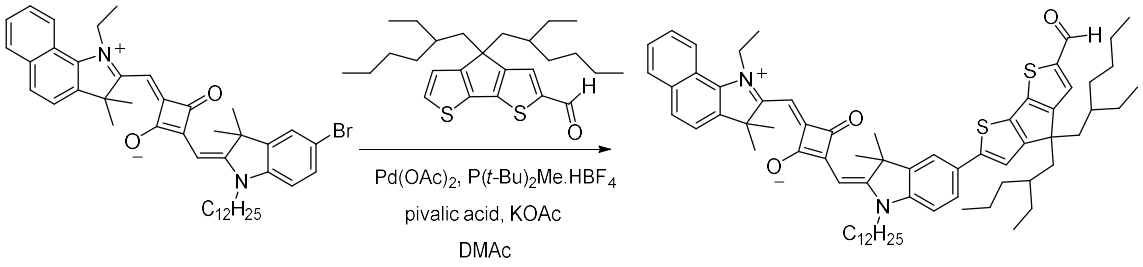

To a 10 mL oven-dried microwave vial charged with a stir bar and cooled under nitrogen was added (*E*)-2-(((*E*)-5-bromo-1-dodecyl-3,3-dimethylindolin-2-ylidene)methyl)-4-((1-ethyl-3,3-dimethyl-3*H*-benzo[*g*]indol-1-ium-2-yl)methylene)-3-oxocyclobut-1-en-1-olate (86 mg, 0.12 mmol), 4,4-bis(2-ethylhexyl)-4H-cyclopenta[1,2-b:5,4-b']dithiophene-2-carbaldehyde (135 mg, 0.313 mmol), palladium(II) acetate (2.4 mg, 0.011 mmol), di-*tert*-butyl(methyl)phosphonium tetrafluoroborate (10 mg, 0.039 mmol), pivalic acid (11 mg, 0.11 mmol), and potassium acetate (32 mg, 0.32 mmol). The vial was kept for 10 min under high vacuum in a dessicator, then was sealed and flushed with nitrogen. After 3 cycles of pulling high vacuum, then flushing with nitrogen, anhydrous degassed dimethylacetamide (1.9 mL) was added. The flask was flushed with nitrogen, then the reaction was heated to 120 °C for 21 hrs. The reaction was cooled, then the mixture was poured over a plug of silica gel topped with celite packed in a Buchner funnel. The plug was rinsed with CH_2Cl_2 and a green band was eluted. The solvent was switched to 98:2 CH_2Cl_2:MeOH, and additional green material was eluted. All green material was combined and the solvent was removed on a rotary evaporator. The green solid was then

purified by size exclusion column (SEC) chromatography (S-X1 Biobeads in THF (without stabilizers, HPLC grade or from solvent purification system)). First a one foot column of 1 inch diameter was run, and the main green band was collected and the solvent removed on a rotary evaporator. A 3 foot column of 1.5 inch diameter SEC was then run, and again the main green band was collected and the solvent removed on a rotary evaporator. The edges of the main band were collected, and re-ran on both SECs to obtain the main band, which was then purified via silica gel chromatography on the Biotage Isolera system (10 g silica gel cartridge, dry loaded by dissolving in CH_2Cl_2, adding 1 g silica gel, and removing the solvent on a rotary evaporator). The column was run in 85:15 hexanes:EtOAc, increasing to 70:30, then 25:75 hexanes:EtOAc to remove the last of the main band. All main bands were combined and an additional column was run as described. The solvent was removed on a rotary evaporator to give the purified product as a dark green solid (40 mg, 32% yield). The reaction was repeated to obtain additional product (22 mg, 20%). ^{1}H NMR (400 MHz, $CDCl_3$) δ (ppm) = 9.84 (s, 1H), 8.29 (d, *J* = 8.7 Hz, 1H), 7.94 (d, *J* = 7.4 Hz, 1H), 7.72 (d, *J* = 8.3 Hz, 1H), 7.62-7.47 (m, 6H), 7.21 (s, 1H), 6.98 (d, *J* = 8.1 Hz, 1H), 6.17 (s, 1H), 6.00 (s, 1H), 4.64 (d, *J* = 6.8 Hz, 2H), 3.98 (s, 2H), 2.04-1.91 (m, 4H), 1.86 (s, 4H), 1.84 (s, 8H), 1.72 (t, *J* = 7.1 Hz, 3H), 1.50-1.40 (m, 2H), 1.40-1.33 (m, 2H), 1.26 (s, 16H), 1.07-0.90 (m, 16H), 0.88 (t, *J* = 6.8 Hz, 3H), 0.76 (t, *J* = 6.5 Hz, 3H), 0.72 (t, *J* = 6.9 Hz, 3H), 0.63 (t, *J* = 7.2 Hz, 3H), 0.62 (td, *J* = 7.5, 1.2 Hz, 3H). ^{13}C{^{1}H} NMR (101 MHz, $CDCl_3$) δ (ppm) = 182.51, 182.43, 182.36, 180.35, 178.32, 172.14, 168.55, 163.18, 163.16, 157.22, 157.14, 157.06, 148.77, 148.75, 148.17, 148.13, 148.10, 143.24, 142.86, 142.61, 140.13, 136.35, 134.79, 134.78, 134.75, 134.67, 130.68, 130.17, 130.15, 130.00, 126.89, 125.56, 125.41, 121.12, 120.89,

119.89, 119.47, 118.10, 117.93, 117.77, 109.59, 87.20, 86.99, 54.19, 54.17, 49.12, 49.05, 43.84, 43.19, 43.16, 43.11, 43.07, 42.22, 35.31, 35.26, 34.23, 34.20, 34.10, 31.91, 29.70, 29.61, 29.55, 29.50, 29.39, 29.34, 28.55, 27.56, 27.52, 27.29, 27.25, 27.11, 27.09, 27.05, 22.79, 22.76, 22.69, 14.13, 14.07, 13.83, 10.74, 10.71, 10.60. HRMS (ESI): m/z 1070.6380 $[M]^+$ (calcd for $C_{70}H_{90}N_2O_3S_2$: 1070.6387). Anal. Calcd for $C_{70}H_{90}N_2O_3S_2$: C, 78.36; H, 8.39; N, 2.65; S, 6.06. Found: C, 78.07; H, 8.59; N, 2.59; S, 5.79.

2.9.4.5 Synthesis of (*E*)-2-(((*E*)-5-(6-((*E*)-2-carboxy-2-cyanovinyl)-4,4-bis(2-ethylhexyl)-4*H*-cyclopenta[2,1-*b*:3,4-*b'*]dithiophen-2-yl)-1-dodecyl-3,3-dimethylindolin-2-ylidene)methyl)-4-((1-ethyl-3,3-dimethyl-3*H*-benzo[*g*]indol-1-ium-2-yl)methylene)-3-oxocyclobut-1-en-1-olate

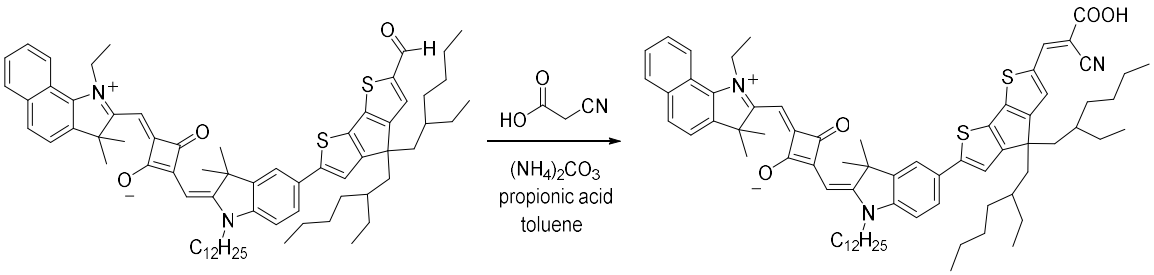

(*E*)-2-(((*E*)-5-(4,4-bis(2-ethylhexyl)-6-formyl-4*H*-cyclopenta[2,1-*b*:3,4-*b'*]dithiophen-2-yl)-1-dodecyl-3,3-dimethylindolin-2-ylidene)methyl)-4-((1-ethyl-3,3-dimethyl-3*H*-benzo[*g*]indol-1-ium-2-yl)methylene)-3-oxocyclobut-1-en-1-olate (40 mg, 0.037 mmol) was transfered into a vial, capped and filled with nitrogen, then dissolved in anhydrous toluene (1 mL, from a solvent purification system) and stirred under nitrogen for 5 min. Ammonium carbonate (15 mg, 0.16 mmol) and cyanoacetic acid (7 mg, 0.08 mmol) were added to a separate oven-dried round-bottom flask with a reflux condenser. The flask was kept under high vacuum for several minutes, then filled with nitrogen. The solution of the

starting material in toluene was added. Additional toluene (2 mL) was added to the vial to obtain any residual starting material, then transferred to the main reaction flask. the solution was stirred under nitrogen for 5 min. Propanoic acid (0.07 mL, 0.9 mmol) was added and the solution was stirred overnight under nitrogen at 100 °C overnight. The organic layer was extracted by CH_2Cl_2 and rinsed with water, then dried over Na_2SO_4, filtered, and the solvent was removed under reduced pressure. The product was purified by silica gel column chromatography using 10 g of silica gel (Sorbtech). The eluents were as follows: 100% CH_2Cl_2, followed by 100% hexanes (yellow impurity exited the column), then 1:1 hexanes:EtOAc, slowly moving to 1:3 hexanes:EtOAc (blue and brown impurities exited the column), followed by 100% hexanes, then 100% CH_2Cl_2, then 98:2 CH_2Cl_2:MeOH (blue impurity exited the column), then 96:4 CH_2Cl_2:MeOH (green material exited the column), then 96:2:2 CH_2Cl_2:MeOH:acetic acid (green main band quickly exited the column). The green main band fractions were combined, and the solvent was removed under reduced pressure. The main band fraction was dissolved in THF and purified by size exclusion column chromatography (SEC) (S-X1 Biobeads in THF (THF was HPLC grade or from a solvent purification system)). First, a one-foot column of one-inch diameter was run, and the main green band was collected and the solvent removed under reduced pressure. A three-foot column of 1.5-inch diameter SEC was then run, and again the main green band was collected and the solvent removed under reduced pressure. The edges of the main band were collected, and re-ran on the short SEC column before combining with the main band. The combined material was ran on the short SEC column a final time, then the solvent was removed under reduced pressure. The material was dissolved in distilled CH_2Cl_2 and washed with water. The

organic layer was dried over Na_2SO_4 and the solvent was removed under reduced pressure. The remaining solid was then dissolved in distilled CH_2Cl_2 and filtered through a 0.2 μm PTFE filter. The solvent was removed under reduced pressure to yield the product as a dark green solid (16 mg, 37% yield). ^{1}H NMR (500 MHz, $CDCl_3$) δ (ppm) = 8.37 (s, 1H), 8.32 (d, *J* = 8.9 Hz, 1H), 7.95 (d, *J* = 7.9 Hz, 1H), 7.74 (d, *J* = 8.4 Hz, 1H), 7.70-7.45 (m, 6H), 7.24 (s, 1H), 7.00 (d, *J* = 8.3 Hz, 1H), 6.24 (s, 1H), 6.04 (s, 1H), 4.70 (d, *J* = 4.7 Hz, 2H), 4.04 (s, 2H), 2.08-1.93 (m, 4H), 1.93-1.86 (m, 6H), 1.85 (s, 8H), 1.73 (t, *J* = 10.4 Hz, 3H), 1.53-1.41 (m, 2H), 1.41-1.33 (m, 2H), 1.33-1.19 (m, 16H), 1.14-0.90 (m, 16H), 0.86 (t, *J* = 7.1 Hz, 3H), 0.77 (t, *J* = 6.5 Hz, 3H), 0.72 (t, *J* = 6.9 Hz, 3H), 0.70-0.61 (m, 6H). ^{13}C{^{1}H} NMR (126 MHz, $CDCl_3$) δ (ppm) = 182.92, 178.10, 175.76, 172.68, 168.91, 166.23, 163.83, 158.02, 149.85, 147.22, 143.33, 142.77, 140.37, 136.27, 135.93, 134.87, 134.67, 131.37, 130.08, 130.00, 127.00, 125.84, 125.69, 125.47, 121.19, 120.97, 119.84, 119.47, 118.20, 118.03, 117.55, 109.77, 94.39, 87.29, 77.69, 54.21, 49.20, 49.09, 43.90, 43.12, 42.44, 35.36, 34.17, 31.92, 29.62, 29.58, 29.51, 29.43, 29.35, 28.57, 28.49, 27.47, 27.35, 27.21, 27.14, 27.09, 26.93, 22.80, 22.70, 14.13, 14.08, 13.83, 10.70, 10.65. HRMS (ESI): m/z 1138.6522 $[M+H]^+$ (calcd for $C_{73}H_{92}O_4N_3S_2$: 1138.6524). Anal. Calcd for $C_{73}H_{91}N_3O_4S_2(H_2O)$: C, 75.80; H, 8.10; N, 3.63. Found: C, 75.81; H, 8.48; N, 3.34.

2.9.5 Synthesis of sensitizer 2.6

The synthesis of 4,4-bis(2-ethylhexyl)-4*H*-cyclopenta[2,1-*b*:3,4-*b'*]dithiophene-2-carbaldehyde was previously described in section 2.9.4.3.

2.9.5.1 Synthesis of 7-bromo-1,1,2-trimethyl-1*H*-benzo[*e*]indole

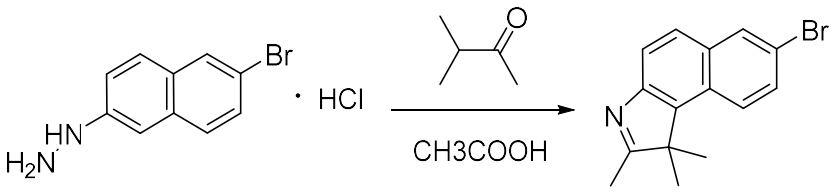

(6-Bromonaphthalen-2-yl)hydrazine hydrochloride (5.00 g, 18.3 mmol) and 3-methyl-2-butanone (1.97 mL, 18.3 mmol) were added to a round-bottom flask fitted with a reflux condenser. Glacial acetic acid (60 mL) was added while filling with nitrogen. Slowing the flow of nitrogen, the reaction mixture was heated to 100 °C and stirred for 27 h. After cooling to room temperature, the solvent was removed under reduced pressure and the product was dissolved in CH_2Cl_2 and rinsed with H_2O. The solvent was removed under reduced pressure to yield a brown-red oil which was used without further purification (3.93 g, 75%). The ^{1}H NMR spectrum was consistent with that of the commercial product. ^{1}H NMR (500 MHz, $CDCl_3$): δ (ppm) = 8.10 (d, J = 2.0 Hz, 1H), 7.88 (d, J = 9.0 Hz, 1H), 7.77 (q, J = 9.0 Hz, 2H), 7.60 (dd, J = 8.9, 2.0 Hz, 1H), 2.37 (s, 3H), 1.52 (s, 6H).

2.9.5.2 Synthesis of 7-mesityl-1,1,2-trimethyl-1*H*-benzo[*e*]indole

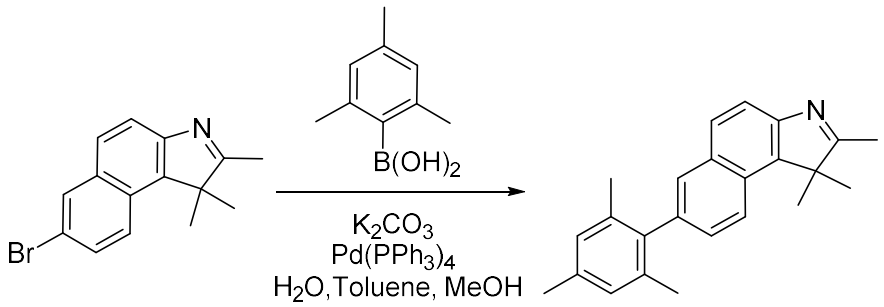

7-Bromo-1,1,2-trimethyl-1*H*-benzo[*e*]indole (1.93 g, 6.70 mmol) and boronic acid were dissolved in toluene (75 mL) and MeOH (35 mL). The reaction mixture was degassed with nitrogen and heated to 85-100 °C. $Pd(PPh_3)_4$ (0.77 g, 0.67 mmol) was added under positive nitrogen pressure, and the reaction was stirred and degassed for 30 min. During this time, the potassium carbonate was dissolved in water and degassed with nitrogen in a separate flask. After adding the potassium carbonate solution to the reaction mixture, the reaction mixture was stirred at 85 °C with nitrogen bubbling directly into the solution for 18 h. After allowing the reaction mixture to cool to room temperature, the solution was washed 3 times with water. The organic phase was dried over magnesium sulfate, the solid removed by vacuum filtration, and the solvent removed under reduced pressure. The residue was purified by silica gel column chromatography using 25 g of silica gel (Biotage Isolera column) and eluting with hexanes:EtOAc 95:5, then 90:10. The main band was removed and the solvent was removed under reduced pressure (0.56 g, 26%). ^{1}H NMR (400 MHz, $CDCl_3$): δ (ppm) = 8.05 (d, *J* = 8.6 Hz, 1H), 7.81 (dd, *J* = 12.0, 8.5 Hz, 2H), 7.70 (d, *J* = 1.5 Hz, 1H), 7.34 (dd, *J* = 8.6, 1.7 Hz, 1H), 6.97 (s, 2H), 2.38 (s, 3H), 2.34 (s, 3H), 2.04 (s, 6H), 1.56 (s, 6H). $^{13}C\{^1H\}$ NMR (126 MHz, $CDCl_3$): δ (ppm) = 189.27, 150.76, 138.65, 138.63, 137.11, 136.66, 136.13, 132.37, 129.52, 128.70, 128.37, 128.12, 127.45, 122.51, 120.00, 55.26, 22.77, 21.03, 20.87, 15.25. HRMS (ESI): m/z 327.1991 $[M]^+$ (calcd for $C_{24}H_{25}N$: 327.1987). Anal. Calcd for $C_{24}H_{25}N$ (%): C, 88.03; H, 7.70; N, 4.28. Found: C, 88.07; H, 7.70; N, 4.19.

2.9.5.3 Synthesis of 3-ethyl-7-mesityl-1,1,2-trimethyl-1*H*-benzo[*e*]indol-3-ium iodide

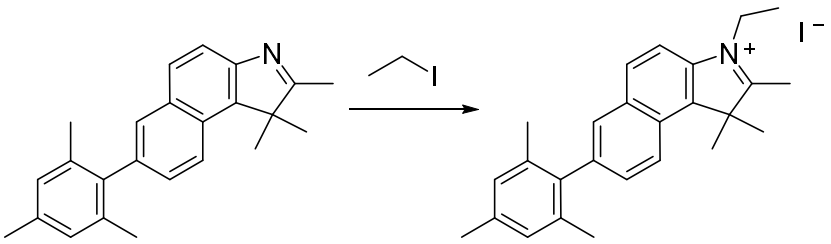

7-Mesityl-1,1,2-trimethyl-1*H*-benzo[*e*]indole (0.60 g, 1.8 mmol) and iodoethane (0.19 g, 1.2 mmol) were heated in a sealed 10 mL microwave vial at 85 °C overnight. The solution was cooled to room temperature, after which ether was added. The solution was stored at -10 °C for 1 h. The solid was then removed by vacuum filtration and washed with cold ether to obtain an off-white brownish solid, which was then dried under high vacuum (0.64 g, 86%). 25 mg of product was further washed ether and separated by vacuum filtration to obtain 18 mg of analytically pure sample. ^{1}H NMR (400 MHz, $CDCl_3$): δ (ppm) = 8.12 (d, *J* = 17.2, 8.8 Hz, 2H), 7.88 (d, *J* = 8.9 Hz, 1H), 7.83 (d, *J* = 1.6 Hz, 1H), 7.55 (d, *J* = 8.6, 1.7 Hz, 1H), 7.00 (d, *J* = 0.4 Hz, 2H), 4.92 (q, *J* = 7.4 Hz, 2H), 3.27 (s, 6H), 2.37 (s, 6H), 2.02 (s, 3H). ^{13}C{^{1}H} NMR (101 MHz, $CDCl_3$): δ (ppm) = 194.70, 140.88, 137.85, 137.46, 137.40, 137.26, 135.84, 134.00, 131.47, 130.82, 130.06, 128.34, 126.71, 122.96, 112.64, 55.93, 45.84, 22.76, 21.08, 20.84, 16.78, 13.77. HRMS (ESI): m/z 356.2368 $[M]^+$ (calcd for $C_{26}H_{30}N$: 356.2373). Anal. Calcd for $C_{26}H_{30}IN$ (%): C, 64.60; H, 6.26; N, 2.90. Found: C, 64.35; H, 6.29; N, 2.78.

2.9.5.4 Synthesis of (*E*)-2-((*E*)-(5-bromo-1-dodecyl-3,3-dimethylindolin-2-ylidene)methyl)-4-((3-ethyl-7-mesityl-1,1-dimethyl-1*H*-benzo[*e*]indol-3-ium-2-yl)methylene)-3-oxocyclobut-1-enolate

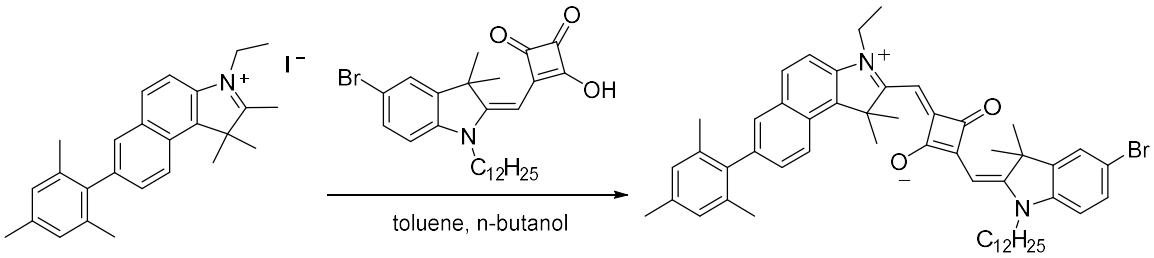

(*E*)-3-((5-Bromo-1-dodecyl-3,3-dimethylindolin-2-ylidene)methyl)-4-hydroxycyclobut-3-ene-1,2-dione (0.700 g, 1.39 mmol) and 3-ethyl-7-mesityl-1,1,2-trimethyl-1*H*-benzo[*e*]indol-3-ium iodide (0.673 g, 1.39 mmol) were dissolved in a solution of toluene (7 mL) and *n*-butanol (7 mL). The reaction was fitted with a Dean-Stark water separator and heated to 110 °C. The solution gradually turned from yellow to a deep blue, and the reaction was complete after 18 h. The solvent was removed under reduced pressure and the product was purified by column chromatography using hexanes:EtOAc (60% EtOAc then gradually increasing to 80% EtOAc). The main band fractions were combined, and the solvent was removed under reduced pressure to yield an analytically pure red/blue solid (0.947 mg, 81%). ^{1}H NMR (500 MHz, $CDCl_3$): δ (ppm) = 8.23 (d, *J* = 8.7 Hz, 1H), 7.87 (d, *J* = 8.7 Hz, 1H), 7.67 (d, *J* = 1.5 Hz, 1H), 7.44 (d, *J* = 1.6 Hz, 1H), 7.39 (d, *J* = 8.4, 5.6, 1.8 Hz, 2H), 7.34 (d, *J* = 8.8 Hz, 1H), 6.99 (s, 2H), 6.81 (d, *J* = 8.4 Hz, 1H), 6.06 (s, 1H), 5.94 (s, 1H), 4.25 (d, *J* = 4.8 Hz, 2H), 3.91 (s, 2H), 2.36 (s, 3H), 2.11 (s, 6H), 2.05 (s, 6H), 1.8 (s, 7H), 1.71 (s, 3H), 1.47 (t, *J* = 7.2 Hz, 3H), 1.41 (s, 2H), 1.35 (s, 2H), 0.88 (t, *J* = 6.9 Hz, 3H). ^{13}C{^{1}H} NMR (126 MHz, $CDCl_3$): δ (ppm) = 182.30, 180.34,

177.72, 172.20, 168.05, 144.21, 141.82, 138.83, 138.32, 137.48, 136.89, 136.14, 134.94, 131.63, 130.55, 129.79, 129.66, 129.59, 128.20, 127.47, 125.64, 122.64, 115.92, 110.27, 110.07, 86.81, 86.39, 51.59, 49.03, 43.69, 38.83, 31.92, 29.60, 29.53, 29.50, 29.38, 29.33, 27.20, 27.09, 26.9, 26.70, 22.69, 21.07, 20.87, 14.13, 12.47. HRMS (ESI): m/z 838.4058 $[M]^+$ (calcd for $C_{53}H_{63}BrN_2O_2$: 838.4067). Anal. Calcd for $C_{53}H_{63}BrN_2O_2$ (%): C, 75.78; H, 7.56; N, 3.33. Found: C, 75.52; H, 7.61; N, 3.33.

2.9.5.5 Synthesis of (*E*)-2-(((*E*)-5-(4,4-bis(2-ethylhexyl)-6-formyl-4*H*-cyclopenta[2,1-*b*:3,4-*b'*]dithiophen-2-yl)-1-dodecyl-3,3-dimethylindolin-2-ylidene)methyl)-4-((3-ethyl-7-mesityl-1,1-dimethyl-1*H*-benzo[*e*]indol-3-ium-2-yl)methylene)-3-oxocyclobut-1-en-1-olate

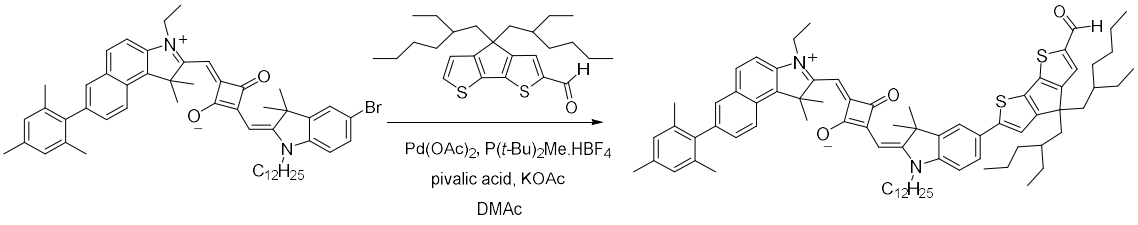

To a 20 mL oven-dried microwave vial cooled under nitrogen charged with a stir bar was added (*E*)-2-((*E*)-(5-bromo-1-dodecyl-3,3-dimethylindolin-2-ylidene)methyl)-4-((3-ethyl-7-mesityl-1,1-dimethyl-1*H*-benzo[*e*]indol-3-ium-2-yl)methylene)-3-oxocyclobut-1-enolate (75 mg, 0.089 mmol), 4,4-bis(2-ethylhexyl)-4*H*-cyclopenta[1,2-*b*:5,4-*b'*]dithiophene-2-carbaldehyde (70 mg, 0.16 mmol), palladium(II) acetate (2 mg, 0.008 mmol), di-*tert*-butyl(methyl)phosphonium tetrafluoroborate (4 mg, 0.02 mmol), pivalic acid (8 mg, 0.08 mmol), and potassium acetate (24 mg, 0.24 mmol), and the vial was sealed. After three cycles of high vacuum, then filling with nitrogen, anhydrous degassed dimethylacetamide (1.4 mL) was added. The flask was filled with nitrogen, then the

solution was heated to 120 °C overnight. The reaction was cooled to room temperature and extracted with CH_2Cl_2 and water. The organic layer was dried over Na_2SO_4, the Na_2SO_4 removed by vacuum filtration, and the solvent removed under reduced pressure. The residue was purified by silica gel chromatography (hexane:EtOAc 100:0 gradually increasing to 20:80), with the main band collected and the solvent removed under reduced pressure. The residue was further purified by size exclusion columns (S-X1, Biobeads, THF, 1 inch diameter, 1 ft. height column, then 4 ft. height column) and filtered through a PTFE filter (0.2 μm) to yield a dark green solid (48 mg, 45%). ^{1}H NMR (500 MHz, $CDCl_3$): δ (ppm) = 9.84 (s, 1H), 8.24 (d, *J* = 8.7 Hz, 1H), 7.87 (d, *J* = 8.7 Hz, 1H), 7.68 (d, *J* = 1.5 Hz, 1H), 7.58 (t, *J* = 4.3 Hz, 1H), 7.57-7.52 (m, 2H), 7.39 (dd, J = 8.7, 1.7 Hz, 1H), 7.35 (d, *J* = 8.8 Hz, 1H), 7.21 (s, 1H), 6.99 (s, 2H), 6.97 (d, *J* = 8.2 Hz, 1H), 6.08 (s, 1H), 6.00 (s, 1H), 4.26 (s, 2H), 3.97 (s, 2H), 2.37 (s, 3H), 2.12 (s, 6H), 2.05 (s, 6H), 2.03-1.92 (m, 4H), 1.91-1.78 (m, 6H), 1.48 (t, *J* = 7.2 Hz, 3H), 1.46-1.41 (m, 2H), 1.38 (quin, *J* = 6.7 Hz, 2H), 1.34-1.28 (m, 2H), 1.26 (s, 14H), 1.08-0.96 (m, 11H), 0.96-0.90 (m, 6H), 0.88 (t, *J* = 6.9 Hz, 3H), 0.76 (t, *J* = 7.0 Hz, 3H), 0.72 (t, *J* = 6.9 Hz, 3H), 0.64 (t, *J* = 7.3 Hz, 3H), 0.63 (td, *J* = 7.5, 1.7 Hz, 3H). ^{13}C{^{1}H} NMR (126 MHz, $CDCl_3$): δ (ppm) = 182.49, 182.42, 179.97, 177.52, 171.99, 168.15, 163.19, 163.17, 157.19, 157.12, 157.04, 148.83, 148.2, 148.16, 143.2, 142.83, 142.68, 138.85, 138.31, 137.43, 136.89, 136.14, 134.89, 134.71, 131.59, 130.68, 129.98, 129.78, 129.65, 129.57, 128.19, 127.46, 125.52, 122.64, 119.46, 118.05, 117.88, 110.06, 109.46, 87.14, 86.37, 54.15, 51.56, 48.94, 43.76, 43.19, 43.11, 43.07, 38.8, 35.31, 35.26, 34.23, 34.19, 34.09, 31.91, 29.61, 29.55, 29.51, 29.4, 29.34, 28.55, 28.53, 27.55, 27.52, 27.29, 27.12, 27.06, 26.71, 22.79, 22.75, 22.69, 21.07, 20.87, 14.14, 14.07, 12.47, 10.73, 10.71, 10.61.

HRMS (ESI): m/z 1188.7168 $[M]^+$ (calcd for $C_{79}H_{100}N_2O_3S_2$: 1188.7170). Anal. Calcd for $C_{79}H_{100}N_2O_3S_2$ (%): C, 79.75; H, 8.47; N, 2.35; S, 5.39. Found: C, 79.41; H, 8.53; N, 2.41; S, 5.44.

2.9.5.6 Synthesis of (*E*)-2-(((*E*)-5-(6-((*E*)-2-carboxy-2-cyanovinyl)-4,4-bis(2-ethylhexyl)-4*H*-cyclopenta[2,1-*b*:3,4-*b'*]dithiophen-2-yl)-1-dodecyl-3,3-dimethylindolin-2-ylidene)methyl)-4-((3-ethyl-7-mesityl-1,1-dimethyl-1*H*-benzo[*e*]indol-3-ium-2-yl)methylene)-3-oxocyclobut-1-en-1-olate

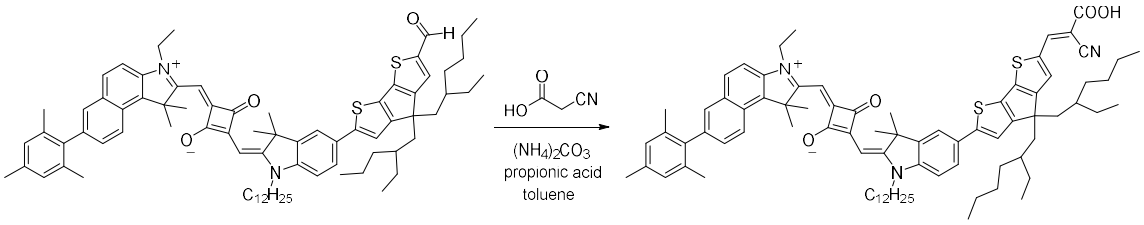

(*E*)-2-((*E*)-(1-Dodecyl-5-(4-(2-ethylhexyl)-4-(2-ethylpentyl)-6-formyl-4*H*-cyclopenta[1,2-*b*:5,4-*b'*]dithiophen-2-yl)-3,3-dimethylindolin-2-ylidene)methyl)-4-((3-ethyl-7-mesityl-1,1-dimethyl-1*H*-benzo[*e*]indol-3-ium-2-yl)methylene)-3-oxocyclobut-1-enolate (45 mg, 0.038 mmol) was placed in an oven-dried round-bottom flask with reflux condenser and the capped system was filled with nitrogen. Anhydrous toluene (3 mL) was added and stirred under nitrogen for 5 min. Ammonium carbonate (15 mg, 0.16 mmol) and cyanoacetic acid (7 mg, 0.08 mmol) were added and the solution was stirred under nitrogen for 5 min. Propanoic acid (0.07 mL, 1.0 mmol) was added and the solution was stirred overnight under nitrogen at 100 °C. The solution was cooled and the solvent was removed slowly under reduced pressure. The residue was dissolved in CH_2Cl_2, extracted three times with water, dried over Na_2SO_4, and filtered. The solvent was removed under reduced pressure followed by high vacuum. The product was purified

by silica gel column chromatography using 10-15 g of silica gel (Sorbtech) and eluting in 100% CH_2Cl_2, then 98:2 CH_2Cl_2:MeOH for several column volumes, then the ratio was changed to 96:2:2 CH_2Cl_2:MeOH:acetic acid (dark green main band quickly exited the column). The main band fractions were combined, and the solvent was removed under reduced pressure followed by high vacuum to yield a dark green solid. The main band fraction was dissolved in THF and purified by size exclusion column chromatography (SEC) (S-X1 Biobeads in THF (THF was HPLC grade or from a solvent purification system)). First, a one-foot column of one-inch diameter was run, and the main green band was collected and the solvent removed under reduced pressure. A three-foot column of 1.5-inch diameter SEC was then run, and again the main green band was collected and the solvent removed under reduced pressure followed by high vacuum. Two additional three-foot SEC columns were run before the product was purified. The sample was then dissolved in distilled CH_2Cl_2, filtered through a 0.2 um PTFE filter, and the solvent removed under reduced pressure followed by high vacuum (23 mg, 48% yield). ^{1}H NMR (500 MHz, $CDCl_3$): δ (ppm) = 8.39 (s, 1H), 8.26 (d, *J* = 8.7 Hz, 1H), 7.89 (d, *J* = 8.9 Hz, 1H), 7.69 (s, 1H), 7.67-7.57 (m, 1H), 7.56 (s, 2H), 7.41 (d, *J* = 9.4 Hz, 1H), 7.37 (d, *J* = 8.9 Hz, 1H), 7.24 (s, 1H), 7.00 (s, 3H), 6.17 (s, 1H), 6.06 (s, 1H), 4.32 (s, 2H), 4.05 (s, 2H), 2.37 (s, 3H), 2.13 (s, 6H), 2.06 (s, 6H), 1.99 (s, 3H), 1.89 (s, 8H), 1.50 (t, *J* = 7.1 Hz, 3H), 1.48-1.28 (m, 7H), 1.26 (s, 15H), 1.13-0.91 (m, 16H), 0.86 (t, *J* = 7.0 Hz, 3H), 0.77 (t, *J* = 7.0 Hz, 3H), 0.73 (t, *J* = 6.8 Hz, 3H), 0.67 (t, *J* = 7.1 Hz, 3H), 0.66 (td, *J* = 7.0, 0.8 Hz, 3H) (COOH resonance not observed). ^{13}C{^{1}H} NMR (101 MHz, $CDCl_3$) δ (ppm) = 183.34, 177.45, 174.79, 172.75, 168.73, 166.12, 163.87, 158.09, 157.94, 149.94, 149.70, 147.22, 143.41, 142.96, 138.90, 138.43, 137.69, 137.02, 136.26, 136.06, 135.32, 134.96,

131.82, 131.34, 130.08, 129.97, 129.76, 128.32, 127.52, 125.79, 122.85, 119.57, 118.28, 118.11, 117.76, 110.30, 109.81, 94.78, 87.39, 86.87, 54.32, 51.74, 49.11, 43.98, 43.23, 39.21, 35.47, 34.30, 32.04, 29.75, 29.64, 29.57, 29.47, 28.70, 28.61, 27.59, 27.47, 27.36, 27.21, 26.74, 22.92, 22.82, 21.19, 21.00, 14.25, 12.64, 10.82, 10.77. HRMS (ESI): m/z 1255.7216 $[M]^+$ (calcd for $C_{82}H_{101}O_4N_3S_2$: 1255.7228). Anal. Calcd for $C_{82}H_{101}N_3O_4S_2(H_2O)_{0.5}$: C, 77.81; H, 8.12; N, 3.32. Found: C, 77.84; H, 8.10; N, 3.38.

2.9.6 Synthesis of sensitizer 2.7

The synthesis of (*E*)-2-((*E*)-(5-bromo-1-dodecyl-3,3-dimethylindolin-2-ylidene)methyl)-4-((3-ethyl-7-mesityl-1,1-dimethyl-1*H*-benzo[*e*]indol-3-ium-2-yl)methylene)-3-oxocyclobut-1-enolate (or Mes-Bz[*e*]Sq-Br) was previously described in section 2.9.5.4. The synthesis of 4,4-bis(2-ethylhexyl)-4*H*-cyclopenta[2,1-*b*:3,4-*b'*]dithiophene-2-carbaldehyde was previously described in section 2.9.4.3.

2.9.6.1 Synthesis of 6-(7-bromobenzo[*c*][1,2,5]thiadiazol-4-yl)-4-(2-ethylhexyl)-4-(2-ethylpentyl)-4*H*-cyclopenta[2,1-*b*:3,4-*b'*]dithiophene-2-carbaldehyde

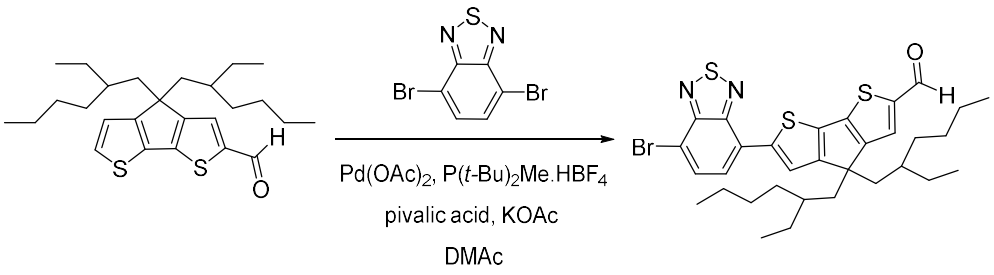

To a 10 mL oven-dried microwave vial charged with a stir bar and cooled under nitrogen was added 4,4-bis(2-ethylhexyl)-4*H*-cyclopenta[1,2-*b*:5,4-*b'*]dithiophene-2-carbaldehyde (RH-IV-131, 50 mg, 0.12 mmol), 4,7-dibromobenzo[*c*][1,2,5]thiadiazole (171 mg, 0.580

mmol), palladium(II) acetate (2.4 mg, 0.011 mmol), di-*tert*-butyl(methyl)phosphonium tetrafluoroborate (5.2 mg, 0.021 mmol), pivalic acid (11 mg, 0.11 mmol), and potassium acetate (31 mg, 0.32 mmol). The vial was kept for 10 min under high vacuum in a desiccator, then was sealed and filled with nitrogen. After three cycles of high vacuum, then filling with nitrogen, anhydrous degassed dimethylacetamide (DMAc) (1.9 mL) was added. The flask was filled with nitrogen, then the solution was heated to 120 °C for 11 h. The organic layer was extracted by CH_2Cl_2 and rinsed with water, then dried over Na_2SO_4, filtered, and the solvent was removed under reduced pressure. The product was purified by silica gel column chromatography chromatography on the Biotage Isolera system (10 g silica gel cartridge, dry loaded by dissolving in CH_2Cl_2, adding 1 g silica gel, and removing the solvent under reduced pressure). An initial column was run in hexanes:EtOAc, starting with 0% EtOAc and increasing to 1-3%. After the solvent was removed on a rotary evaporator followed by high vacuum removal of residual solvents, a second column was run in hexanes:EtOAc, starting with 0% EtOAc and increasing to 1% for effective separation. The main band was collected and the solvent removed under reduced pressure to yield the purified product as a red oil (49 mg, 66% yield). A portion of this material was then sonicated in isopropanol and water, decanting the water/isopropanol mixture and retaining the solid not dissolved, to remove any remaining impurities (15 mg obtained with analytical purity). ^{1}H NMR (500 MHz, $CDCl_3$) δ (ppm) = 9.87 (s, 1H), 8.10 (t, *J* = 6.9 Hz, 1H), 7.87 (d, *J* = 7.8 Hz, 1H), 7.74 (dt, *J* = 7.7, 2.5 Hz, 1H), 7.62 (t, *J* = 4.4 Hz, 1H), 2.10-1.92 (m, 4H), 1.07-0.88 (m, 16H), 0.74 (t, *J* = 6.8 Hz, 3H), 0.72-0.66 (m, 2H), 0.66-0.58 (m, 9H). ^{13}C{^{1}H} NMR (126 MHz, $CDCl_3$) δ (ppm) = 182.68, 182.60, 162.63, 162.58, 158.26, 158.22, 153.87, 151.49, 147.39, 143.84, 142.51,

137.78, 132.29, 130.64, 127.27, 125.10, 123.48, 123.33, 112.63, 54.29, 43.05, 35.32, 35.28, 34.33, 34.10, 28.55, 28.46, 27.55, 27.30, 22.71, 14.05, 13.99, 10.72, 10.60. HRMS (ESI): m/z 642.1393 $[M]^+$ (calcd for $C_{32}H_{39}BrN_2OS_3$: 642.1408). Anal. Calcd for $C_{32}H_{39}BrN_2OS_3$ (%): C, 59.70; H, 6.11; N, 4.35. Found: C, 59.41; H, 6.36; N, 4.10.

2.9.6.2 Synthesis of (*E*)-2-(((*E*)-1-dodecyl-3,3-dimethyl-5-(4,4,5,5-tetramethyl-1,3,2-dioxaborolan-2-yl)indolin-2-ylidene)methyl)-4-((3-ethyl-7-mesityl-1,1-dimethyl-1*H*-benzo[*e*]indol-3-ium-2-yl)methylene)-3-oxocyclobut-1-en-1-olate

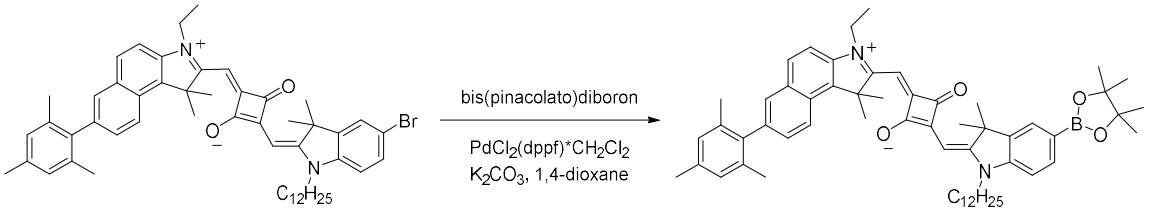

(*E*)-2-(((*E*)-5-Bromo-1-dodecyl-3,3-dimethylindolin-2-ylidene)methyl)-4-((3-ethyl-7-mesityl-1,1-dimethyl-1*H*-benzo[*e*]indol-3-ium-2-yl)methylene)-3-oxocyclobut-1-en-1-olate, (50 mg, 0.060 mmol, RH-I-276D and RH-I-230K) and potassium acetate (35 mg, 0.36 mmol) were added to an oven-dried 10 mL microwave vial that had been equipped with a stir bar and cooled under nitrogen. The vial opening was covered with a Kim-wipe and rubber band, and the vial was kept under high vacuum in the desiccator until a pressure of <10 mTorr was attained. The bis(pinacolato)diboron (250 mg, 0.387 mmol, Frontier Scientific) added to the vial, which was again kept under high vacuum in the desiccator until a pressure of <10 mTorr was attained. The vial was then capped and filled with nitrogen. Anhydrous 1,4-dioxane that had been poured over molecular sieves and degassed for 30 min was added (5 mL, Acros). After again degassing the solution for 10-15 min, the cap of the vial was removed and the dichloro[1,1'-

bis(diphenylphosphino)-ferrocene]-palladium(II) (13 mg, 0.015 mmol) was added under positive nitrogen pressure. The vial was capped under positive nitrogen pressure, then filled with nitrogen. The vial was heated at a temperature of 90 °C overnight (17 h). The solvent was removed under reduced pressure and the remnant was dissolved in CH_2Cl_2. The solution was poured over a bed of silica gel (3 cm) and Celite (1 cm) in a Buchner funnel, and was eluted with a CH_2Cl_2:MeOH mixture (about 95:5). The blue filtrate was collected, and the solvent was removed under reduced pressure. The material was then purified by size exclusion column (SEC) chromatography (S-X1 Biobeads in THF (without stabilizers, HPLC grade or from a solvent purification system)), first on a one-foot column of one-inch diameter, then on a three-foot column of 1.5-inch diameter. The main blue band was collected and the solvent was removed under reduced pressure to yield the purified product as a blue-green solid (43 mg, 81%). ^{1}H NMR (500 MHz, $CDCl_3$) δ (ppm) = 8.24 (d, *J* = 8.7 Hz, 1H), 7.87 (d, *J* = 8.7 Hz, 1H), 7.81-7.76 (m, 2H), 7.67 (d, *J* = 1.5 Hz, 1H), 7.39 (dd, *J* = 8.6, 1.7 Hz, 1H), 7.33 (d, *J* = 8.8 Hz, 1H), 6.99 (s, 2H), 6.96 (d, *J* = 7.9 Hz, 1H), 6.06 (s, 1H), 6.00 (s, 1H), 4.24 (s, 2H), 3.97 (s, 2H), 2.36 (s, 3H), 2.12 (s, 6H), 2.05 (s, 6H), 1.89-1.75 (m, 8H), 1.46 (t, *J* = 7.3 Hz, 3H), 1.45-1.39 (m, 2H), 1.37 (s, 12H), 1.26 (s, 16H), 0.87 (t, *J* = 7.1 Hz, 3H). ^{13}C{^{1}H} NMR (126 MHz, $CDCl_3$) δ (ppm) = 182.46, 179.92, 178.29, 171.75, 169.31, 145.25, 141.49, 138.91, 138.34, 137.33, 136.85, 136.14, 135.06, 134.76, 131.53, 129.73, 129.63, 129.52, 128.24, 128.18, 127.48, 123.42, 122.62, 110.03, 108.54, 86.97, 86.23, 83.82, 77.62, 69.49, 67.96, 53.83, 51.47, 48.91, 43.61, 38.73, 31.90, 31.75, 29.69, 29.59, 29.53, 29.49, 29.37, 29.33, 27.15, 27.07, 27.03, 26.74, 25.60, 24.87, 22.68, 21.06, 20.87, 14.13, 12.42. HRMS (ESI):

m/z 887.5886 $[M+H]^+$ (calcd for $C_{59}H_{76}O_4N_2B$: 887.5893). Anal. Calcd for $C_{59}H_{75}O_4N_2B$ (%): C, 79.89; H, 8.52; N, 3.16. Found: C, 79.72; H, 8.64; N, 3.03.

2.9.6.3 Synthesis of (*E*)-2-(((*E*)-5-(7-(4,4-bis(2-ethylhexyl)-6-formyl-4*H*-cyclopenta[2,1-*b*:3,4-*b'*]dithiophen-2-yl)benzo[*c*][1,2,5]thiadiazol-4-yl)-1-dodecyl-3,3-dimethylindolin-2-ylidene)methyl)-4-((3-ethyl-7-mesityl-1,1-dimethyl-1*H*-benzo[*e*]indol-3-ium-2-yl)methylene)-3-oxocyclobut-1-en-1-olate

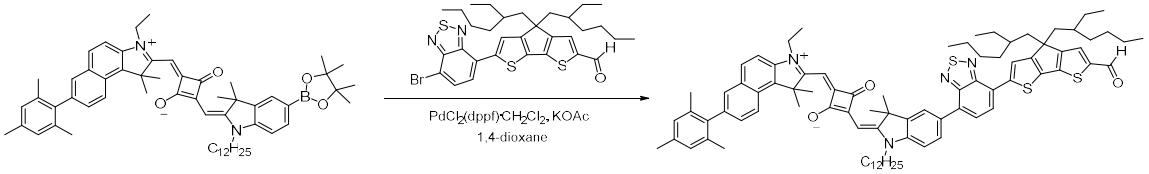

(*E*)-2-(((*E*)-1-Dodecyl-3,3-dimethyl-5-(4,4,5,5-tetramethyl-1,3,2-dioxaborolan-2-yl)indolin-2-ylidene)methyl)-4-((3-ethyl-7-mesityl-1,1-dimethyl-1*H*-benzo[*e*]indol-3-ium-2-yl)methylene)-3-oxocyclobut-1-en-1-olate (40 mg, 0.045 mmol), 6-(7-bromobenzo[*c*][1,2,5]thiadiazol-4-yl)-4,4-bis(2-ethylhexyl)-4*H*-cyclopenta[2,1-*b*:3,4-*b'*]dithiophene-2-carbaldehyde (38 mg, 0.059 mmol), $Pd(dppf)Cl_2$ (8 mg, 0.01 mmol), and potassium carbonate (39 mg, 0.28 mmol) were combined in an oven-dried 25 mL round-bottom flask with a reflux condenser and kept under vacuum for 10 min. Distilled 1,4-dioxane (30 mL) was added under nitrogen, and the reaction mixture was degassed for 5 min. The reaction mixture was stirred under nitrogen at 80 °C overnight. The erroneous use of potassium carbonate was discovered, and potassium acetate (33 mg, 0.34 mmol) was added to the reaction mixture. The reaction mixture was again stirred under nitrogen at 80 °C overnight. The reaction mixture was cooled to room temperature, then poured over a plug of silica gel topped with Celite packed in a Buchner funnel. The

plug was rinsed with CH_2Cl_2 and 8:2 CH_2Cl_2:MeOH. All colored fractions were combined and the solvent was removed under reduced pressure. The crude reaction mixture was purified via silica gel chromatography on the Biotage Isolera system (10 g silica gel cartridge, dry loaded by dissolving in CH_2Cl_2, adding 1 g silica gel, and removing the solvent under reduced pressure). The column was run in hexanes:EtOAc, starting with 5% EtOAc and increasing to 30-40% EtOAc to remove the main band. The green solid was further purified by size exclusion column (SEC) chromatography (S-X1 Biobeads in THF (without stabilizers, HPLC grade or from a solvent purification system)). First, a one-foot column of one-inch diameter was run, and the main green band was collected and the solvent removed under reduced pressure. This column was repeated for further purification. An SEC on a three-foot column of 1.5-inch diameter was then run, and again the main green band was collected and the solvent was removed under reduced pressure. The purified product was then dissolved in distilled CH_2Cl_2 and filtered through a 0.2 um PFTE filter to yield a dark green solid (22 mg, 37%). ^{1}H NMR (500 MHz, $CDCl_3$) δ (ppm) = 9.87 (s, 1H), 8.24 (d, *J* = 8.6 Hz, 1H), 8.15 (s, 1H), 8.02 (d, *J* = 8.4 Hz, 1H), 7.99 (d, *J* = 7.5 Hz, 1H), 7.95 (s, 1H), 7.87 (d, *J* = 8.7 Hz, 1H), 7.78 (d, *J* = 7.6 Hz, 1H), 7.67 (s, 1H), 7.62 (s, 1H), 7.39 (d, *J* = 8.6 Hz, 1H), 7.34 (d, *J* = 8.8 Hz, 1H), 7.13 (d, *J* = 8.2 Hz, 1H), 6.99 (s, 2H), 6.08 (s, 1H), 6.05 (s, 1H), 4.26 (s, 2H), 4.03 (s, 2H), 2.36 (s, 3H), 2.13 (s, 6H), 2.05 (s, 6H), 2.22-1.93 (m, 4H), 1.91 (s, 6H), 1.88 (quin, *J* = 7.7 Hz, 4H), 1.48 (t, *J* = 6.8 Hz, 6H), 1.39 (quin, *J* = 6.7 Hz, 2H), 1.27 (s, 16H), 1.00 (t, *J* = 6.8 Hz, 12H), 0.87 (t, *J* = 6.8 Hz, 3H), 0.76 (t, *J* = 6.6 Hz, 3H), 0.65 (t, *J* = 7.4 Hz, 6H). ^{13}C{^{1}H} NMR (126 MHz, $CDCl_3$) δ (ppm) = 182.54, 179.79, 177.69, 171.96, 168.79, 162.69, 158.09, 154.03, 152.59, 147.82, 143.73, 143.55, 143.02, 142.73, 138.89,

138.33, 137.43, 137.34, 136.88, 136.14, 134.9, 132.7, 132.38, 131.6, 130.65, 129.77, 129.66, 129.57, 129.21, 128.2, 127.49, 126.29, 125.29, 123.04, 122.74, 122.65, 110.07, 109.18, 87.21, 86.35, 77.24, 54.27, 51.54, 49.11, 43.84, 43.18, 43.11, 38.8, 35.38, 35.33, 34.4, 34.13, 31.92, 29.7, 29.62, 29.58, 29.53, 29.43, 29.34, 28.61, 28.51, 27.61, 27.34, 27.16, 26.74, 22.75, 22.69, 21.07, 20.87, 14.13, 14.06, 14.02, 12.48, 10.75, 10.63. HRMS (ESI): m/z 1323.7182 $[M+H]^+$ (calcd for $C_{85}H_{103}N_4O_3S_3$: 1323.7187). Analysis calculated for $C_{85}H_{102}N_4O_3S_3(H_2O)$: C, 76.08; H, 7.81; N, 4.18. Found: C, 76.38; H, 7.80; N, 4.28.

2.9.6.4 Synthesis of (*E*)-2-(((*E*)-5-(7-(6-((*E*)-2-carboxy-2-cyanovinyl)-4,4-bis(2-ethylhexyl)-4*H*-cyclopenta[2,1-*b*:3,4-*b'*]dithiophen-2-yl)benzo[*c*][1,2,5]thiadiazol-4-yl)-1-dodecyl-3,3-dimethylindolin-2-ylidene)methyl)-4-((3-ethyl-7-mesityl-1,1-dimethyl-1*H*-benzo[*e*]indol-3-ium-2-yl)methylene)-3-oxocyclobut-1-en-1-olate

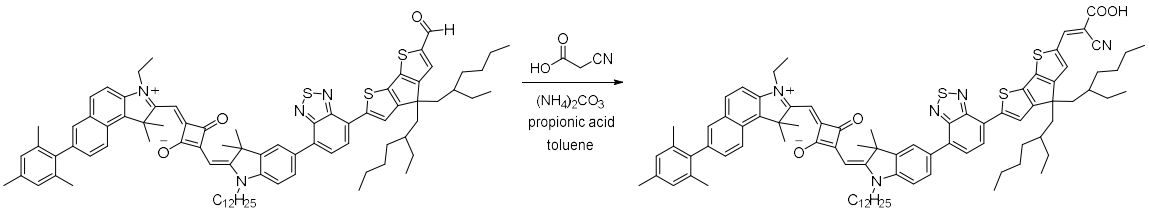

((*E*)-2-(((*E*)-5-(7-(4,4-Bis(2-ethylhexyl)-6-formyl-4*H*-cyclopenta[2,1-*b*:3,4-*b'*]dithiophen-2-yl)benzo[*c*][1,2,5]thiadiazol-4-yl)-1-dodecyl-3,3-dimethylindolin-2-ylidene)methyl)-4-((3-ethyl-7-mesityl-1,1-dimethyl-1*H*-benzo[*e*]indol-3-ium-2-yl)methylene)-3-oxocyclobut-1-en-1-olate) (21 mg, 0.016 mmol) was placed in an oven-dried round-bottom flask with reflux condenser and the capped system was filled with nitrogen. Anhydrous toluene (5 mL) was added and stirred under nitrogen for 5 min. Ammonium carbonate (49 mg, 0.51 mmol) and cyanoacetic acid (22 mg, 0.25 mmol) were added and the solution was stirred under nitrogen for 5 min. Propanoic acid (0.188 mL, 2.54 mmol) was added and the solution was stirred overnight under nitrogen at 100 °C. The solvent was removed slowly under reduced pressure, then the residue was dissolved in CH_2Cl_2. The organic layer was extracted three times with water, then dried over Na_2SO_4, and filtered. The solvent was removed under reduced pressure followed by high vacuum. The product was purified by silica gel column chromatography using 25 g of silica gel (Sorbtech). The eluents were as follows: 100% CH_2Cl_2, followed by 100% hexane (yellow impurity exited the column), then 1:1 hexane:EtOAc, slowly moving to 100% EtOAc (blue impurity exited the column, red/purple impurity moved down the column), followed by 1:1 CH_2Cl_2:EtOAc, then 100% CH_2Cl_2, then 98:2 CH_2Cl_2:MeOH (blue impurity exited the column, red/purple impurity did not), then 97:2:1 CH_2Cl_2:MeOH:acetic acid (purple main band quickly exited the column). The main band fractions were combined, and the solvent was removed under reduced pressure followed by high vacuum. The crude product from the major fraction was dissolved in THF and purified by size exclusion column chromatography (SEC) (S-X1 Biobeads in THF (THF was HPLC grade or from a solvent purification system)). First, a one-foot column of one-

inch diameter was run, and the main black/purple band was collected and the solvent removed under reduced pressure. A three-foot column of 1.5-inch diameter SEC was then run, and again the main black/purple band was collected and the solvent removed under reduced pressure followed by high vacuum. Impurity previously seen by NMR spectroscopy was removed by SEC, but additional impurities were introduced. The one-foot column of one-inch diameter SEC was again run, and a strong impurity band (the ^{1}H NMR spectrum was similar to the product, but with very broad peaks) exited the column first, followed by the main band. The main black/purple band was collected and the solvent removed under reduced pressure followed by high vacuum (9 mg, 41% yield). ^{1}H NMR (800 MHz, $CDCl_3$): 8.38 (s, 1H), 8.25 (d, J = 8.5 Hz, 1H), 8.19 (s, 1H), 8.03 (dd, J = 7.9, 1.0 Hz, 1H), 8.00 (d, J = 7.2 Hz, 1H), 7.97 (s, 1H), 7.88 (d, J = 8.8 Hz, 1H), 7.79 (d, J = 7.4 Hz, 1H), 7.71 (s, 1H), 7.68 (s, 1H), 7.40 (dd, J = 8.4, 1.3 Hz, 1H), 7.35 (d, J = 8.8 Hz, 1H), 7.14 (d, J = 8.2 Hz, 1H), 6.99 (s, 2H), 6.13 (s, 1H), 6.06 (s, 1H), 4.3 (s, 2H), 4.06 (s, 2H), 2.37 (s, 2H), 2.13 (s, 4H), 2.06 (s, 7H), 2.10-2.06 (m, 1H), 2.03-1.98 (m, 1H), 1.92 (s, 4H), 1.88 (quin, J = 6.3 Hz, 2H), 1.49 (t, J = 7.4 Hz, 3H), 1.48-1.46 (m, 1H), 1.38 (quin, J = 7.2 Hz, 2H), 1.34-1.16 (m, 16H), 1.09-0.91 (m, 16H), 0.88 (t, J = 7.2 Hz, 3H), 0.77 (t, J = 7.2 Hz, 3H), 0.76-0.70 (m, 2H), 0.67 (t, J = 7.0 Hz, 2H), 0.65 (q, J = 7.4 Hz, 6H). ^{13}C{^{1}H} NMR (201 MHz, $CDCl_3$) δ (ppm) = 182.58, 178.30, 176.06, 172.33, 169.09, 166.00, 163.50, 159.03, 154.02, 152.58, 149.72, 147.41, 144.97, 143.08, 142.83, 138.86, 138.34, 137.5, 137.2, 136.91, 136.51, 136.17, 135.07, 132.93, 132.41, 131.66, 131.38, 129.81, 129.67, 129.6, 129.24, 128.2, 127.47, 126.14, 125.53, 123.09, 122.96, 122.71, 117.22, 110.14, 109.29, 94.42, 87.21, 86.61, 54.34, 51.6, 49.15, 43.88, 43.18, 43.08, 38.97, 35.43, 34.35, 34.20, 31.94, 29.65, 29.56, 29.47, 29.37, 28.56, 27.56,

27.38, 27.28, 27.16, 26.69, 22.8, 22.71, 21.08, 20.89, 14.14, 14.08, 12.51, 10.75, 10.67. HRMS (ESI): m/z 1389.7167 $[M]^+$ (calcd for $C_{88}H_{103}N_5O_4S_3$: 1389.7167).

2.9.7 Synthesis of sensitizer 2.8

The synthesis of 6-(7-bromobenzo[*c*][1,2,5]thiadiazol-4-yl)-4-(2-ethylhexyl)-4-(2-ethylpentyl)-4*H*-cyclopenta[2,1-*b*:3,4-*b*']dithiophene-2-carbaldehyde is described in section 2.9.6.1.

2.9.7.1 Synthesis of 6-(7-(4,4-bis(2-ethylhexyl)-4*H*-cyclopenta[2,1-*b*:3,4-*b*']dithiophen-2-yl)benzo[*c*][1,2,5]thiadiazol-4-yl)-4,4-bis(2-ethylhexyl)-4*H*-cyclopenta[2,1-*b*:3,4-*b*']dithiophene-2-carbaldehyde

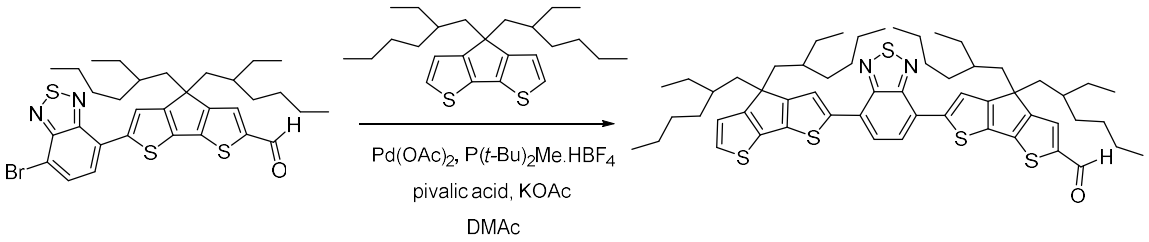

To a 20 mL oven-dried microwave vial charged with a stir bar and cooled under nitrogen was added 6-(7-bromobenzo[*c*][1,2,5]thiadiazol-4-yl)-4-(2-ethylhexyl)-4-(2-ethylpentyl)-4*H*-cyclopenta[2,1-*b*:3,4-*b*']dithiophene-2-carbaldehyde (0.195 g, 0.303 mmol), 4,4-bis(2-ethylhexyl)-4*H*-cyclopenta[2,1-*b*:3,4-*b*']dithiophene (0.610 g, 1.52 mmol), palladium(II) acetate (6 mg, 0.03 mmol), di-*tert*-butyl(methyl)phosphonium tetrafluoroborate (14 mg, 0.055 mmol), pivalic acid (28 mg, 0.28 mmol), and potassium acetate (81 mg, 0.83 mmol). The vial was kept for 10 min under high vacuum in a desiccator, then was sealed and filled with nitrogen. After three cycles of high vacuum, then filling with nitrogen, anhydrous degassed dimethylacetamide (DMAc) (4.8 mL) was

added. The flask was flushed with nitrogen, then the sealed vial was heated to 120 °C overnight. The reaction mixture was cooled to room temperature, then poured over a plug of silica gel topped with Celite packed in a Buchner funnel. The plug was rinsed with 1:1 hexanes:EtOAc, then 100% EtOAc. The purple-colored main band was collected and the solvent was removed under reduced pressure followed by high vacuum overnight. The product was purified by silica gel column chromatography chromatography on the Biotage Isolera system (25 g silica gel cartridge, dry loaded by dissolving in CH_2Cl_2, adding 1 g silica gel, and removing the solvent under reduced pressure). An initial column was run in hexanes:EtOAc, starting with 0% EtOAc and increasing to 5% EtOAc. The red-purple main band was collected and the solvent was removed under reduced pressure. The red-purple residue was further purified by size exclusion column (SEC) chromatography (S-X1 Biobeads in THF (without stabilizers, HPLC grade or from a solvent purification system)). First, a one-foot column of one-inch diameter was run, and the main red-purple band was collected and the solvent removed under reduced pressure. This column was repeated for further purification. An SEC on a three-foot column of 1.5-inch diameter was then run, and again the main red-purple band was collected and the solvent was removed under reduced pressure. A final one-foot SEC column of one-inch diameter was run, and the main red-purple band was collected and the solvent removed under reduced pressure to yield a dark red-purple solid (94 mg, 32%). ^{1}H NMR (500 MHz, $CDCl_3$) δ (ppm) = 9.87 (s, 1H), 8.12 (t, *J* = 8.3 Hz, 2H), 7.85 (q, *J* = 8.7 Hz, 2H), 7.61 (d, *J* = 4.4 Hz, 1H), 7.22 (d, *J* = 4.9 Hz, 1H), 6.98 (dt, *J* = 4.6, 4.9 Hz, 1H), 2.11-1.88 (m, 8H), 1.12-0.86 (m, 28H), 0.75 (t, *J* = 6.6 Hz, 8H), 0.72 (quin, *J* = 5.5 Hz, 4H), 0.64 (t, *J* = 7.5 Hz, 20H). ^{13}C{^{1}H} NMR (126 MHz, $CDCl_3$) δ (ppm) =

182.52, 182.45, 182.38, 162.79, 162.74, 162.68, 158.7, 158.67, 158.64, 158.59, 158.54, 157.95, 157.91, 152.43, 152.39, 147.92, 144.06, 143.38, 139.49, 139.44, 139.43, 139.39, 138.73, 138.7, 138.67, 137.07, 137, 136.95, 136.84, 130.61, 127.37, 125.63, 125.35, 124.87, 123.76, 123.41, 123.24, 123.08, 122.46, 122.41, 122.38, 122.25, 122.23, 122.08, 54.19, 53.75, 43.25, 43.14, 43.09, 35.31, 35.27, 35.16, 35.13, 34.37, 34.35, 34.19, 34.1, 28.62, 28.57, 28.52, 28.47, 27.57, 27.45, 27.34, 22.75, 22.72, 14.08, 14.06, 14.04, 14.01, 14, 13.99, 10.77, 10.73, 10.63. HRMS (ESI) : m/z 964.4542 $[M]^+$ (calcd for $C_{57}H_{76}ON_2S_5$: 964.4556). Analysis calculated for $C_{57}H_{76}N_2OS_5$: C, 70.91; H, 7.93; N, 2.90. Found: C, 70.85; H, 7.77; N, 2.94.

2.9.7.2 Synthesis of (*E*)-2-((*E*)-(7-bromo-3-dodecyl-1,1-dimethyl-1,3-dihydro-2*H*-benzo[*e*]indol-2-ylidene)methyl)-4-((7-bromo-3-dodecyl-1,1-dimethyl-1*H*-benzo[*e*]indol-3-ium-2-yl)methylene)-3-oxocyclobut-1-en-1-olate

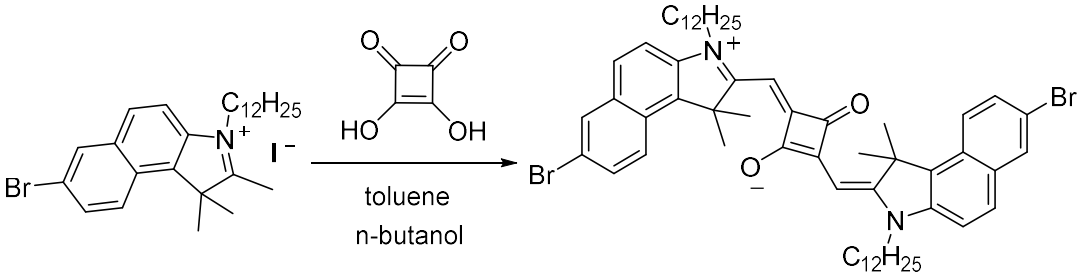

3,4-Dihydroxycyclobut-3-ene-1,2-dione (80 mg, 0.70 mmol) and 7-bromo-3-dodecyl-1,1,2-trimethyl-1*H*-benzo[*e*]indol-3-ium iodide (ID-II-171, 0.41 g, 0.701 mmol) (adding this amount was an error, 2 equiv. should have been added) were dissolved in a solution of 4 mL of toluene and 4 mL *n*-butanol. The mixture was refluxed for 19 h into a Dean-Stark apparatus filled with toluene. The solvent was then removed under reduced pressure, with the remaining solvent afterwards removed under high vacuum overnight.

Flash chromatography (25 g silica gel column on the Biotage Isolera system, starting with hexanes and gradually increasing to hexanes:EtOAc 3:2, when the main band exited the column). Removal of solvent under reduced pressure yielded the product as green crystals (43 mg, analytically pure) and a green solid (140 mg) (183 mg, 26%). ^{1}H NMR (500 MHz, $CDCl_3$) δ (ppm) = 8.06 (d, *J* = 9.2 Hz, 2H), 8.05 (d, *J* = 1.9 Hz, 2H), 7.77 (d, *J* = 8.8 Hz, 2H), 7.64 (dd, *J* = 9.0, 2.0 Hz, 2H), 7.30 (d, *J* = 8.8 Hz, 2H), 6.03 (s, 2H), 4.08 (s, 4H), 2.06 (s, 12H), 1.86 (quin, *J* = 7.1 Hz, 4H), 1.46 (quin, *J* = 7.3 Hz, 4H), 1.37 (quin, *J* = 6.5 Hz, 4H), 1.33-1.19 (m, 28H), 0.87 (t, *J* = 7.1 Hz, 6H). $^{13}C\{^{1}H\}$ NMR (126 MHz, $CDCl_3$) δ (ppm) = 182.46, 178.61, 171.10, 139.99, 134.64, 132.26, 131.57, 130.62, 128.73, 127.13, 124.14, 117.90, 111.18, 86.60, 55.98, 51.06, 43.90, 31.90, 29.59, 29.52, 29.49, 29.37, 29.32, 27.35, 27.08, 26.88, 22.68, 14.13. HRMS (ESI): m/z 988.4103 $[M]^+$ (calcd for $C_{58}H_{74}Br_2N_2O_2$: 988.4112). Anal. Calcd for $C_{58}H_{74}Br_2N_2O_2$ (%): C, 70.29; H, 7.53; N, 2.83. Found: C, 70.32; H, 7.64; N, 2.91.

2.9.7.3 Synthesis of (*E*)-2-((*E*)-(7-(6-(7-(4,4-bis(2-ethylhexyl)-6-formyl-4*H*-cyclopenta[2,1-*b*:3,4-*b'*]dithiophen-2-yl)benzo[*c*][1,2,5]thiadiazol-4-yl)-4,4-bis(2-ethylhexyl)-4*H*-cyclopenta[2,1-*b*:3,4-*b'*]dithiophen-2-yl)-3-dodecyl-1,1-dimethyl-1,3-dihydro-2*H*-benzo[*e*]indol-2-ylidene)methyl)-4-((7-bromo-3-dodecyl-1,1-dimethyl-1*H*-benzo[*e*]indol-3-ium-2-yl)methylene)-3-oxocyclobut-1-en-1-olate

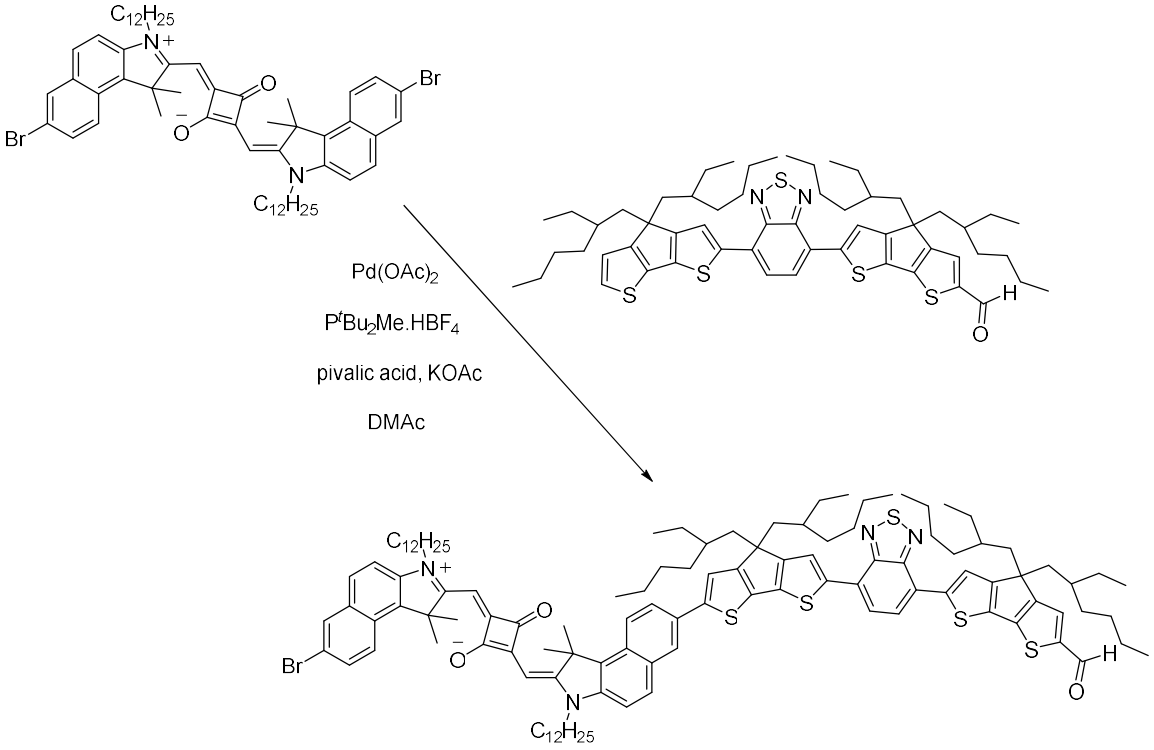

To a 10 mL oven-dried microwave vial charged with a stir bar and cooled under nitrogen was added 6-(7-(4,4-bis(2-ethylhexyl)-4*H*-cyclopenta[2,1-*b*:3,4-*b'*]dithiophen-2-yl)benzo[*c*][1,2,5]thiadiazol-4-yl)-4,4-bis(2-ethylhexyl)-4*H*-cyclopenta[2,1-*b*:3,4-*b'*]dithiophene-2-carbaldehyde (0.092 g, 0.095 mmol), (*E*)-2-((*E*)-(7-bromo-3-dodecyl-1,1-dimethyl-1,3-dihydro-2*H*-benzo[*e*]indol-2-ylidene)methyl)-4-((7-bromo-3-dodecyl-1,1-dimethyl-1*H*-benzo[*e*]indol-3-ium-2-yl)methylene)-3-oxocyclobut-1-en-1-olate

(0.141 g, 0.142 mmol), palladium(II) acetate (2 mg, 0.009 mmol), di-*tert*-butyl(methyl)phosphonium tetrafluoroborate (4 mg, 0.02 mmol), pivalic acid (9 mg, 0.09 mmol), and potassium acetate (26 mg, 0.26 mmol). The vial was kept for 10 min under high vacuum in a desiccator, then was sealed and filled with nitrogen. After three cycles of high vacuum, then filling with nitrogen, anhydrous degassed dimethylacetamide (DMAc) (1.5 mL) was added. The flask was flushed with nitrogen, then the sealed vial was heated to 120 °C overnight. The organic layer was extracted by CH_2Cl_2 and rinsed with water, then dried over Na_2SO_4, filtered, and the solvent was removed under reduced pressure followed by high vacuum overnight. The product was purified by silica gel column chromatography chromatography on the Biotage Isolera system (25 g silica gel cartridge) with CH_2Cl_2 as the eluent. The dark blue main band was collected and the solvent was removed under reduced pressure. The residue was further purified by size exclusion column (SEC) chromatography (S-X1 Biobeads in THF (without stabilizers, HPLC grade or from a solvent purification system)). First, a one-foot column of one-inch diameter was run, and the main dark blue band was collected and the solvent removed under reduced pressure. This column was repeated for further purification. An SEC on a three-foot column of 1.5-inch diameter was then run, and again the main dark blue band was collected and the solvent was removed under reduced pressure. The residue was purified by silica gel column chromatography chromatography on the Biotage Isolera system (25 g silica gel cartridge) using CH_2Cl_2 as the eluent, and gradually increasing to CH_2Cl_2:MeOH 98:2. The dark blue main band was collected and the solvent was removed under reduced pressure. The residue was purified by silica gel column chromatography chromatography on the Biotage Isolera system (10 g silica gel cartridge)

using hexanes:EtOAc 90:10 as the eluent, and gradually increasing to hexanes:EtOAc 75:25. The dark blue main band was collected and the solvent was removed under reduced pressure to yield a dark red-purple solid (43 mg, 24%). ^{1}H NMR (800 MHz, $CDCl_3$): δ (ppm) = 9.87 (s, 1H), 8.22 (d, *J* = 8.3 Hz, 1H), 8.16-8.11 (m, 2H), 8.09 (dd, *J* = 5.2, 3.5 Hz, 1H), 8.07 (d, *J* = 8.9 Hz, 1H), 8.04 (d, *J* = 1.4 Hz, 1H), 7.94-7.84 (m, 5H), 7.77 (d, *J* = 8.6 Hz, 1H), 7.64 (dd, *J* = 9.0, 1.6 Hz, 1H), 7.61 (d, *J* = 6.8 Hz, 1H), 7.38 (s, 1H), 7.31 (q, *J* = 8.2 Hz, 2H), 6.06 (s, 1H), 6.04 (s, 1H), 4.12 (s, 2H), 4.08 (s, 2H), 2.11 (s, 6H), 2.07 (s, 6H), 2.10-1.96 (m, 8H), 1.92-1.83 (m, 4H), 1.54-1.44 (m, 4H), 1.38 (sext, br, *J* = 7.3 Hz, 4H), 1.35-1.28 (m, 4H), 1.26 (s, 28H), 1.10-0.92 (m, 24H), 0.88 (t, *J* = 7.1 Hz, 6H), 0.86-0.81 (m, 4H), 0.76 (t, *J* = 7.0 Hz, 3H), 0.72 (t, *J* = 6.5 Hz, 6H), 0.64 (t, *J* = 7.3 Hz, 6H). ^{13}C{^{1}H} NMR (201 MHz, $CDCl_3$) δ (ppm) = 182.58, 182.5, 178.53, 177.73, 171.35, 170.72, 166.83, 162.85, 162.80, 159.75, 158.71, 158.64, 158.58, 158.02, 157.99, 152.51, 152.46, 147.93, 144.99, 144.95, 144.91, 144.06, 143.45, 140.10, 139.68, 139.62, 139.54, 139.38, 137.12, 137.07, 136.78, 134.88, 134.58, 132.23, 131.64, 131.58, 131.20, 130.60, 129.71, 128.72, 127.70, 127.31, 127.19, 125.39, 125.02, 124.81, 124.16, 123.85, 123.23, 123.11, 122.97, 122.49, 122.34, 122.18, 118.86, 118.77, 118.67, 117.82, 117.39, 117.27, 111.18, 110.95, 86.71, 86.57, 55.99, 54.24, 51.14, 50.97, 43.99, 43.86, 43.33, 43.27, 43.19, 43.14, 35.35, 35.32, 34.39, 34.32, 34.24, 34.14, 31.92, 29.71, 29.62, 29.54, 29.53, 29.41, 29.34, 28.73, 28.6, 28.52, 27.6, 27.47, 27.35, 27.11, 26.93, 26.86, 22.82, 22.76, 22.70, 14.15, 14.08, 14.06, 14.03, 10.83, 10.75, 10.64. HRMS (ESI): m/z 937.4766 $[M+2H]^{2+}$ (calcd for $C_{115}H_{151}BrN_4O_3S_5$: 937.4781). Anal. Calcd for $C_{115}H_{149}BrN_4O_3S_5$ (%): C, 73.64; H, 8.01; N, 2.99. Found: C, 73.93; H, 8.00; N, 3.06.

2.9.7.4 Synthesis of (*E*)-2-((*E*)-(7-(6-(7-(4,4-bis(2-ethylhexyl)-6-formyl-4*H*-cyclopenta[2,1-*b*:3,4-*b'*]dithiophen-2-yl)benzo[*c*][1,2,5]thiadiazol-4-yl)-4,4-bis(2-ethylhexyl)-4*H*-cyclopenta[2,1-*b*:3,4-*b'*]dithiophen-2-yl)-3-dodecyl-1,1-dimethyl-1,3-dihydro-2*H*-benzo[*e*]indol-2-ylidene)methyl)-4-((3-dodecyl-7-mesityl-1,1-dimethyl-1*H*-benzo[*e*]indol-3-ium-2-yl)methylene)-3-oxocyclobut-1-en-1-olate

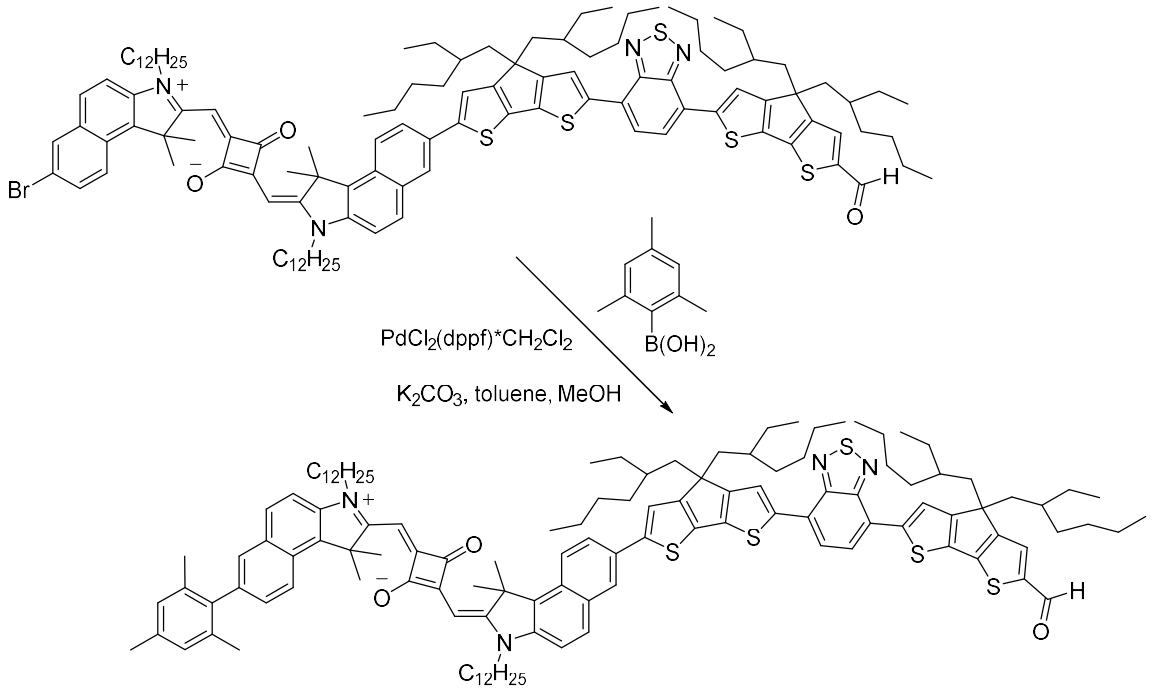

In a 20 mL vial capped with a septum, (*E*)-2-((*E*)-(7-(6-(7-(4,4-bis(2-ethylhexyl)-6-formyl-4*H*-cyclopenta[2,1-*b*:3,4-*b'*]dithiophen-2-yl)benzo[*c*][1,2,5]thiadiazol-4-yl)-4,4-bis(2-ethylhexyl)-4*H*-cyclopenta[2,1-*b*:3,4-*b'*]dithiophen-2-yl)-3-dodecyl-1,1-dimethyl-1,3-dihydro-2*H*-benzo[*e*]indol-2-ylidene)methyl)-4-((7-bromo-3-dodecyl-1,1-dimethyl-1*H*-benzo[*e*]indol-3-ium-2-yl)methylene)-3-oxocyclobut-1-en-1-olate (38 mg, 0.020 mmol) was dissolved in toluene (1 mL) and MeOH (1 mL) and degassed for 10 min before adding to a capped 10 mL oven-dried microwave tube of 2,4,6-

trimethylphenylboronic acid (10 mg, 0.061 mmol), $PdCl_2(dppf)\cdot CH_2Cl_2$ (2 mg, 0.002 mmol), and potassium carbonate (14 mg, 0.10 mmol) that had been pumped and refilled 3 times with nitrogen. The tube was heated to 70 °C for 18 h, then was cooled to room temperature and passed through a silica gel plug (CH_2Cl_2:MeOH = 8:2). The solvent was removed under reduced pressure and high vacuum overnight. The residue was purified by flash chromatography (Biotage Isolera system, 10 g silica gel). The eluents were as follows: hexanes:EtOAc 100:0, gradually increasing to 60:40, where an impurity exited the column, then to 35:65, when the main band exited the column gradually as eluent was increased to 20:80. Further purification by size exclusion column (S-X1, Biobeads, THF) yielded the purified product as a dark blue-black solid (23 mg, 59%). ^{1}H NMR (400 MHz, $CDCl_3$) δ (ppm) = 9.86 (s, 1H), 8.23 (t, *J* = 10.0 Hz, 2H), 8.13 (q, *J* = 6.0 Hz, 2H), 8.09 (d, *J* = 1.7 Hz, 1H), 7.94-7.84 (m, 5H), 7.67 (d, *J* = 1.5 Hz, 1H), 7.61 (d, *J* = 3.4 Hz, 1H), 7.39 (dd, *J* = 8.8, 1.6 Hz, 1H), 7.38 (s, 1H) 7.31 (dd, *J* = 8.9, 4.5 Hz, 2H), 7.00 (s, 2H), 6.07 (s, 1H), 6.04 (s, 1H), 4.13 (s, 4H), 2.37 (s, 3H), 2.14 (s, 4H), 2.11 (s, 6H), 2.06 (s, 8H), 2.05-1.95 (m, 6H), 1.94-1.82 (m, 4H), 1.75 (s, 3H), 1.54-1.43 (m, 4H), 1.39 (quin, *J* = 6.8 Hz, 4H), 1.34-1.29 (m, 4H), 1.26 (s, 24H), 1.13-0.92 (m, 30H), 0.88 (td, *J* = 6.9, 1.0 Hz, 6H), 0.89-0.80 (m, 4H), 0.78-0.70 (m, 7H), 0.66 (td, *J* = 7.1, 1.4 Hz, 12H), 0.63 (t, *J* = 7.5 Hz, 6H). ^{13}C{^{1}H} NMR (101 MHz, $CDCl_3$) δ (ppm) = 182.60, 182.52, 178.14, 177.48, 171.47, 170.63, 166.81, 162.83, 162.78, 159.73, 159.69, 158.66, 158.59, 158.53, 157.99, 157.96, 152.48, 152.44, 147.94, 145.06, 145.02, 144.06, 143.40, 139.82, 139.70, 139.63, 139.54, 139.29, 138.39, 137.16, 137.09, 137.04, 136.84, 136.67, 136.18, 134.62, 131.48, 131.39, 131.00, 130.67, 129.62, 129.47, 128.18, 127.74, 127.48, 127.30, 125.37, 124.97, 124.80, 123.81, 123.18, 123.11, 122.94, 122.63, 122.45, 122.29, 118.78,

118.68, 118.59, 110.87, 110.25, 86.45, 86.41, 55.98, 54.21, 51.29, 50.95, 43.88, 43.24, 43.11, 35.29, 34.30, 34.21, 34.11, 31.91, 31.59, 29.70, 29.61, 29.54, 29.42, 29.33, 28.70, 28.58, 28.49, 27.58, 27.44, 27.32, 27.12, 26.89, 26.85, 22.81, 22.75, 22.69, 21.07, 20.89, 14.14, 14.07, 10.82, 10.74, 10.62. HRMS (ESI): m/z 1913.1067 $[M]^+$ (calcd for $C_{124}H_{160}N_4O_3S_5$: 1913.1088).

2.9.7.5 Synthesis of (*E*)-2-((*E*)-(7-(6-(7-(6-((*E*)-2-carboxy-2-cyanovinyl)-4,4-bis(2-ethylhexyl)-4*H*-cyclopenta[2,1-*b*:3,4-*b'*]dithiophen-2-yl)benzo[*c*][1,2,5]thiadiazol-4-yl)-4,4-bis(2-ethylhexyl)-4*H*-cyclopenta[2,1-*b*:3,4-*b'*]dithiophen-2-yl)-3-dodecyl-1,1-dimethyl-1,3-dihydro-2*H*-benzo[*e*]indol-2-ylidene)methyl)-4-((3-dodecyl-7-mesityl-1,1-dimethyl-1*H*-benzo[*e*]indol-3-ium-2-yl)methylene)-3-oxocyclobut-1-en-1-olate

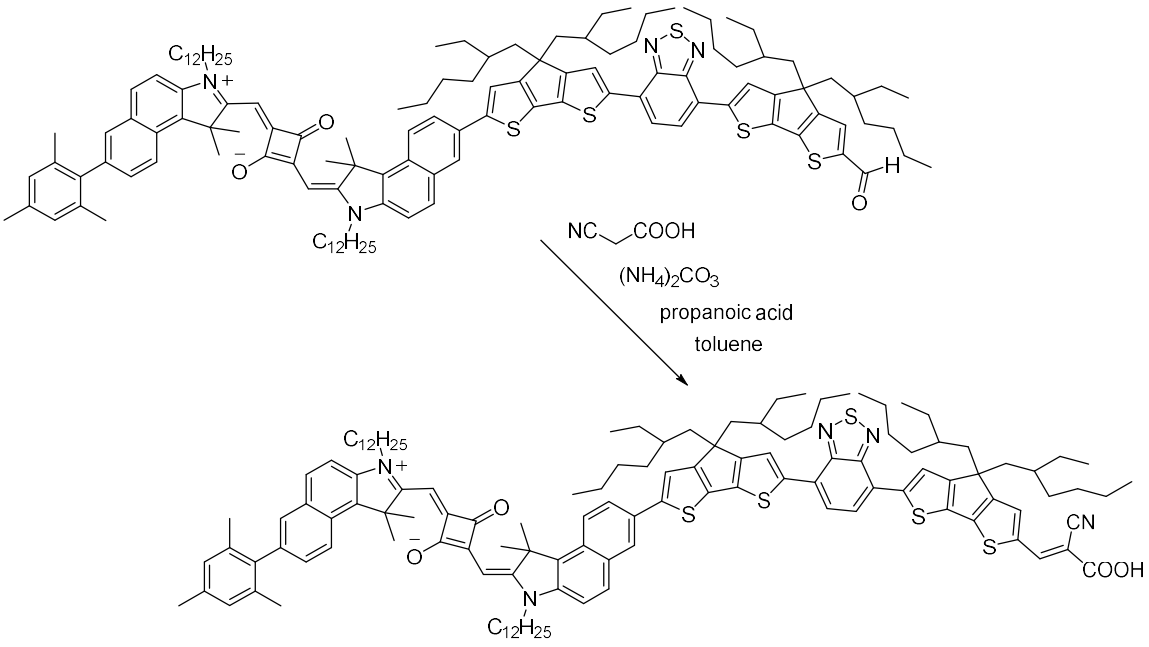

(*E*)-2-((*E*)-(7-(6-(7-(4,4-Bis(2-ethylhexyl)-6-formyl-4*H*-cyclopenta[2,1-*b*:3,4-*b'*]dithiophen-2-yl)benzo[*c*][1,2,5]thiadiazol-4-yl)-4,4-bis(2-ethylhexyl)-4*H*-

cyclopenta[2,1-*b*:3,4-*b'*]dithiophen-2-yl)-3-dodecyl-1,1-dimethyl-1,3-dihydro-2*H*-benzo[*e*]indol-2-ylidene)methyl)-4-((3-dodecyl-7-mesityl-1,1-dimethyl-1*H*-benzo[*e*]indol-3-ium-2-yl)methylene)-3-oxocyclobut-1-en-1-olate (22 mg, 0.011 mmol) was placed in an oven-dried round-bottom flask with reflux condenser and the capped system was filled with nitrogen. Anhydrous toluene (1 mL) was added and stirred under nitrogen for 5 min. Ammonium carbonate (9 mg, 0.097 mmol) and cyanoacetic acid (4 mg, 0.048 mmol) were added and the solution was stirred under nitrogen for 5 min. Propanoic acid (0.043 mL, 0.574 mmol) was added and the solution was stirred overnight under nitrogen at 100 °C. The solvent was removed slowly under reduced pressure, then the residue was dissolved in CH_2Cl_2. The organic layer was extracted three times with water, then dried over Na_2SO_4, and filtered. The solvent was removed under reduced pressure followed by high vacuum. The residue was further purified by silica gel column chromatography (Biotage Isolera system, 10 g silica gel, hexane:EtOAc 100:0 increasing gradually to 0:100, then increasing gradually to 10% MeOH). The main band was collected and the solvent removed under reduced pressure followed by high vacuum. The crude product from the major fraction was dissolved in THF and purified by size exclusion column chromatography (SEC) (S-X1 Biobeads in THF (THF was HPLC grade or from a solvent purification system)). A one-foot column of one-inch diameter was run, and the main black/purple band was collected and the solvent removed under reduced pressure. A one-foot gel permeation column (Sephadex LH-20) of one-inch diameter was run. The main dark band was collected and the solvent removed under reduced pressure. The residue was then purified by reverse phase silica gel (C18, 10 g) column chromatography in MeOH:EtOAc 100:0, gradually increasing to 0:100, with the

main band collected and the solvent removed under reduced pressure to yield a dark blue-black solid (1.5 mg, 6.5% yield). ^{1}H NMR (700 MHz, $CDCl_3$) δ (ppm) = 8.34 (s, 1H), 8.26 (d, *J* = 7.6 Hz, 1H), 8.23 (d, *J* = 7.5 Hz, 1H), 8.16 (q, *J* = 10.3 Hz, 2H), 8.10 (s, 1H), 7.93 (d, *J* = 5.6 Hz, 1H), 7.89 (q, *J* = 9.1 Hz, 2H), 7.74 (d, *J* = 3.4 Hz, 2H), 7.69 (s, 1H), 7.58-7.53 (m, 2H), 7.43-7.38 (m, 1H), 7.36-7.32 (m, 1H), 7.14 (s, br, 1H), 6.83 (d, *J* = 5.2 Hz, 1H), 6.09 (s, 1H), 6.06 (s, 1H), 4.21-4.04 (m, 4H), 2.39 (s, 3H), 2.13 (s, 6H), 2.08 (s, 8H), 2.07-1.99 (m, 6H), 1.94-1.87 (m, 4H), 1.69-1.63 (m, 3H), 1.53-1.46 (m, 4H), 1.44-1.36 (m, 4H), 1.36-1.18 (m, 26H), 1.10-0.93 (m, 24H), 0.93-0.81 (m, 22H), 0.79 (q, *J* = 6.4 Hz, 4H), 0.74 (q, *J* = 6.8 Hz, 4H), 0.69 (t, br, *J* = 6.7 Hz, 12H). $^{13}C\{^{1}H\}$ NMR (176 MHz, $CDCl_3$) δ (ppm) = 184.84, 178.14, 167.79, 163.21, 152.46, 147.91, 141.91, 132.29, 130.98, 129.67, 128.83, 128.17, 127.8, 126.96, 125.84, 123.78, 122.66, 122.1, 119.58, 113.97, 110.99, 101.64, 92.67, 56.06, 43.17, 35.39, 34.25, 33.72, 33.47, 31.96, 30.97, 30.21, 29.82, 29.62, 29.47, 29.37, 28.99, 28.76, 28.53, 27.46, 27.16, 26.85, 23.02, 22.85, 22.73, 20.9, 19.53, 19.15, 14.19, 14.06, 13.73, 12.13, 11.44, 10.76 (small and few peaks observed due to limited material and poor solubility). HRMS (ESI): m/z 1980.1130 $[M]^+$ (calcd for $C_{127}H_{161}N_5O_4S_5$: 1980.1147).

CHAPTER 3. ASYMMETRIC SQUARAINE SENSITIZERS FOR NEAR-IR SENSITIZATION OF DYE-SENSITIZED SOLAR CELLS: THE ROLE OF OUT-OF-PLANE SUBSTITUENTS

This work was accomplished in collaboration with Parnian Ferdowsi in the group of Prof. Anders Hagfeldt. Training and assistance were provided by Dr. M. D. Zakeeruddin, Dr. Kazuteru Nonomura, Dr. Nick Vlachopoulos, and Dr. Stephen Shiring in the group of Prof. Jean-Luc Brédas. The author performed synthesis, device fabrication and optimization, cyclic voltammetry, photoelectrochemical device characterization, and computational modeling.

3.1 Introduction

Aggregation has historically played a large role in the DSSC performance of sensitizers. He *et al*. (Hagfeldt) demonstrated that strategies to reduce aggregation of zinc phthalocyanines (sensitizer **ZnPcTyr**) on the surface of TiO_2 achieved IPCE values of ~24%,[156] relative to the 4% IPCE achieved by a zinc phthalocyanine substituted by four ester groups (Figure 3-1).[157] Further studies incorporating bulky *tert*-butyl substituents on the phthalocyanine core resulted in an IPCE maximum value of over 70% (sensitizer **PCH001**, Figure 3-1),[158] with an IPCE maximum value of near 90% seen when using *tert*-butyl substituents and a more effective anchoring strategy (sensitizer **TT1**, Figure 3-1).[159]

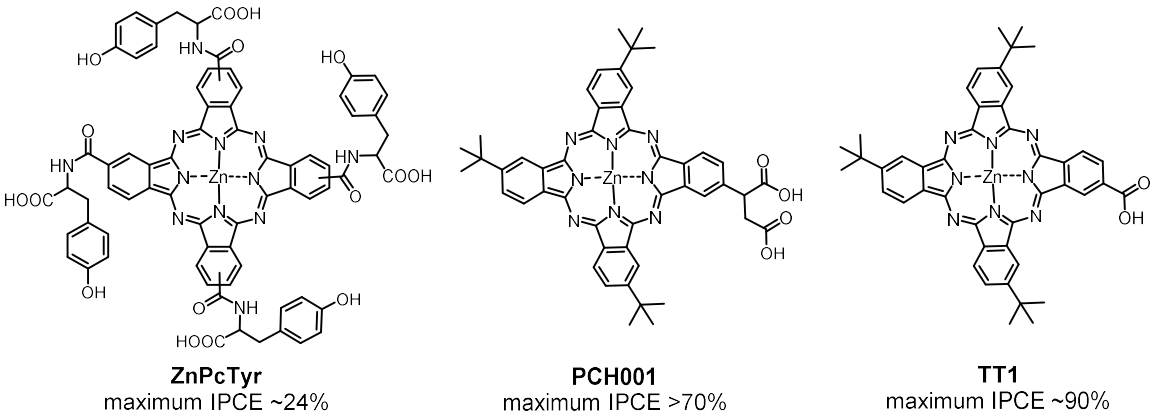

Figure 3-1. Zinc phthalocyanine sensitizers **ZnPcTyr**, **PCH001**, and **TT1** incorporating out-of-plane groups for reduced aggregation.

The performance of porphyrin sensitizers shows a large dependence on the extent of reducing dye-dye aggregation at the semiconductor surface. A maximum IPCE value of over 80% was seen when using bulky *tert*-butyl substituents in the *meta* position of the *meso*-phenyl rings attached to the porphyrin core (sensitizer **YD-2**),[160] with a further increase to an IPCE max value of over 90% when employing alkoxy groups in the *ortho* position of the *meso*-phenyl rings attached to the porphyrin core (**YD-2-*o*-C8**) (Figure 3-2).[20]

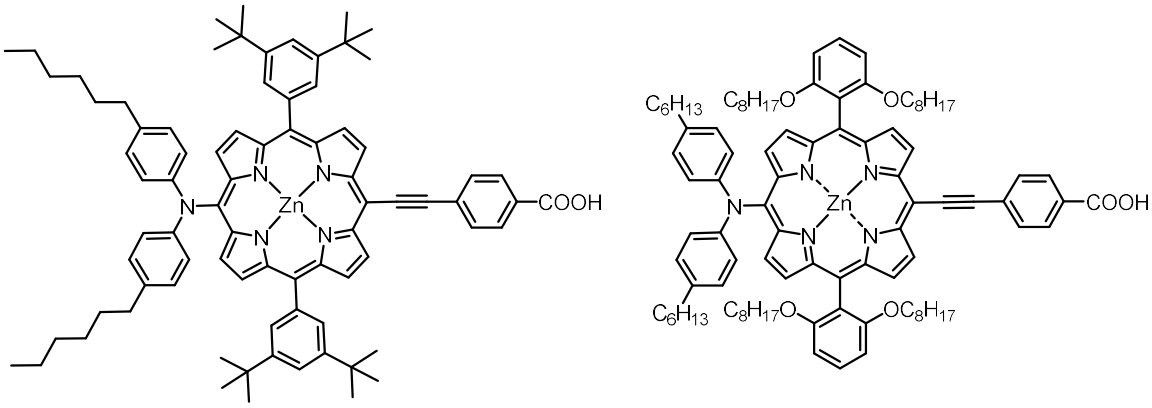

YD-2 **YD-2-*o*-C8**

Figure 3-2. Porphyrin sensitizers **YD-2** and **YD-2-*o*-C8**.

Squaraine sensitizers have also been shown to aggregate at the semiconductor surface, as observed on dye-sensitized TiO_2 films by the presence of absorption to the high-energy side of the main absorption peak attributed to H-aggregates.[113] In merocyanines, it was observed that the dye molecules could stack parallel to one another, or plane-to-plane, to form an H-aggregate with hypsochromically shifted absorption, or in a head-to-tail, end-to-end, arrangement to form a J-aggregate with bathochromically shifted absorption (Figure 3-3).

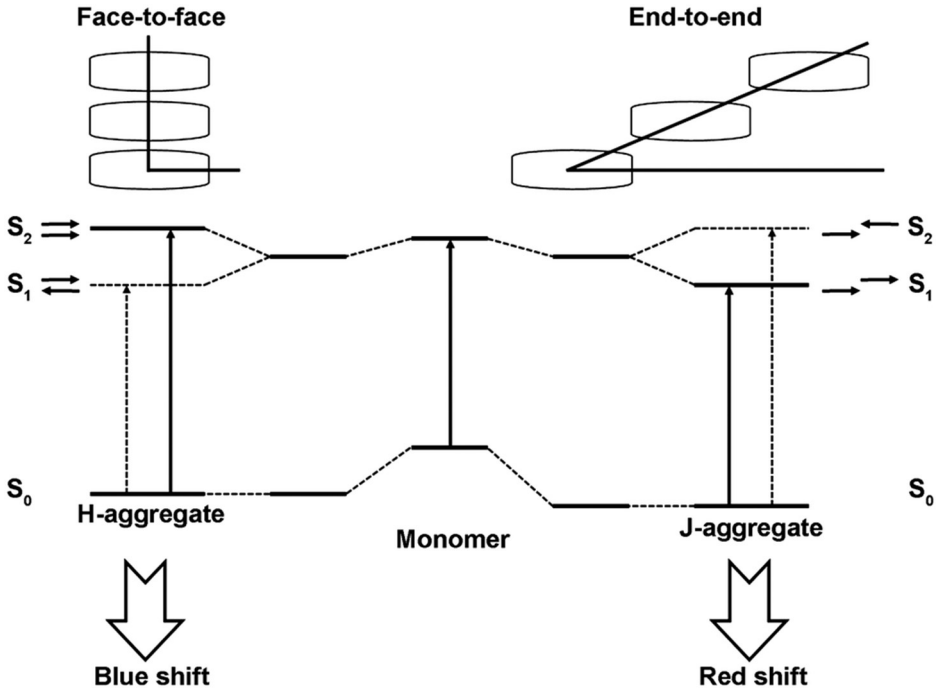

Figure 3-3. Schematic presentation of the relationship between dye molecule arrangement and spectral shift of H-aggregate and J-aggregate based on molecular exciton theory. Reproduced from Zhai *et al*. with permission from The Royal Society of Chemistry.

It is known that for sensitizer **MSqb** for DSSCs, the H-aggregate quenches fluorescence and provides a loss mechanism preventing electron injection (Figure 3-4). Tatay *et al*. (Durrant) utilized emission quenching data and transient absorption studies to demonstrate that electron injection was mainly achieved by the monomeric squaraine sensitizers, while the aggregate population exhibited an order of magnitude lower injection yield.[112]

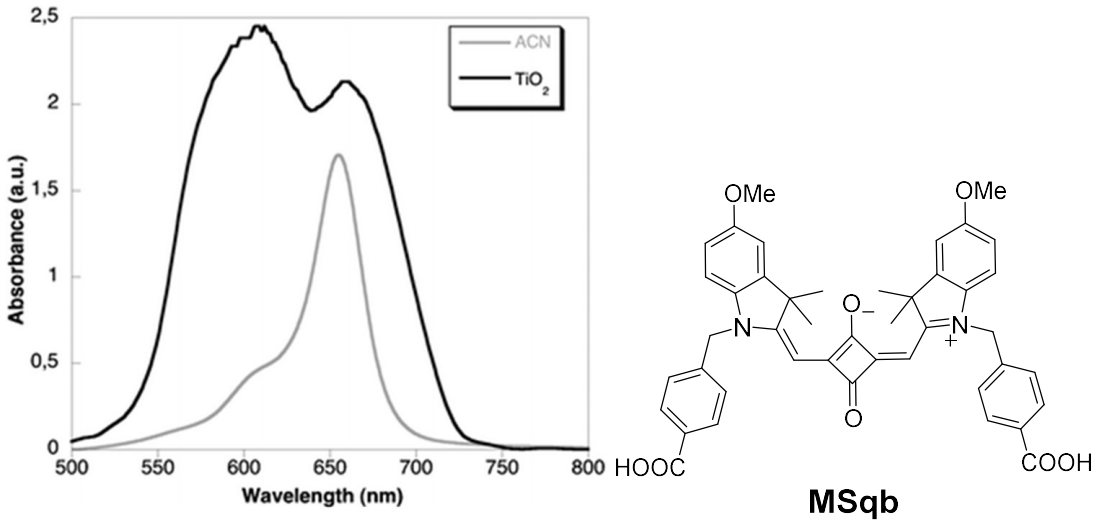

Figure 3-4. Left: **MSqb** solution absorption in MeCN and absorption when adsorbed on TiO_2, exhibiting a characteristic blue-shifted aggregate peak. Right: Molecular structure of **MSqb**. Reproduced from Tatay *et al.*[112] with permission from The Royal Society of Chemistry.

Various structural modifications along with the use of high concentrations of the coadsorbent chenodeoxycholic acid (CDCA) in the dye bath have been used to decrease squaraine aggregation on the TiO_2 surface. The effect of out-of-plane substituents on aggregation was explored on the indolinium moiety via a *gem*-di-butyl group, with an increase in J_{SC} from 2.32 mA/cm^2 with the standard dimethyl (**Sq1**) to 3.05 mA/cm^2 with the dibutyl functionality (**Sq3**) (Figure 3-5).[34]

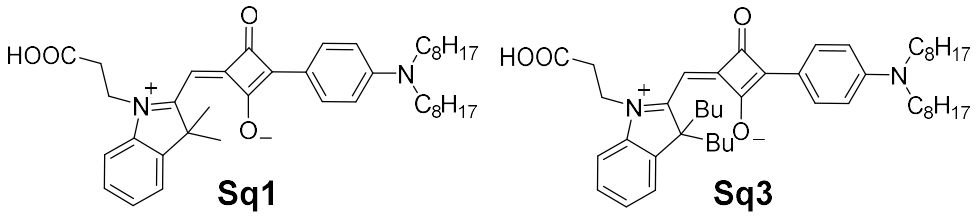

Figure 3-5. Squaraine sensitizers **Sq1** and **Sq3** examined by Otsuaka *et al.*[34]

Delcamp *et al*. and Jradi *et al*. explored out-of-plane substituents through the use of π-bridges with *gem*-di-alkyl substituents on **JD10** and **DTS-CA** (Figure 3-6), for PCEs of 7.4 and 8.9% (no mask), respectively.[61,139] However, both the central atom on the bridge (C or Si) and the *gem*-di-alkyl substituents were varied, and the use of a mask was not identical, so no direct comparison can be made. Bisht *et al*. saw interesting effects on the J_{SC} and V_{OC} when incorporating in-plane substituents with branched alkyl chains (**RSQ2**) vs linear alkyl chains (**RSQ1**), with an increase in the V_{OC} of 49 mV when moving from a straight to a branched chain, while J_{SC} decreased by 0.26 mA/cm2 for the branched 2-ethylhexyl-substituted **RSQ2**, which had an overall PCE of 6.8%.[161]

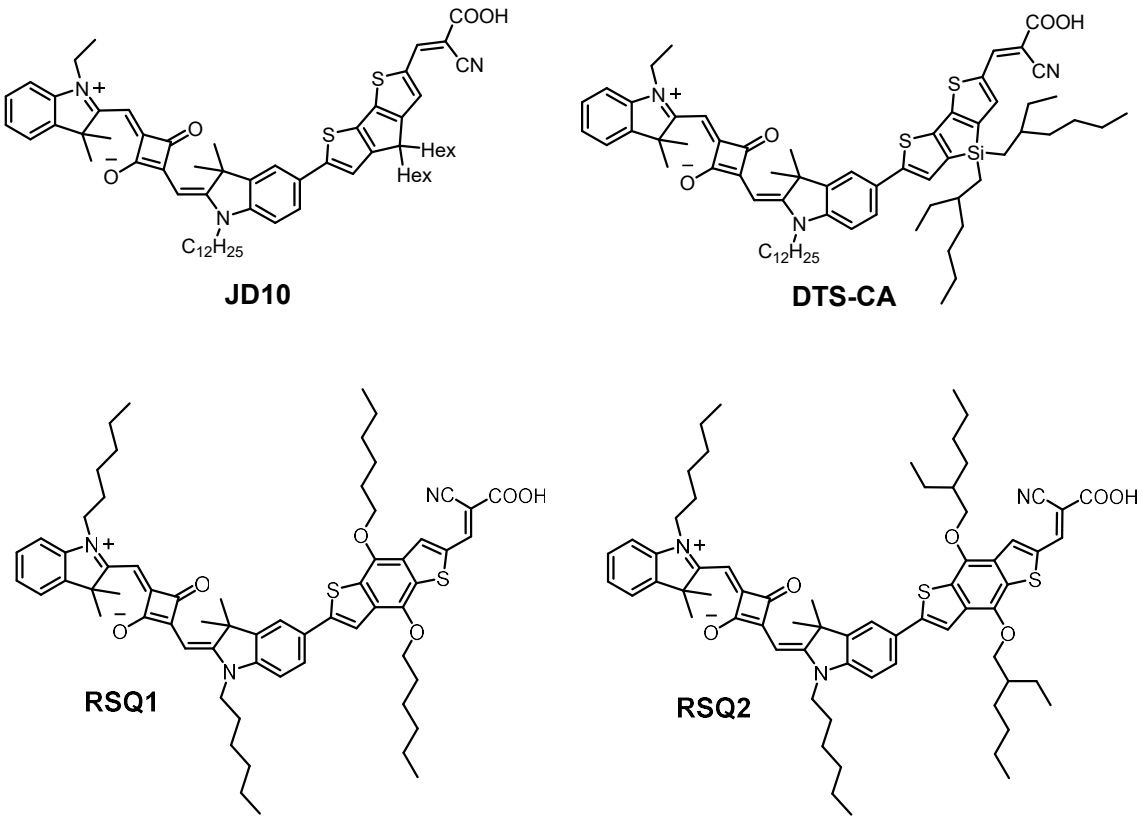

Figure 3-6. Molecular structures of squaraine sensitizers JD10, DTS-CA, RSQ1, and RSQ2.

This chapter will make direct comparisons between linear and branched chains, and between DTS and CPDT. The work examines out-of-plane alkyl groups on region I, the "donor end" of the squaraine; region II, the dialkyl-substituted indole; and region III, the π-bridge (Figure 3-7). On region I, the influence of a mesityl group is explored through sensitizers **3.2** and **3.7** (Figure 3-8). For region II, the effects of the dibutyl-substitued indole are examined through sensitizer **3.3** (Figure 3-8). On region III, linear vs. branched alkyl chains in sensitizers **3.5** and **3.6** and cyclopentadithiophene vs. dithienosilole π-bridges in sensitizers **3.7** and **3.8** are compared (Figure 3-8). Sensitizers **2.1** (**YR6**), **2.2**, **2.4**, and **2.6** previously examined in Chapter 2 are used here for comparison purposes, and are labeled **3.1**, **3.4**, **3.6**, and **3.7**, respectively.

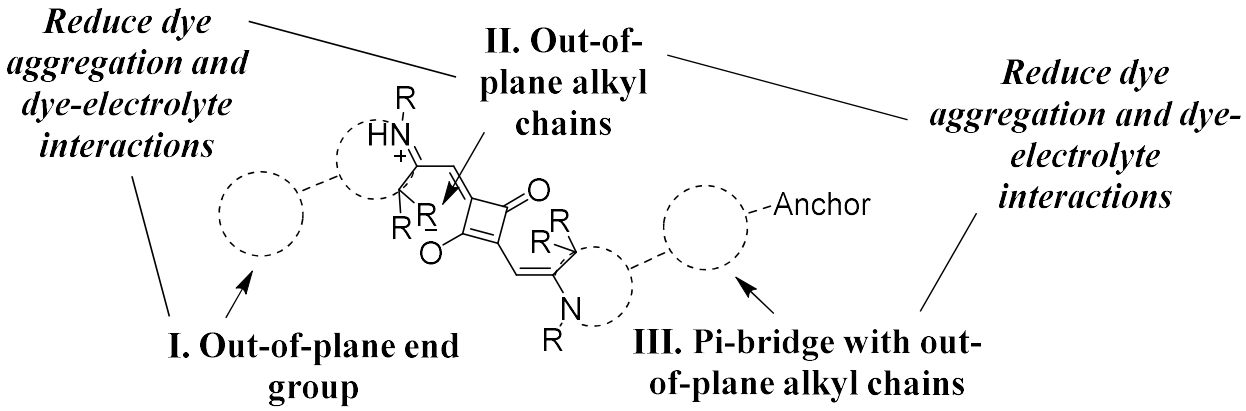

Figure 3-7. Areas for incorporation of out-of-plane groups on the squaraine structure.

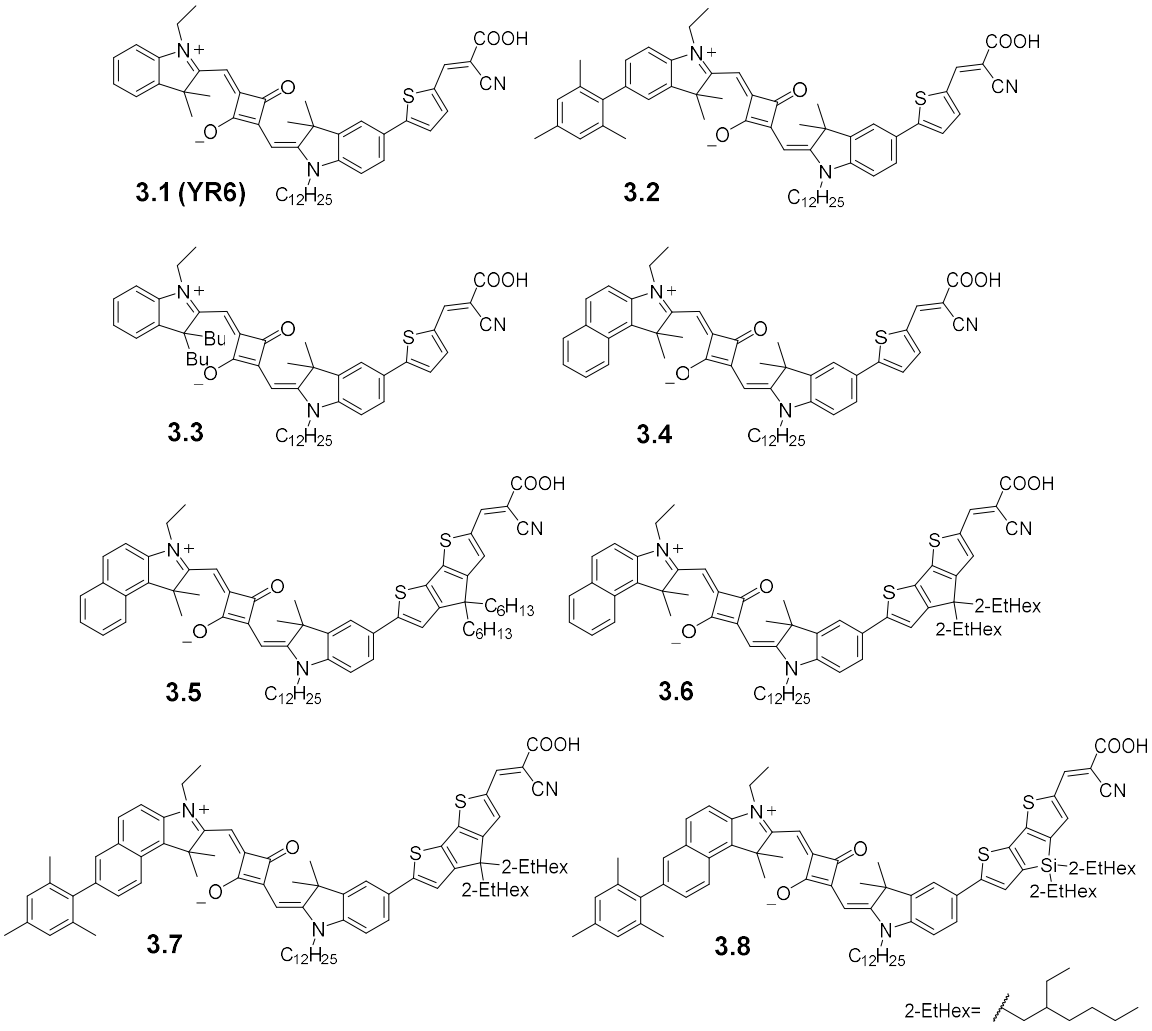

Figure 3-8. Sensitizer molecular structures 3.1-3.8.

3.2 Sensitizer Synthesis

The target squaraine sensitizers **3.2-3.8** were synthesized following the asymmetric strategy described in Chapter 2 and reported for sensitizer **3.1**,[123] beginning with a Fischer indole condensation of the appropriate aryl-hydrazine and ketone and passing through a hydrazone intermediate.[124,125] For the synthesis of sensitizer **3.3**, the necessary ketone was first synthesized via deprotonation of ethyl acetoacetate and subsequent

substitution with bromobutane, which was then repeated (Scheme 3-1). A decarboxylation yielded 3-butylheptan-2-one for use in the Fischer-Indole condensation.

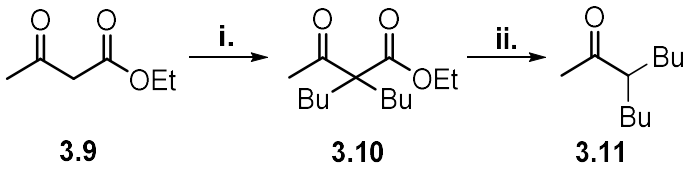

Scheme 3-1. Preparation of 3-butylheptan-2-one (**3.11**): **i.** a) 1,2-dimethoxyethane, 1 eq. *t*-BuOK, room temperature, 30 min. b)1 eq. 1-bromobutane, reflux, 24 h; c) 1 eq. *t*-BuOK in 1,2-dimethoxyethane, room temperature, 30 min; d)1 eq. 1-bromobutane, reflux, 72 h; 46%. **ii.** DMSO, 1.1 eq. LiCl, 1.1 eq. H_2O, 150 °C, 5 d.; 38%.

N-alkylation using iodoethane or iododododecane was performed to obtain the indolinium salt **3.14** (Scheme 3-2).[128] The 1-ethyl-5-mesityl-2,3,3-trimethyl-3*H*-indol-1-ium iodide **3.15** (Scheme 3-3) was synthesized by Iryna Davydenko following similar methods.[126]

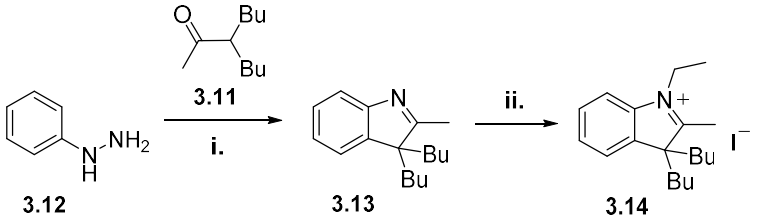

Scheme 3-2. Synthesis of indolinium salt for sensitizer **3.3**. **i**. **3.11**, acetic acid, 100 °C, 24 h, 29%. **ii**. iodoethane, acetonitrile, reflux, 11 h, 38%.

The obtained indolinium salts (compounds **3.14** and **3.15**) and the semi-squaric acid **2.28** described in section 2.2 were condensed to form the squaraines **3.16** and **3.17** under basic conditions using a Dean-Stark apparatus for water removal (Scheme 3-3).

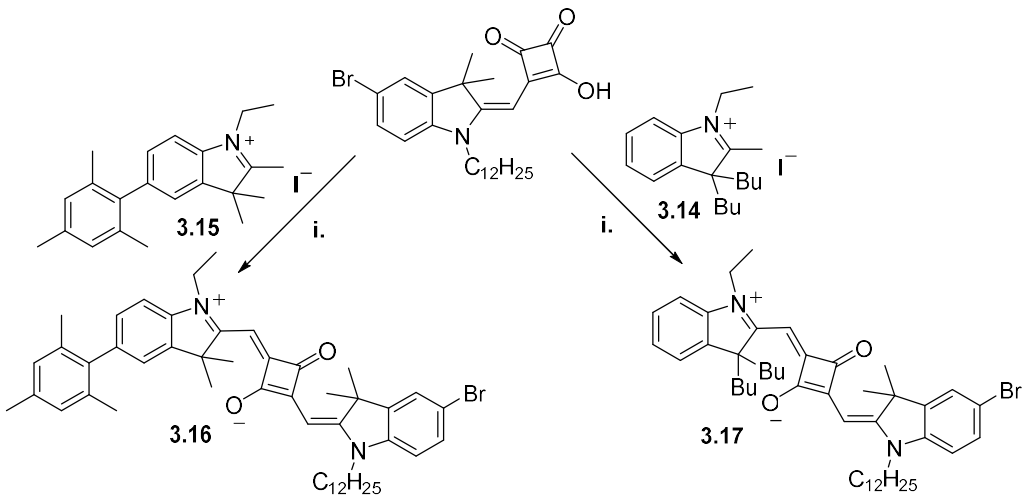

Scheme 3-3. Condensation to form full squaraine. **i.** *n*-butanol, toluene, Dean-Stark apparatus for water removal, 18 h, 46-60%.

For sensitizer **3.5**, as described in section 2.2, *N*-alkylation with iodoethane and condensation with semi-squaric acid **2.28** were performed starting from 1,1,2-trimethyl-1*H*-benzo[*e*]indole to yield compound **2.30** (Scheme 3-4). For sensitizer **3.8**, as described in section 2.2, a Suzuki coupling of 7-bromo-1,1,2-trimethyl-1*H*-benzo[*e*]indole to mesitylboronic acid formed 7-mesityl-1,1,2-trimethyl-1*H*-benzo[*e*]indole, followed by *N*-alkylation with iodoethane, then condensation with semi-squaric acid **2.28** to yield compound **2.31**.

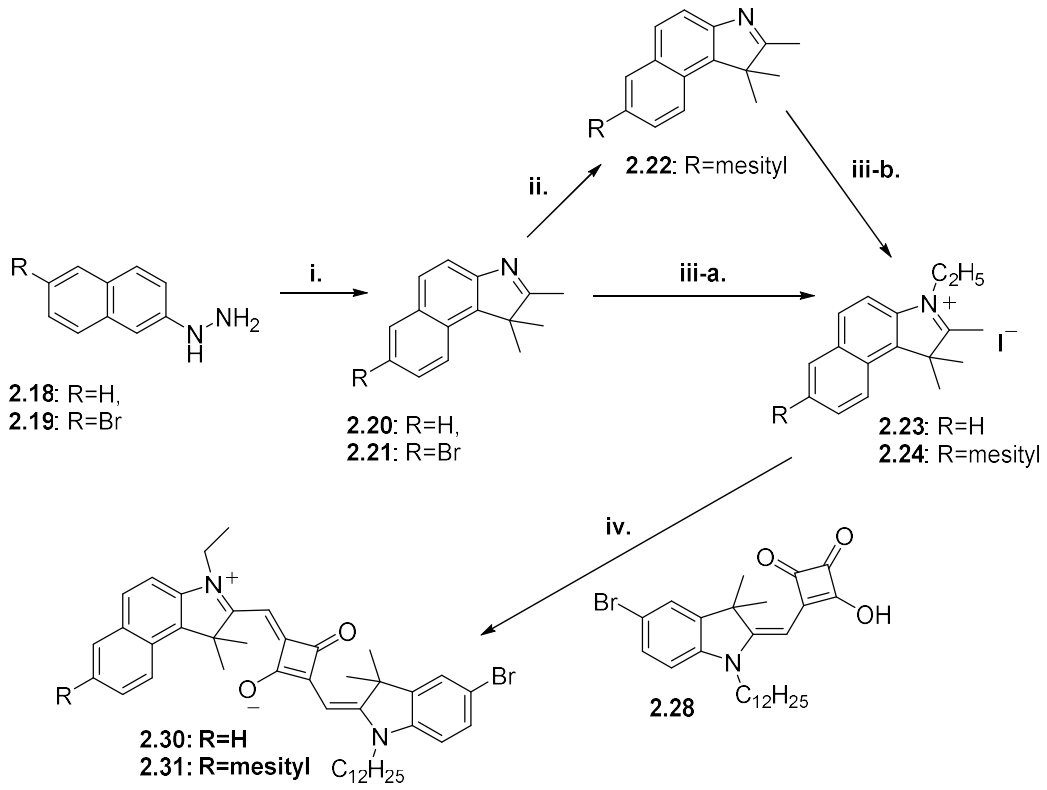

Scheme 3-4. Synthesis of indolinium salts and condensation to form squaraine. **i**. 3-methylbutan-2-one, acetic acid, 100 °C, 23 h, 75+%. **ii**. mesitylene-2-boronic acid, $Pd(PPh_3)_4$, potassium carbonate, toluene, MeOH, water, 85 °C, 26%. **iii**. a) iodoethane, acetonitrile, reflux, 6-7 d., 68%; b) iodoethane, microwave vial, 85 °C, overnight, 86%. **iv**. *n*-butanol, toluene, Dean-Stark apparatus for water removal, 18 h, 78-81%.

The synthesis of cyclopentadithiophene **3.18** with *gem*-di-*n*-hexyl substituents was accomplished according to literature procedures,[129–131] and a Vilsmeier-Haack reaction was performed to obtain compound **3.19** (Scheme 3-5). Cyclopentadithiophene **3.19** and compound **2.31** were then coupled under C-H activation cross-coupling reaction conditions described in section 2.2, with a yield of 68% for the desired compound **3.23**. 4,4-bis(2-ethylhexyl)-4*H*-silolo[3,2-*b*:4,5-*b'*]dithiophene (**3.20**) synthesized by Fadi Jradi[61] was coupled to squaraine **2.31** via Stille cross-coupling conditions. A Vilsmeier-

Haack reaction was performed to obtain compound **3.24**. The commercially available (5-formylthiophen-2-yl)boronic acid was coupled to squaraine **3.17** using Suzuki cross-coupling conditions. A Knoevenagel condensation of the aldehydes **3.21**, **3.22**, **3.23**, and **3.25** with cyanoacetic acid yielded the final sensitizers **3.2**, **3.3**, **3.5**, and **3.8**.

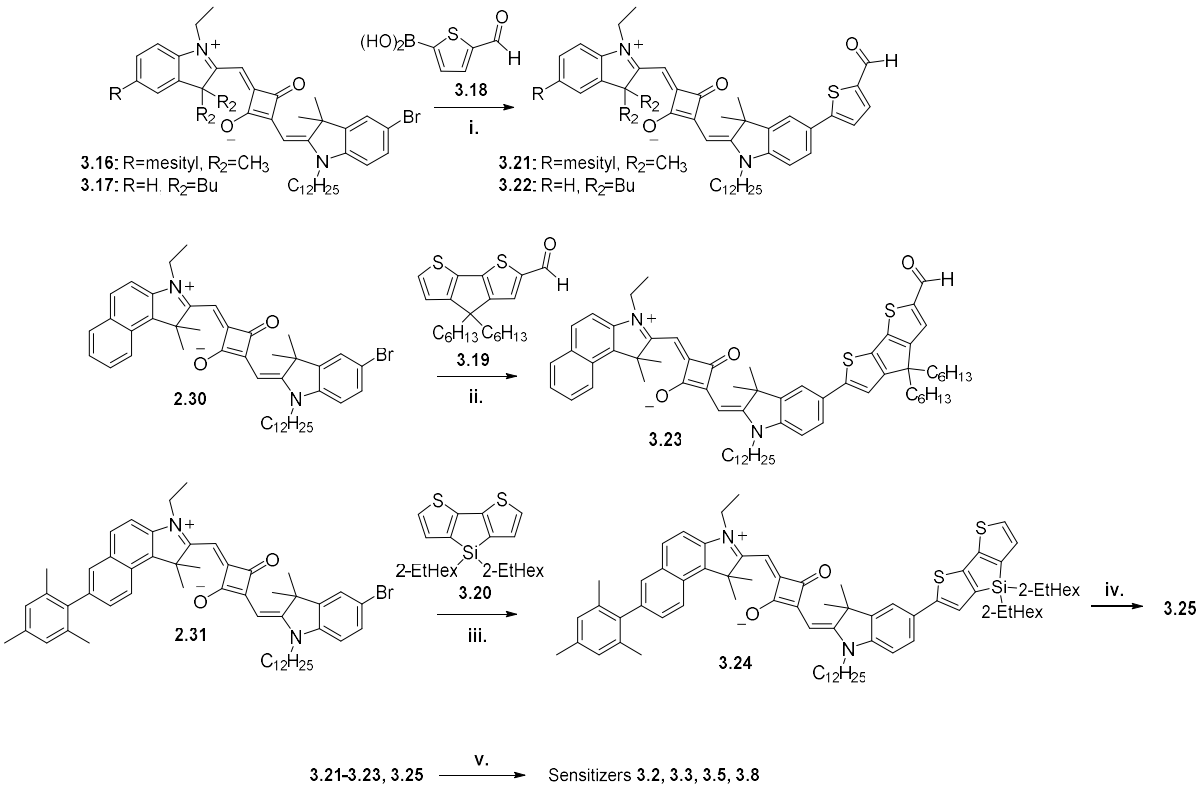

Scheme 3-5. Stille, Suzuki-Miyara, and C-H activation cross coupling reactions, followed by Knoevenegal condensations to yield the final sensitizers **3.2**, **3.3**, **3.5**, and **3.8**. **i**. $PdCl_2(dppf)\cdot CH_2Cl_2$, potassium carbonate, toluene, MeOH, 70 °C, microwave for 15 min, 67-85%. **ii**. palladium(II) acetate, $(t\text{-Bu})_2PMeHBF_4$, pivalic acid, potassium acetate, dimethylacetamide, 120 °C, 12 h, 68%. **iii**. $PdCl_2(PPh_3)_2$, toluene, 80 °C, overnight, 80%. **iv**. 1) dimethylformamide, $POCl_3$, 1,2-dichloroethane, 0 °C, 2 h. 2) **3.24**, 70 °C, 6 h. **v**. $(NH_4)_2CO_3$, cyanoacetic acid, propanoic acid, toluene, 100 °C, overnight, 32-62%.

3.3 Optical and Electrochemical Properties

The UV-Vis/NIR spectra in $CHCl_3$ showed absorption spectra with the range of maxima (670 to 699 nm) expected based on previously published squaraines (Table 3-1).[61,123,139] To obtain the oxidation potential of the adsorbed dye,[135,136] the squaraine dyes were adsorbed onto TiO_2 films without $TiCl_4$ pretreatment that were dipped for 4 h in a 0.05 mM dye solution in ethanol. Cyclic voltammetry was performed using the sensitized films in a solution of acetonitrile with a Ag/AgCl reference electrode calibrated to ferrocenium/ferrocene (0.63 V vs. NHE)[137] to yield the ground-state oxidation potential of the adsorbed dye. The ground-state oxidation potentials left at least 0.4 V of driving force for dye regeneration by the I_3^-/I^- redox couple (at ~0.35 V vs. NHE),[138] which for similar systems has been shown to be sufficient,[61,123,139] although as much as 0.5 V may be optimal depending on the sensitizer.[32]

Table 3-1. Optical and electrochemical properties of the squaraine sensitizers **3.1**-**3.8**.

Dyes	λ_{max} [nm][a)]	ε [10^5 $M^{-1}cm^{-1}$][a)]	$E_{0-0}{}^{opt}$ [eV][b)]	$E_{(S^+/S)}$ [V][c)]	$E_{(S^+/S^*)}$ [V][d)]
3.1	670	2.0	1.82	+0.80	−1.02
3.2	678	2.0	1.82	+0.84	−0.98
3.3	676	2.5	1.82	+0.83	−0.99
3.4	688	2.0	1.79	+0.82	−0.97
3.5	696	1.9	1.73	+0.80	−0.93
3.6	695	2.5	1.72	+0.79	−0.93
3.7	699	2.9	1.72	+0.78	−0.94
3.8	695	1.8	1.74	+0.79	−0.95

[a)] Measured in chloroform; [b)] Determined from the intersection of the normalized absorption and emission spectra in chloroform. [c)] Half-wave ground state oxidation potentials vs. NHE determined via cyclic voltammetry on TiO_2 films in a solution of 0.1 M lithium bistrifluoromethanesulfonimidate (LiTFSI) in MeCN. [d)] Excited state oxidation potentials calculated according to the following equation: $E_{(S^+/S^*)} = E_{(S^+/S)} - E_{0-0}$.

3.4 Absorption Spectra of Dyes Adsorbed on TiO_2 Films

The UV-vis absorption spectra for the dyes adsorbed on TiO_2 films are significantly broadened and include the appearance of a peak on the high-energy side of the main absorption, which has previously been ascribed to H-type aggregation on the TiO_2 surface for squaraine sensitizers.[113] As its origin may not necessarily be due to well-defined H-aggregates for this specific group of sensitizers, this peak will be referred to as the "aggregate" peak. In the presence of CDCA, the intensity of the absorption spectra for the sensitizers **3.1**-**3.8** adsorbed on TiO_2 films decreases significantly due to co-sensitization of CDCA with the squaraine sensitizers at the TiO_2 surface (Figure 3-10, Figure 3-12, Figure 3-14).

Absorption spectra on TiO_2 for sensitizers **3.1**-**3.3** with structures based on indoline donors and a thiophene π-bridge show a pronounced main absorption and blue-shifted aggregate peak (Figure 3-9, Figure 3-10). Sensitizer **3.2** employs a terminal mesityl group (region I), whereas sensitizer **3.3** employs *gem*-dibutyl substitution on the indole (region II), and sensitizer **3.1** is used as a control. Without the presence of CDCA, sensitizer **3.2**, which employs a mesityl group on the far end of the squaraine, showed a reduced aggregate peak compared to sensitzer **3.1**. However, in the presence of CDCA, both sensitizers **3.1** and **3.2** had reduced aggregate peaks. The film spectrum of sensitizer **3.3** without CDCA in the dipping solution has the smallest aggregate peak of the series of squaraines without CDCA. This points to the effectiveness of employing out-of-plane alkyl chains in region II as a strategy for reducing aggregation.

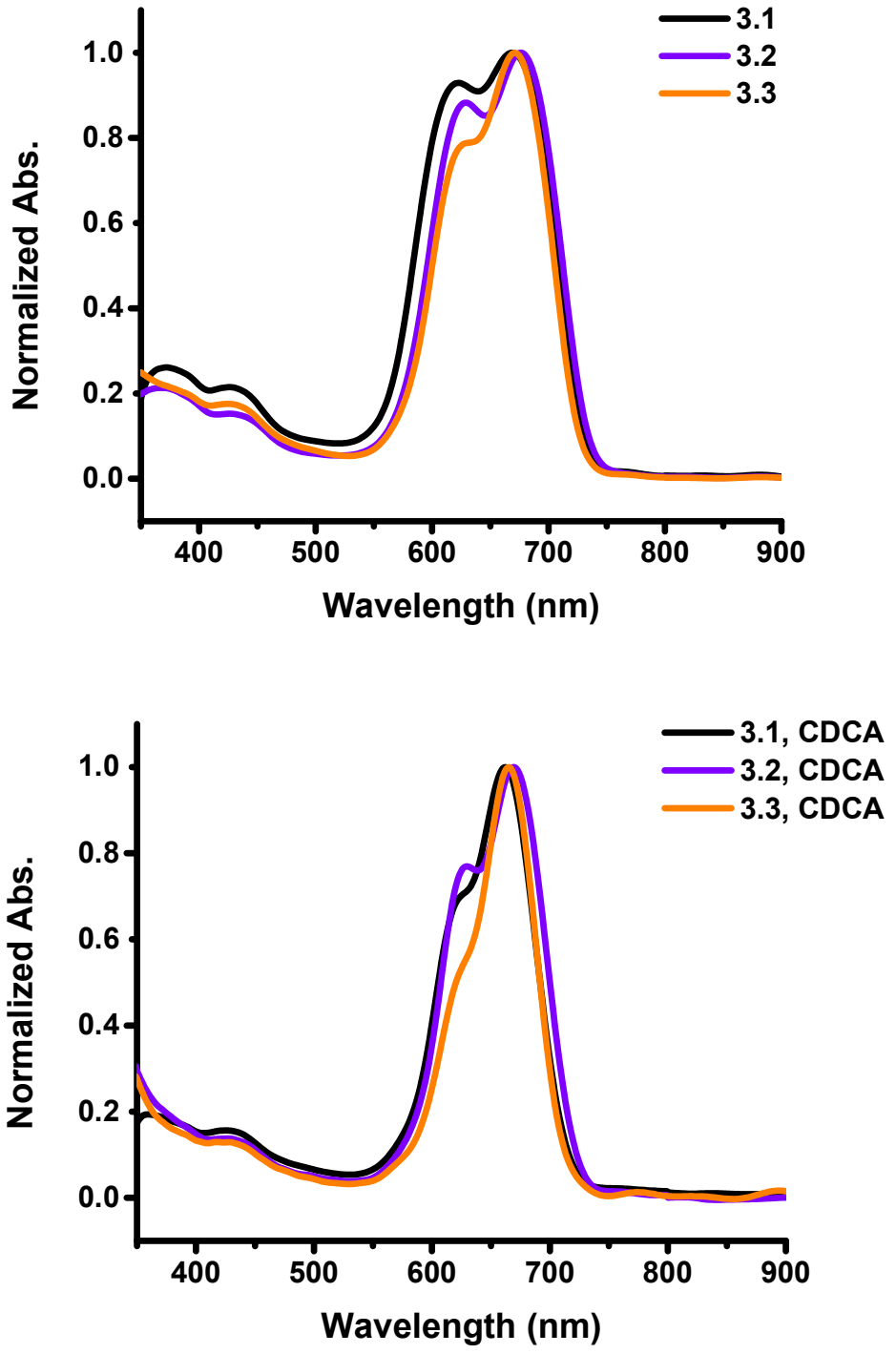

Figure 3-9. Normalized absorption spectra of sensitizers **3.1**-**3.3** adsorbed on TiO_2 films without (top) and with (bottom) 20 mM CDCA.

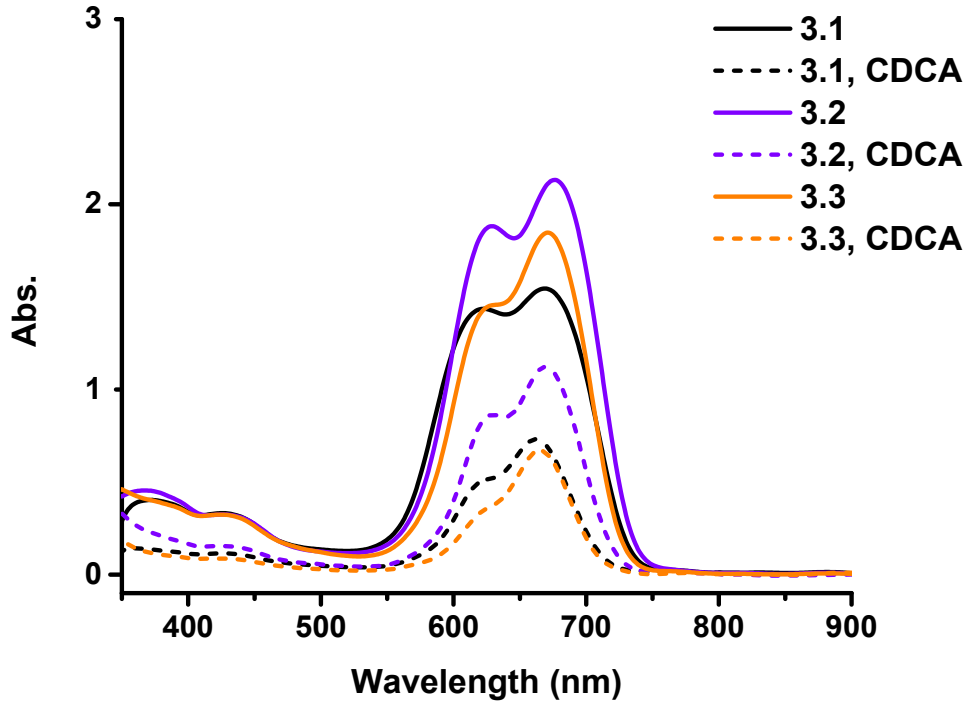

Figure 3-10. Absorption spectra of sensitizers **3.1**-**3.3** adsorbed on TiO_2 films.

Sensitizers **3.4**-**3.6** have structures based on benzo[*e*]indoline donors with various π-bridges (region III) that modulate their absorption spectra on TiO_2 (Figure 3-11, Figure 3-12). Sensitizer **3.4** employs a thiophene, and acts as a comparison to sensitizers **3.5** and **3.6**. Sensitizer **3.5** employs CPDT with *gem*-di-*n*-hexyl substituents, while sensitizer **3.6** employs CPDT with *gem*-di-2-ethylhexyl substituents. Sensitizers **3.5** and **3.6** show the presence of a high-energy visible absorption band at ~450 nm from the CPDT, as seen previously by Delcamp *et al.*[139] Without CDCA, sensitizer **3.6** with branched alkyl chains exhibits a more pronounced aggregate peak than the sensitizer **3.5** with linear alkyl chains on the CPDT, while in the presence of CDCA, the opposite is seen. Sensitizer **3.4**

incorporates a benzo[*e*]indole in region I of the squaraine and a thiophene π-bridge (region III). Without CDCA, sensitizer **3.4** displays a pronounced aggregate peak compared to that of the indoline sensitizer **3.1** seen previously, presumably due to the additional aromatic ring on sensitizer **3.4** which may favor aggregation. Without CDCA, the aggregate peak is most pronounced for sensitizer **3.6**, suggesting that the 2-ethylhexyl-substituted CPDT may actually promote aggregate formation on the TiO_2 surface in the absence of CDCA.

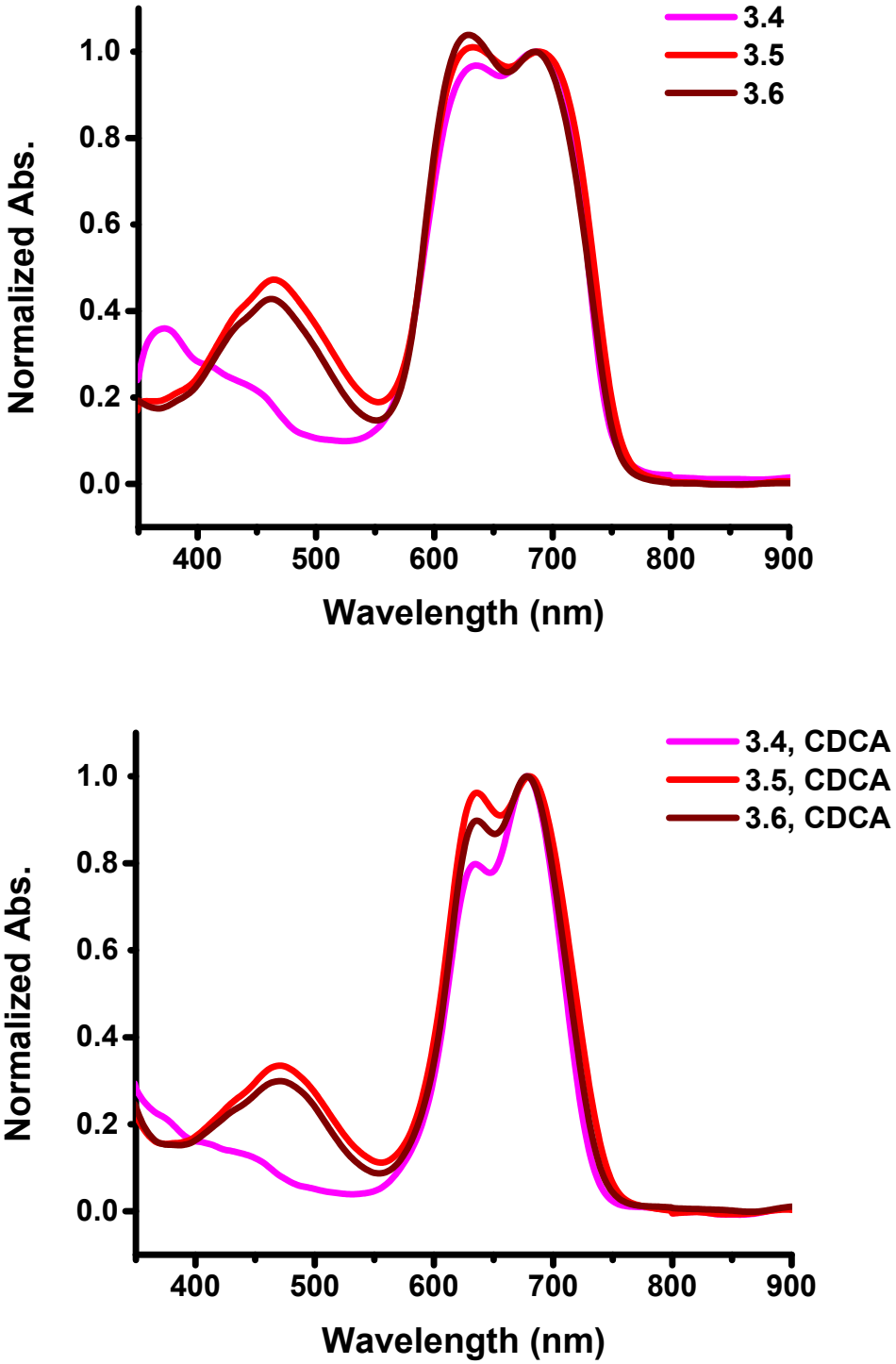

Figure 3-11. Normalized absorption spectra of sensitizers **3.4**-**3.6** adsorbed on TiO_2 films without (top) and with (bottom) 20 mM CDCA.

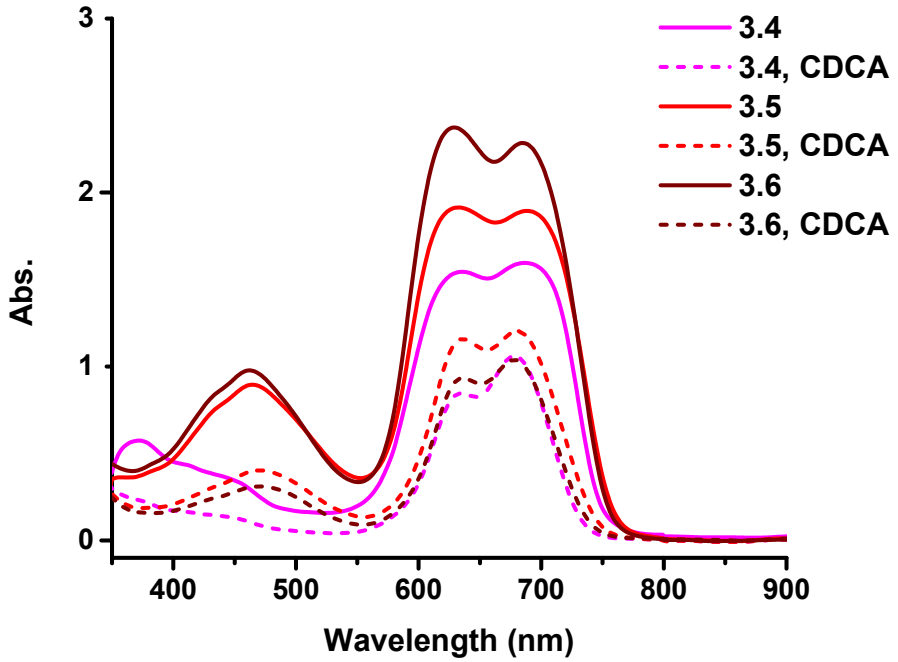

Figure 3-12. Absorption spectra of sensitizers **3.4**-**3.6** adsorbed on TiO_2 films.

The structures of sensitizers **3.6**-**3.8** are based on benzo[*e*]indoline donors, mesityl end groups, and *gem*-di-2-ethylhexyl CPDT or DTS π-bridges. Sensitizers **3.6** and **3.7** have *gem*-di-2-ethylhexyl CPDT π-bridges (region III), while sensitizer **3.6** has no terminal mesityl group (region I) and sensitizer **3.7** does. Sensitizers **3.7** and **3.8** both employ a terminal mesityl group (region I), while sensitizer **3.7** includes a *gem*-di-2-ethylhexyl CPDT π-bridge (region III) and sensitizer **3.8** has a *gem*-di-2-ethylhexyl DTS π-bridge. Interestingly, without CDCA, the DTS-bridged sensitizer **3.8** shows a decrease in the overall absorption intensity compared to CPDT-bridged sensitzers **3.6** and **3.7** (Figure 3-13, Figure 3-14). Sensitizer **3.8** also shows a lower aggregate peak ratio relative to sensitizers **3.6** and **3.7**. There is only a slight difference between the ratios of aggregate

to main absorption peaks for the sensitizer **3.6** without a mesityl group and the sensitizer **3.7** with the mesityl group, with both displaying similar absorption intensity and significant aggregate peak absorption. This indicates that in the presence of a *gem*-di-2-ethylhexyl CPDT π-bridge, the mesityl group is not as effective at preventing aggregate formation.

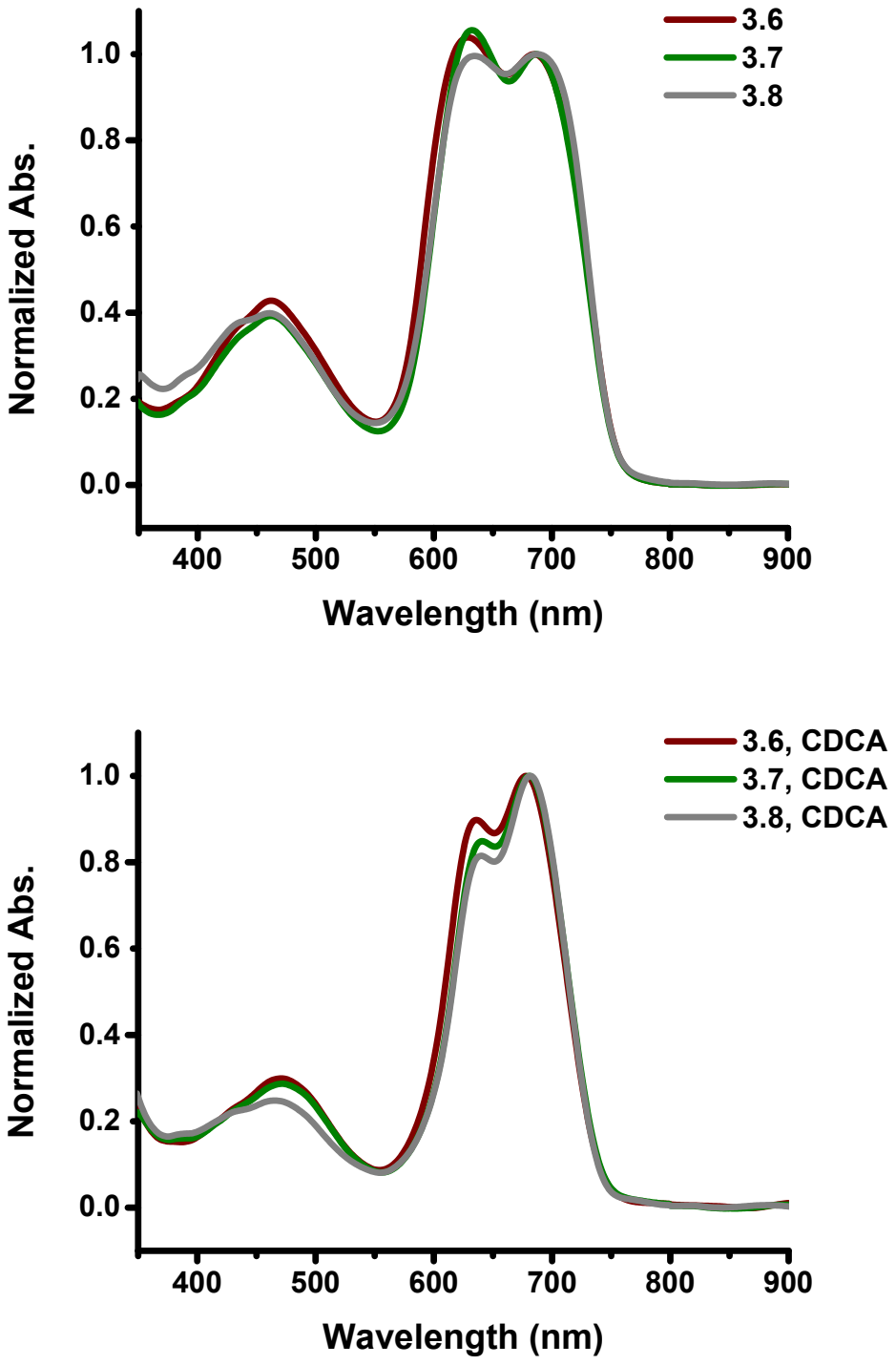

Figure 3-13. Normalized absorption spectra of sensitizers **3.6**-**3.8** adsorbed on TiO_2 films without (top) and with (bottom) 20 mM CDCA.

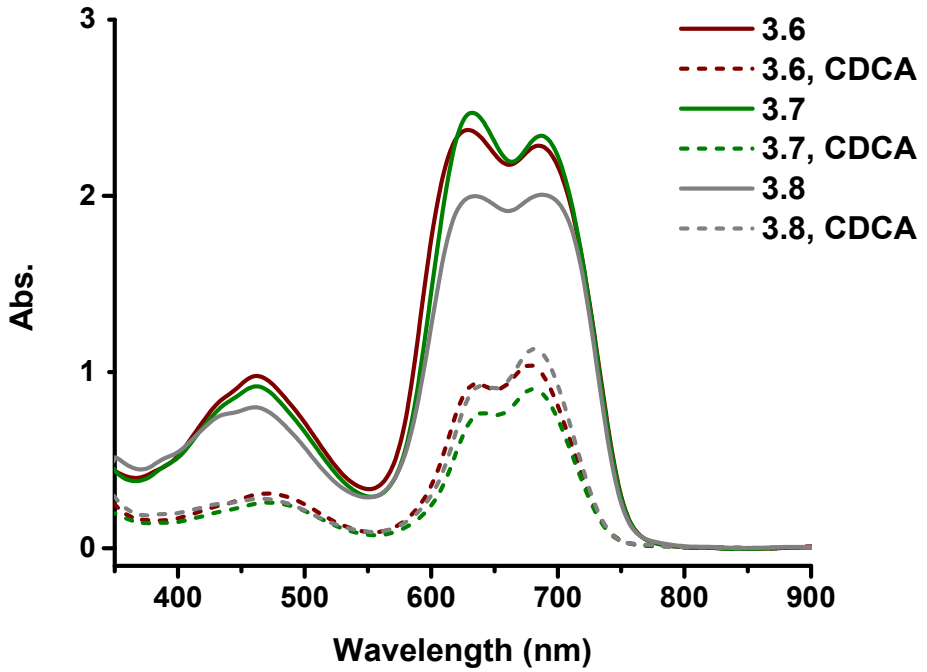

Figure 3-14. Absorption spectra of sensitizers **3.6**-**3.8** adsorbed on TiO_2 films.

3.5 Computational Investigation

To attempt to gain further insight into the effect of substituting Si for C in the π-bridge, the differences in bond angles and electron density distribution between sensitizers **3.7** and **3.8** are investigated using density functional theory calculations. The ground-state electronic structure was examined after optimization at the m06-2X/6-31G(d) level, with little to no differences seen in the molecular orbitals of sensitizers **3.7** and **3.8** (Table 3-2).

Table 3-2. Molecular orbitals for sensitizers **3.7** and **3.8**.

MO	Sensitizer 3.7	Sensitizer 3.8
LUMO	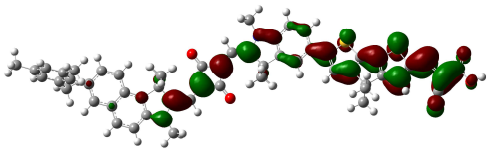	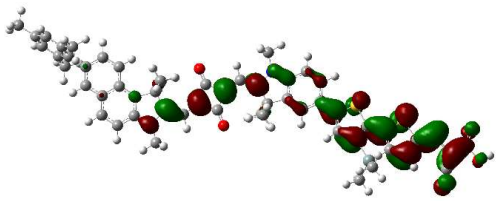
HOMO	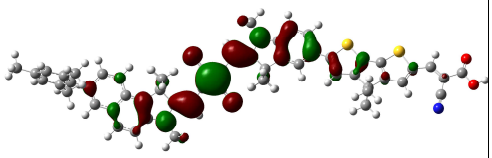	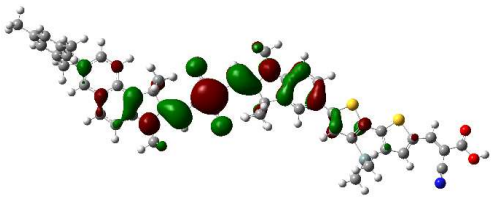

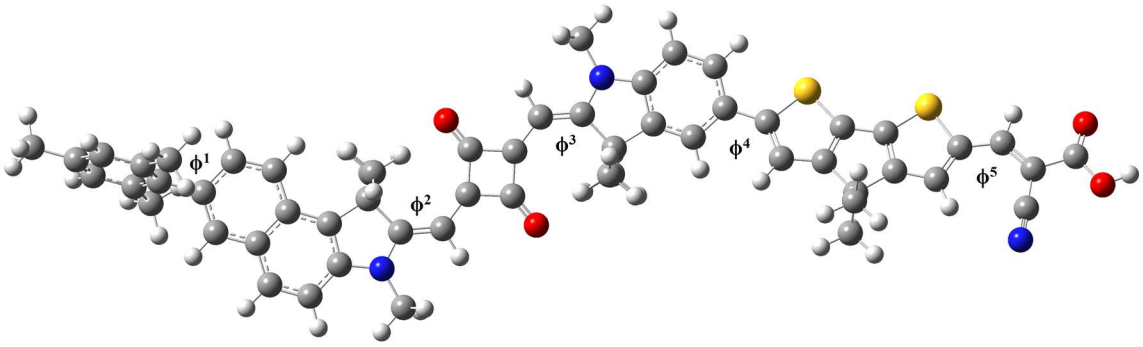

Figure 3-15. Dihedral angles of interest.

Table 3-3. Dihedral angles (°) for sensitizers **3.7** and **3.8** for ground state structures optimized in ethanol at the m06-2X/6-31G(d) level.

Sensitizer	**ϕ^1**	**ϕ^2**	**ϕ^3**	**ϕ^4**	**ϕ^5**
3.7	72.89	0.87	0.34	24.79	0.32
3.8	72.60	0.62	0.48	25.72	0.22

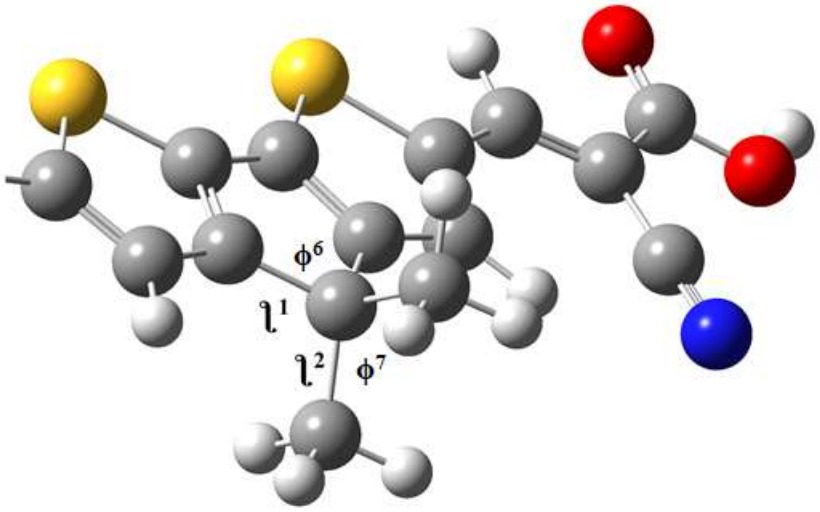

Figure 3-16. Bond lengths and angles of interest indicated on CPDT.

Table 3-4. Bond lengths and angles near the Si/C of interest for sensitizers **3.7** and **3.8** for ground state structures optimized in ethanol at the m06-2X/6-31G(d) level.

Sensitizer	**ɭ¹ (Å)**	**ɭ² (Å)**	**ϕ⁶ (°)**	**ϕ⁷ (°)**
3.7	1.52	1.54	110.57	100.10
3.8	1.89	1.87	112.20	90.62

Although the dihedral angles along the squaraine core (Figure 3-15) do not show differences in dihedral angles of more than 0.3° (Table 3-3) between sensitizers **3.7** and **3.8**, the difference between bond angles near the gem-di-2-ethylhexyl-substituents is 1.6 Å for angle **ϕ⁶** and 9.5 Å for angle **ϕ⁷** (Table 3-4), with sensitizer **3.7** exhibiting the larger

angle between 2-ethylhexyl substituents. These differences between sensitizers **3.7** and **3.8** are slight, but could change how the sensitizers aggregate and may result in noticeable changes in device performance.

3.6 Photovoltaic Characterization

Table 3-5. Photovoltaic performance of the squaraine-based DSSCs under uniform conditions. [a,b,c,d]

	V_{OC} [mV]	J_{SC} [mA/cm^2]	FF [%]	PCE [%]
3.1	643 ± 5	10.81 ± 0.25	64.1 ± 5.0	4.46 ± 0.48
3.2	669 ± 4	12.43 ± 0.47	72.6 ± 1.1	6.03 ± 0.17
3.3	667 ± 6	13.81 ± 0.12	72.9 ± 0.5	6.71 ± 0.07
3.4	667 ± 6	11.58 ± 0.01	71.5 ± 0.5	5.52 ± 0.01
3.5	616 ± 2	14.40 ± 0.07	69.9 ± 0.6	6.19 ± 0.11
3.6	658 ± 5	13.43 ± 0.34	70.3 ± 3.7	6.22 ± 0.40
3.7	658 ± 6	13.50 ± 0.13	71.9 ± 0.8	6.38 ± 0.20
3.8	666 ± 1	12.45 ± 0.25	72.4 ± 0.3	6.00 ± 0.16

[a]Based on measurements of 2-4 devices for all dyes with the standard deviation shown. [b]The photovoltaic measurements were conducted using a mask to restrict the cell active area to 0.16 cm^2. The dye solutions were 0.05 mM dye and 20 mM CDCA in ethanol with a dipping time of 4 h, and assembled under conditions described in section 0. [c]YR6 was also tested at optimal literature conditions with 10 mM CDCA to yield the following: V_{OC}=0.65 ± 0.01 mV, J_{SC}=11.3 ± 0.2 mA/cm^2, FF=68 ± 1 %, PCE=5.02 ± 0.1 %. [d]A table of *J-V* results for films prepared without CDCA is included in Appendix A.

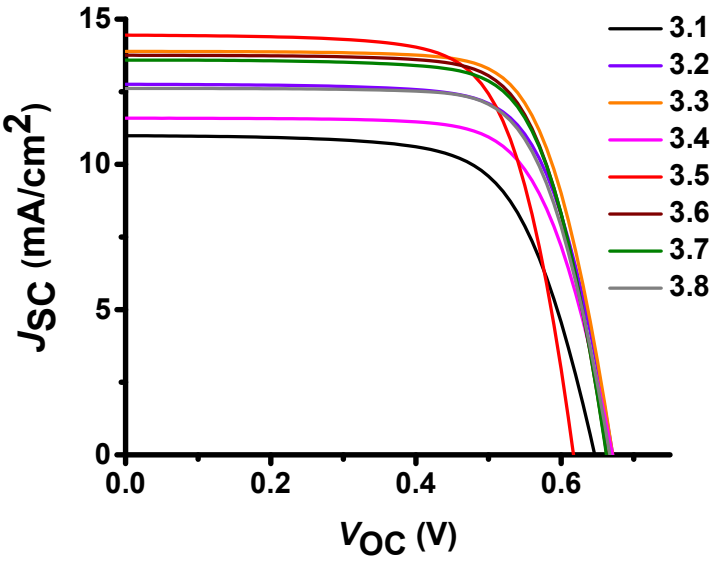

Figure 3-17. *J-V* curves with maximum PCE for sensitizers **3.1**-**3.8**.

Examining photovoltaic performance across the series **3.1**-**3.3** with structures based on indoline donors and a thiophene π-bridge (Table 3-5, Figure 3-17), the effects of a terminal mesityl group (region I, sensitizer **3.2**) and of *gem*-dibutyl substitution on the indole (region II, sensitizer **3.3**) can be elucidated when compared to the unsubstituted sensitizer **3.1**. For the mesityl-substituted sensitizer **3.2**, an increase of over 1.5 mA/cm^2 in J_{SC} and 20 mV in V_{OC} relative to sensitizer **3.1** is seen. Sensitizer **3.3** incorporating a dibutyl-substituted indole gives a similar increase in voltage as sensitizer **3.2**, but with a larger increase in J J_{SC} of 2.0 mA/cm^2 relative to sensitizer **3.1**. This increase in J_{SC} suggests that, in this case, incorporating out-of-plane alkyl chains in region II is more effective at preventing losses in current than incorporating out-of-plane alkyl chains in the terminal region I.

Across the series **3.4**-**3.6**, a benzo[e]indole-substituted squaraine incorporates either a thiophene (**3.4**), CPDT with *gem*-di-*n*-hexyl substituents (**3.5**), or CPDT with *gem*-di-2-ethylhexyl substituents (**3.6**). Both CPDT-substituted sensitizers **3.5** and **3.6** exhibit an increase in J_{SC}. For sensitizer **3.5**, with *gem*-di-*n*-hexyl-substituted CPDT, a relatively large increase of 2.8 mA/cm^2 in the J_{SC} is seen, but is accompanied by a decrease of over 50 mV in the V_{OC} relative to the thiophene-substituted sensitizer **3.4**. For sensitizer **3.6**, with *gem*-di-2-ethylhexyl-substituted CPDT, J_{SC} increases by 1.9 mA/cm^2 while maintaining a similar V_{OC} (9 mV decrease) to that of the thiophene-substituted sensitizer **3.4**.

Examining photovoltaic performance across the series **3.6**-**3.8** with structures based on benzo[e]indoline donors, the effect of a terminal mesityl group (region I) when employed with a *gem*-di-2-ethylhexyl CPDT (region III, sensitizer **3.7**) or *gem*-di-2-ethylhexyl DTS π-bridge (region III, sensitizer **3.8**) can be seen. The incorporation of the mesityl group on the end of sensitizer **3.7** gave a nearly identical J_{SC} and V_{OC} compared to sensitizer **3.6** without the mesityl group, with a slight increase in the FF. This is consistent with the absorption on TiO_2, where very similar ratios of aggregate to main absorption peaks were seen for the sensitizers **3.6** and **3.7**. This contrasts with the marked differences in absorption on TiO_2 and *J*-*V* results seen between sensitizer **3.1** without a mesityl group and sensitizer **3.2** with a mesityl group. For sensitizer **3.8** employing a mesityl group and a dithienosilole group, the J_{SC} decreased by over 1 mA/cm^2 relative to sensitizer **3.7**, with a similar but slightly increased (8 mV) V_{OC} seen.

3.6.1 IPCE

Comparing sensitizers **3.1**-**3.3** (Figure 3-18), sensitizer **3.2**, incorporating the mesityl moiety on the end of the squaraine, and sensitizer **3.3**, incorporating a dibutyl-substituted indole, had increased IPCE relative to the control sensitizer **3.1**. Sensitizers **3.2** and **3.3** also exhibited less of a decrease in IPCE near 550 nm than seen for sensitizer **3.1**, though the absorption when adsorbed onto TiO_2 was similar in this region. Despite the stronger absorption of sensitizer **3.2** when adsorbed onto TiO_2, the IPCE of sensitizer **3.2** was lower than that of sensitizer **3.3**. This is consistent with the decreased H-aggregate absorption seen for sensitizer **3.3**, since the H-aggregate in squaraines has been shown to have decreased electron-injection efficiency. The maximum IPCE of sensitizer **3.3** reached around 63%, which is a promising improvement over that of sensitizer **3.1**.

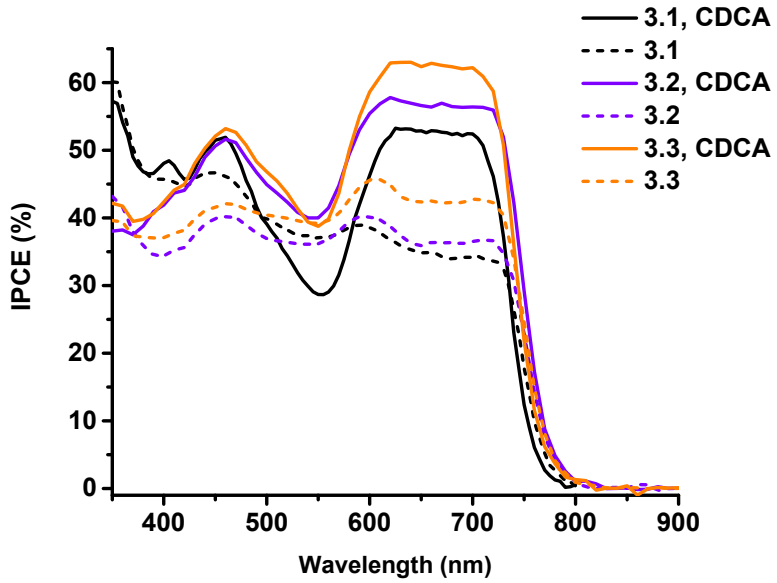

Figure 3-18. IPCE spectra of sensitizers **3.1**, **3.2**, and **3.3**.

The incorporation of CPDT in sensitizers **3.5** and **3.6** versus thiophene in sensitizer **3.4** increases the IPCE from near 40% to near 50% in the region from 350 to 600 nm (Figure 3-19). However, at the absorption maximum, sensitizer **3.4** has an IPCE of 63%, compared to the IPCE near 55% for sensitizers **3.5** and **3.6**. Sensitizer **3.5**, with linear hexyl chains, exhibits a lower IPCE in the high-energy visible region of the spectrum relative to sensitizer **3.6** and an increased IPCE in the low-energy region from 600-750 nm relative to sensitizer **3.6**. Sensitizer **3.6**, with branched 2-ethylhexyl chains, is the opposite, with a higher IPCE in the high-energy visible region of the spectrum and a decreased IPCE in the low-energy region from 600-750 nm. It is interesting that a branched chain on the π-bridge increases the IPCE slightly in the high-energy visible region of the spectrum, when no corresponding change in absorption intensity on TiO_2 was seen between sensitizers **3.5** and **3.6**.

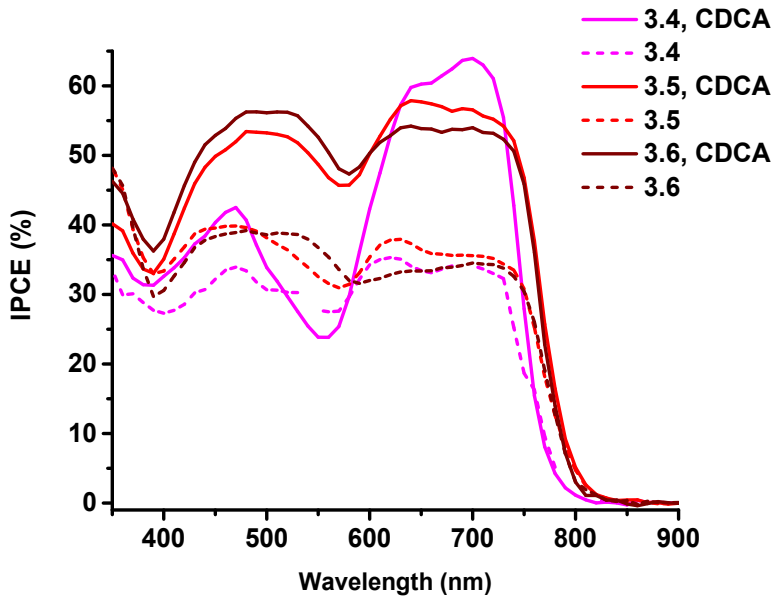

Figure 3-19. IPCE spectra of sensitizers **3.4**, **3.5**, and **3.6**.

The incorporation of the mesityl group on the end of sensitizer **3.7** increased the IPCE in the region from 600-750 nm to near 60% (Figure 3-20), an increase of around 5% relative to sensitizer **3.6** without the mesityl group, consistent with the mesityl group disrupting squaraine-squaraine interactions. However, for sensitizer **3.8**, employing a mesityl group and a DTS group, at the absorption maximum the IPCE is lower from 450-750 nm than that of sensitizer **3.7** with a mesityl group and CPDT. The DTS-subsititued sensitizer **3.8** appeared to decrease the ratio of H-aggregate peak to main absorption peak in the absorption spectrum of the dye on the TiO_2 film when compared to the CPDT-substituted sensitizer **3.7**, however, this decrease in the aggregate peak does not correspond to an increased IPCE. This decrease in current may be due to a difference in how the two π-bridges aggregate based on a difference in bond angles for the out-of-plane substituents (section 0).

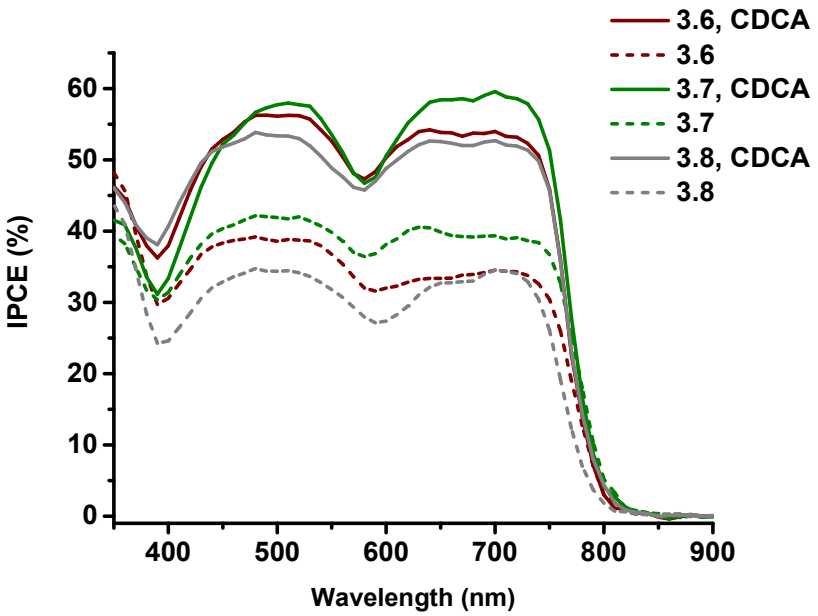

Figure 3-20. IPCE spectra of sensitizers **3.6**, **3.7**, and **3.8**.

3.7 Photoelectrochemical Characterization

3.7.1 Electron (charge) transport lifetime

Electron transport measurements describe how photoinduced excess charge moves in a concentration gradient; essentially how charges move through the TiO_2. The electron transport lifetime for sensitizers **3.1**-**3.8** exhibited a fairly tight distribution of curves (Figure 3-21), with a slight increase in electron transport on average with the use of CDCA. Sensitizer **3.5** exhibited lower electron transport than the bulk of the other squaraine sensitizers. This is could indicate that surface traps are facilitated by the binding of sensitizer **3.5**, which could be consistent with the low V_{OC} (section 3.6) and increased TiO_2-electrolyte recombination (section 3.7.3) observed for sensitizer **3.5**.

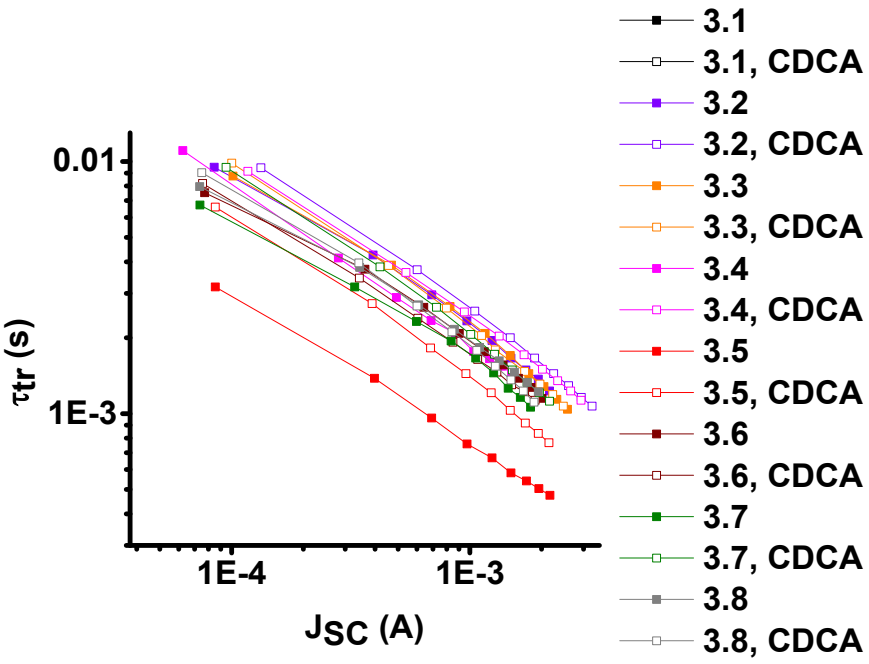

Figure 3-21. Charge transport lifetime versus short circuit current for sensitizers **3.1**-**3.8**.

3.7.2 Charge extraction measurements

Charge extraction measurements can provide an understanding of the relative shifts in the TiO_2 conduction band for different sensitizers or amounts of coadsorbent. In the presence of CDCA, the charge extraction of all sensitizers is within a similar range (Figure 3-22). Without CDCA, the sensitizers **3.1**, **3.2**, and **3.3**, which all employ thiophene, show a slight increase in charge extraction relative to sensitizers **3.4**-**3.8**, which employ CPDT or DTS. One could imagine that the shorter and less bulky thiophene could promote an angle of binding to the surface that shifts the Fermi level energy.

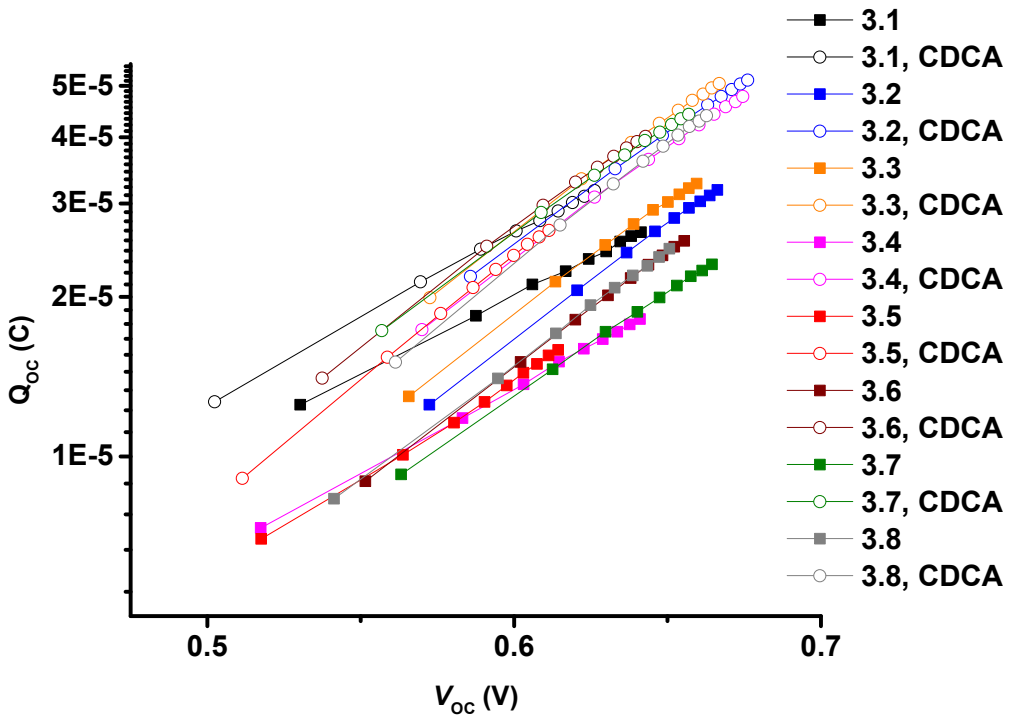

Figure 3-22. Charge extraction vs. voltage at open circuit for sensitizers **3.1**-**3.8**.

3.7.3 Electron lifetime

Electron lifetime (τ_n) was obtained using small-modulation techniques under constant current conditions that allow photogenerated electrons to recombine with acceptors in the electrolyte rather than extracting the electrons at the counter electrode. Under these conditions, the response time of the photovoltage is nearly equal to the electron lifetime. Electron lifetime measurements can provide an understanding of the relative amounts of recombination that may decrease the electron lifetime. To focus on differences in electron recombination, shifts in the TiO_2 conduction band position are accounted for using the change in V_{OC} from charge extraction measurements, providing the adjusted plots (Figure 3-23).

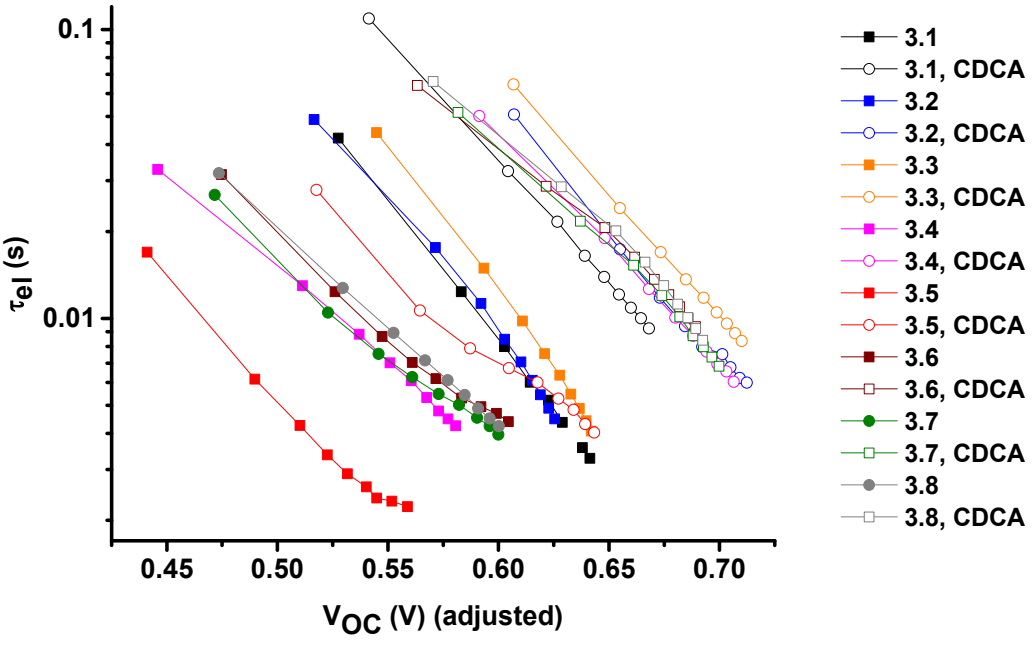

Figure 3-23. Electron lifetime vs. open circuit voltage for sensitizers **3.1**-**3.8**.

In the presence of CDCA, the electron lifetime increases for each sensitizer. Without CDCA, sensitizers **3.4**, **3.6**, **3.7**, and **3.8** have similar electron lifetimes, while sensitizer **3.5** has a lower electron lifetime than this group, indicating that recombination may play a role in the lower V_{OC} observed for sensitizer **3.5** in *J-V* measurements. Sensitizers **3.1**, **3.2**, and **3.3** which employ a thiophene π-bridge have higher electron lifetimes than sensitizers **3.4**-**3.8**. Sensitizer **3.3** that employs a dibutyl-substituted indole and thiophene π-bridge exhibits the highest electron lifetime. The out-of-plane substituents above and below the squaraine core in sensitizer **3.3** may aid in decreasing either electrolyte-dye or dye-dye recombination.

3.8 Conclusion

This work developed squaraine sensitizers with out-of-plane alkyl chains for preventing dye-dye aggregation and decreased electron injection in dye-sensitized solar cells. On sensitizers **3.1**-**3.8**, alkyl chains were placed in regions I, II, and III (Figure 3-7) on the squaraine end, center, and π-bridge. Linear vs. branched alkyl chains were examined, along with a comparison of CPDT and DTS π-bridges. When comparing the mesityl group attached to the end indole (region I) vs. the unsubstituted indole (sensitizer **3.2** vs **3.1**), the ratio of the aggregate peak absorbance to the monomer peak absorbance when adsorbed on TiO_2 was roughly similar between the sensitizers, with a slight increase in the aggregate peak for the mesityl-substituted sensitizer **3.2** compared to sensitizer **3.1** when coadsorbed with CDCA. In devices, the mesityl-substituted sensitizer **3.2** demonstrated improved V_{OC}, J_{SC}, and FF, for a PCE of 6.0% for sensitizer **3.2**

compared to a PCE of 4.5% for sensitizer **3.1**. The electron lifetime was also slightly higher than for sensitizer **3.1**, indicating lower TiO_2-electrolyte recombination for sensitizer **3.2**.

Comparing the *gem*-*n*-butyl group on the end indole (region II) vs. the standard *gem*-methyl indole (sensitizer **3.3** vs **3.1**), the ratio of the aggregate peak absorbance to the monomer peak absorbance when adsorbed on TiO_2 was decreased for the dibutyl-substituted sensitizer **3.3**, with a significant decrease in the aggregate peak for sensitizer **3.3** when coadsorbed with CDCA. The absorption on the film when coadsorbed with CDCA resembled the solution absorption, and indicated that substitution at this position (region II) decreased aggregation dramatically. Sensitizer **3.3** exhibited the highest device performance with improved V_{OC}, J_{SC}, and FF for an overall PCE of 6.71%. Additionally, the highest electron lifetime was seen for sensitizer **3.3**, indicating that the *gem*-*n*-butyl substitution on the indole was the most effective substitution for preventing TiO_2-electrolyte recombination.

With a benzo[e]indole end group, CPDT π-bridges with linear and branched alkyl chains on sensitizers **3.5** and **3.6**, respectively, were compared to each other and to a thiophene π-bridge (sensitizer **3.4**). The thiophene-substituted sensitizer **3.4** exhibited a lower aggregate peak than either CPDT-substituted sensitizer, with the linear chain *gem*-*n*-hexyl-substituted sensitizer **3.5** having the highest ratio of the aggregate peak absorbance to the monomer peak absorbance when coadsorbed with CDCA. For *J*-*V* measurements, the linear chain-substituted sensitizer **3.5** exhibited the highest J_{SC} of the series of sensitizers, but with a low V_{OC} and slightly lower FF for a PCE of 6.2%. The branched chain *gem*-2-ethylhexyl-substituted sensitizer **3.6** had a slightly higher V_{OC} and

slightly lower J_{SC} compared to sensitizer **3.5** for an identical PCE of 6.2%. Electron lifetime measurements showed a very low electron lifetime for sensitizer **3.5**, clarifying the significant role of TiO_2-electrolyte recombination in the decreased V_{OC} observed for this sensitizer, while sensitizer **3.6** demonstrated an average electron lifetime similar to that of sensitizer **3.4** employing a thiophene π-bridge.

The influence of the mesityl group when employed with a bulky *gem*-2-ethylhexyl CPDT π-bridge was then examined. The mesityl-substituted sensitizer **3.7** decreased the ratio of the aggregate peak absorbance to the monomer peak absorbance when coadsorbed with CDCA relative to sensitizer **3.6** without the mesityl. Devices for sensitizer **3.7** produced a similar, but very slightly higher J_{SC} and FF than that of sensitizer **3.6** for a PCE of 6.4% for sensitizer **3.7**. The mesityl- and CPDT-substituted sensitizer **3.7** was also compared to the mesityl- and DTS-substitued sensitizer **3.8**. The DTS-substituted sensitizer **3.8** exhibited a very similar but slightly decreased aggregate peak compared to sensitizer **3.7**. DTS-substituted sensitizer **3.8** demonstrated a slightly higher V_{OC} and slightly lower J_{SC} compared to CPDT-substituted sensitizer **3.7** for an overall lower PCE of 6.0% for sensitizer **3.8**. The electron lifetime for sensitizers **3.7** and **3.8** were similar, with a very slight increase for sensitizer **3.8** consistent with the slightly higher V_{OC}. The origin of the lower J_{SC} for the DTS-substituted sensitizer **3.8** is unclear.

An interesting picture of how out-of-plane substituents affect aggregation has emerged from this series of squaraine dyes. Out-of-plane substituents on different regions of the squaraine structure can have very different effects on device performance and photoelectrochemical characterization. It is clear that the whole is not the sum of its parts; for example, a terminal mesityl will have a different magnitude of effect depending on

whether a bulky π-bridge is also present. Interestingly, sensitizers **3.2**-**3.3** with out-of-plane groups in the terminal regions I and II and without out-of-plane groups in region III on the π-bridge exhibited the highest electron lifetimes. As noted previously, sensitizer **3.3** exhibited the highest device performance with a V_{OC} of 667 mV, a J_{SC} of 13.81 mA/cm2, an *FF* of 72.9, and an overall PCE of 6.71%. The chapter results indicate that it is necessary to design out-of-plane groups in regions I-III not only for decreased dye aggregation, but also for how the presence of the out-of-plane group may affect the ability of the electrolyte to reach the TiO_2 surface. An ideal out-of-plane group would prevent close interaction of the squaraine sensitizers, while still allowing for the squaraines to bind to the surface in a way that covers the surface and prevents TiO_2-electrolyte recombination. Building directly upon this work, a future study could examine the effect of equally bulky out-of-plane groups employed simultaneously in regions I-III on the squaraine end, center, and π-bridge.

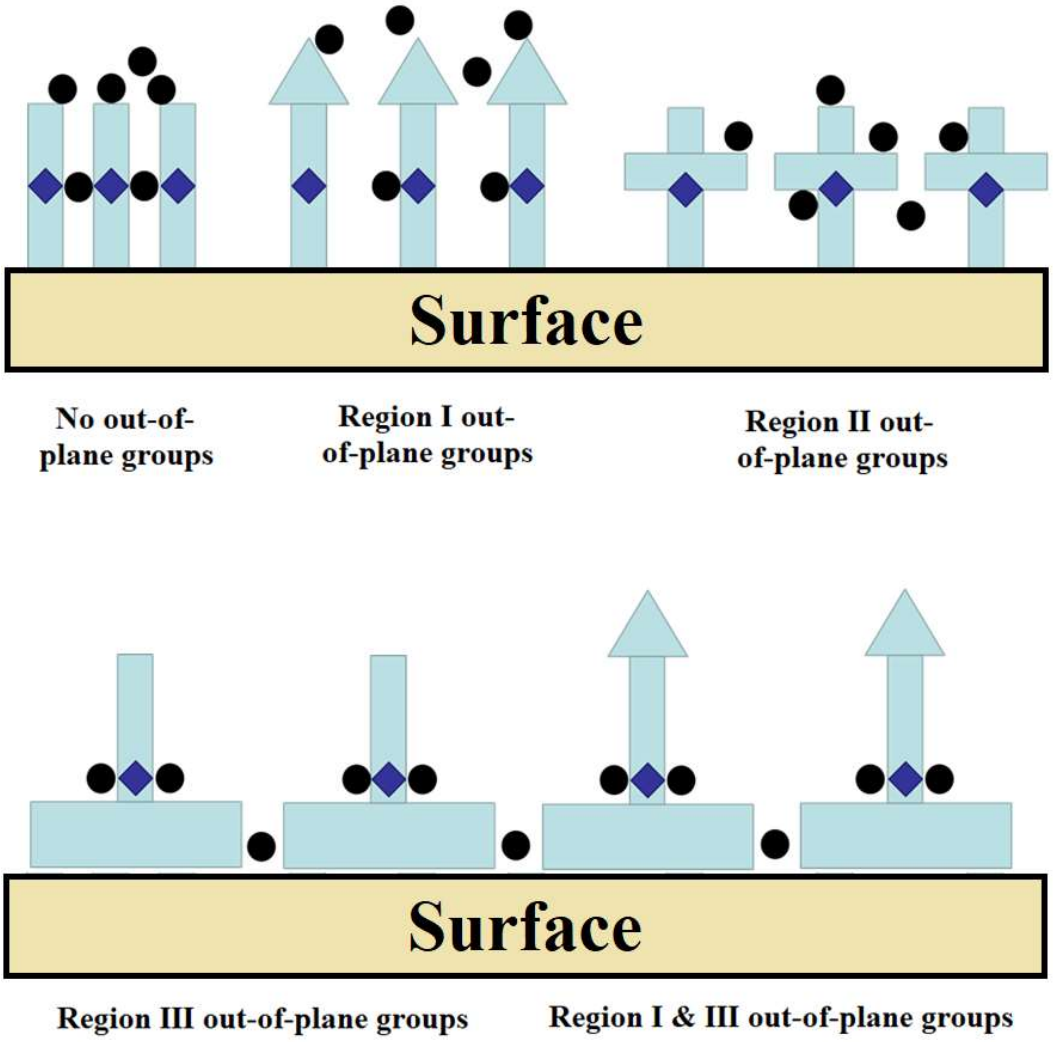

Figure 3-24. Schematic representation of motifs in sensitizers **3.1**-**3.8.** Black circles represent the electrolyte, blue diamonds indicate the squaraine core. The scheme is meant to illustrate that the packing of sensitizers on the TiO_2 will influence the amount of electrolyte that may reach the surface and recombine.

3.9 Experimental Methods

The synthesis of sensitizers 3.4, 3.6, and 3.7 are described in section 0.

*3.9.1 Synthesis of sensitizer **3.2***

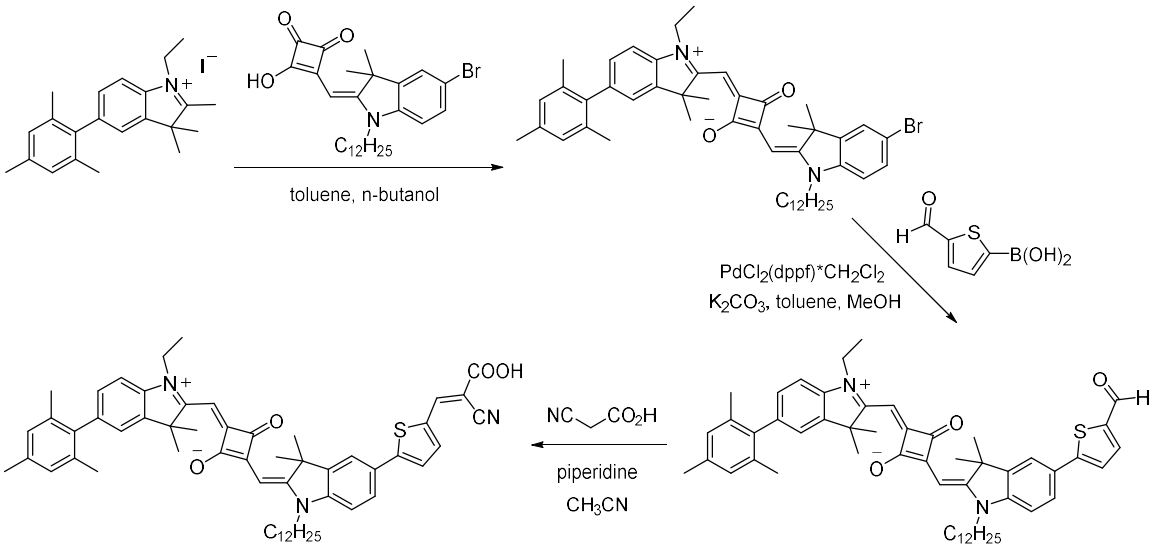

Figure 3-25. Synthesis of sensitizer **3.2**.

3.9.1.1 Synthesis of (*E*)-2-((*E*)-(5-bromo-1-dodecyl-3,3-dimethylindolin-2-ylidene)methyl)-4-((1-ethyl-5-mesityl-3,3-dimethyl-3*H*-indol-1-ium-2-yl)methylene)-3-oxocyclobut-1-enolate

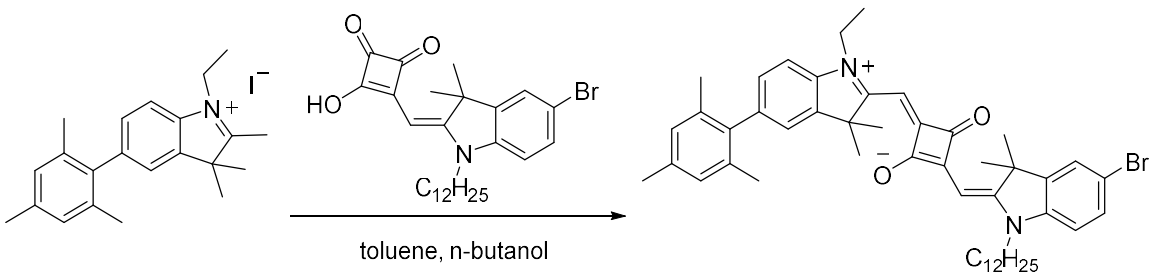

(*E*)-3-((5-Bromo-1-dodecyl-3,3-dimethylindolin-2-ylidene)methyl)-4-hydroxycyclobut-3-ene-1,2-dione (0.345 g, 0.796 mmol) and 1-ethyl-5-mesityl-2,3,3-trimethyl-3*H*-indol-1-ium iodide (0.400 g, 0.796 mmol) were dissolved in a solution of toluene (3 mL) and *n*-butanol (3 mL). The reaction was fitted with a Dean-Stark water separator and heated to 110 °C. The solution gradually turned from yellow to a deep blue, and the reaction was complete after 18 h. The solvent was removed under reduced pressure and the product was purified by column chromatography (CH_2Cl_2:MeOH = 95:5) to yield a blue/red solid greater than 95% pure (0.537 g, 85%). 90 mg of this material was further purified by column chromatography using hexanes:EtOAc (0% EtOAc then gradually increasing to 75% EtOAc, then 85% EtOAc). The main band fractions were combined, and the solvent was removed under reduced pressure. The residue was dissolved in THF and purified by size exclusion column chromatography (SEC) (S-X1 Biobeads in THF (THF was HPLC grade or from a solvent purification system)). First, a one-foot column of one-inch diameter was run, and the main green band was collected and the solvent removed under reduced pressure. A three-foot column of 1.5-inch diameter SEC was run, and again the main green band was collected and the solvent removed under reduced pressure. The residue was dissolved in distilled CH_2Cl_2, then filtered through a 0.2 μm PTFE filter and the solvent was removed under reduced pressure followed by high vacuum to yield an analytically pure red/blue solid (49 mg, 46%). ^{1}H NMR (400 MHz, $CDCl_3$): δ (ppm) = 7.43 (d, *J* = 1.8 Hz, 1H), 7.4 (d, *J* = 8.3, 1.9 Hz, 1H), 7.15 (d, *J* = 1.2 Hz, 1H), 7.10 (d, *J* = 8.1, 1.5 Hz, 1H), 7.07 (d, *J* = 8.1 Hz, 1H), 6.96 (s, 2H), 6.81 (d, *J* = 8.4 Hz, 1H), 6.02 (s, 1H), 5.93 (s, 1H), 4.14 (d, *J* = 4.8 Hz, 2H), 3.90 (s, 2H), 2.34 (s, 3H), 2.02 (s, 6H), 1.81 (s, 6H), 1.79 (s, 8H), 1.47 (t, *J* = 7.2 Hz, 3H), 1.44-1.36 (m, 2H), 1.36-1.31 (m, 2H),

1.31-1.27 (m, 2H), 1.25 (s, 12H), 0.87 (t, J = 7.0 Hz, 3H). $^{13}C\{^{1}H\}$ NMR (101 MHz, $CDCl_3$) δ (ppm) = 182.29, 180.75, 178.38, 170.52, 168.28, 144.12, 142.65, 141.67, 140.37, 138.27, 137.21, 136.81, 136.02, 130.5, 128.7, 128.13, 125.57, 123.48, 115.98, 110.29, 109.21, 86.73, 86.57, 49.53, 49, 43.64, 38.69, 31.88, 31.84, 29.64, 29.52, 29.45, 29.41, 29.3, 29.26, 27.09, 27, 26.83, 22.62, 20.96, 20.8, 14.08, 12.15. HRMS (MALDI): m/z 788.3984 $[M]^+$ (calcd for $C_{49}H_{61}BrN_2O_2$: 788.3916). Anal. Calcd for $C_{49}H_{61}BrN_2O_2$ (%): C, 74.50; H, 7.78; N, 3.55. Found: C, 74.80; H, 7.92; N, 3.47.

3.9.1.2 Synthesis of (*E*)-2-((*E*)-(1-dodecyl-5-(5-formylthiophen-2-yl)-3,3-dimethylindolin-2-ylidene)methyl)-4-((1-ethyl-5-mesityl-3,3-dimethyl-3*H*-indol-1-ium-2-yl)methylene)-3-oxocyclobut-1-enolate

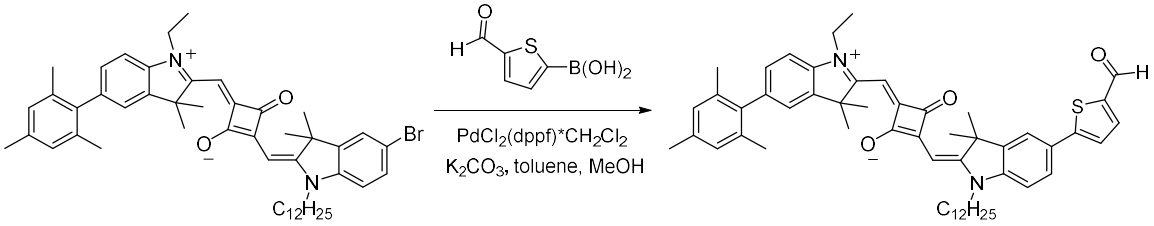

(*E*)-2-((*E*)-(5-Bromo-1-dodecyl-3,3-dimethylindolin-2-ylidene)methyl)-4-((1-ethyl-5-mesityl-3,3-dimethyl-3*H*-indol-1-ium-2-yl)methylene)-3-oxocyclobut-1-enolate (447 mg, 0.566 mmol) and 5-formylthiophen-2-ylboronic acid (265 mg, 1.698 mmol), $PdCl_2(dppf)\cdot CH_2Cl_2$ (46 mg, 0.057 mmol), and potassium carbonate (391 mg, 2.83 mmol) were combined in an oven-dried microwave tube. After filling with nitrogen via needle for 20 min, toluene (4 mL) and MeOH (4 mL) were added and the tube was capped. The microwave reactor (Biotage, Initiator 2.5) was set to 70 °C with a hold time of 15 min. The reaction mixture was passed through a silica gel plug (CH_2Cl_2:MeOH, 0%

MeOH moving gradually to 10% MeOH). The main band was collected and solvent was removed under reduced pressure. The residue was further purified by silica gel column chromatography using CH_2Cl_2:MeOH 99:1, and the main band was collected and solvent was removed under reduced pressure. This was followed by silica gel column chromatography using hexanes, EtOAc, and MeOH (starting with 9:1 hexane:EtOAc, moving to 6:4 hexane:EtOAc, then 100% EtOAc, and finishing with 99:1 EtOAc:MeOH). The main band was collected and the solvent removed under reduced pressure until only a small amount of solvent remained, and the product precipitated out of solution. The precipitate was washed with hexanes three times and dried under high vacuum to yield an analytically pure blue-green solid. (394 mg, 85%). ^{1}H NMR (500 MHz, $CDCl_3$) δ (ppm) = 9.88 (s, 1H), 7.73 (d, *J* = 3.9 Hz, 1H), 7.61 (d, *J* = 8.2 Hz, 1H), 7.59 (s, 1H), 7.38 (d, *J* = 3.9 Hz, 1H), 7.16 (s, 1H), 7.10 (dd, *J* = 8.1, 1.1 Hz, 1H), 7.07 (d, *J* = 8.0 Hz, 1H), 6.97 (s, 1H), 6.95 (s, 2H), 6.05 (s, 1H), 5.97 (s, 1H), 4.16 (d, *J* = 6.8 Hz, 2H), 3.95 (s, 2H), 2.33 (s, 3H), 2.01 (s, 6H), 1.84 (s, 6H), 1.81 (s, br, 8H), 1.47 (t, *J* = 7.2 Hz, 3H), 1.43 (t, *J* = 7.3 Hz, 2H), 1.36 (quin, *J* = 6.5 Hz, 2H), 1.32-1.27 (m, 2H), 1.25 (s, 12H), 0.87 (t, *J* = 6.8 Hz, 3H). ^{13}C{^{1}H} NMR (126 MHz, $CDCl_3$) δ (ppm) = 201.18, 182.42, 182.01, 178.52, 171.11, 168.17, 154.3, 143.98, 143.36, 142.9, 141.99, 140.47, 138.36, 137.65, 137.36, 136.93, 136.08, 128.91, 128.32, 128.27, 126.6, 123.69, 123.46, 120.28, 109.42, 87.55, 86.97, 49.82, 48.9, 43.83, 38.89, 31.93, 29.61, 29.54, 29.5, 29.4, 29.33, 27.4, 27.13, 27.07, 26.96, 22.69, 21.01, 20.82, 14.08, 12.26. HRMS (MALDI): m/z 820.4594 $[M]^+$ (calcd for $C_{54}H_{64}N_2O_3S$: 820.4638). Anal. Calcd for $C_{54}H_{64}N_2O_3S$ (%): C, 78.98; H, 7.86; N, 3.41; S, 3.90. Found: C, 78.62; H, 7.91; N, 3.32; S, 3.79.

3.9.1.3 Synthesis of (*E*)-2-((*E*)-(5-(5-((*E*)-2-carboxy-2-cyanovinyl)thiophen-2-yl)-1-dodecyl-3,3-dimethylindolin-2-ylidene)methyl)-4-((1-ethyl-5-mesityl-3,3-dimethyl-3*H*-indol-1-ium-2-yl)methylene)-3-oxocyclobut-1-enolate

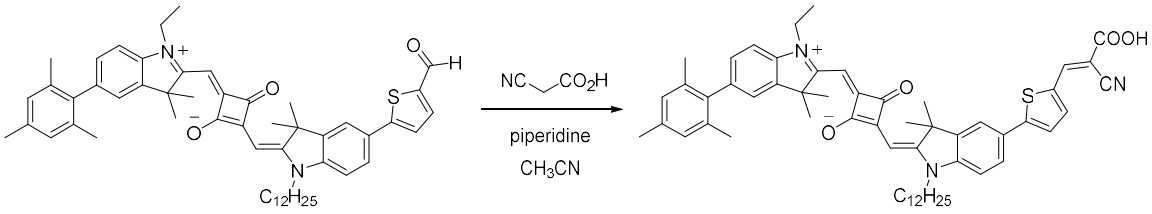

(*E*)-2-((*E*)-(1-Dodecyl-5-(5-formylthiophen-2-yl)-3,3-dimethylindolin-2-ylidene)methyl)-4-((1-ethyl-5-mesityl-3,3-dimethyl-3*H*-indol-1-ium-2-yl)methylene)-3-oxocyclobut-1-enolate (350 mg, 0.426 mmol) and cyanoacetic acid (76 mg, 0.895 mmol) were added to an oven-dried round-bottom flask, then evacuated and filled with nitrogen three times before anhydrous acetonitrile (25 mL) was added. Piperidine (50 μL) was added, and the reaction mixture was refluxed overnight. The solution was then cooled, and piperidine (50 μL) and cyanoacetic acid (76 mg, 0.895 mmol) were added. The solvent was removed slowly under reduced pressure (250 Torr, 40 °C for 4 h, then lower). The crude product was purified by column chromatography (CH_2Cl_2:MeOH:acetic acid = 96:2:2). The main band was collected and the solvent was removed under reduced pressure. The residue was dissolved in CH_2Cl_2 and filtered through a 0.2 μm polypropylene filter to remove residual silica gel. The product crystallized in CH_2Cl_2 and acetonitrile overnight. The fine precipitate was filtered, then recrystallized 3 additional times until the crystallization solvent was no longer pink after recrystallization. The solvent was removed from the crystals under reduced pressure and the residue was dried under high vacuum overnight to yield a gold precipitate (225 mg, 59%). ^{1}H NMR (500 MHz,

$CDCl_3$): δ (ppm) = 8.38 (s, 1H), 7.77 (d, *J* = 2.5 Hz, 1H), 7.67 (d, *J* = 8.3 Hz, 1H), 7.62 (s, 1H), 7.41 (d, *J* = 3.1 Hz, 1H), 7.17 (s, 1H), 7.12 (s, 2H), 7.00 (d, *J* = 8.4 Hz, 1H), 6.96 (s, 2H), 6.14 (s, 1H), 6.02 (s, 1H), 4.22 (d, *J* = 6.0 Hz, 2H), 4.02 (m, 2H), 2.34 (s, 3H), 2.02 (s, 6H), 1.85 (s, 6H), 1.82 (s, 8H), 1.50 (t, *J* = 7.1 Hz, 3H), 1.47-1.39 (m, 2H), 1.39-1.31 (m, 2H), 1.31-1.26 (m, 2H), 1.22 (s, 12H), 0.85 (t, *J* = 6.8 Hz, 3H) (COOH resonance not observed). $^{13}C\{^1H\}$ NMR (126 MHz, $CDCl_3$): δ = 179.22, 175.59, 171.76, 168.73, 164.85, 154.38, 146.45, 144.09, 143.41, 143.04, 141.34, 140.40, 138.88, 138.33, 137.91, 136.95, 136.08, 134.71, 129.01, 128.77, 128.29, 128.23, 127.27, 127.19, 126.80, 123.70, 120.24, 116.59, 109.69, 98.44, 87.60, 87.35, 49.92, 49.00, 43.96, 39.17, 31.93, 29.72, 29.64, 29.63, 29.58, 29.53, 29.45, 29.34, 27.35, 27.15, 27.11, 26.83, 22.69, 21.02, 20.83, 14.09, 12.34 ppm. HRMS (MALDI): m/z 887.4680 $[M]^+$ (calcd for $C_{57}H_{65}N_3O_4S$: 887.4696). Anal. Calcd for $C_{57}H_{65}N_3O_4S$ (%): C, 77.08; H, 7.38; N, 4.73; S, 3.61. Found: C, 77.07; H, 7.45; N, 4.73; S, 3.57.

*3.9.2 Synthesis of sensitizer **3.3***

3.9.2.1 Synthesis of 3-butylheptan-2-one

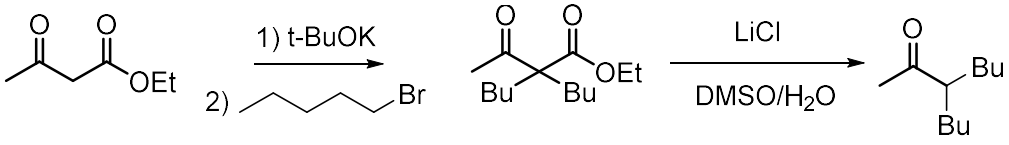

Ethyl acetoacetate (16.1 mL, 16.4 g, 126 mmol) and dry 1,2-dimethoxyethane (DME) (350 mL) were placed in an oven-dried 3-neck round-bottom flask equipped with a condenser. A suspension of potassium *tert*-butoxide in DME (63 mL, 2 M, 126 mmol) was added and the mixture was stirred and allowed to cool for 30 min. Dry 1-

bromobutane (13.6 mL, 17.3 g, 126 mmol) was slowly added over 5 min. The mixture was refluxed and stirred for 24 h. The solution was cooled to room temperature and a second aliquot of potassium *tert*-butoxide in DME (63 mL, 2 M, 126 mmol) was added. After allowing the mixture to cool for 30 min, a second aliquot of dry 1-bromobutane (13.6 mL, 17.3 g, 126 mmol) was added as before. The solution was then refluxed and stirred for an additional 72 h. The reaction mixture was cooled to room temperature, quenched with 3 N hydrochloric acid, and extracted three times with diethyl ether. The combined organic extracts were washed with DI water and dried over magnesium sulfate. The solvent was removed under reduced pressure, yielding a brown oil (37.65 g). The oil was purified by short path distillation to yield the clear oil of ethyl 2-acetyl-2-butylhexanoate (14.14 g, 46%).

Ethyl 2-acetyl-2-butylhexanoate (13.795 g, 56.922 mmol) was dissolved in DMSO (140 mL) in an oven-dried, 500 mL, 3-neck round-bottom flask with condenser and stir bar. To this solution was added anhydrous LiCl (2.65 g, 62.6 mmol) and DI water (1.13 mL, 62.6 mmol). The reaction mixture was heated under nitrogen for 5 d., maintaining an oil bath temperature of 149-152 °C. After cooling to room temperature, the reaction mixture was quenched with 200 mL of DI water and extracted with CH_2Cl_2 (3 x 100 mL). The organic layers were combined, washed with DI water (3 x 140 mL) and dried over $MgSO_4$. The solvent was removed under reduced pressure and the residue was placed over CaH_2 and stirred overnight before distillation through a Vigreux under 2 Torr vacuum. An impurity distilled off at room temperature, followed by the product at 70 °C and 5 Torr. A second impurity distilled off at 100 °C and 3 Torr. The product was a clear

oil (3.71 g, 38%). The ^{1}H NMR spectrum was consistent with that previously reported in the literature.[162]

3.9.2.2 Synthesis of 3,3-dibutyl-2-methyl-3*H*-indole

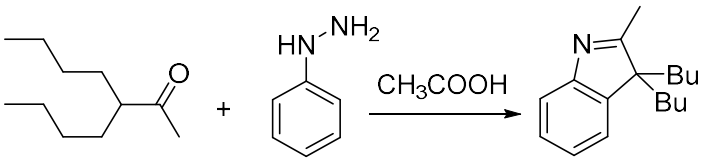

Phenylhydrazine (2.15 mL, 21.8 mmol) and 3-butylheptan-2-one (3.71 g, 21.8 mmol) were placed in a round-bottom flask. Acetic acid (110 mL) was added, and the mixture was heated at 100 °C for 24 h. Over the course of the reaction, the mixture turned from an original amber color to a dark orange color. After cooling to room temperature, the solvent was evaporated under reduced pressure. The resulting crude product was extracted with CH_2Cl_2 and water, and the organic layer was dried over magnesium sulfate. The solvent was evaporated under reduced pressure, yielding a brown oil (4.66 g). The brown oil was purified by silica gel column chromatography eluting with CH_2Cl_2. The main fractions were combined and the solvent removed under reduced pressure to yield an amber oil (1.56 g, 29%). The ^{1}H NMR spectrum was consistent with that previously reported in the literature.[163]

3.9.2.3 Synthesis of 3,3-dibutyl-1-ethyl-2-methyl-3*H*-indol-1-ium iodide

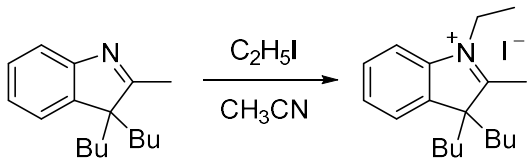

3,3-Dibutyl-2-methyl-3*H*-indole and ethyl iodide were dissolved in acetonitrile and refluxed under nitrogen for 11 h. The solution was then cooled to room temperature, and diethyl ether was added, and the mixture was cooled briefly in the freezer. The resulting solid was collected by vacuum filtration to yield a pinkish off-white solid (0.182 g, 38%). ^{1}H NMR (500 MHz, $CDCl_3$) δ (ppm) = 7.82 (dd, *J* =7.1, 2.0-1.6 Hz, 1H), 7.65 (dqd, *J* = 5.8, 7.4, 1.5, 2H), 7.53 (dd, *J* = 6.4, 1.6 Hz, 1H), 4.99 (q, *J* = 7.4 Hz, 2H), 3.19 (s, 3H), 2.23-2.06 (m, 4H), 1.62 (t, *J* = 7.4 Hz, 3H), 1.29-1.11 (m, 4H), 0.84-0.73 (m, 2H), 0.77 (t, *J* = 11.0 Hz, 6H), 0.66-0.54 (m, 2H). ^{13}C{^{1}H} NMR (126 MHz, $CDCl_3$) δ (ppm) = 195.50, 141.82, 138.89, 130.20, 129.86, 123.65, 115.46, 63.65, 45.79, 37.13, 25.87, 22.50, 17.18, 14.21, 13.55. HRMS (ESI): m/z 272.2373 $[M]^+$ (calcd for $C_{19}H_{30}N$: 272.2373). Anal. Calcd for $C_{19}H_{30}NI$: C, 57.14; H, 7.57; N, 3.51. Found: C, 56.85; H, 7.55; N, 3.43.

3.9.2.4 Synthesis of (*E*)-2-(((*E*)-5-bromo-1-dodecyl-3,3-dimethylindolin-2-ylidene)methyl)-4-((3,3-dibutyl-1-ethyl-3*H*-indol-1-ium-2-yl)methylene)-3-oxocyclobut-1-en-1-olate

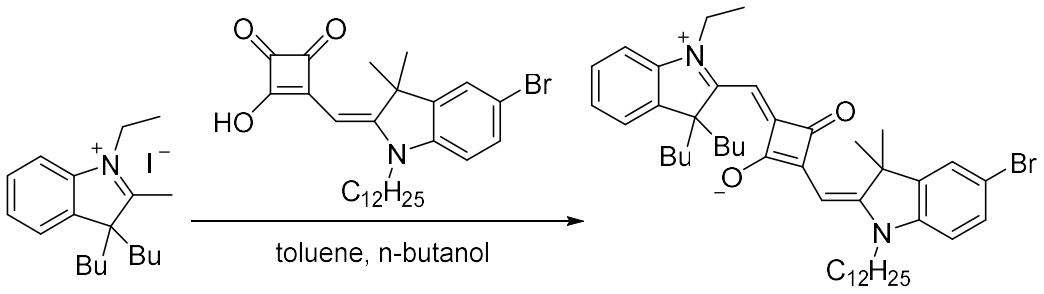

(*E*)-3-((5-Bromo-1-dodecyl-3,3-dimethylindolin-2-ylidene)methyl)-4-hydroxycyclobut-3-ene-1,2-dione (0.208 g, 0.414 mmol) and 3,3-dibutyl-1-ethyl-2-methyl-3*H*-indol-1-ium iodide (0.165 g, 0.414 mmol) were dissolved in a solution of toluene (2 mL) and *n*-

butanol (2 mL). The reaction was fitted with a Dean-Stark water separator and heated to 110 °C. The reaction turned from yellow to green, then a deep blue. After 18 h, the solvent was removed from the solution under reduced pressure. The residue was purified by silica gel column chromatography (Biotage Isolera system, 25 g silica gel, CH_2Cl_2:MeOH 100:0, then 99:1). The main band fractions were combined, and the solvent was removed under reduced pressure. The residue was further purified by silica gel column chromatography (Biotage Isolera system, 25 g silica gel, CH_2Cl_2:MeOH 100:0 increasing gradually to 97:3). The main band fractions were combined, and the solvent was removed under reduced pressure. The blue solid was further purified by size exclusion column (SEC) chromatography (Biobeads in THF (without stabilizers, HPLC grade or from a solvent purification system)). A one-foot column of one-inch diameter of S-X1 Biobeads was run, and the main blue band was collected and the solvent removed under reduced pressure. This column was repeated. A third SEC was performed using a two-foot column of 1.5-inch diameter of S-X8 Biobeads, and again the main blue band was collected and the solvent was removed under reduced pressure. A fourth SEC on a three-foot column of 1.5-inch diameter of S-X1 Biobeads was then run, and again the main green band was collected and the solvent was removed under reduced pressure. This column was then repeated. The residue was purified by silica gel chromatography (dry loaded, hexane:EtOAc 100:0 gradually increasing to 50:50), with the main band collected and the solvent removed under reduced pressure. The purified product was then dissolved in distilled CH_2Cl_2 and filtered through a 0.2 um PFTE filter to yield a blue solid (0.187 g, 60%). ^{1}H NMR (500 MHz, $CDCl_3$) δ (ppm) = 7.43 (d, J = 1.8 Hz, 1H), 7.4 (dd, J = 8.3, 1.9 Hz, 1H), 7.33 (td, J = 7.6, 1.0 Hz, 1H), 7.31 (d, J = 7.6 Hz, 1H), 7.19 (t, J = 7.2

Hz, 1H), 7.02 (d, *J* = 7.8 Hz, 1H), 6.80 (d, *J* = 8.4 Hz, 1H), 6.09 (s, 1H), 5.92 (s, 1H), 4.10 (s, 2H), 3.90 (s, 2H), 3.02 (s, 2H), 2.01 (td, *J* = 12.7, 3.0 Hz, 2H), 1.79 (s, 6H), 1.78-1.73 (m, 2H), 1.39 (t, *J* = 7.2 Hz, 2H), 1.44-1.36 (m, 2H), 1.36-1.32 (m, 2H), 1.32-1.28 (m, 2H), 1.26 (s, br, 14H), 1.19-1.02 (m, 4H), 0.88 (t, *J* = 7.0 Hz, 3H), 0.82-0.70 (m, 2H), 0.67 (t, *J* = 7.3 Hz, 6H), 0.52-0.41 (s, 2H). $^{13}C\{^{1}H\}$ NMR (126 MHz, $CDCl_3$) δ (ppm) = 182.47, 180.78, 178.02, 169.06, 168.07, 144.20, 143.47, 141.78, 139.26, 130.53, 127.79, 125.61, 124.08, 122.48, 115.92, 110.3, 109.01, 87.39, 86.82, 58.79, 49.01, 43.65, 39.82, 38.46, 31.90, 29.69, 29.58, 29.51, 29.47, 29.37, 29.32, 29.27, 27.16, 27.07, 26.93, 26.24, 22.72, 22.68, 14.13, 13.85, 12.21. HRMS (ESI): m/z 755.4133 $[M+H]^+$ (calcd for $C_{46}H_{64}N_2O_2Br$: 755.4146). Anal. Calcd for $C_{46}H_{63}BrN_2O_2(H_2O)_{0.5}$: C, 72.23; H, 8.43; N, 3.66. Found: C, 72.58; H, 8.50; N, 3.61.

3.9.2.5 Synthesis of (*E*)-4-((3,3-dibutyl-1-ethyl-3*H*-indol-1-ium-2-yl)methylene)-2-(((*E*)-1-dodecyl-5-(5-formylthiophen-2-yl)-3,3-dimethylindolin-2-ylidene)methyl)-3-oxocyclobut-1-en-1-olate

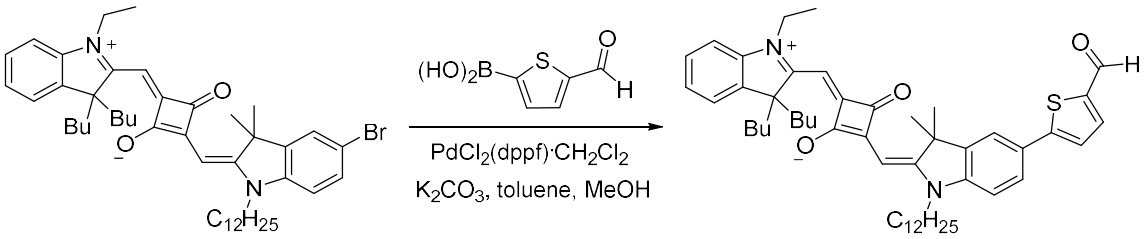

(*E*)-2-(((*E*)-5-Bromo-1-dodecyl-3,3-dimethylindolin-2-ylidene)methyl)-4-((3,3-dibutyl-1-ethyl-3*H*-indol-1-ium-2-yl)methylene)-3-oxocyclobut-1-en-1-olate (150 mg, 0.198 mmol), 5-formylthiophen-2-ylboronic acid (93 mg, 0.60 mmol), $PdCl_2(dppf)\cdot CH_2Cl_2$ (16 mg, 0.020 mmol), and potassium carbonate (137 mg, 0.992 mmol) were added to an oven-dried microwave tube. The tube was placed in a desiccator and pumped under high

vacuum, then filled with nitrogen (3x). The vial was capped under positive nitrogen pressure, then filled with nitrogen. HPLC grade MeOH (3 mL) and anhydrous toluene from a solvent purification system (3 mL) were added, and the vial was stirred and heated for 1.5 d. The reaction mixture was cooled to room temperature, then poured over a plug of silica gel topped with Celite packed in a Buchner funnel. The plug was rinsed with 1:1 CH_2Cl_2:EtOAc. All colored solvent was collected and the solvent was removed under reduced pressure. The crude product was purified via silica gel chromatography on the Biotage Isolera system (25 g silica gel cartridge, dry loaded by dissolving in CH_2Cl_2, adding 1 g silica gel, and removing the solvent under reduced pressure). The column was run in hexanes:EtOAc, starting with 5% EtOAc and increasing to 40% EtOAc to remove the main band. The green solid was further purified by size exclusion column (SEC) chromatography (S-X1 Biobeads in THF (without stabilizers, HPLC grade or from a solvent purification system)). A one-foot long column of one-inch diameter was run, and the main green band was collected and the solvent removed under reduced pressure. This column was repeated for further purification. The purified product was then dissolved in distilled CH_2Cl_2 and filtered through a 0.2 um PFTE filter to yield a dark solid (105 mg, 67%). ^{1}H NMR (500 MHz, $CDCl_3$) δ (ppm) = 9.88 (s, 1H), 7.75 (d, *J* = 4.0 Hz, 1H), 7.62 (dd, *J* = 8.2, 1.8 Hz, 1H), 7.60 (s, 1H), 7.39 (d, *J* = 4.0 Hz, 1H), 7.34 (dt, *J* = 7.5, 1.0 Hz, 1H), 7.32 (d, *J* = 7.5 Hz, 1H), 7.21 (t, *J* = 7.2 Hz, 1H), 7.04 (d, *J* = 7.8 Hz, 1H), 6.97 (d, *J* = 8.2 Hz, 1H), 6.11 (s, 1H), 5.97 (s, 1H), 4.11 (s, 2H), 3.94 (t, *J* = 7.1 Hz, 2H), 3.03 (s, 2H), 2.01 (dt, *J* = 12.9, 3.6 Hz, 2H), 1.85 (s, 6H), 1.81 (quin, *J* = 7.6 Hz, 2H), 1.47-1.42 (m, 2H), 1.40 (t, *J* = 7.2 Hz, 3H), 1.38-1.33 (m, 2H), 1.32-1.27 (m, 2H), 1.26 (s, 12H), 1.19-1.03 (m, 4H), 0.88 (t, *J* = 6.9 Hz, 3H), 0.75 (s, br, 2H), 0.67 (t, *J* = 7.3 Hz, 6H),

0.52-0.41 (m, 2H). $^{13}C\{^{1}H\}$ NMR (126 MHz, $CDCl_3$) δ (ppm) = 206.94, 182.57, 181.62, 177.77, 169.48, 167.75, 154.33, 143.91, 143.43, 143.17, 141.75, 139.33, 137.62, 128.08, 127.85, 126.54, 124.28, 123.40, 122.52, 120.18, 109.36, 109.17, 87.56, 87.41, 67.97, 58.94, 48.74, 43.69, 39.84, 38.56, 31.90, 30.93, 29.69, 29.59, 29.53, 29.48, 29.39, 29.33, 27.31, 27.11, 27.05, 26.24, 25.61, 14.13, 13.86, 12.27. HRMS (ESI): m/z 786.4768 $[M]^+$ (calcd for $C_{51}H_{66}O_3N_2S$: 786.4789). Anal. Calcd for $C_{51}H_{66}N_2O_3S(H_2O)_{0.5}$: C, 76.94; H, 8.48; N, 3.52. Found: C, 76.72; H, 8.61; N, 3.42.

3.9.2.6 Synthesis of (*E*)-2-(((*E*)-5-(5-((*E*)-2-carboxy-2-cyanovinyl)thiophen-2-yl)-1-dodecyl-3,3-dimethylindolin-2-ylidene)methyl)-4-((3,3-dibutyl-1-ethyl-3*H*-indol-1-ium-2-yl)methylene)-3-oxocyclobut-1-en-1-olate

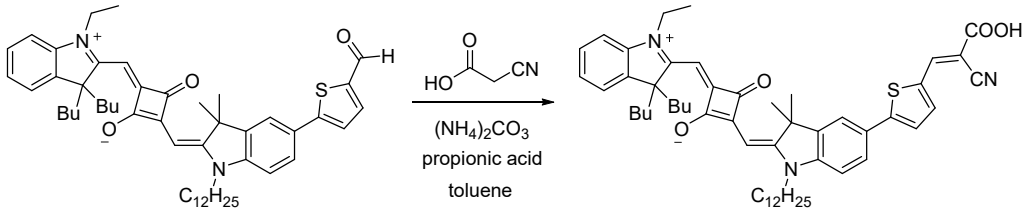

(*E*)-4-((3,3-Dibutyl-1-ethyl-3*H*-indol-1-ium-2-yl)methylene)-2-(((*E*)-1-dodecyl-5-(5-formylthiophen-2-yl)-3,3-dimethylindolin-2-ylidene)methyl)-3-oxocyclobut-1-en-1-olate (75 mg, 0.095 mmol) was added to an oven-dried round-bottom flask with an attached reflux condenser under nitrogen. Anhydrous toluene (24 mL) was added and stirred under nitrogen for 5 min. Ammonium carbonate (380 mg, 4.00 mmol) and cyanoacetic acid (170 mg, 2.00 mmol) were added and the solution was stirred under nitrogen for 5 min. Propanoic acid (1.8 mL, 24 mmol) was added and the solution was stirred overnight under nitrogen at 100 °C. The solvent was removed slowly under reduced pressure, then the residue was dissolved in CH_2Cl_2. The organic layer was extracted three times with

water (until water had a neutral pH), then dried over Na_2SO_4 and filtered. The solvent was removed under reduced pressure followed by high vacuum. The product was purified by silica gel column chromatography using 13 g of silica gel (Sorbtech). The eluents were as follows: 100% CH_2Cl_2, followed by 100% hexane (yellow impurity exited the column), then 1:1 hexane:EtOAc, slowly moving to 100% EtOAc (blue impurity exited the column), followed by 1:1 CH_2Cl_2:EtOAc, then 100% CH_2Cl_2, then 98:2 CH_2Cl_2:MeOH (blue impurity exited the column), then 96:2:2 CH_2Cl_2:MeOH:acetic acid (blue-green main band quickly exited the column). The main band fractions were combined, and the solvent was removed under reduced pressure followed by high vacuum. The major fraction was dissolved in THF and purified by SEC using a one-foot column of one-inch diameter. The main blue-green band was collected and the solvent removed under reduced pressure. A reverse phase column was run in 1:3 acetone:water, with little improvement in purity seen. Another silica gel column was run as previously described. The main blue-green band was collected and the solvent removed under reduced pressure, then the material was dissolved in distilled CH_2Cl_2 and filtered through a 0.2 um PTFE filter. Another one-foot SEC column of one-inch diameter was then run, and again the main blue-green band was collected and the solvent removed under reduced pressure to yield a shiny blue-green solid (26.4 mg, 32%). ^{1}H NMR (500 MHz, $CDCl_3$) δ (ppm) = 8.38 (s, 1H), 7.77 (d, *J* = 3.5 Hz, 1H), 7.67 (dd, *J* = 8.2, 1.5 Hz, 1H), 7.62 (s, 1H), 7.41 (d, *J* = 3.8 Hz, 2H), 7.36 (t, *J* = 7.5 Hz, 1H), 7.34 (d, *J* = 7.4 Hz, 1H), 7.22 (t, *J* = 7.5 Hz, 1H), 7.07 (d, *J* = 8.0 Hz, 1H), 6.99 (d, *J* = 8.4 Hz, 1H), 6.18 (s, 1H), 6.02 (s, 1H), 4.21 (s, 2H), 4.02 (s, 2H), 2.99 (s, 2H), 2.03 (t, *J* = 12.4 Hz, 2H), 1.86 (s, 9H), 1.48-1.40 (m, 2H), 1.42 (t, *J* = 7.1 Hz, 2H), 1.34 (quint, *J* = 6.7 Hz, 2H), 1.26 (m, 6H), 1.23 (s,

11H), 1.19-1.04 (m, 5H), 0.85 (t, J = 7.1 Hz, 4H), 0.82-0.72 (m, 2H), 0.69 (t, J = 7.3 Hz, 6H), 0.54-0.42 (m, 2H). $^{13}C\{^{1}H\}$ NMR (126 MHz, $CDCl_3$) δ (ppm) = 184.1, 181.64, 178.48, 174.74, 170.21, 168.41, 164.98, 154.25, 146.47, 144, 143.4, 139.38, 139.05, 134.63, 128.07, 127.95, 126.75, 124.55, 123.72, 122.54, 120.14, 116.78, 109.65, 109.53, 98.46, 87.88, 87.53, 59.06, 48.88, 43.82, 39.77, 38.98, 31.91, 29.61, 29.46, 29.34, 27.26, 27.12, 26.21, 22.72, 14.14, 13.84, 12.35. HRMS (ESI): m/z 853.4840 $[M]^+$ (calcd for $C_{54}H_{67}O_4N_3S$: 853.4847). Anal. Calcd for $C_{54}H_{67}N_3O_4S(H_2O)_{0.5}$: C, 75.14; H, 7.94; N, 4.87. Found: C, 75.14; H, 8.27; N, 4.54.

*3.9.3 Synthesis of sensitizer **3.5***

See section 2.9.1.8 for the synthesis of Bz[*e*]IndSq-Br ((*E*)-2-((*Z*)-(5-bromo-1-dodecyl-3,3-dimethylindolin-2-ylidene)methyl)-4-((3-ethyl-1,1-dimethyl-1*H*-benzo[*e*]indol-3-ium-2-yl)methylene)-3-oxocyclobut-1-enolate).

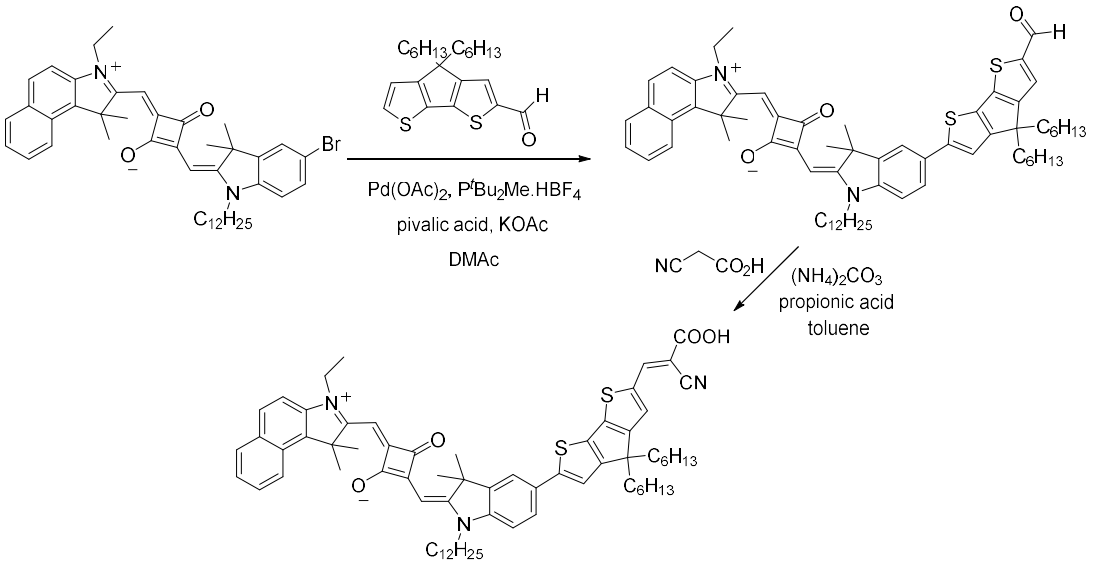

Figure 3-26. Synthesis of sensitizer **3.5**.

3.9.3.1 Synthesis of (*E*)-2-(((*E*)-1-dodecyl-5-(6-formyl-4,4-dihexyl-4*H*-cyclopenta[2,1-*b*:3,4-*b'*]dithiophen-2-yl)-3,3-dimethylindolin-2-ylidene)methyl)-4-((3-ethyl-1,1-dimethyl-1*H*-benzo[*e*]indol-3-ium-2-yl)methylene)-3-oxocyclobut-1-en-1-olate

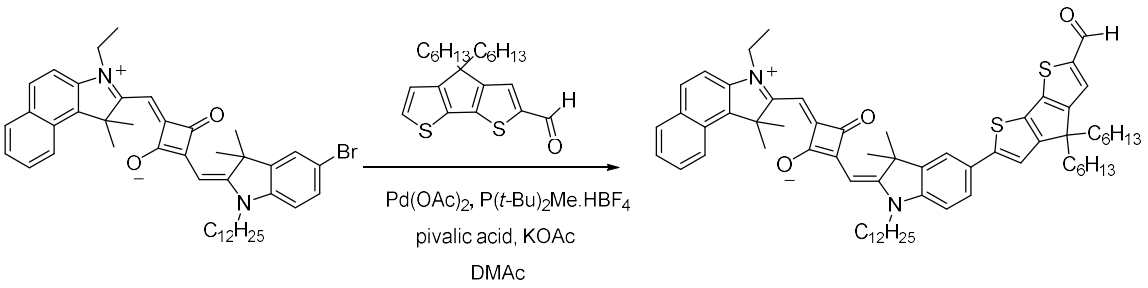

To a 20 mL oven-dried microwave vial cooled under nitrogen charged with a stir bar was added (*E*)-2-(((*E*)-5-bromo-1-dodecyl-3,3-dimethylindolin-2-ylidene)methyl)-4-((3-ethyl-1,1-dimethyl-1*H*-benzo[*e*]indol-3-ium-2-yl)methylene)-3-oxocyclobut-1-en-1-olate (200 mg, 0.277 mmol), 4,4-dihexyl-4*H*-cyclopenta[1,2-*b*:5,4-*b'*]dithiophene-2-carbaldehyde (189 mg, 0.504 mmol), palladium(II) acetate (6 mg, 0.03 mmol), di-*tert*-butyl(methyl)phosphonium tetrafluoroborate (13 mg, 0.050 mmol), pivalic acid (26 mg, 0.252 mmol), and potassium acetate (74 mg, 0.756 mmol), and the vial was sealed. After three cycles of high vacuum, then filling with nitrogen, anhydrous degassed dimethylacetamide (4.43 mL) was added. The flask was filled with nitrogen, then the solution was stirred at 120 °C overnight. The reaction was worked up by dilution with CH_2Cl_2 (200 mL) and filtered through a pad of silica gel (200 mL) with 100% CH_2Cl_2 until a dark green compound begins to elute. The solvent mixture was then switched to 3% MeOH: CH_2Cl_2 until the green color had fully eluted and stopped just before a blue band begins to elute. After removal of solvent from the 3% MeOH:CH_2Cl_2 fraction, the

mixture was purified via silica gel chromatography using 3-6% MeOH in CH_2Cl_2 to give the product as a dark green solid (185 mg, 68%). 77 mg of product was further purified by silica gel chromatography (CH_2Cl_2:MeOH 99:1 to 98:2). The residue was further purified by silica gel chromatography (hexanes:EtOAc 100:0, gradually increasing to 15:85). The residue was further purified by size exclusion column (S-X1, Biobeads, THF, 1 inch diameter, 4 ft. height column) and filtered through a PTFE filter (0.2 μm) to yield 40 mg of analytically pure sample. ^{1}H NMR (500 MHz, $CDCl_3$): δ (ppm) = 9.84 (s, 1H), 8.20 (d, *J* = 8.5 Hz, 1H), 7.90 (t, *J* = 8.2 Hz, 2H), 7.63-7.55 (m, 4H), 7.44 (ddd, *J* = 8.1, 7, 0.8 Hz, 1H), 7.33 (d, *J* = 8.8 Hz, 1H), 7.20 (s, 1H), 6.97 (d, *J* = 8.8 Hz, 1H), 6.06 (s, 1H), 6.00 (s, 1H), 4.24 (s, 2H), 3.97 (s, 2H), 2.08 (s, 6H), 1.99-1.79 (m, 14H), 1.47 (t, *J* = 7.2 Hz, 3H), 1.43 (quin, *J* = 7.7 Hz, 2H), 1.37 (quin, *J* = 6.6 Hz, 2H), 1.27 (s, 2H), 1.26 (s, br, 16H), 1.23-1.10 (m, 15H), 1.06-0.94 (m, 4H), 0.88 (t, *J* = 6.9 Hz, 3H), 0.82 (t, *J* = 7.0 Hz, 6H). ^{13}C{^{1}H} NMR (126 MHz, $CDCl_3$): δ (ppm) = 182.43, 181.15, 180.01, 177.57, 172.11, 168.19, 163.59, 157.49, 149.29, 147.95, 143.2, 143.09, 142.67, 138.94, 134.86, 134.26, 131.44, 129.9, 129.84, 129.74, 128.69, 127.41, 125.53, 124.53, 122.6, 119.43, 117.12, 109.97, 109.48, 87.17, 86.37, 54.22, 51.51, 48.96, 43.77, 38.8, 37.78, 31.91, 31.58, 29.7, 29.63, 29.6, 29.54, 29.5, 29.39, 29.33, 27.32, 27.25, 27.1, 27.05, 26.64, 24.58, 22.69, 22.6, 19.26, 14.13, 14.02, 12.46. HRMS (ESI): m/z 1015.5829 $[M+H]^+$ (calcd for $C_{66}H_{83}O_3N_2S_2$: 1015.5840). Anal. Calcd for $C_{66}H_{82}O_3N_2S_2$ (%): C, 78.06; H, 8.14; N, 2.76; S, 6.32. Found: C, 78.10; H, 8.18; N, 2.73; S, 6.20.

3.9.3.2 Synthesis of (*E*)-2-(((*E*)-5-(6-((*E*)-2-carboxy-2-cyanovinyl)-4,4-dihexyl-4*H*-cyclopenta[2,1-*b*:3,4-*b'*]dithiophen-2-yl)-1-dodecyl-3,3-dimethylindolin-2-ylidene)methyl)-4-((3-ethyl-1,1-dimethyl-1*H*-benzo[*e*]indol-3-ium-2-yl)methylene)-3-oxocyclobut-1-en-1-olate

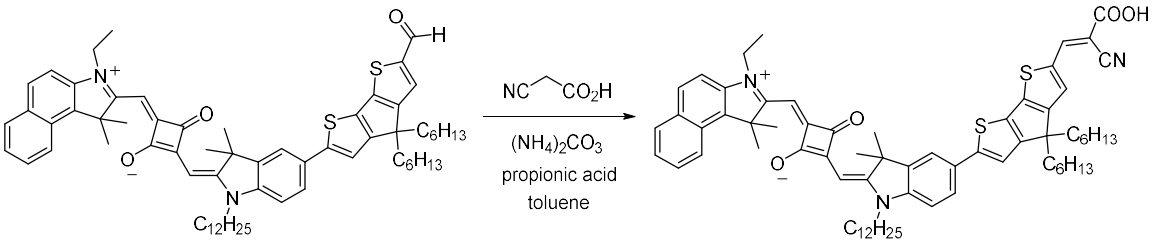

(*E*)-2-((*E*)-(1-Dodecyl-5-(5-formylthiophen-2-yl)-3,3-dimethylindolin-2-ylidene)methyl)-4-((1-ethyl-5-mesityl-3,3-dimethyl-3*H*-indol-1-ium-2-yl)methylene)-3-oxocyclobut-1-enolate (100 mg, 0.098 mmol) was added to a round-bottom flask with a reflux condenser, dissolved in anhydrous toluene (8 mL), and stirred under nitrogen for 5 min. Ammonium carbonate (40 mg, 0.41 mmol) and cyanoacetic acid (18 mg, 0.21 mmol) were added, and the solution was stirred under nitrogen for 5 min. Propanoic acid (0.18 mL, 2.5 mmol) was added, and the solution was stirred overnight under nitrogen at 100 °C. The solution was cooled and additional cyanoacetic acid (0.13 g) was added, then the solvent was removed slowly under reduced pressure. The residue was dissolved in CH_2Cl_2, then extracted three times with water, dried over Na_2SO_4, and filtered. The solvent was removed under reduced pressure. The product was purified by silica gel column chromatography using 10-15 g of silica gel (Sorbtech) and eluting with 98:2 CH_2Cl_2:MeOH. The main band was removed and the solvent was removed under reduced pressure. A second column was run, staying at 98:2 CH_2Cl_2:MeOH for several column volumes as blue, green, and red impurities exited the column. The eluent was changed to

96:2:2 CH_2Cl_2:MeOH:acetic acid, and the dark green main band quickly exited the column. The main band fractions were combined, and the solvent was removed under reduced pressure. The residue was dissolved in CH_2Cl_2, extracted three times with water, dried over Na_2SO_4, and filtered. The product crystallized overnight from chloroform using hexane. The fine, dark green precipitate was then collected by vacuum filtration (66 mg, 62%). ^{1}H NMR (500 MHz, $CDCl_3$): δ (ppm) = 8.35 (s, 1H), 8.21 (d, *J* = 8.6 Hz, 1H), 7.91 (d, *J* = 5.6 Hz, 1H), 7.89 (d, *J* = 6.4 Hz, 1H), 7.65 (s, 1H), 7.63-7.55 (m, 3H), 7.44 (t, *J* = 7.6 Hz, 1H), 7.33 (d, *J* = 8.9 Hz, 1H), 7.21 (s, 1H), 6.98 (d, *J* = 8.9 Hz, 1H), 6.13 (s, 1H), 6.03 (s, 1H), 4.29 (d, *J* = 6.4 Hz, 2H), 4.05 (s, 2H), 2.08 (s, 6H), 2.01-1.91 (m, 4H), 1.88 (s, 6H), 1.86-1.79 (m, 2H), 1.49 (t, *J* = 7.2 Hz, 3H), 1.46-1.28 (m, 7H), 1.25 (s, 14H), 1.23-1.12 (m, 12H), 1.01 (quint, *J* = 6.7 Hz, 4H), 0.87 (t, *J* = 6.7 Hz, 4H), 0.83 (t, *J* = 7.0 Hz, 6H) (COOH resonance not observed). ^{13}C{^{1}H} NMR (126 MHz, $CDCl_3$): δ (ppm) = 182.39, 178.04, 172.64, 171.08, 167.09, 164.93, 155.58, 154.62, 147.01, 146.5, 144.25, 144.07, 143.21, 140.66, 139.03, 134.93, 134.37, 127.58, 126.68, 126.25, 123.6, 120.3, 120.11, 116.69, 115.38, 110.43, 109.29, 97.98, 87.17, 67.97, 50.06, 48.55, 43.65, 39.22, 31.9, 31.42, 29.61, 29.45, 29.33, 27.32, 27.08, 27.03, 26.5, 22.68, 19.29, 14.13, 13.89, 12.42. HRMS (ESI): m/z 1082.5887 $[M+H]^+$ (calcd for $C_{69}H_{84}N_3O_4S_2$: 1082.5898). Anal. Calcd for $C_{69}H_{83}N_3O_4S_2$ (%): C, 76.55; H, 7.73; N, 3.88; S, 5.92. Found: C, 76.29; H, 7.96; N, 3.69; S, 5.74.

*3.9.4 Synthesis of sensitizer **3.8***

3.9.4.1 Synthesis of (*E*)-2-((*E*)-(5-(4,4-bis(2-ethylhexyl)-4*H*-silolo[3,2-*b*:4,5-*b'*]dithiophen-2-yl)-1-dodecyl-3,3-dimethylindolin-2-ylidene)methyl)-4-((3-ethyl-7-mesityl-1,1-dimethyl-1*H*-benzo[*e*]indol-3-ium-2-yl)methylene)-3-oxocyclobut-1-enolate

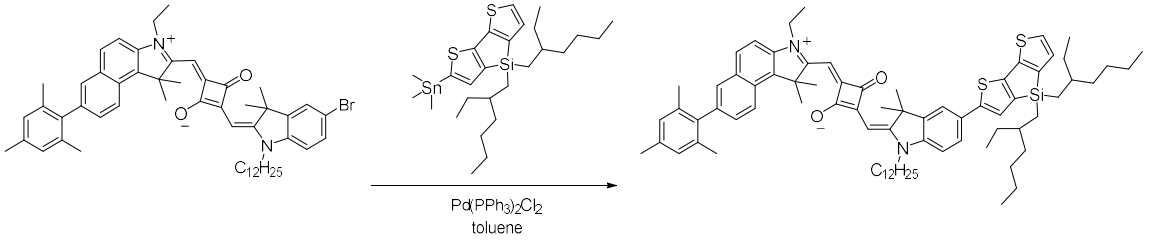

(*E*)-2-((*E*)-(5-Bromo-1-dodecyl-3,3-dimethylindolin-2-ylidene)methyl)-4-((3-ethyl-7-mesityl-1,1-dimethyl-1*H*-benzo[*e*]indol-3-ium-2-yl)methylene)-3-oxocyclobut-1-enolate (0.100 g, 0.119 mmol), 4,4-bis(2-ethylhexyl)-2-(trimethylstannyl)-4*H*-silolo[3,2-*b*:4,5-*b'*]dithiophene (0.173 g, 0.298 mmol), and bis(triphenylphosphine)palladium(II) dichloride (4 mg, 0.006 mmol) were added to a reaction flask equipped with a reflux condenser. After three cycles of high vacuum, then filling with nitrogen, anhydrous toluene (4 mL) was added and the reaction was stirred overnight at 80 °C. The reaction was cooled to room temperature and extracted with CH_2Cl_2 and water. The organic layer was dried over Na_2SO_4, the Na_2SO_4 removed by vacuum filtration, and the solvent removed under reduced pressure. The residue was purified by silica gel chromatography (dry loaded, hexane:EtOAc 100:0 gradually increasing to 20:80), with the main band collected and the solvent removed under reduced pressure. The green solid was further purified by size exclusion column (SEC) chromatography (S-X1 Biobeads in THF

(without stabilizers, HPLC grade or from a solvent purification system)). First, a one-foot column of one-inch diameter was run, and the main green band was collected and the solvent removed under reduced pressure. An SEC on a three-foot column of 1.5-inch diameter was then run, and again the main green band was collected and the solvent was removed under reduced pressure. The purified product was then dissolved in distilled CH_2Cl_2 and filtered through a 0.2 um PFTE filter to yield a dark green solid (113 mg, 80%). ^{1}H NMR (500 MHz, $CDCl_3$) δ (ppm) = 8.24 (d, *J* = 8.7 Hz, 1H), 7.86 (d, *J* = 8.8 Hz, 1H), 7.66 (d, *J* = 1.1 Hz, 1H), 7.55 (d, *J* = 1.4 Hz, 1H), 7.53 (dd, *J* = 8.2, 1.6 Hz, 1H), 7.38 (dd, *J* = 8.7, 1.6 Hz, 1H), 7.33 (d, *J* = 8.8 Hz, 1H), 7.26 (t, *J* = 3.8 Hz, 1H), 7.21 (d, *J* = 4.7 Hz, 1H), 7.06 (d, *J* = 4.7 Hz, 1H), 6.99 (s, 2H), 6.96 (d, *J* = 8.3 Hz, 1H), 6.06 (s, 1H), 6.00 (s, 1H), 4.24 (s, 2H), 3.98 (s, 2H), 2.36 (s, 3H), 2.12 (s, 6H), 2.05 (s, 6H), 1.86 (s, 6H), 1.84-1.79 (m, 2H), 1.47 (t, *J* = 7.3 Hz, 3H), 1.46-1.41 (m, 4H), 1.40-1.34 (m, 2H), 1.33-1.26 (m, 4H), 1.26 (s, 14H), 1.25-1.11 (m, 12H), 1.04-0.92 (m, 4H), 0.87 (t, *J* = 6.9 Hz, 3H), 0.84 (t, *J* = 6.4 Hz, 3H), 0.83 (t, *J* = 6.8 Hz, 3H), 0.79 (t, *J* = 7.4 Hz, 3H), 0.78 (t, *J* = 7.4 Hz, 3H). ^{13}C NMR (126 MHz, $CDCl_3$) δ (ppm) = 210.81, 182.61, 178.95, 177.76, 171.47, 168.78, 148.99, 148.95, 148.91, 147.81, 144.55, 144.51, 144.47, 144.27, 144.23, 144.19, 143.06, 142.29, 142.19, 142.09, 141.78, 138.98, 138.37, 137.28, 136.85, 136.15, 134.70, 131.50, 130.57, 129.90, 129.71, 129.64, 129.52, 128.19, 127.52, 125.48, 125.34, 125.16, 122.63, 119.53, 119.49, 119.45, 110.02, 109.52, 86.95, 86.21, 69.52, 53.83, 51.41, 49.13, 43.82, 38.70, 35.93, 35.90, 35.66, 35.61, 31.92, 31.74, 29.70, 29.61, 29.55, 29.51, 29.40, 29.34, 29.28, 28.92, 28.89, 28.86, 27.22, 27.11, 26.76, 23.01, 22.99, 22.69, 21.07, 20.87, 17.75, 17.69, 14.17, 14.13, 12.42, 10.83, 10.80. HRMS (ESI): m/z

1177.7039 $[M+H]^+$ (calcd for $C_{77}H_{101}O_2N_2S_2Si$: 1177.7068). Anal. Calcd for $C_{77}H_{100}O_2N_2S_2Si$ (%): C, 78.52; H, 8.56; N, 2.38. Found: C, 78.24; H, 8.76; N, 2.31.

3.9.4.2 Synthesis of (*E*)-2-((*E*)-(5-(4,4-bis(2-ethylhexyl)-6-formyl-4*H*-silolo[3,2-*b*:4,5-*b'*]dithiophen-2-yl)-1-dodecyl-3,3-dimethylindolin-2-ylidene)methyl)-4-((3-ethyl-7-mesityl-1,1-dimethyl-1*H*-benzo[*e*]indol-3-ium-2-yl)methylene)-3-oxocyclobut-1-enolate

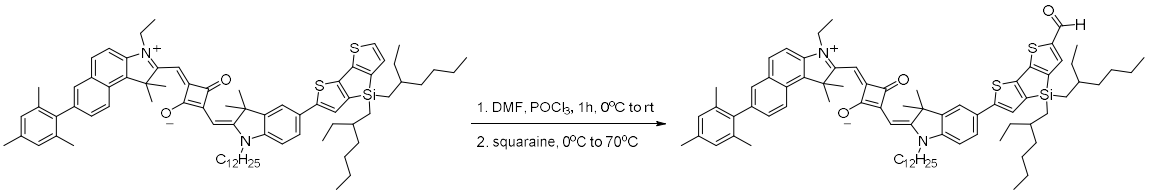

To a sealed microwave vial with N,N-dimethylformide (29 mg, 0.40 mmol) in 1,2-dichloroethane (1.6 mL) at 0 °C, phosphoryl trichloride (61 mg, 0.40 mmol) was added under nitrogen. The reaction solution was stirred at 0 °C for 2 h. (*E*)-2-((*E*)-(5-(4,4-bis(2-ethylhexyl)-4*H*-silolo[3,2-*b*:4,5-*b'*]dithiophen-2-yl)-1-dodecyl-3,3-dimethylindolin-2-ylidene)methyl)-4-((3-ethyl-7-mesityl-1,1-dimethyl-1*H*-benzo[*e*]indol-3-ium-2-yl)methylene)-3-oxocyclobut-1-enolate (94 mg, 0.080 mmol) was then added, and the reaction mixture was heated to 70 °C for 6 h. The solution was cooled to room temperature, and saturated sodium acetate aqueous solution (8 mL) was added. The mixture was further stirred at room temperature overnight. The crude product was extracted into CH_2Cl_2, which was then washed with brine and water and dried over anhydrous sodium sulfate. After removing solvent under reduced pressure, the residue was purified by silica gel column chromatography (dry loaded, hexanes:EtOAc 100:0 gradually increasing to 20:80, with main band exiting the column at 60% EtOAc), with

the main band collected and the solvent removed under reduced pressure. The green solid was further purified by size exclusion column (SEC) chromatography (S-X1 Biobeads in THF (without stabilizers, HPLC grade or from a solvent purification system)). First, a one-foot column of one-inch diameter was run, and the main green band was collected and the solvent removed under reduced pressure. An SEC on a three-foot column of 1.5-inch diameter was then run, and again the main green band was collected and the solvent was removed under reduced pressure. The residue was then purified by reverse phase silica gel (C18) column chromatography in MeOH, with the main band collected and the solvent removed under reduced pressure to yield a dark green solid (26 mg, 27%). ^{1}H NMR (500 MHz, $CDCl_3$) δ (ppm) = 9.88 (s, 1H), 8.24 (d, *J* = 8.6 Hz, 1H), 7.87 (d, *J* = 8.7 Hz, 1H), 7.71 (s, 1H), 7.67 (s, 1H), 7.56 (s, 1H), 7.55 (s, 1H), 7.39 (d, *J* = 8.6 Hz, 1H), 7.34 (d, *J* = 8.8 Hz, 1H), 7.32 (s, 1H), 6.99 (s, 2H), 6.97 (d, *J* = 8.3 Hz, 1H), 6.08 (s, 1H), 6.00 (s, 1H), 4.26 (s, 2H), 3.98 (s, 2H), 2.36 (s, 3H), 2.12 (s, 6H), 2.05 (s, 6H), 1.93-1.79 (m, 8H), 1.77-1.67 (m, 2H), 1.66-1.56 (m, 2H), 1.55-1.50 (m, 2H), 1.47 (t, *J* = 7.3 Hz, 3H), 1.46-1.41 (m, 2H), 1.40-1.31 (m, 4H), 1.27 (s, 20H), 1.22-1.09 (m, 4H), 1.08-0.98 (m, 2H), 0.96 (d, *J* = 6.6 Hz, 2H), 0.93-0.77 (m, 15H). $^{13}C\{^{1}H\}$ NMR (126 MHz, $CDCl_3$): δ (ppm) = 182.55, 179.88, 177.53, 172.01, 168.29, 167.73, 158.56, 149.16, 148.92, 146.20, 144.41, 143.20, 143.03, 142.91, 142.80, 142.65, 139.75, 138.89, 138.35, 137.47, 136.91, 136.16, 134.92, 132.36, 131.63, 130.92, 129.80, 129.69, 129.60, 129.53, 128.85, 128.22, 127.51, 125.88, 125.66, 122.67, 119.77, 110.07, 109.48, 87.16, 86.41, 66.23, 65.92, 51.58, 48.98, 43.80, 41.38, 38.82, 36.10, 35.94, 35.92, 35.71, 35.66, 34.69, 34.55, 31.95, 31.62, 29.73, 29.64, 29.58, 29.54, 29.42, 29.37, 29.28, 29.09, 28.93, 28.89, 28.62, 27.70, 27.30, 27.14, 27.09, 26.74, 25.30, 23.00, 22.68, 21.08, 20.88, 20.71, 20.47,

18.77, 17.61, 17.51, 14.33, 14.13, 12.48, 11.44, 10.82. HRMS (ESI): m/z 1205.7005 [M+] (calcd for $C_{78}H_{100}N_2O_3S_2Si$: 1205.7017). See Figure A-1 in Appendix A for HPLC trace.

3.9.4.3 Synthesis of (*E*)-2-(((*E*)-5-(6-((*E*)-2-carboxy-2-cyanovinyl)-4,4-bis(2-ethylhexyl)-4*H*-silolo[3,2-*b*:4,5-*b'*]dithiophen-2-yl)-1-dodecyl-3,3-dimethylindolin-2-ylidene)methyl)-4-((3-ethyl-7-mesityl-1,1-dimethyl-1*H*-benzo[*e*]indol-3-ium-2-yl)methylene)-3-oxocyclobut-1-en-1-olate

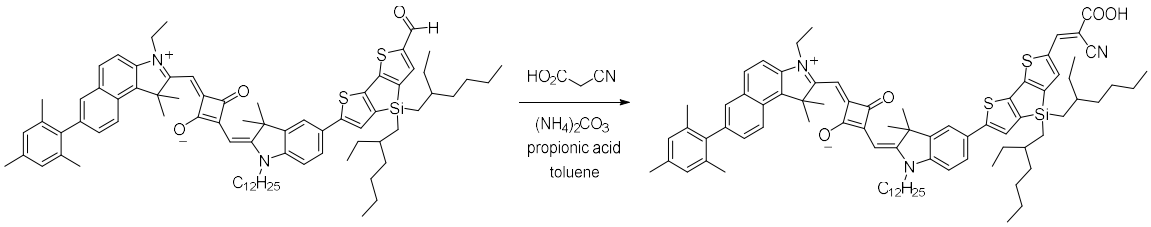

(*E*)-2-((*E*)-(5-(4,4-Bis(2-ethylhexyl)-6-formyl-4*H*-silolo[3,2-*b*:4,5-*b'*]dithiophen-2-yl)-1-dodecyl-3,3-dimethylindolin-2-ylidene)methyl)-4-((3-ethyl-7-mesityl-1,1-dimethyl-1*H*-benzo[*e*]indol-3-ium-2-yl)methylene)-3-oxocyclobut-1-enolate (25 mg, 0.021 mmol) was placed in an oven-dried round-bottom flask with reflux condenser and the capped system was filled with nitrogen. Anhydrous toluene (6 mL) was added and stirred under nitrogen for 5 min. Ammonium carbonate (64 mg, 0.66 mmol) and cyanoacetic acid (28 mg, 0.33 mmol) were added and the solution was stirred under nitrogen for 5 min. Propanoic acid (0.25 mL, 3.3 mmol) was added and the solution was stirred overnight under nitrogen at 100 °C. The solution was cooled and additional cyanoacetic acid (0.13 g) was added, then the solvent was removed slowly under reduced pressure. The residue was dissolved in CH_2Cl_2, then extracted three times with water, dried over Na_2SO_4, and filtered. The solvent was removed under reduced pressure followed by high vacuum. The product was

purified by silica gel column chromatography using 10-15 g of silica gel (Sorbtech). The eluents were as follows: 100% CH_2Cl_2, followed by 100% hexane (impurities exited the column), then 1:1 hexane:EtOAc, slowly moving to 100% EtOAc (impurities exited the column), followed by 100% CH_2Cl_2, then 98:2 CH_2Cl_2:MeOH for several column volumes until the column looked very clean except for the main band. Then 96:2:2 CH_2Cl_2:MeOH:acetic acid to elute a dark green main band. The main band fractions were combined, and the solvent was removed under reduced pressure to yield the purified dark green solid (16 mg, 61% yield). ^{1}H NMR (500 MHz, $CDCl_3$): δ (ppm) = 8.40 (s, 1H), 8.25 (d, *J* = 8.8 Hz, 1H), 7.88 (d, *J* = 8.9 Hz, 1H), 7.74 (s, 1H), 7.68 (s, 1H), 7.56 (d, *J* = 8.1 Hz, 2H), 7.40 (dd, *J* = 8.6, 1.5 Hz, 1H), 7.36 (d, *J* = 9.0 Hz, 1H), 7.34 (t, *J* = 2.0 Hz, 1H), 6.99 (s, 3H), 6.15 (s, 1H), 6.04 (s, 1H), 4.31 (s, 2H), 4.03 (s, 2H), 2.36 (s, 3H), 2.12 (s, 6H), 2.05 (s, 6H), 1.87 (s, 8H), 1.50 (t, *J* = 7.2 Hz, 3H), 1.48-1.26 (m, 14H), 1.25 (s, 12H), 1.19 (d, *J* = 5.2 Hz, 11H), 1.10-0.98 (m, 4H), 0.89-0.77 (m, 15H) (COOH resonance not observed). $^{13}C\{^1H\}$ NMR (126 MHz, $CDCl_3$): δ (ppm) = 182.89, 177.45, 175.67, 174.96, 172.54, 168.66, 166.5, 159.78, 149.75, 146.94, 146.15, 143.78, 143.64, 143.50, 143.23, 142.74, 141.36, 138.81, 138.32, 137.55, 137.18, 136.91, 136.16, 135.16, 131.69, 129.84, 129.61, 128.20, 127.42, 126.02, 125.78, 122.73, 119.69, 117.24, 110.17, 109.71, 95.67, 87.25, 86.70, 51.61, 48.99, 43.87, 39.04, 35.89, 35.66, 31.93, 29.64, 29.46, 29.36, 28.87, 27.23, 27.12, 26.64, 22.99, 22.70, 21.08, 20.89, 17.58, 17.48, 14.17, 12.52, 10.81. HRMS (ESI): m/z 1271.7014 $[M]^+$ (calcd for $C_{81}H_{101}O_4N_3S_2Si$: 1271.6997). Anal. Calcd for $C_{81}H_{101}N_3O_4S_2Si(H_2O)$: C, 75.36; H, 8.04; N, 3.26; S, 4.97. Found: C, 75.49; H, 8.08; N, 3.33; S, 4.75.

CHAPTER 4. EXPLORING THE ROLE OF PHOSPHONIC ACIDS IN RHODANINE ACCEPTOR ANCHORS FOR DYE-SENSITIZED SOLAR CELLS

This work was accomplished in collaboration with Parnian Ferdowsi in the group of Prof. Anders Hagfeldt. Training and assistance were provided by Dr. M. D. Zakeeruddin, Dr. Kazuteru Nonomura, Dr. Nick Vlachopoulos, and Dr. Stephen Shiring in the group of Prof. Jean-Luc Brédas. The author performed synthesis, device fabrication and optimization, cyclic voltammetry, photoelectrochemical device characterization, and computational modeling.

4.1 Introduction

The highest efficiency DSSC devices have reached power conversion efficiencies (PCEs) of 12-14%.[20,21,23] A notable device reported was co-sensitized with sensitizers **LEG4** and **ADEKA-1** (Figure 4-1), and reached 14.3% PCE. **ADEKA-1** employs a silyl anchoring group rather than the cyanoacrylic acid anchoring group more widely used in sensitizers for DSSCs. Silane-based anchoring groups have been employed in various surface modifiers due to their ability to form stable, robust monolayers. However, silane monolayer formation can be very irreproducible, as homocondensation products can form in the presence of an excess of water, resulting in a polymeric multilayer instead of the desired monolayer.[164] The synthesis and use of the **ADEKA-1** dye in a further study has resulted in devices of significantly decreased PCEs,[165] which could be related to the difficulty in producing a pristine monolayer using silane-based anchors. Although studies

on the binding of **ADEKA-1** to the surface have not been reported, the calculated LUMO distribution makes it clear that electronic coupling with the metal oxide is unlikely to pass through the silane anchor.[23]

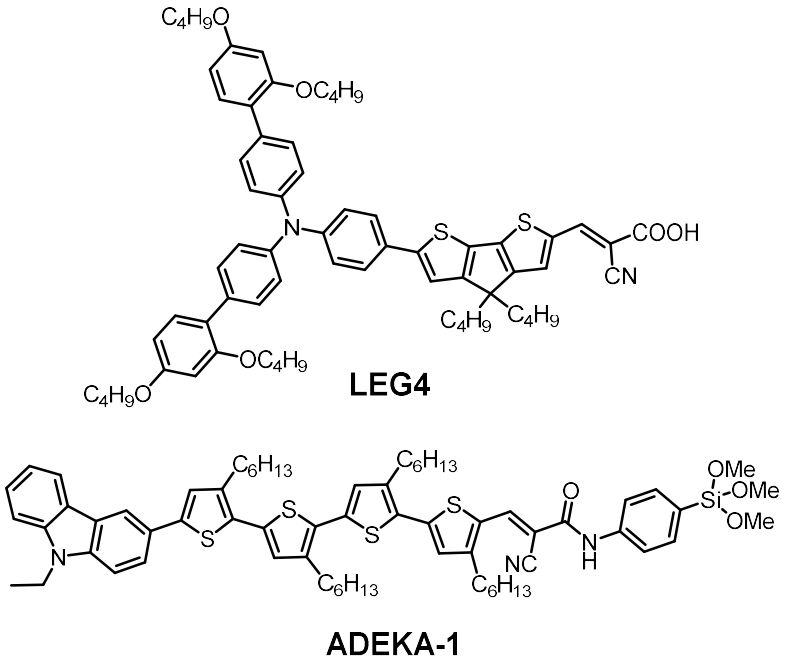

Figure 4-1. Molecular structures of sensitizers **LEG4** and **ADEKA-1**.

Phosphonic acid-based anchoring groups are a strong-binding alternative to silane-based anchoring groups.[166,167] Phosphonic acids have been shown to bind more strongly to metal oxides than carboxylic acids,[168–170] and bind in a fashion unlikely to produce the homocondensation products seen in silane-based anchoring groups.[167] Unlike carboxylic acids, which have been shown to have surface coverages at less than ¼ of a theoretical monolayer, phosphonic acid modifiers have been shown to exhibit surface

coverages near that of a theoretical monolayer.[168] However, a trigonal planar carbon in a carboxylic acid may facilitate stronger electronic coupling with a metal oxide surface than a tetrahedral phosphonic acid.[61,171,172] Electronic coupling with the metal oxide has been shown to be beneficial for effective photo-induced electron transfer in DSSC sensitizers.[172]

A strategy for both strong binding and electronic coupling to the surface is to decouple the binding and electron transfer roles of the anchoring group. One example of this has been accomplished in the literature using carboxylic acids attached to rhodanine anchoring groups,[173–186] most commonly as rhodanine-3-acetic acid. A carboxylic acid was incorporated into the rhodanine dye, but with a methylene ($-CH_2-$) group preventing π-conjugation between the carboxylic acid and the dye. The authors hypothesized that electron transfer proceeds via the oxygen and/or nitrogen atoms of the rhodanine, which are thought to be in close proximity to the TiO_2 surface.

This study employs rhodanine anchoring groups incorporating alkyl phosphonic acids compared directly with rhodanine anchoring groups incorporating alkyl carboxylic acids via the sensitizer structures shown in Figure 4-2. As the anchoring group is not thought to be involved in electron transfer, replacing a carboxylic acid with a phosphonic acid could provide effective electron injection and strong binding. Other possible effects include a difference in the packing of the dye on the surface, the phosphonic acid binding mono-, bi-, or tri-dentate, the angle of the dye to the surface, and the strength of binding for the phosphonic acid sensitizers vs. the carboxylic acid sensitizers. A tighter packing of the phosphonic acid-anchored sensitizers could increase or decrease current depending on sensitizer-sensitizer interactions and their effect on electron injection. Another result

may be that the phosphonic acid either increases or decreases current by providing either a better or a worse binding angle for the interaction of the oxygen of the rhodanine with the metal oxide, resulting in either increased or decreased electron injection into the metal oxide.

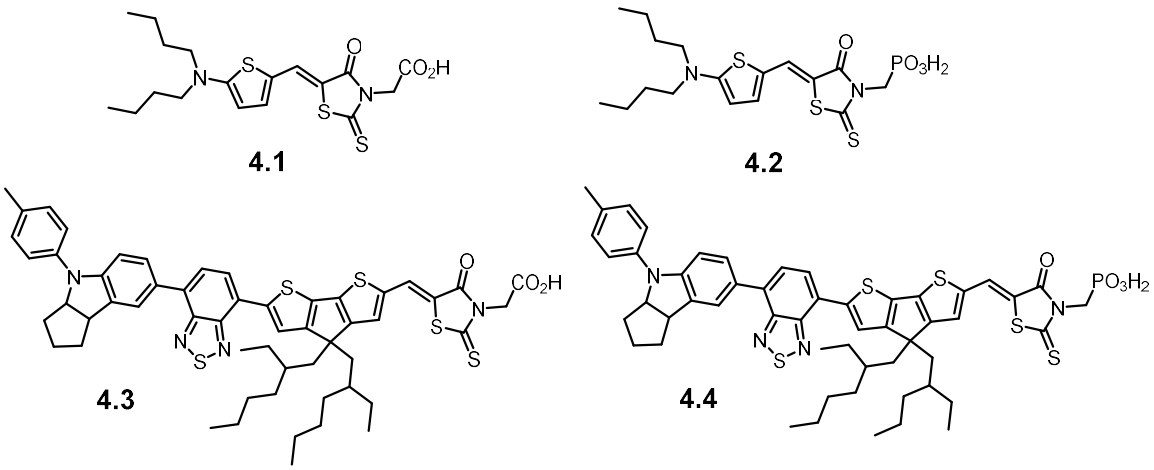

Figure 4-2. Structure of dyes synthesized incorporating rhodanine anchors with either carboxylic or phosphonic acids.

4.2 Synthesis of Donor-π-Acceptor Rhodanine-Anchored Dyes

Although the incorporation of an *N*-alkyl phosphonic acid into a rhodanine unit had been proposed in the patent literature on photographic sensitizing dyes,[187] no synthetic method for doing so was proposed or known. First the condensation of the rhodanine using (aminomethyl)phosphonic acid was attempted, but no desired product observed (Figure 4-3). Second, a substitution reaction between the chloro-substituted methyl

diethylphosphonate and the rhodanine potassium salt was attempted, again with no desired product observed. Another substitution reaction, this time using the iodo-methyl diethyl phosphonate, was attempted and showed the presence of a compound with an NMR spectrum potentially consistent with the presence of the desired product, but no product ion was observed by MS.

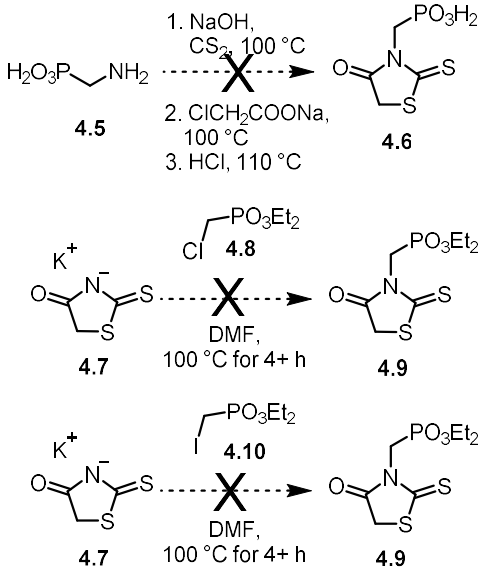

Figure 4-3. Attempted syntheses of rhodanine-3-methyl phosphonic acid or ethyl ester.

The rhodanine-3-methyl phosphonic ester (compound **4.9**) was able to be synthesized by a substitution reaction between the rhodanine sodium salt (Figure 4-4) and (diethoxyphosphinyl)methyl triflate, following a patent procedure for a similar molecule (using thiazolidine-2,4-dione),[188] with the specific conditions for the deprotonation using sodium hydride from Sevov *et al.*[189] The desired *N*-methylated product was produced

along with the *S*-methylated product in a ratio of 1:1.4, respectively, with separation achieved by silica gel chromatography.

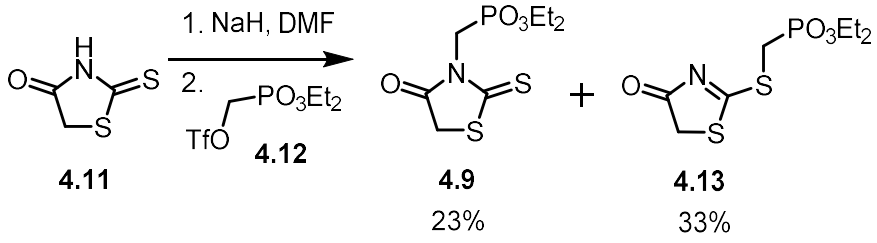

Figure 4-4. The synthesis of compound **4.9**, rhodanine-3-methyl phosphonic ester, and compound **4.13**, rhodanine-2-methyl phosphonic ester.

4-Bromo-7-(4-(*p*-tolyl)-1,2,3,3a,4,8b-hexahydrocyclopenta[*b*]indol-7-yl)benzo[*c*][1,2,5]thiadiazole was synthesized following literature procedures via a hydroboration/reduction, Buchwald-Hartwig cross-coupling, bromination, borylation, and Suzuki coupling (Figure 4-5). C-H cross-coupling conditions were employed to form 4,4-bis(2-ethylhexyl)-6-(7-(4-(*p*-tolyl)-1,2,3,3a,4,8b-hexahydrocyclopenta[*b*]indol-7-yl)benzo[*c*][1,2,5]thiadiazol-4-yl)-4*H*-cyclopenta[2,1-*b*:3,4-*b'*]dithiophene-2-carbaldehyde. 5-(Dibutylamino)thiophene-2-carbaldehyde (**4.21**, Figure 4-7) was previously synthesized by Yanrong Shi from the Marder group, and was repurified and fully characterized.

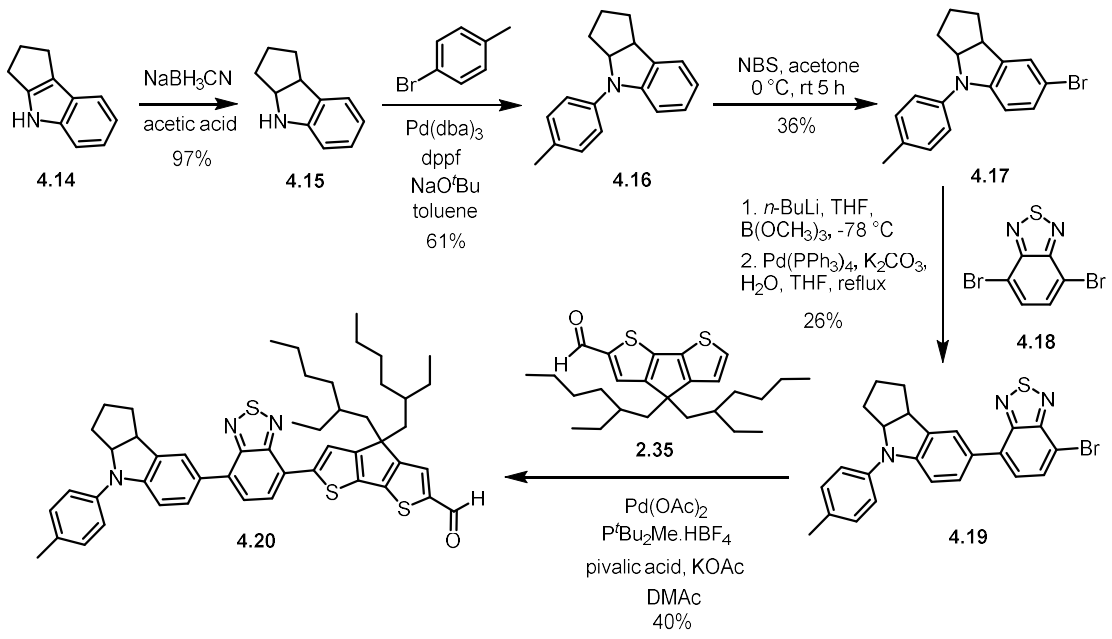

Figure 4-5. Donor-π-acceptor dye synthesis for condensation with rhodanine anchors.

The aldehyde-terminated compounds **4.20** and **4.21** were condensed with rhodanine-3-acetic acid (**4.22**) and rhodanine-3-methyldiethylphosphonate (**4.9**) to yield the final sensitizers **4.1** and **4.3** and the diethylphosphonate intermediates **4.23** and **4.24** (Figure 4-6, Figure 4-7). Compounds **4.23** and **4.24** were deprotected under literature conditions to yield the final sensitizers **4.2** and **4.4**.

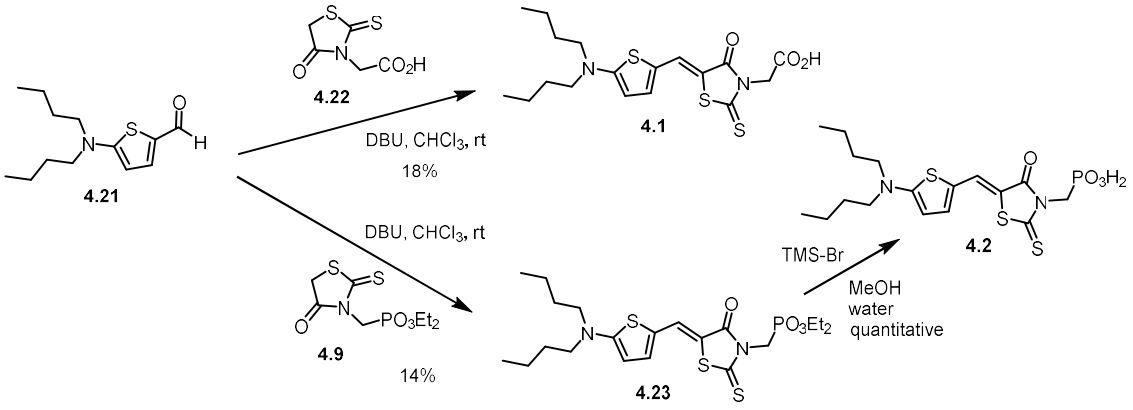

Figure 4-6. Condensation and deprotection to yield final sensitizers **4.1**-**4.2**.

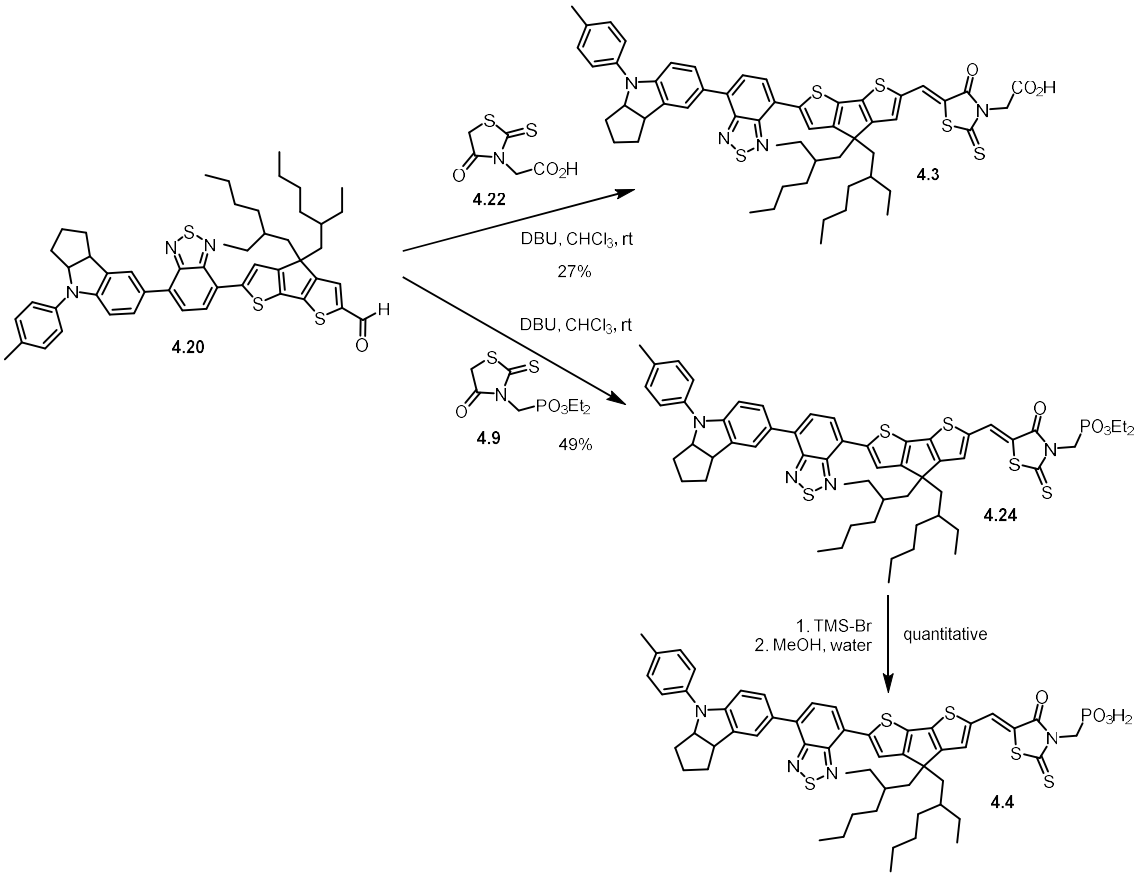

Figure 4-7. Condensation and deprotection to yield final sensitizers **4.3**-**4.4**.

4.3 Optical and Electrochemical Properties

The UV-Vis/NIR spectra in $CHCl_3$ showed absorption spectra with absorption maxima at near 530 and 580 nm (Table 4-1), as expected based on literature donor-π-acceptor sensitizers.[121,122] To obtain the oxidation potentials of the adsorbed dyes,[135,136] the donor-π-acceptor dyes were adsorbed onto TiO_2 films without $TiCl_4$ pretreatment that were dipped for 4 h in a 0.05 mM dye solution in 1:4 chloroform:ethanol with 0 or 6 mM CDCA. Cyclic voltammetry was performed using the sensitized films in a solution of acetonitrile with a Ag/AgCl reference electrode calibrated to ferrocenium/ferrocene (0.63 V vs. NHE)[137] to yield the ground-state oxidation potential of the adsorbed dye. The ground-state oxidation potentials provide at least 0.6 V of driving force for dye regeneration by the I_3^-/I^- redox couple (at ~0.35 V vs. NHE),[138] which is more than sufficient, as no more than 0.5 V of driving force is generally needed, depending on the sensitizer.[32]

Table 4-1. Optical and electrochemical properties of sensitizers **4.1**-**4.4**.

Dyes	λ_{max} [nm][a)]	$E_{0-0}{}^{opt}$ [eV][b)]	$E_{(S^+/S)}$ [V][c)]	$E_{(S^+/S^*)}$ [V][d)]
4.1	533	2.26	+1.02	−1.24
4.2	534	2.20	+1.03	−1.17
4.3	588	1.87	+0.95	−0.92
4.4	580	1.82	+0.96	−0.86

[a)] Measured in chloroform; [b)] Determined from the intersection of the normalized absorption and emission spectra in chloroform. [c)] Half-wave ground state oxidation potentials vs. NHE determined via cyclic voltammetry on TiO_2 films in a solution of 0.1 M lithium bistrifluoromethanesulfonimidate (LiTFSI) in MeCN. [d)] Excited-state oxidation potentials calculated according to the following equation: $E_{(S^+/S^*)} = E_{(S^+/S)} - E_{0-0}$.

4.4 Computational Investigation

To examine the extent of conjugation between the rhodanine acceptor and the carboxylic or phosphonic acid binding groups, the molecular orbitals of sensitizers **4.1**-**4.4** were calculated using density functional theory, with the ground-state electronic structure optimized at the M06-2X/6-31G(d) level (Table 4-2). As expected, the electron density in these orbitals did not extend onto the carboxylic or phosphonic acid anchoring groups. In the LUMO, a larger distribution of electron density was seen on the sulfur atom of the rhodanaine for all sensitizers. The previous authors had hypothesized that electron transfer proceded through the oxygen of the rhodanine, but the LUMO electron density distribution suggests that electron transfer may proceed through the sulfur.

Table 4-2. HOMO and LUMO for sensitizers **4.1**-**4.4** for ground state structures optimized in vacuum at the M06-2X/6-31G(d) level. For sensitizers **4.1**-**4.2**, the C=S is pointing downward, while for sensitizers 4.3-4.4, it is pointing upward.

MO	HOMO	LUMO
4.1	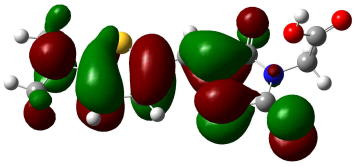	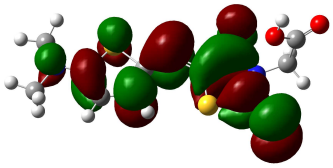
4.2	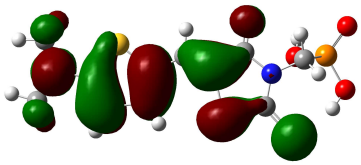	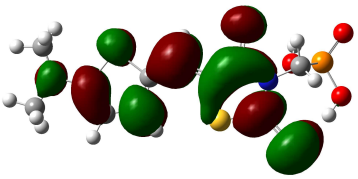
4.3	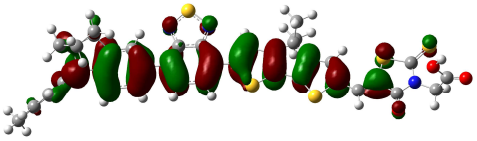	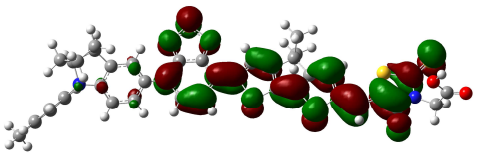
4.4	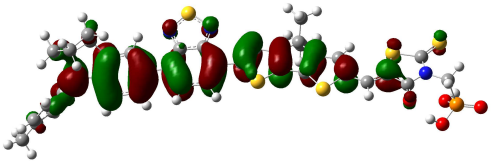	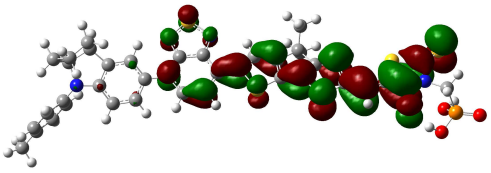

4.5 Absorption Spectra of Dyes Adsorbed on TiO_2 Films

In Figure 4-8, the UV-vis absorption spectra for sensitizers **4.1**-**4.4** adsorbed on TiO_2 films in the presence of 0 or 6 mM CDCA exhibits broadening compared to the peaks seen in the solution spectra (Figure 4-8). In the presence of CDCA, the intensity of the absorption spectra for the dibutylaminothiophene-substituted sensitizers **4.1** and **4.2** decreases, as expected due to co-sensitization of CDCA at the TiO_2 surface. The intensity of the absorption spectra for the indoline-BTD-CPDT-substituted sensitizers **4.3** and **4.4** in the presence of CDCA unexpectedly increases by a minor amount, potentially due to CDCA creating more favorable conditions for dye adsorption.

The spectra illustrate that for dyes **4.1** and **4.2**, there is a large difference in dye coverage between the carboxylic acid anchored sensitizer **4.1** and the phosphonic acid anchored sensitizer **4.2**, with the phosphonic acid promoting increased dye adsorbed. Sensitizers **4.3** and **4.4** do not show an appreciable difference in dye adsorbed between the carboxylic (**4.3**) and phosphonic acid (**4.4**) sensitizers. This may indicate that the packing of the indoline-BTD-CPDT-substituted sensitizers on the surface is determining the extent of adsorption more than the strength of the binding group present.

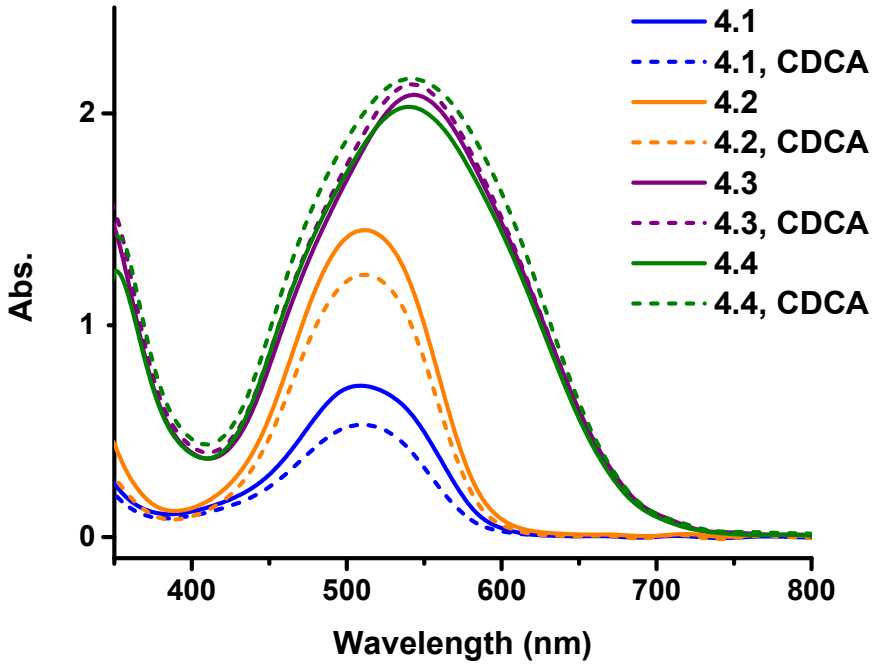

Figure 4-8. Absorption spectra of TiO_2 films sensitized with sensitizers **4.1**-**4.4**.

4.6 Photovoltaic Characterization of Dye-Sensitized Solar Cells

Examining the photovoltaic performance across the series **4.1**-**4.4** (Table 4-3, Figure 4-9), a large variation was seen in the performance was seen. Compared to the carboxylic acid-substituted dibutylaminothiophene-based sensitizer **4.1**, the phosphonic acid-substituted dibutylaminothiophene-based sensitizer **4.2** exhibited a decrease of around 30% PCE, derived from decreases in both J_{SC} and V_{OC}. Examining the indoline-BTD-CPDT-substituted sensitizers **4.3** and **4.4**, an even greater decrease of around 60% in the PCE was seen when moving from the carboxylic acid-substituted sensitizer **4.3** to the phosphonic acid-substituted sensitizer **4.4**.

Table 4-3. Photovoltaic characterization of dye-sensitized solar cell devices.

	V_{OC} (mV)	J_{SC} (mA/cm^2)	FF	PCE (%)
4.1, CDCA	0.475 ± 0.008	3.46 ± 0.77	0.506 ± 0.119	0.86 ± 0.41
4.1	0.474 ± 0.001	4.06 ± 0.08	0.614 ± 0.004	1.18 ± 0.01
4.2, CDCA	0.447 ± 0.001	2.24 ± 0.09	0.593 ± 0.016	0.59 ± 0.01
4.2	0.441 ± 0.007	3.25 ± 0.27	0.589 ± 0.052	0.84 ± 0.01
4.3, CDCA	0.599 ± 0.004	4.88 ± 0.56	0.741 ± 0.009	2.17 ± 0.29
4.3	0.597 ± 0.001	5.02 ± 0.08	0.748 ± 0.008	2.24 ± 0.01
4.4, CDCA	0.546 ± 0.007	2.61 ± 0.23	0.716 ± 0.043	0.95 ± 0.14
4.4	0.553 ± 0.007	2.58 ± 0.02	0.763 ± 0.006	1.09 ± 0.03

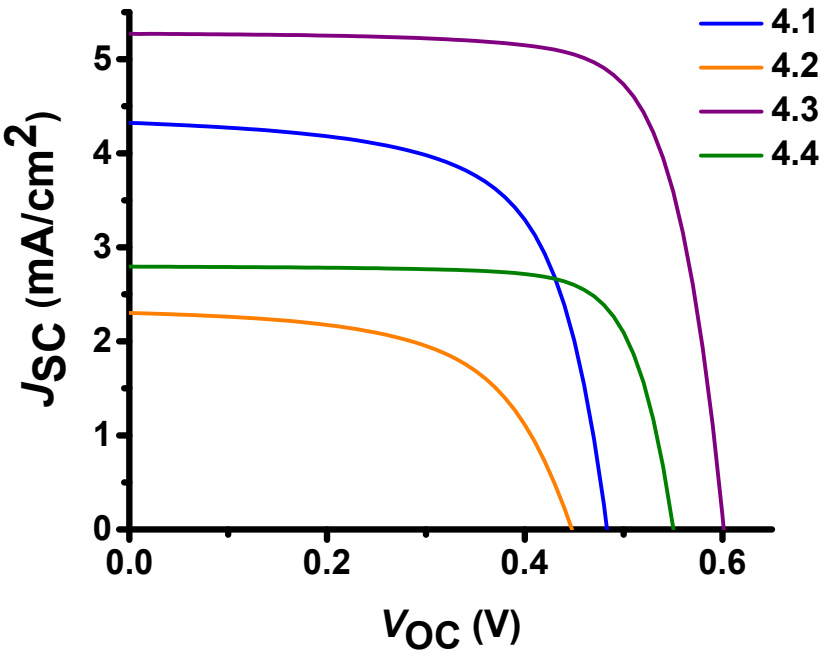

Figure 4-9. *J-V* curves with maximum PCE for sensitizers **4.1**-**4.4** coadsorbed with CDCA.

4.6.1 IPCE

Compared to the carboxylic acid-substituted dibutylaminothiophene-based sensitizer **4.1**, the phosphonic acid-substituted dibutylaminothiophene-based sensitizer **4.2** exhibited a nearly 50% increase in peak absorbance when adsorbed on TiO_2, while exhibiting a decrease in IPCE % of approximately 50% compared to that of sensitizer **4.1** (Figure 4-10). This could be due to a higher percentage of dye on the surface leading to tightly packed sensitizers, potentially preventing the rhodanine acceptor from interacting with the TiO_2 surface. Examining the indoline-BTD-CPDT-substituted sensitizers **4.3** and **4.4**, the phosphonic acid-substituted sensitizer **4.4** exhibited a decrease in IPCE % of approximately 50% compared to that of the carboxylic acid-substituted sensitizer **4.3**, even though the absorption when adsorbed on TiO_2 was not appreciably different between the carboxylic (**4.3**) and phosphonic acid (**4.4**) sensitizers. The decrease in IPCE % for phosphonic acid-based sensitizer **4.4** relative to carboxylic acid based sensitizer **4.3** may indicate that the lower current seen for phosphonic acid-based rhodanine acceptor sensitizers is not simply due to tight packing on the surface as could be hypothesized for sensitizer **4.2**, based on differences in absorption on TiO_2, but that there may be a general problem with electron injection from the rhodanine-3-methylphosphonic acid anchor.

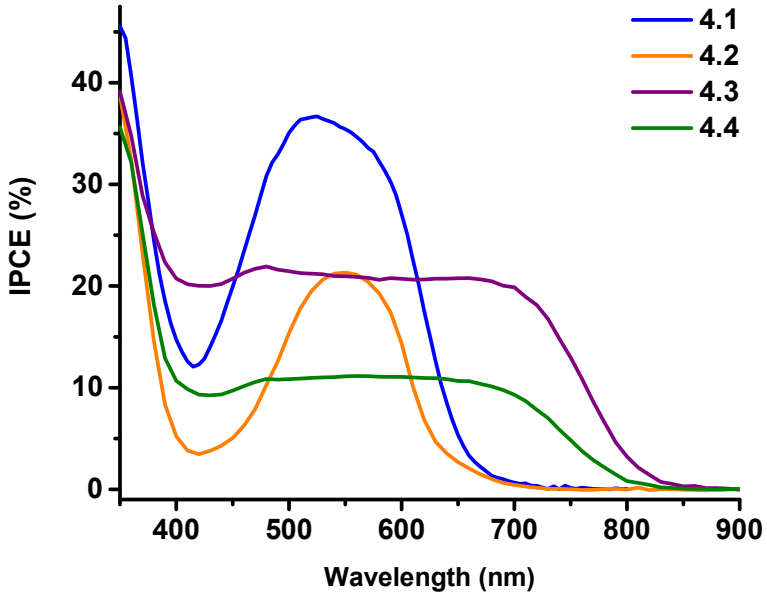

Figure 4-10. IPCE spectra of sensitizers **4.1**-**4.4** coadsorbed with CDCA.

4.7 Photoelectrochemical Characterization

Photoelectrochemical methods may help elucidate the factors behind the low J_{SC} and V_{OC} seen for the rhodanine-3-methylphosphonic acid anchor.

4.7.1 Charge transport lifetime

Charge transport lifetime provides a measure of the ability of the charges to be transported in the device, and can be largely affected by modifications to the TiO_2 and electrolyte, but is often less affected by the dyes' structure. Interestingly, the electron transport lifetime varied widely in magnitude between the dibutylaminothiophene-substituted rhodanine sensitizers **4.1**-**4.2** and the indoline-BTD-susbstituted rhodanine

sensitizers **4.3**-**4.4** (Figure 4-11). The shape of the plots was also different, with curved electron transport plots observed for the indoline-BTD-susbstituted rhodanine sensitizers **4.3** and **4.4**. The charge transport observed for sensitizers **4.1** and **4.2** correlates with the *J*-*V* results, with increased charge transport, J_{SC} and IPCE % for sensitizer **4.1** relative to sensitizer **4.2**. However, the charge transport observed for sensitizers **4.3** and **4.4** does not correlate to the *J*-*V* results, with sensitizer **4.4** exhibiting a slight increase in charge transport, but a decrease in J_{SC} and IPCE% compared to sensitizer **4.3**. This may indicate that that the charge transport lifetime is affected by variation in the sensitizer anchoring group, but that this is not the largest factor in determining device performance.

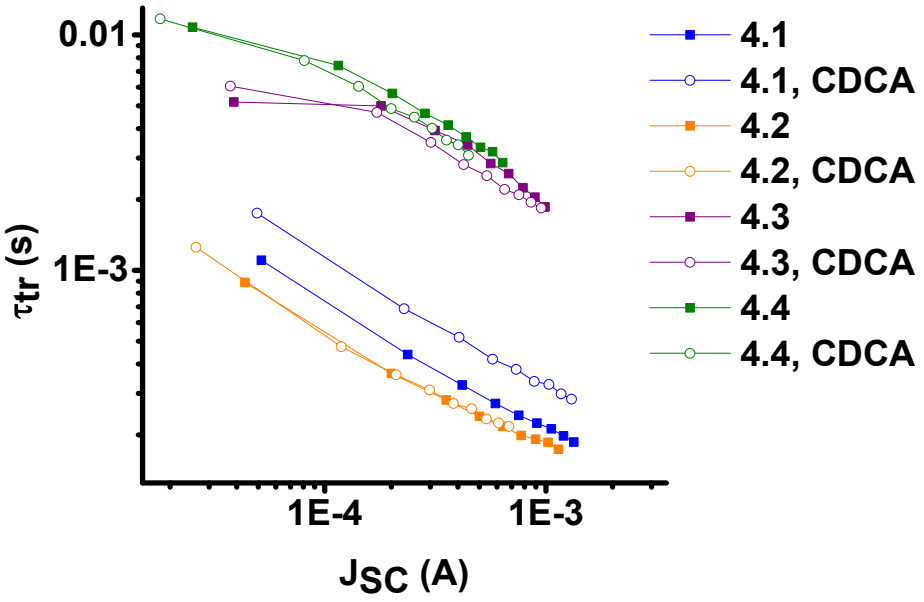

Figure 4-11. Charge transport lifetime versus short circuit current for sensitizers **4.1**-**4.4**.

4.7.2 Charge extraction measurements

Charge extraction measurements can provide an understanding of the relative shifts in the TiO_2 conduction band for different sensitizers or amounts of coadsorbent. In the presence of CDCA, the charge extraction of the dibutylaminothiophene-substituted rhodanine sensitizers **4.1** and **4.2** increases, while the charge extraction of the indoline-BTD-susbstituted rhodanine sensitizers **4.3** and **4.4** decreases (Figure 4-12). The charge extraction observed for sensitizers **4.1** and **4.2** is nearly identical, while the carboxylic acid-substituted sensitizer **4.3** displays a slight increase in charge extraction.

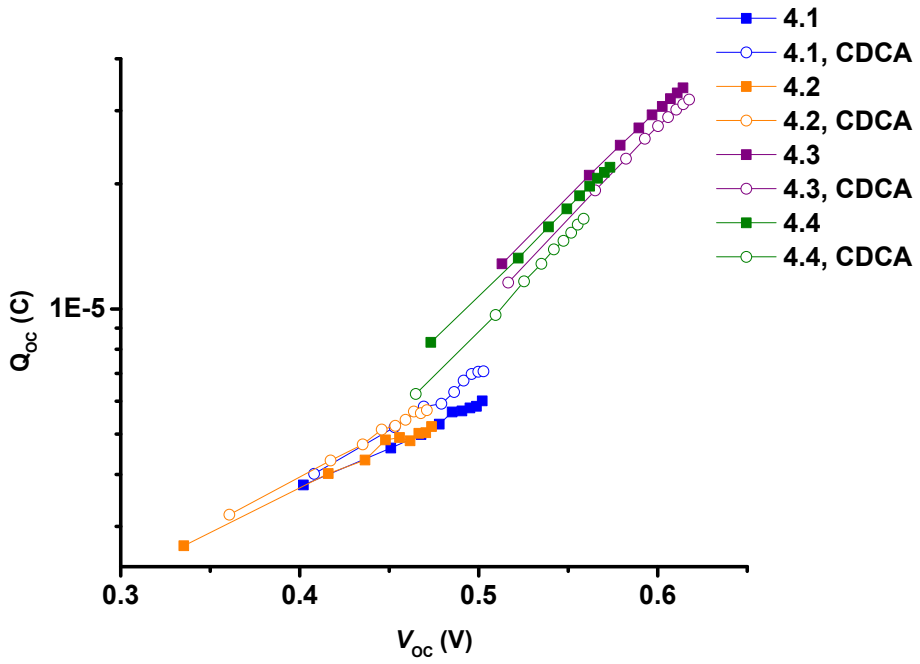

Figure 4-12. Charge extraction vs. open circuit voltage for sensitizers **4.1**-**4.4**.

4.7.3 Electron lifetime

Electron lifetime measurements can provide an understanding of the relative amounts of recombination that decrease the electron lifetime. To focus on differences in electron recombination, shifts in the TiO_2 conduction band position are accounted for using the change in V_{OC} from charge extraction measurements, providing the adjusted plots. As the slope of the charge extraction plots for sensitizers **4.1**-**4.2** differed from those of **4.3**-**4.4**, the V_{OC} for each group was normalized separately (Figure 4-13).

The phosphonic acid sensitizers **4.2** and **4.4** exhibit a lower electron lifetime than the corresponding carboxylic acid sensitizers **4.1** and **4.3**. This data is in agreement with the lower V_{OC} observed for sensitizers **4.2** and **4.4** and indicates that the use of a rhodanine-3-methylphosphonic acid anchor promotes recombination to a greater extent than the rhodanine-3-acetic acid anchor.

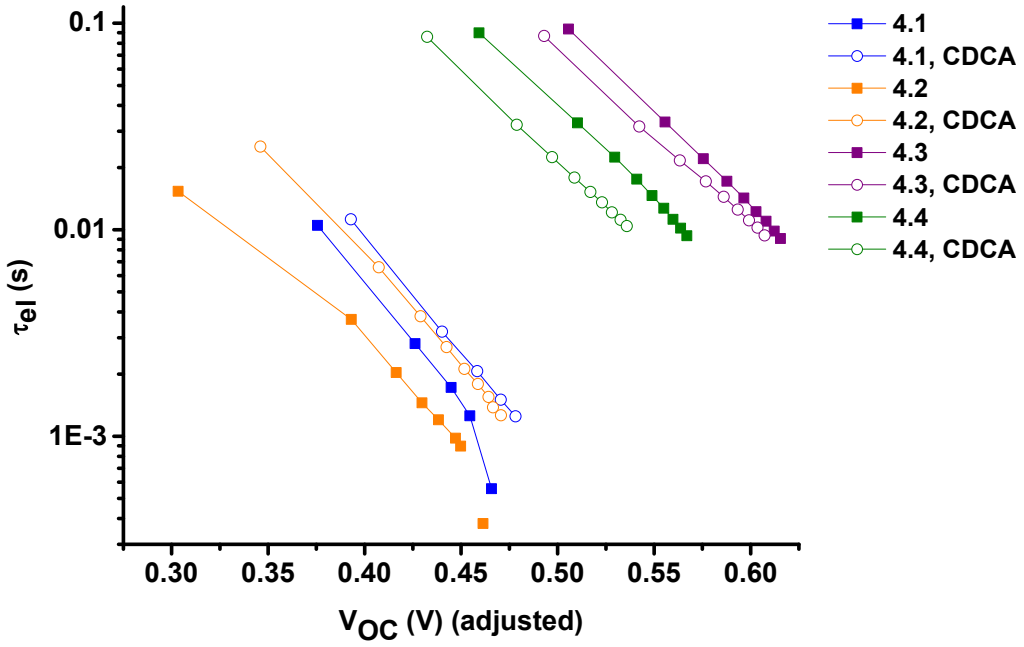

Figure 4-13. Electron lifetime vs. open circuit voltage, adjusted using the change in the V_{OC} from charge extraction measurements, for sensitizers **4.1**-**4.4**.

4.8 Sensitized Film Stability

Sensitizer desorption from the TiO_2 surface is an important factor contributing to DSSC device stability and commercialization. To examine the effect of the anchoring group on desorption of the sensitizers, several conditions for potential sensitizer desorption were successively examined: soaking in an acetonitrile solution, soaking in electrolyte, and heating at 85 °C in electrolyte. First, the sensitized films were soaked in an acetonitrile solution for 5 wks. For the dibutylaminothiophene-based sensitizers **4.1** and **4.2** (Figure 4-14), the phosphonic acid-based sensitizer **4.2** retained its initial

absorption intensity, while the absorption for the carboxylic acid-based sensitizer **4.1** decreased to one third of its original intensity. For the indoline-BTD-CPDT-substituted sensitizers **4.3** and **4.4** (Figure 4-15), the phosphonic acid-based sensitizer **4.4** retained and sharpened its initial absorption intensity, while the absorption for the carboxylic acid-based sensitizer **4.1** decreased by one sixth.

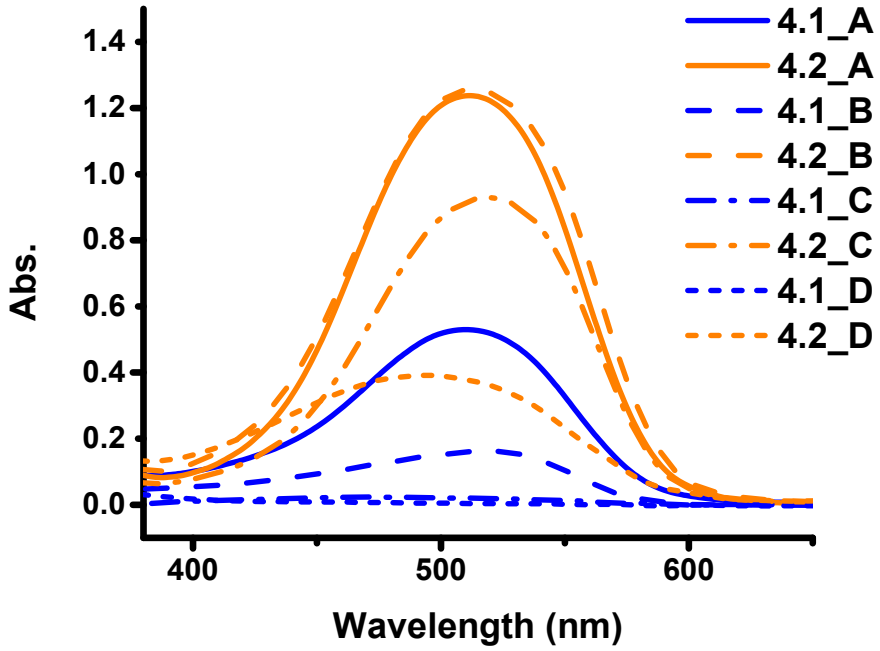

Figure 4-14. Absorption of sensitizers **4.1** and **4.2** on TiO_2 A) after sensitization in dye bath with 6 mM CDCA, then after successive exposure to the following conditions: B) soaking in acetonitrile for 5 wks, C) soaking in electrolyte for 1 d, and D) heating at 85 °C in electrolyte for 3 d.

The subsequent soaking in electrolyte solution for 1 d did not have an appreciable effect on the sensitized film absorption intensity for the indoline-BTD-CPDT-based sensitizers **4.3** and **4.4** (Figure 4-15). For the dibutylaminothiophene-based sensitizers **4.1**

and **4.2** (Figure 4-14), the phosphonic acid-based sensitizer **4.2** decreased to three fourths of its initial absorption intensity, while the absorption for the carboxylic acid-based sensitizer **4.1** decreased significantly to less than 5% of its original absorption.

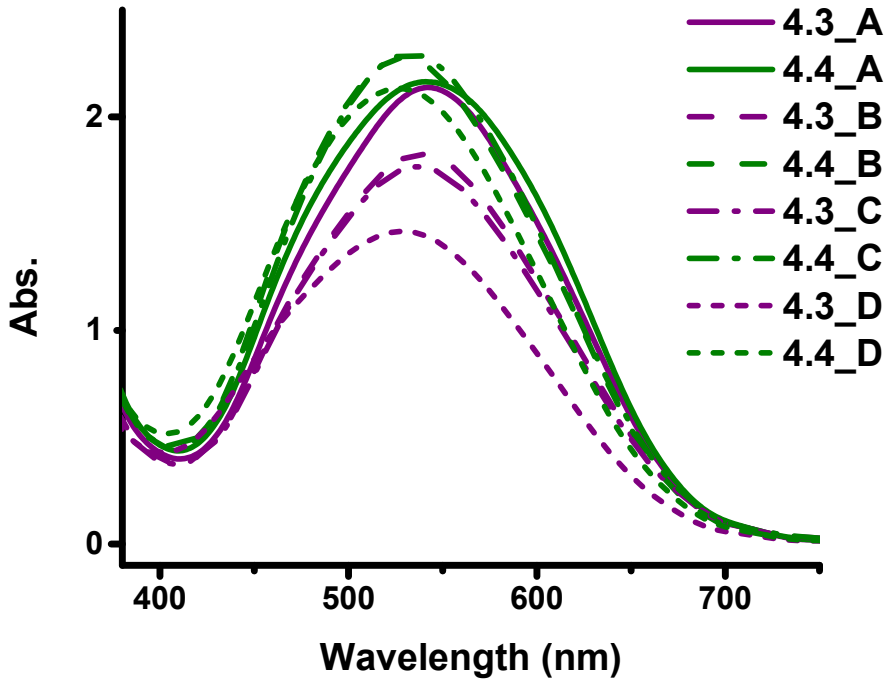

Figure 4-15. Absorption of sensitizers **4.3** and **4.4** on TiO_2: A) after sensitization in dye bath with 6 mM CDCA, then after successive exposure to the following conditions: B) soaking in acetonitrile for 5 wks, C) soaking in electrolyte for 1 d, and D) heating at 85 °C in electrolyte for 3 d.

Last, the sensitized films were heated in electrolyte at 85 °C for 3 d. For the dibutylaminothiophene-based sensitizers **4.1** and **4.2** (Figure 4-14), the absorption for the phosphonic acid-based sensitizer **4.2** decreased to one-third of its original absorption intensity, while the absorption for the carboxylic acid-based sensitizer **4.1** decreased to zero. For the indoline-BTD-CPDT-substituted sensitizers **4.3** and **4.4** (Figure 4-15), the

phosphonic acid-based sensitizer **4.4** saw less than a one-tenth decrease of the sharpened absorption, while the absorption for the carboxylic acid-based sensitizer **4.1** decreased to two-thirds of its original absorption intensity.

For sensitizers **4.1**-**4.4**, the phosphonic acid-substituted rhodanine anchor imparts increased stability against desorption under device-relevant conditions when compared to the carboxylic acid-substituted rhodanine anchor. The dye structure also appears to play a large role in determining the extent of dye desorption, potentially due to differences in monolayer formation at the surface.

4.9 Conclusion

This study examined whether the use of phosphonic acids in conjunction with rhodanine anchoring groups could promote both strong binding and efficient electron injection. A comparison between rhodanine-3-methylphosphonic acid and rhodanine-3-acetic acid on two donor-π-acceptor sensitizers with dibutylaminothiophene or indoline-benzothiadiazole functionalities was made to see differences in the stability and performance for the two anchoring groups. Incorporating the rhodanine-3-methylphosphonic acid revealed an overall decrease in the IPCE by nearly 50% for both **4.2** and **4.4**, which translated into a decrease in the PCE of 30-60%. A lower J_{SC} was seen for the rhodanine-3-methylphosphonic acid-substituted sensitizers **4.2** and **4.4** than was seen for the control sensitizers employing rhodanine-3-acetic acid. This may be due to the angle of the phosphonic acid binding to the TiO_2 surface, with one possible binding angle illustrated schematically in Figure 4-16. A lower V_{OC} by approximately 30 mV is seen for sensitizer **4.2** vs. sensitizer **4.1**, with a lower V_{OC} by approximately 50 mV seen for

sensitizer **4.4** vs. **4.3**. The lower V_{OC} relates to the lower electron lifetimes and higher recombination observed for the phosphonic acid-substituted sensitizers **4.2** and **4.4** vs. the carboxylic acid-substituted sensitizers **4.1** & **4.3**.

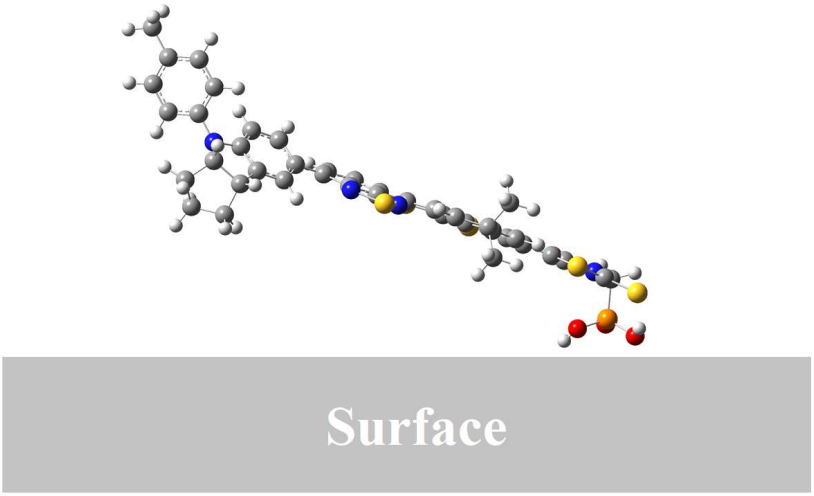

Figure 4-16. Schematic drawing of potential binding angle for sensitizer **4.4**, illustrating that the O and S of the rhodanine may not necessarily be in contact with the TiO_2 surface.

HOMO and LUMO calculations demonstrated that electron density does not rest on the methylene of the phosphonic acid, suggesting that electron injection would proceed through the rhodanine acceptor. In many binding configurations, the rhodanine C=S or C=O may have difficulty interacting with the surface, preventing effective electron injection and resulting in the decreased currents observed. It was also observed that the phosphonic acid-substituted rhodanine anchor imparts increased stability against dye desorption under device-relevant conditions when compared to the carboxylic acid-substituted rhodanine anchor. Phosphonic acids have promise for preventing dye

desorption, and future studies could examine alternate structures incorporating phosphonic acids where stronger binding may still allow ancillary acceptors to interact with the surface.

4.10 Experimental Methods

4.10.1 Synthesis of sensitizer 4.1

4.10.1.1 Synthesis of 5-(dibutylamino)thiophene-2-carbaldehyde

Synthesis by Yanrong Shi, characterization by author.

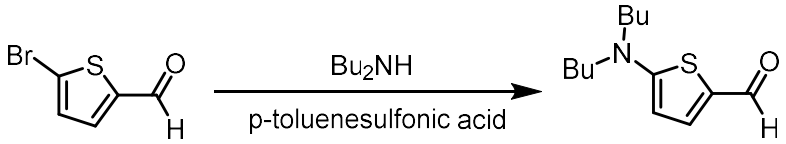

5-Bromothiophene-2-carbaldehyde (19.7 g, 0.1 mol), dibutylamine (50 mL, 0.3 mol), and *p*-toluenesulfonic acid (0.57 g, 0.3 mol) were heated at 100 °C for 24 h. After cooling to room temperature, water (200 mL) was added and the mixture was stirred for 30 min. The solution was extracted three times with CH_2Cl_2, dried over $MgSO_4$, and filtered. The solvent was removed under reduced pressure. The product was purified by silica gel column chromatography (toluene:EtOAc = 15:1). The main band was collected and the solvent removed under reduced pressure. The product was further purified by silica gel column chromatography (toluene:EtOAc = 15:1). The main band was collected and the solvent removed under reduced pressure to yield a clear yellow oil (12.6 g, 53%). ^{1}H NMR (500 MHz, $CDCl_3$): δ (ppm) = 9.46 (s, 1H), 7.44 (d, J = 4.5 Hz, 1H), 5.9 (d, J = 4.5

Hz, 1H), 3.33 (t, J = 7.7 Hz, 4H), 1.68-1.61 (m, 4H), 1.36 (sext, J = 7.5 Hz, 4H), 0.96 (t, J = 7.4 Hz, 6H). $^{13}C\{^{1}H\}$ NMR (126 MHz, $CDCl_3$): δ (ppm) = 179.65, 167.05, 140.74, 125.17, 102.75, 53.53, 28.94, 20.14, 13.83. HRMS (ESI): m/z 240.1415 $[M]^+$ (calcd for $C_{13}H_{22}NOS$: 240.1417). Anal. Calcd for $C_{13}H_{21}NOS$ (%): C, 65.23; H, 8.84; N, 5.85. Found: C, 65.29; H, 8.81; N, 5.88.

4.10.1.2 Syntheis of (*Z*)-2-(5-((5-(dibutylamino)thiophen-2-yl)methylene)-4-oxo-2-thioxothiazolidin-3-yl)acetic acid

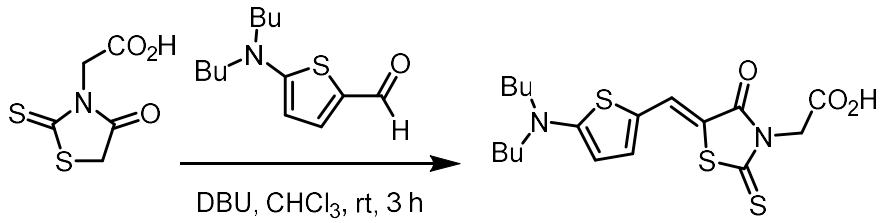

To a stirred solution of 5-(dibutylamino)thiophene-2-carbaldehyde (0.600 g, 2.51 mmol) and rhodanine-3-acetic acid (4.79 g, 25.1 mmol) in HPLC grade chloroform (12 mL), DBU (3.82 mL, 25.1 mmol) was added dropwise. The reaction was stirred at room temperature and monitored by TLC. After 1 h, additional DBU was added (0.37 mL, 2.51 mmol). The reaction was stirred at room temperature and stopped when complete (3 h). The solution was acidified with 2 N HCl, extracted three times with CH_2Cl_2, dried over Na_2SO_4, and filtered. The solvent was removed under reduced pressure. The crude product was purified via silica gel chromatography on the Biotage Isolera system (25 g silica gel cartridge). The column was run in CH_2Cl_2:MeOH 100:0, gradually increasing to 85:15 to remove the main band. The main red band was collected and the solvent removed under reduced pressure. The residue was further purified by size exclusion column (SEC) chromatography (S-X1 Biobeads in THF (without stabilizers, HPLC grade

or from a solvent purification system)). A one-foot long column of one-inch diameter was run, and the main band was collected and the solvent removed under reduced pressure. A three-foot column of 1.5-inch diameter was run, and the main band was collected and the solvent removed under reduced pressure to yield 0.58 g. For an analytically pure sample, the residue was further purified via silica gel chromatography on the Biotage Isolera system (50 g silica gel cartridge, dry loaded). The column was run in hexane:EtOAc 100:0, gradually increasing to 15:85 to remove the main band. The solvent was removed under reduced pressure to yield a red solid (0.182 g, 18%). ^{1}H NMR (500 MHz, $CDCl_3$): δ (ppm) = 7.79 (s, 1H), 7.28 (d, *J* = 4.5 Hz, 1H), 6.02 (d, *J* = 4.6 Hz, 1H), 4.84 (s, 2H), 3.43-3.35 (m, 4H), 1.68 (quin, *J* = 7.7 Hz, 4H), 1.40 (sext, *J* = 7.4 Hz, 4H), 0.99 (t, *J* = 7.4 Hz, 6H). $^{13}C\{^{1}H\}$ NMR (126 MHz, $CDCl_3$): δ (ppm) = 192.04, 168.64, 168.23, 167.11, 140.78, 129.05, 120.74, 108.34, 105.03, 53.99, 45.04, 29.29, 20.27, 13.89. HRMS (ESI): m/z 411.0872 $[M]^-$ (calcd for $C_{18}H_{23}N_2O_3S_3$: 411.0876). Anal. Calcd for $C_{18}H_{24}N_2O_3S_3(H_2O)_{0.5}$ (%): C, 51.28; H, 5.98; N, 6.64. Found: C, 51.43; H, 6.04; N, 6.42.

4.10.2 Synthesis of sensitizer 4.2

4.10.2.1 Synthesis of (diethoxyphosphinyl)methyl triflate

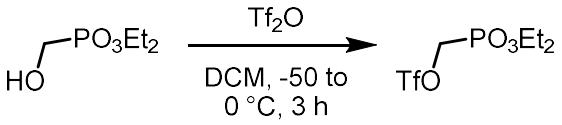

To a stirred solution of dialkyl (hydroxymethyl)phosphonate (3.00 g, 17.8 mmol) and 2,6- lutidine (2.56 mL, 21.9 mmol) in anhydrous CH_2Cl_2 (30 mL) at -78 °C under N_2 was added trifluoromethanesulfonic anhydride (3.48 mL, 20.7 mmol) dropwise. The resulting

mixture was allowed to warm to 0 °C over a period of 3 h, whereupon the dark brown solution was diluted with ether (180 mL). The precipitates formed were removed by filtration. The ethereal solution was successively washed with water, 1 N HCl, and brine, dried over Na_2SO_4, and filtered. After concentration, a yellow oil was obtained, which was used in the next step without further purification (3.61 g, 67% yield). ^{1}H NMR was consistent with that of Xu et al.[190]

4.10.2.2 Synthesis of 3-(((diethyl-λ^3-oxidaneyl)(λ^1-oxidaneyl)phosphoryl)methyl)-2-thioxothiazolidin-4-one

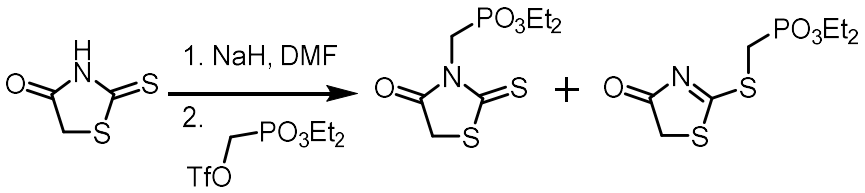

An oven-dried round bottom flask (100 mL) was flushed with nitrogen gas and subsequently charged with rhodanine (1.00 g, 7.51 mmol), DMF (6 mL), and a magnetic stirbar. While under nitrogen, the flask was placed in an ice bath and NaH (60% w/w, 0.36 g, 9.01 mmol, 1.2 equiv) was added in 3 portions. A white suspension formed, then the evolution of gas ceased. The flask was removed from the ice bath and allowed to warm to room temperature. Diethoxyphosphinyl)methyl triflate (2.71 g, 9.01 mmol, 1.2 equiv) was added in one portion. The reaction was stirred at room temperature and monitored until starting material was no longer visible by NMR (3 hours). After 16 h, the solution was allowed to cool to room temperature and water was added (20 mL). The neutral aqueous solution was washed with CH_2Cl_2 (3 x 25 mL). The aqueous solution was then acidified with a 2N solution of HCl (5 mL), and extracted with CH_2Cl_2 (1 x 25

mL). The combined organic solution was washed with brine (50 mL), dried over Na_2SO_4, and filtered. The solvent was removed under reduced pressure, followed by high vacuum. The residue was purified by silica gel chromatography on the Biotage Isolera system (100 g silica gel cartridge). The column was run in CH_2Cl_2:acetone 100:0, gradually increasing to remove the main bands, which exited the column from 5-30% acetone. The *N*-alkylated product was collected, followed by the *S*-alkylated product, both as light yellow oils, and the solvent removed under reduced pressure. *N*-methylated product (0.52 g, 23%): ^{1}H NMR (400 MHz, $CDCl_3$): δ (ppm) = 4.48 (d, *J* = 12.4 Hz, 2H), 4.17 (dq, *J* = 7.8, 7.2 Hz, 4H), 4.06 (s, 2H), 1.33 (t, *J* = 7.1 Hz, 6H). ^{13}C{^{1}H} NMR (101 MHz, $CDCl_3$): δ (ppm) = 199.65, 199.63, 172.70, 62.97, 62.91, 40.66, 39.11, 35.30, 16.39, 16.32. ^{31}P NMR (162 MHz, $CDCl_3$): δ (ppm) = 18.54. S-methylated product (0.75 g, 33%): ^{1}H NMR (400 MHz, $CDCl_3$): δ (ppm) = 4.18 (dq, *J* = 8.3, 7.1 Hz, 4H), 4.12 (s, 2H), 3.74 (d, *J* = 13.9 Hz, 2H), 1.34 (t, *J* = 7.1 Hz, 6H). ^{13}C{^{1}H} NMR (101 MHz, $CDCl_3$): δ (ppm) = 200.22, 200.15, 186.08, 62.69, 62.63, 39.82, 26.95, 25.48, 15.85, 15.80. ^{31}P NMR (162 MHz, $CDCl_3$): δ (ppm) = 20.15.

4.10.2.3 Synthesis of (*Z*)-5-((5-(dibutylamino)thiophen-2-yl)methylene)-3-(((diethyl- λ^3-oxidaneyl)(λ^1-oxidaneyl)phosphoryl)methyl)-2-thioxothiazolidin-4-one

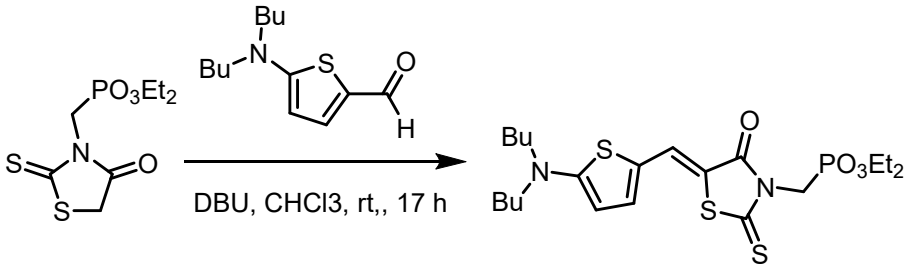

To a stirred solution of 5-(dibutylamino)thiophene-2-carbaldehyde (0.100 g, 0.418 mmol) and rhodanine-3-acetic acid (0.118 g, 0.418 mmol) in HPLC grade chloroform (1 mL), DBU (64 μL, 0.418 mmol) was added dropwise. The reaction was stirred at room temperature and monitored by TLC. The reaction was stirred at room temperature and stopped when complete (17 h). The solution was acidified with 2 N HCl, extracted three times with CH_2Cl_2, dried over Na_2SO_4, and filtered. The solvent was removed under reduced pressure. The crude product was purified by silica gel chromatography on the Biotage Isolera system (100 g silica gel cartridge). The column was run in CH_2Cl_2:acetone 100:0, gradually increasing to 97:3. The main red band was collected and the solvent removed under reduced pressure. The residue was further purified purified by silica gel chromatography on the Biotage Isolera system (100 g silica gel cartridge). The column was run in CH_2Cl_2:EtOAc 100:0, gradually increasing to 97:3. The main red band was collected and the solvent removed under reduced pressure to yield a bright pink-red solid (29 mg, 14%). ^{1}H NMR (400 MHz, $CDCl_3$): δ (ppm) = 7.77 (s, 1H), 7.22 (d, *J* = 4.8 Hz, 1H), 5.97 (d, *J* = 4.5 Hz, 1H), 4.62 (d, *J* = 12.4 Hz, 2H), 4.28-4.11 (m, *J* = 2.9 Hz, 4H), 3.36 (t, *J* = 7.7 Hz, 4H), 1.66 (quin, *J* = 7.7 Hz, 4H), 1.39 (sext, *J* = 7.6 Hz, 4H), 1.32 (td, *J* = 7.1, 0.4 Hz, 6H), 0.98 (t, *J* = 7.3 Hz, 6H). ^{13}C{^{1}H} NMR (101 MHz, $CDCl_3$): δ (ppm) = 190.73, 167.54, 166.32, 139.91, 128.44, 120.61, 108.47, 104.45, 53.79, 40.69, 39.15, 29.67, 29.13, 20.14, 16.39, 16.32, 13.81. ^{31}P NMR (162 MHz, $CDCl_3$): δ (ppm) = 19.14. HRMS (ESI): m/z 504.1337 [M+] (calcd for $C_{21}H_{33}N_2O_4PS_3$: 504.1335). See Figure A-2 in Appendix A for the HPLC.

4.10.2.4 Synthesis of (*Z*)-((5-((5-(dibutylamino)thiophen-2-yl)methylene)-4-oxo-2-thioxothiazolidin-3-yl)methyl)phosphonic acid

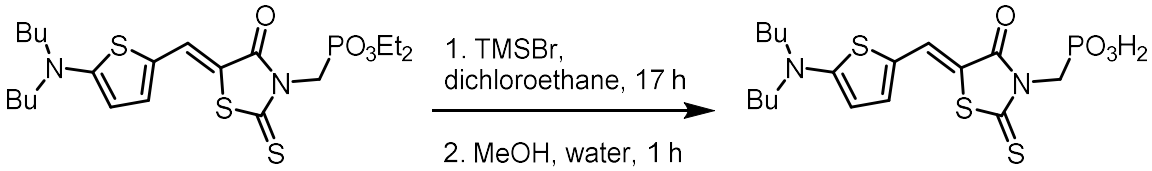

Diethyl (Z)-((5-((5-(dibutylamino)thiophen-2-yl)methylene)-4-oxo-2-thioxothiazolidin-3-yl)methyl)phosphonate (20 mg, 0.040 mmol) was added to an oven-dried round-bottom flask with a Dean-Stark water separator and condenser, then evacuated and filled with nitrogen three times. 1,2-Dichloroethane (1.25 mL) was added and the solution was stirred for 10 minutes at room temperature. Bromotrimethylsilane (0.05 mL, 0.4 mmol) was added and the reaction was stirred at 75 °C for 17 h. MeOH (1.6 mL) and water (2.4 mL) were added to quench the reaction, and the mixture was stirred and allowed to cool to room temperature for 1 h. The organic layer was extracted from CH_2Cl_2, dried over Na_2SO_4, and filtered. The solvent was removed under reduced pressure followed by high vacuum. The residue was dissolved in distilled CH_2Cl_2 and filtered through a 0.2 um PTFE filter. The solution was concentrated to minimal solvent under reduced pressure, then hexane was added and a precipiate formed. The solid was removed by vacuum filtration, washed with hexane, and dried under reduced pressure to yield a red solid (18 mg, quantitative). ^{1}H NMR (500 MHz, $CDCl_3$, CD_3OD, CF_3CO_2D): δ (ppm) = 7.66 (s, 1H), 7.26 (s, 1H), 6.07 (s, 1H), 4.46 (d, *J* = 12.7 Hz, 2H), 3.35 (s, br, 4H), 1.6 (quin, *J* =

7.6 Hz, 4H), 1.29 (sext, J = 7.6 Hz, 4H), 0.90 (t, J = 7.4 Hz, 6H). $^{13}C\{^{1}H\}$ NMR (101 MHz, $CDCl_3$, CD_3OD, CF_3CO_2D): δ (ppm) = 190.56, 141.53, 129.09, 105.3, 55.38, 42.14, 40.63, 28.95, 19.9, 13.32 (resonances not observed due to poor solubility). ^{31}P NMR (203 MHz, $CDCl_3$): δ (ppm) = 17.22. HRMS (ESI): m/z 447.0634 [M-] (calcd for $C_{17}H_{24}N_2O_4PS_3$: 447.0641). See Figure A-3 in Appendix A for HPLC trace.

4.10.3 Synthesis of sensitizer 4.3

4.10.3.1 Synthesis of 4,4-bis(2-ethylhexyl)-6-(7-(4-(*p*-tolyl)-1,2,3,3a,4,8b-hexahydrocyclopenta[*b*]indol-7-yl)benzo[*c*][1,2,5]thiadiazol-4-yl)-4*H*-cyclopenta[2,1-*b*:3,4-*b'*]dithiophene-2-carbaldehyde

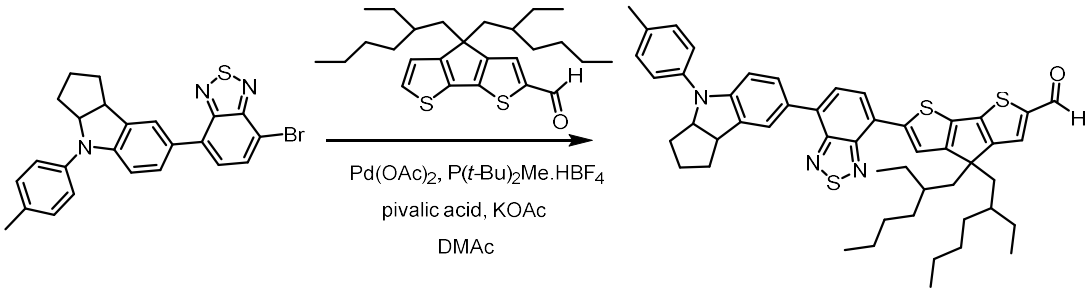

To a 20 mL oven-dried microwave vial cooled under nitrogen charged with a stir bar was added 4-bromo-7-(4-(*p*-tolyl)-1,2,3,3a,4,8b-hexahydrocyclopenta[*b*]indol-7-yl)benzo[*c*][1,2,5]thiadiazole (0.333 g, 0.720 mmol), 4,4-bis(2-ethylhexyl)-4*H*-cyclopenta[1,2-*b*:5,4-*b'*]dithiophene-2-carbaldehyde (0.367 g, 0.852 mmol), palladium(II) acetate (15 mg, 0.066 mmol), di-*tert*-butyl(methyl)phosphonium tetrafluoroborate (59 mg, 0.238 mmol), pivalic acid (67 mg, 0.65 mmol), and potassium acetate (0.193 g, 1.96 mmol), and the vial was sealed. After three cycles of high vacuum, then filling with nitrogen, anhydrous degassed dimethylacetamide (11.5 mL) was added.

The flask was filled with nitrogen, then the solution was heated to 120 °C for 12 h. The reaction mixture was cooled to room temperature, then poured over a plug of silica gel topped with Celite packed in a Buchner funnel. The plug was rinsed with CH_2Cl_2, the main red band collected, and the solvent was removed under reduced pressure. The residue was left under high vacuum overnight to remove residual dimethylacetamide. The crude product was purified via silica gel chromatography on the Biotage Isolera system (100 g silica gel cartridge, dry loaded by dissolving in CH_2Cl_2, adding 1 g silica gel, and removing the solvent under reduced pressure). The column was run in hexane:EtOAc, starting with 0% EtOAc and increasing to 1% EtOAc to remove the main band. The main dark red band was collected and the solvent removed under reduced pressure. The dark red residue was further purified by size exclusion column (SEC) chromatography (S-X1 Biobeads in THF (without stabilizers, HPLC grade or from a solvent purification system)). A one-foot long column of one-inch diameter was run, and the main band was collected and the solvent removed under reduced pressure. This column was repeated for further purification, then a three-foot column of 1.5-inch diameter was run, and the main band was collected and the solvent removed under reduced pressure. The residue was further purified via silica gel chromatography on the Biotage Isolera system in hexane:EtOAc, starting with 0% EtOAc and increasing to 1% EtOAc acetate to remove the main band. The main dark red band was collected and the solvent removed under reduced pressure to yield a dark red solid (232 mg, 40%). 80 mg of product was then purified additionally by reverse phase silica gel (C18) column chromatography in MeOH, with the main band collected and the solvent removed under reduced pressure to yield 71 mg of an analytically pure red solid. ^{1}H NMR (500 MHz,

$CDCl_3$): δ (ppm) = 9.85 (s, 1H), 8.08 (t, *J* = 6.5 Hz, 1H), 7.93 (dt, *J* = 7.6, 3.5 Hz, 1H), 7.81-7.78 (m, 1H), 7.73 (dtd, *J* = 8.3, 3.7, 1.8 Hz, 1H), 7.68 (d, *J* = 7.6 Hz, 1H), 7.6 (t, *J* = 4.2 Hz, 1H), 7.25 (d, *J* = 9.5 Hz, 2H), 7.18 (d, *J* = 8.3 Hz, 2H), 7.03 (d, *J* = 8.4 Hz, 1H), 4.87 (dtd, *J* = 8.5, 6.4, 1.8 Hz, 1H), 3.94 (td, *J* = 8.6, 1.8 Hz, 1H), 2.35 (s, 3H), 2.16-2.03 (m, 2H), 2.02 (d, *J* = 5.1 Hz, 2H), 2.00-1.91 (m, 2H), 1.87-1.77 (m, 1H), 1.73-1.65 (m, 1H), 1.65-1.53 (m, 2H), 1.09-0.89 (m, 15H), 0.75 (t, *J* = 6.4 Hz, 3H), 0.73-0.69 (m, 2H), 0.68-0.62 (m, 3H), 0.64 (t, *J* = 7.4 Hz, 6H). $^{13}C\{^1H\}$ NMR (126 MHz, $CDCl_3$): δ (ppm) = 182.58, 182.51, 182.44, 162.76, 162.71, 162.66, 157.89, 157.85, 157.82, 154.13, 152.69, 148.63, 148.1, 144.3, 144.29, 143.24, 140.05, 136.8, 136.75, 136.69, 135.42, 133.77, 133.75, 133.72, 131.82, 130.68, 129.82, 128.9, 127, 126.03, 125.64, 125.51, 124.84, 124.75, 122.24, 122.09, 121.94, 120.4, 107.41, 69.32, 54.18, 45.42, 43.17, 43.12, 35.34, 35.29, 35.22, 34.37, 34.36, 34.11, 33.7, 28.58, 28.5, 27.58, 27.56, 27.31, 24.46, 22.75, 20.83, 14.07, 14.02, 10.74, 10.73, 10.62. HRMS (ESI): m/z 811.3653 $[M]^+$ (calcd for $C_{50}H_{57}N_3OS_3$: 811.3658). Anal. Calcd for $C_{50}H_{57}N_3OS_3$ (%): C, 73.94; H, 7.07; N, 5.17. Found: C, 74.04; H, 7.15; N, 5.09.

4.10.3.2 Synthesis of (*Z*)-2-(5-((4,4-bis(2-ethylhexyl)-6-(7-(4-(*p*-tolyl)-1,2,3,3a,4,8b-hexahydrocyclopenta[*b*]indol-7-yl)benzo[*c*][1,2,5]thiadiazol-4-yl)-4*H*-cyclopenta[2,1-*b*:3,4-*b'*]dithiophen-2-yl)methylene)-4-oxo-2-thioxothiazolidin-3-yl)acetic acid

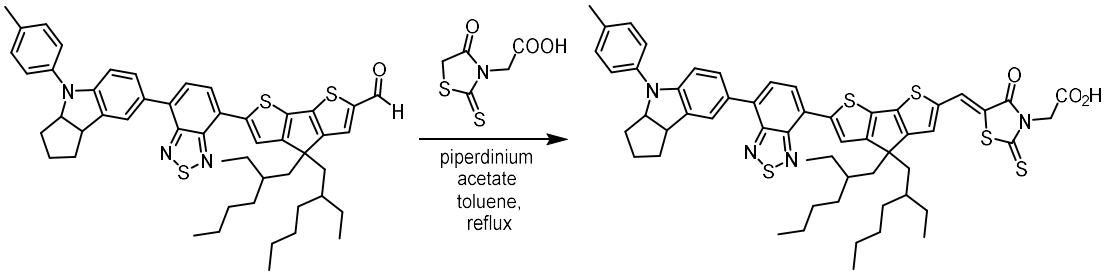

4,4-Bis(2-ethylhexyl)-6-(7-(4-(*p*-tolyl)-1,2,3,3a,4,8b-hexahydrocyclopenta[*b*]indol-7-yl)benzo[*c*][1,2,5]thiadiazol-4-yl)-4*H*-cyclopenta[2,1-*b*:3,4-*b'*]dithiophene-2-carbaldehyde (75 mg, 0.092 mmol), rhodanine-3-acetic acid (31 mg, 0.10 mmol), and piperidinium acetate (30 mg, 0.10 mmol) were added to an oven-dried round-bottom flask with a Dean-Stark water separator and condenser, then evacuated and filled with nitrogen three times before anhydrous toluene (0.8 mL) was added. The content was stirred and heated to reflux under nitrogen for 7 h. The solvent was removed under reduced pressure and then high vacuum. The crude product was purified via silica gel chromatography on the Biotage Isolera system (10 g silica gel cartridge). The column was run in CH_2Cl_2:EtOAc 90:10, then CH_2Cl_2:MeOH 85:15 to remove the main band. The main dark purple band was collected and the solvent removed under reduced pressure. The residue was further purified by size exclusion column (SEC) chromatography (S-X1 Biobeads in THF (without stabilizers, HPLC grade or from a solvent purification system)). A one-foot long column of one-inch diameter was run, and

the main band was collected and the solvent removed under reduced pressure. The residue was then purified by reverse phase silica gel (C18, 10 g) column chromatography in MeOH, with the main band collected and the solvent removed under reduced pressure to yield a dark purple solid (25 mg, 27%). ^{1}H NMR (500 MHz, $CDCl_3$): δ (ppm) = 8.11 (t, *J* = 10.1 Hz, 1H), 7.95 (s, 1H), 7.91 (quin, *J* = 3.6 Hz, 1H), 7.81-7.75 (m, 1H), 7.75-7.68 (m, 1H), 7.66 (d, *J* = 7.5 Hz, 1H), 7.33-7.28 (m, 1H), 7.24 (d, *J* = 8.2 Hz, 2H), 7.18 (d, *J* = 8.2 Hz, 2H), 7.02 (d, *J* = 8.3 Hz, 1H), 4.87 (t, *J* = 7.4 Hz, 1H), 4.84 (s, 2H), 3.94 (t, *J* = 8.1 Hz, 1H), 2.35 (s, 3H), 2.14-1.90 (m, 6H), 1.86-1.78 (m, 1H), 1.73-1.65 (m, 1H), 1.64-1.54 (m, 1H), 1.09-0.90 (m, 17H), 0.75 (t, *J* = 6.0 Hz, 5H), 0.69-0.60 (m, 9H). ^{13}C{^{1}H} NMR (176 MHz, $CDCl_3$): δ (ppm) = 211.41, 191.87, 168.83, 167.26, 162.04, 162.03, 159.6, 159.55, 159.51, 154.15, 152.72, 148.66, 147.63, 147.6, 147.56, 144.21, 144.2, 140.12, 138.2, 138.18, 138.16, 137.14, 137.11, 137.08, 135.51, 133.67, 133.64, 133.62, 131.87, 130.18, 129.89, 129.11, 128.94, 127.54, 127.44, 127.34, 127.07, 126.13, 125.57, 124.91, 124.78, 122.42, 122.25, 122.09, 120.43, 116.87, 116.83, 116.79, 107.46, 69.38, 54.36, 54.34, 45.48, 43.3, 43.26, 43.21, 43.17, 35.42, 35.4, 35.28, 34.37, 34.35, 34.22, 33.76, 29.76, 28.63, 28.56, 27.58, 27.57, 27.37, 24.5, 22.84, 20.84, 14.09, 14.07, 10.78, 10.77, 10.65. HRMS (ESI): m/z 983.3164 [M-] (calcd for $C_{55}H_{59}N_4O_3S_5$: 983.3196). Anal. Calcd for $C_{55}H_{60}N_4O_3S_5(H_2O)$: C, 65.84; H, 6.23; N, 5.58. Found: C, 65.50; H, 6.37; N, 5.29.

4.10.4 Synthesis of sensitizer 4.4

4.10.4.1 Synthesis of diethyl (*Z*)-((5-((4,4-bis(2-ethylhexyl)-6-(7-(4-(*p*-tolyl)-1,2,3,3a,4,8b-hexahydrocyclopenta[*b*]indol-7-yl)benzo[*c*][1,2,5]thiadiazol-4-yl)-4H-cyclopenta[2,1-*b*:3,4-*b*′]dithiophen-2-yl)methylene)-4-oxo-2-thioxothiazolidin-3-yl)methyl)phosphonate

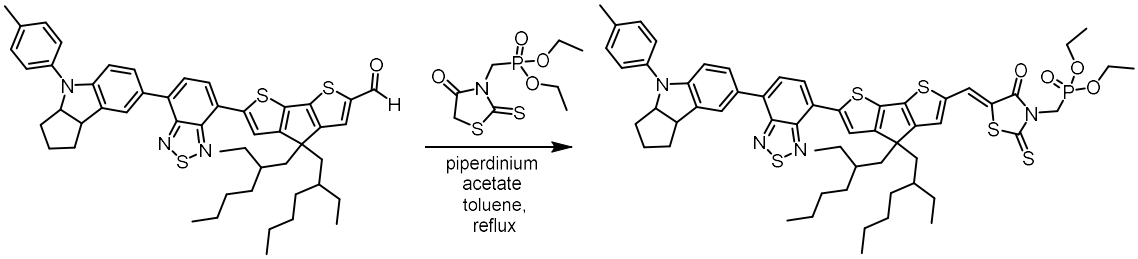

4,4-Bis(2-ethylhexyl)-6-(7-(4-(*p*-tolyl)-1,2,3,3a,4,8b-hexahydrocyclopenta[*b*]indol-7-yl)benzo[*c*][1,2,5]thiadiazol-4-yl)-4*H*-cyclopenta[2,1-*b*:3,4-*b*′]dithiophene-2-carbaldehyde (75 mg, 0.092 mmol), rhodanine-3-acetic acid (55 mg, 0.18 mmol), and piperidinium acetate (2.7 mg, 0.019 mmol) were added to an oven-dried round-bottom flask with a Dean-Stark water separator and condenser, then evacuated and filled with nitrogen three times before anhydrous toluene (0.8 mL) was added and the content was stirred and heated to reflux under nitrogen for 12 h. The solvent was removed under reduced pressure and then high vacuum. The crude product from the major fraction was dissolved in EtOH and purified by gel permeation column chromatography (Sephadex LH-20) on a 6 inch column of one-inch diameter run in MeOH. The crude product was purified via silica gel chromatography on the Biotage Isolera system (25 g silica gel cartridge). The column was run in CH_2Cl_2:acetone 100:0, increasing to 97:3 to remove the main band. The main purple band was collected and the solvent removed under reduced pressure. The residue was further purified by reverse phase silica gel (C18, 10 g) column chromatography in MeOH, with the main band collected and the solvent removed

under reduced pressure to yield a purple solid (49 mg, 49%). ^{1}H NMR (400 MHz, $CDCl_3$): δ (ppm) = 8.09 (t, *J* = 5.3 Hz, 1H), 7.95-7.90 (s, 2H), 7.8 (s, br, 1H), 7.78-7.72 (m, 1H), 7.69 (d, *J* = 7.6 Hz, 1H), 7.40-7.26 (m,1H), 7.25 (d, *J* = 8.6 Hz, 2H), 7.19 (d, *J* = 8.4 Hz, 2H), 7.03 (d, *J* = 8.3 Hz, 1H), 4.88 (t, *J* = 7.5 Hz, 1H), 4.64 (d, *J* = 12.3 Hz, 2H), 4.27-4.15 (m, 4H), 3.95 (t, *J* = 8.3 Hz, 1H), 3.03-2.88 (m, 1H), 2.35 (s, 3H), 2.17 (d, *J* = 0.4 Hz, 2H), 2.02 (s, 6H), 1.86 (d, *J* = 6.4 Hz, 1H), 1.71 (s, 1H), 1.62 (s, 1H), 1.36 (d, *J* = 1.1 Hz, 6H), 1.35 (td, *J* = 7.1, 1.1 Hz, 0H), 0.98 (t, *J* = 5.7 Hz, 15H), 0.74 (t, *J* = 6.5 Hz, 3H), 0.72-0.69 (m, 1H), 0.63 (t, *J* = 7.4 Hz, 9H). ^{13}C{^{1}H} NMR (101 MHz, $CDCl_3$): δ (ppm) = 206.95, 190.54, 184.00, 181.47, 172.87, 171.71, 148.67, 140.06, 129.83, 128.90, 127.21, 126.05, 125.52, 120.44, 116.49, 107.42, 69.35, 63.02, 62.96, 54.27, 45.44, 43.15, 35.36, 35.34, 35.22, 34.3, 34.17, 33.71, 30, 29.69, 28.58, 28.52, 27.5, 27.33, 24.46, 22.76, 20.82, 16.42, 16.36, 14.05, 14.02, 10.73, 10.62. ^{31}P NMR (162 MHz, $CDCl_3$): δ (ppm) = 18.62. HRMS (ESI): m/z 811.3661 [M+] (calcd for $C_{50}H_{57}N_3OS_3$: 811.3658).

4.10.4.2 Synthesis of (*Z*)-((5-((4,4-bis(2-ethylhexyl)-6-(7-(4-(*p*-tolyl)-1,2,3,3a,4,8b-hexahydrocyclopenta[*b*]indol-7-yl)benzo[*c*][1,2,5]thiadiazol-4-yl)-4*H*-cyclopenta[2,1-*b*:3,4-*b*']dithiophen-2-yl)methylene)-4-oxo-2-thioxothiazolidin-3-yl)methyl)phosphonic acid

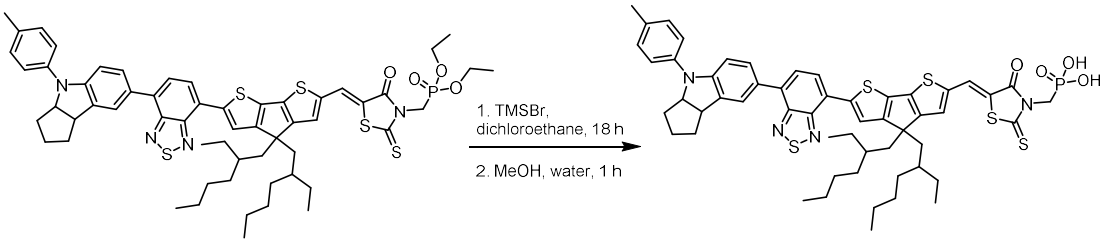

Diethyl (*Z*)-((5-((4,4-bis(2-ethylhexyl)-6-(7-(4-(*p*-tolyl)-1,2,3,3a,4,8b-hexahydrocyclopenta[*b*]indol-7-yl)benzo[*c*][1,2,5]thiadiazol-4-yl)-4H-cyclopenta[2,1-*b*:3,4-*b*′]dithiophen-2-yl)methylene)-4-oxo-2-thioxothiazolidin-3-yl)methyl)phosphonate (40 mg, 0.037 mmol) was added to an oven-dried round-bottom flask and evacuated and filled with nitrogen three times. 1,2-dichloroethane (1.2 mL) was added and the solution was stirred for 10 minutes at room temperature. Bromotrimethylsilane (0.05 mL, 0.38 mmol) was added and the reaction was stirred at 75 °C for 18 h. MeOH (1.5 mL) and water (2.3 mL) were added to quench the reaction, and the mixture was stirred and allowed to cool to room temperature for 1 h. The organic layer was extracted from CH_2Cl_2, dried over Na_2SO_4, and filtered. The solvent was removed under reduced pressure followed by high vacuum. The residue was dissolved in distilled CH_2Cl_2 and filtered through a 0.2 um PTFE filter. The solution was concentrated to minimal solvent under reduced pressure, then hexane was added and a precipiate formed. The solid was removed by vacuum filtration, washed with hexane, and dried under reduced pressure to yield a purple solid (38 mg, quantitative). ^{1}H NMR (700 MHz, $CDCl_3$): δ (ppm) = 8.32-8.05 (m, 1H), 7.95 (s, br, 1H), 7.78 (s, br, 1H), 7.72-7.53 (m, 2H), 7.52-7.40 (m, 1H), 7.40-7.34 (m, 1H), 7.33-7.29 (m, 1H), 7.28-6.99 (m, 4H), 4.67 (s, br, 3H), 2.50-2.26 (m, 1H), 2.19-1.98 (m, 5H), 1.91 (s, 2H), 1.81 (s, 1H), 1.67 (s, 1H), 1.63 (m, 1H), 1.56 (s, 1H), 1.04 (s, br, 16H), 0.88 (t, J = 7.1 Hz, 2H), 0.87-0.81 (m, 2H), 0.77 (s, 3H), 0.70 (s, br, 9H). ^{13}C{^{1}H} NMR (176 MHz, $CDCl_3$): δ (ppm) = 191.26, 170.58, 132.37, 130.92, 129.67, 122.73, 72.62, 68.24, 67.88, 43.91, 43.22, 42.45, 41.57, 36.24, 34.81, 33.71, 33.18, 32.6, 30.35, 30.04, 29.89, 29.24, 28.39, 27.96, 27.37, 27.20, 26.58, 23.43, 23.36, 19.79, 14.30, 12.39, 11.62, 10.97 (resonances not observed due to poor solubility). ^{31}P

NMR (162 MHz, $CDCl_3$): δ (ppm) = 18.83. HRMS (ESI): m/z 1019.2935 [M-] (calcd for $C_{54}H_{60}N_4O_4PS_5$: 1019.2961).

CHAPTER 5. SURFACE MODIFICATION OF ELECTRON TRANSPORT LAYERS FOR LEAD ORGANO-HALIDE PEROVSKITE SOLAR CELLS

5.1 Introduction

Organic-inorganic perovskite solar cells are a promising emerging technology, with the power conversion efficiency (PCE) of perovskite solar cells currently reaching efficiencies of 22-23%.[6,24,27,74,75] Interfaces in perovskite devices are a large focus of research, [2,3,191,192] as they can have a large effect upon not only charge collection,[193,194] but also perovskite crystal growth and overall device stability.[81] The performance of planar perovskite devices has been shown to be especially affected by the ETL/perovskite interface.[192] Two ETLs of interest, fullerenes and tin oxide, are of interest due to their ability to be processed at low temperatures while retaining excellent overall PCE. In section 5.2, surface modification of C_{60} was investigated for its effects on solvent resistance, work function, surface energy, and the electrical properties of C_{60}, as well as stability on a flexible substrate. In section 5.3, dipolar phosphonic acid surface modification of ALD-deposited SnO_2 ETLs was explored for its effects on work function, surface energy, device performance, and device stability in inert atmosphere.

5.2 Flexible Planar Perovskite Solar Cells Processed at Low Temperature

This work was accomplished in collaboration with Seulki Song and Kyoungwon Choi in the group of Prof. Taiho Park and with Konrad Wojciechowski in the group of Henry J. Snaith. Training and assistance was provided by Maximilian Hörantner and

Nakita Noel. Specifically, Konrad Wojciechowski provided initial device fabrication training and discussion. The author accomplished the initial amine selection, initial device fabrication, and initial method development. Further device optimization and all device characterization included here were accomplished by Seulki Song and Kyoungwon Choi. The author performed the amine-fullerene characterization and surface analysis via x-ray photoelectron spectroscopy (XPS) and ultraviolet photoelectron spectroscopy (UPS).

In an n-i-p architecture lead organo-halide perovskite solar cell device, the formation of the perovskite crystal is greatly affected by the electron transport layer's surface energy and solvent resistance. The work function of this interfacial layer is also key to efficient electron transport in the device. Fullerene electron transport layers have the advantage of low temperature processing for flexible substrates, but suffer from pinholes during perovskite layer deposition in an n-i-p device architecture.[7] Coating C_{60} with poly(allylamine) resulted in optimized surface energy for perovskite crystal formation, decreased work function for optimal electron transfer, increased solvent resistance for a pinhole-free fullerene layer, and increased device performance relative to the control after 600 bending cycles on a flexible substrate.

5.2.1 Introduction

As a result of their outstanding properties, including large absorption coefficients,[66,67] bipolar charge transport,[68–70] low band gaps,[70] long carrier diffusion lengths,[71] and small exciton-binding energies,[72,73] perovskites have attracted considerable attention in the field of solar-cell research. The power conversion efficiency (PCE) of

perovskite solar cells based on glass substrates has reached approximately 22% in a period of five years.[24,27,74,195] However, flexible perovskite solar cells have not been comprehensively studied despite their various advantages (*e.g.*, low production cost, less thickness, and lightweight) compared to the glass substrate-based devices. Moreover, solar cells based on flexible substrates can be applied to automotive-integrated photovoltaics (AIPV) or portable and indoor electronics.[196,197]

Flexible perovskite solar cells, particularly those with planar n-i-p structures, generally employ flexible plastic substrates, such as polyethylene naphthalate (PEN) and polyethylene terephthalate (PET), rather than conventional glass substrates. These polymeric substrates are only stable at temperatures below 150 °C. Therefore, in order to successfully fabricate flexible perovskite solar cells, beyond the usual considerations of energy levels, charge transport, and stability under operating conditions, there are additional limitations placed on the materials chosen for various layers of the solar cell, not only regarding their stability to bending, but also the temperatures at which they are processed.

Inorganic TiO_2 (processed at >450 °C)[74,75] and SnO_2 (≥180 °C)[101] have been widely used as electron-transporting layers (ETLs) in planar solar-cell devices. However, the high-processing temperatures for these materials are incompatible with PEN and PET substrates; moreover, these materials from highly brittle thin layers. The Zn_2SnO_4 ETL reported by Seok *et al*. was employed by preheated process (200 ºC), showing PCE of 16.5%.[96] Im *et al*. demonstrated the use of spin-coated ZnO as an ETL material processed at approximately 150 °C, resulting in PCE values of 10.3%–15.6%.[97] However, ZnO is known to degrade the perovskite film.[104] Furthermore, cells incorporating most of these

inorganic ETLs exhibit hysteresis behavior. Therefore, a new ETL material that can be deposited at a low temperature and that does not lead to hysteresis is desirable.

Buckminsterfullerene, C_{60}, has high electron mobility (1.6 $cm^2\ V^{-1}\ s^{-1}$) and conductivity (2.3×10^{-3} S cm^{-1}, as obtained from field-effect transistors), making it an excellent candidate for low-temperature-processable ETLs.[86,198–200] There are many examples of the use of C_{60} and its derivatives as ETLs in p-i-n-type perovskite devices based on glass substrates.[105–110,110] However, C_{60} cannot be easily spin-coated in flexible perovskite solar cells with planar n-i-p structures. It has low solubility in many common organic solvents, which limits the choice of solvents from which it can be deposited, but sufficient solubility in many solvents to afford poor solvent resistance during the casting of subsequent layers, in part caused by poor adhesion to substrates. Wojciechowski *et al*. spin-coated a C_{60} ETL layer in an n-i-p-type device based on a glass substrate and obtained a stabilized PCE of 13.9%.[7] However, the C_{60} layer was dissolved by dimethylformamide (DMF) and chlorobenzene, which are commonly used in the depositions of perovskite and hole-transport layers, respectively. The dissolution of C_{60} resulted in the formation of pinholes, leading to shunting pathways with a concomitant decrease in device efficiency. Therefore, this ETL could not be used to fabricate devices with high reproducibility.

One potential solution to this problem is enhancing the interaction and adhesion of C_{60} with the substrate. However, only one study has attempted to enhance the attraction between C_{60} molecules and flexible substrates. Yoo *et al*. employed a bilayer ETL in which C_{60} was evaporated on ethoxylated polyethylenimine (PEIE) to enhance the adhesion of C_{60} molecules to the PEIE/ITO–PEN layer, affording a PCE of 13.8% for

the flexible substrate-based device.[94] However, the C_{60} molecules were still partially washed off during the spin-coating process perovskite solution. Wojciechowski *et al*. employed reactive C_{60} derivatives that were blended with C_{60} to increase the attractive interactions between C_{60} molecules and ultimately the solvent resistance. The resulting glass-substrate-based devices exhibited stabilized PCEs of approximately 15%–16%.[111] However, a new ETL that strongly adheres to flexible substrates and does not degrade in common solvents is still needed.

To address this need, a highly stable ETL has been developed in which C_{60} is insolubilized by spin-coating 0.08 wt% of PAA, then heating the film in inert atmosphere. The amines on PAA react with C_{60}, leading to insolubilization of the ETL and sufficient adhesion to the ITO–PEN substrate, causing the C_{60} molecules to be robustly fixed on the substrate. In addition, because amine-containing polymers are known to decrease the work function (WF) of organic semiconductors,[201–203] an increased open-circuit voltage (V_{OC}) is expected. A flexible planar perovskite solar cell with 15.2% PCE and negligible hysteresis is demonstrated. This cell also exhibits excellent flexibility with over 83% PCE retention after 600 cycles of bending.

5.2.2 Results and discussion

The solvent resistance of a pure C_{60} ETL was examined by measuring the ultraviolet–visible (UV–Vis) absorption of the films after washing them with a DMF:DMSO (4:1, v/v mixed solvent, which is often used to prepare the perovskite precursor solution. A 50% decrease in the absorption of C_{60} was observed, indicating that the C_{60} molecules did not strongly adhere to the substrate (Figure 5-1 and Figure 5-2c).

When 0.04 wt% PAA solution was deposited onto the C_{60} layer and annealed at 150 °C (see ESI for the detailed procedure), only a slightly smaller (46%) decrease in absorption was observed. Thus, although PAA itself does not dissolve in the DMF:DMSO mixed solvent, 0.04 wt% PAA is evidently insufficient to insolubilize the C_{60} film (Figure 5-1b and Figure 5-2c). On the other hand, no absorption decrease was observed when PAA solutions with concentrations of 0.08 wt%, 0.12 wt%, and 0.16 wt% were used, indicating a solvent-resistant film on the substrate (Figure 5-1 and Figure 5-2). This is attributed to the reaction of the amine groups of PAA with sufficient C_{60} molecules to form a cross-linked film. The films were further investigated via high-resolution scanning electron microscopy (HR-SEM). The HR-SEM images showed inhomogeneity in the solvent-treated C_{60} film, whereas the film formed with 0.08 wt% PAA appeared homogeneous (Figure 5-1d and e; see Figure 5-3 for SEM images showing other PAA concentrations).

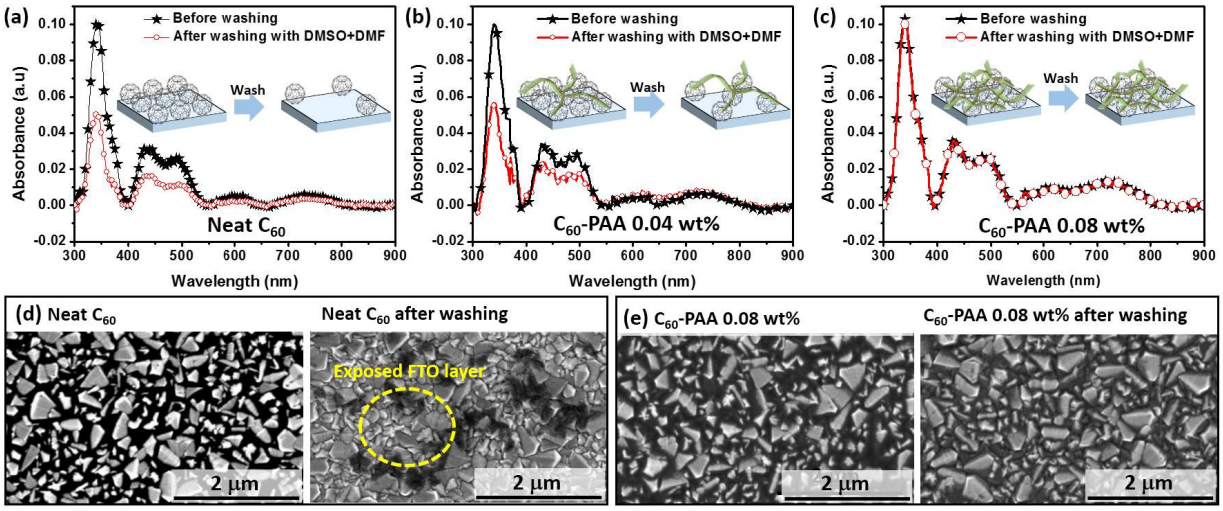

Figure 5-1. Ultraviolet–visible (UV–Vis) absorption spectra of fullerene (C_{60}) and C_{60}–poly(allylamine) (PAA) layers on FTO glass (black line) and C_{60} and C_{60}–PAA films after washing with dimethylformamide (DMF): dimethyl sulfoxide (DMSO) (4:1, v/v; red line): a) neat C_{60}, b) C_{60}–PAA (0.04 wt%), and c) C_{60}–PAA

(0.08 wt%). Top-down high-resolution scanning electron microscopy (HR-SEM) images of d) neat C_{60} and e) C_{60}–PAA (0.08 wt%) layers on FTO substrates before and after washing with DMF:DMSO.

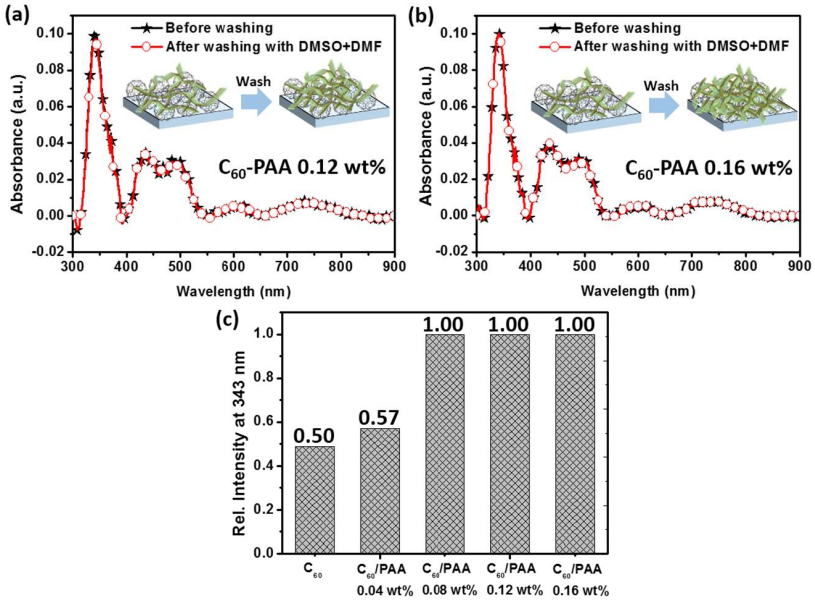

Figure 5-2 UV-vis absorption spectra of a) C_{60}-PAA 0.12 wt% and b) C_{60}-PAA 0.16 wt% film on FTO glass (black line), C_{60}-PAA films after washing with DMF:DMSO=4:1 (v/v) (red line), and c) relative absorption intensity at 343 nm.

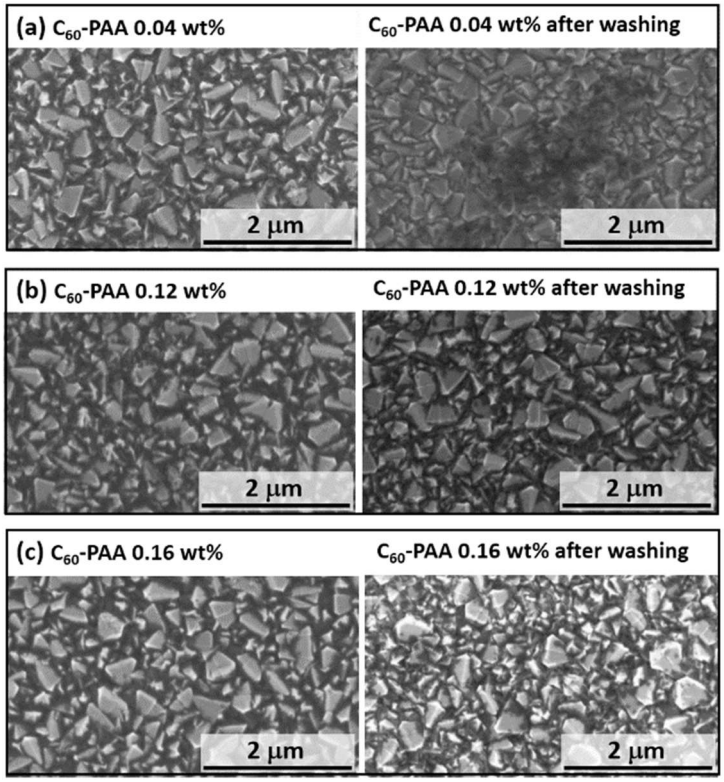

Figure 5-3 Top down scanning electron microscope (SEM) images of a) C_{60}-PAA 0.04 wt%, b) C_{60}-PAA 0.12 wt%, and c) C_{60}-PAA 0.16 wt% layer on FTO substrate and their corresponding images after washing with DMF:DMSO=4:1(v/v).

Amine reactions with C_{60} may proceed by an electron transfer reaction resulting in a protonated amine and n-doped fullerene that interact ionically, or may proceed further to hydroamination or subsequent dehydrogenation.[204] As the film is heated for a limited time at a relatively low temperature (150 °C), it is possible that a mix of electron transfer and hydroamination is occurring. X-ray photoelectron spectroscopy (XPS) can indicate a change in the chemical environment of nitrogen in the films between neat PAA and C_{60}-PAA films (Figure 5-4), aiding in elucidating the possible chemical reaction of the polymer amine functional groups with the C_{60}. For an FTO/PAA sample, the N 1s XPS feature was modelled as three peaks centered at binding energies (BEs) of 401.5,

400.5, and 399.7 eV (with the full width at half maximum (FWHM) of each constrained at 1.25–1.35 eV). Based on previous research,[205,206] the lower BE peaks can likely be attributed to neutral free amine N, whereas the higher BE peaks are likely attributable to quaternary ammonium and hydrogen-bonded amine species, of which there is very little, suggesting very few C_{60}-amine interactions are only electron transfer complexes. For the FTO/C_{60}/PAA sample (0.08 wt% PAA), a strong N 1s peak centered at 399.1 eV was observed in addition to the features at BEs similar to those observed for the FTO/PAA sample. The BE of this new peak is similar to those of purified C_{60}–amine compounds (398.6–398.9 eV)[207] and may indicate that a large portion of the nitrogen atoms in PAA are covalently bound to the C_{60} cage.

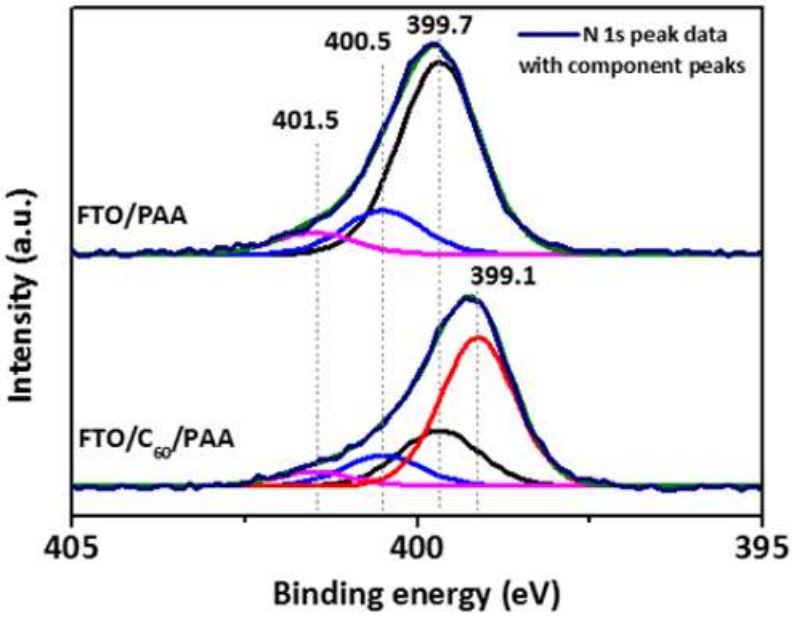

Figure 5-4. X-ray photoelectron spectroscopy (XPS) N 1s peaks for PAA (0.08 wt%) and C60–PAA (0.08 wt%) films on FTO substrates.

As mentioned above, PAA is, by analogy with other work on fullerene-amine systems, expected to decrease the WF of the C_{60} layer,[201] thereby potentially affecting the V_{OC} value of devices. Thus, the effect of PAA on the WF was investigated using ultraviolet photoelectron spectroscopy (UPS) and Kelvin probe (Figure 5-5). The introduction of PAA reduced the WF by *ca*. 1 eV [from 4.6 eV ± 0.1 eV for FTO/C_{60} to 3.7–3.9 eV ± 0.1 eV for FTO/C_{60}/PAA (Figure 5-6)].

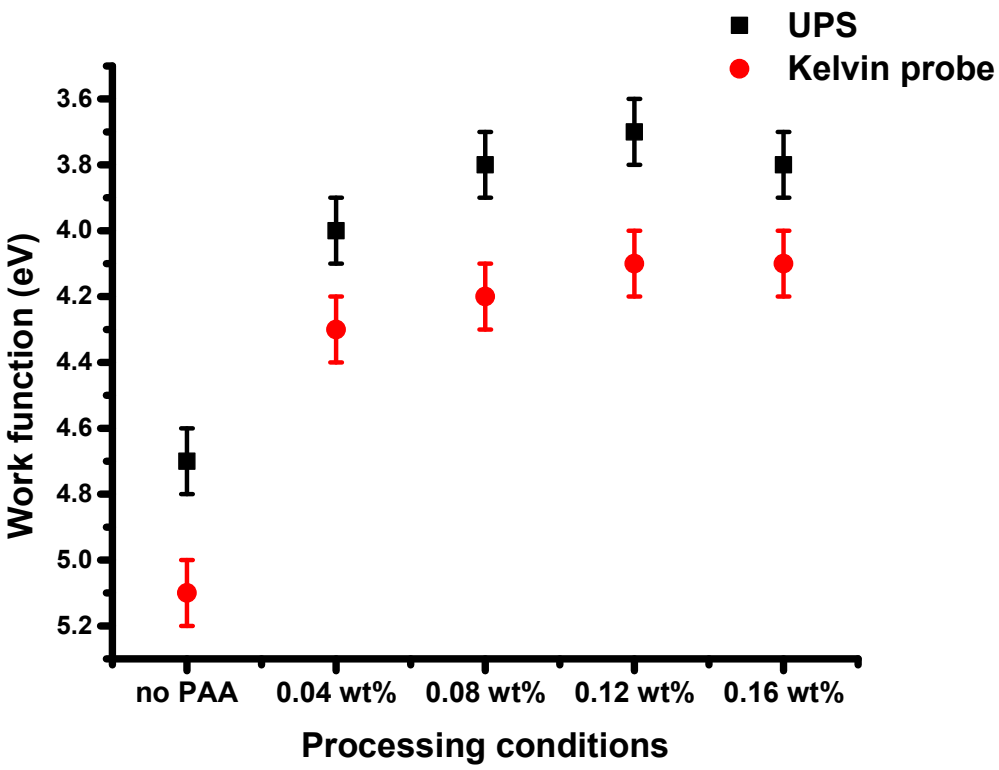

Figure 5-5. Work function values obtained from UPS and Kelvin probe in inert atmosphere. For UPS, 4-9 spots were measured per condition, while for Kelvin probe 3-5 spots each were measured on two substrates per condition, with values calibrated to peeled HOPG every 4-5 samples.

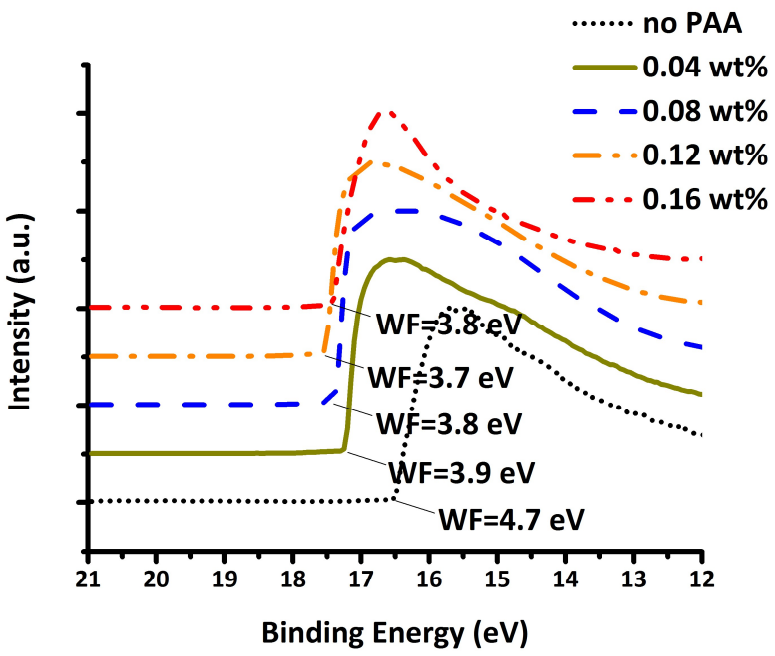

Figure 5-6. Ultraviolet photoelectron spectroscopy (UPS) secondary electron edge cutoffs of a C_{60} film and C_{60}-PAA films (0.04, 0.08, 0.12, 0.16 wt% PAA spin-coated) on FTO substrates.

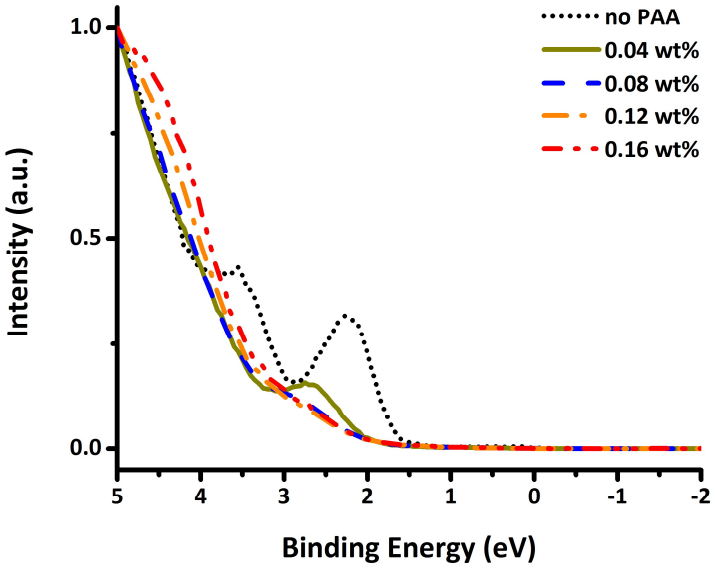

Figure 5-7. Ultraviolet photoelectron spectroscopy (UPS) valence peaks of a C_{60} film and C_{60}-PAA films (0.04, 0.08, 0.12, 0.16 wt% PAA spin-coated) on FTO substrates.

A comparison of shifts in the position of the lowest BE valence peak attributable to C_{60}, at least for low PAA loading (0.08 wt% PAA solution), where this peak is still well defined, suggests that the majority of the total WF shift (0.8 eV) can be attributed to a valence band shift (0.5 eV) associated with n-doping of the C_{60} by the amine, at least at the surface of the films. This is consistent with previous reports on C_{60}–amine systems,[202,203] with the Fermi level for the doped films being pinned close to the C_{60} LUMO (Figure 5-7 and Figure 5-8).

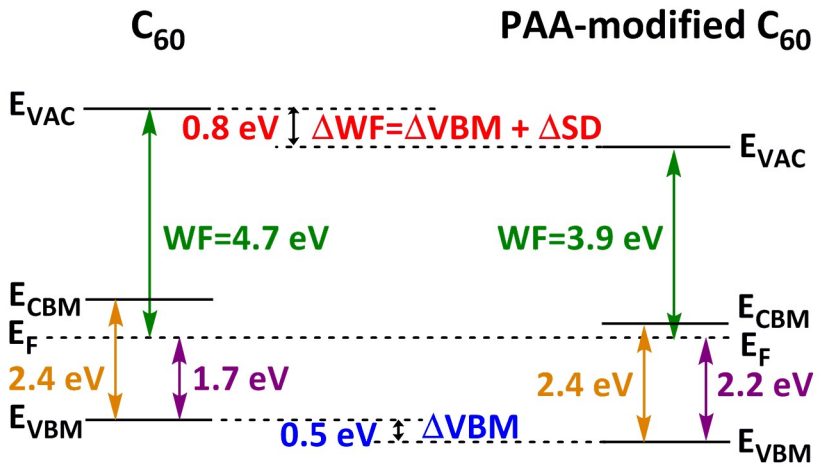

Figure 5-8. Effect of PAA on the electronic structure of C_{60}, as deduced from the UPS secondary electron edge cut-off and valence band peaks of C_{60} and C_{60}–PAA (0.08 wt%) films.

The effects of small amounts of PAA on the surface energy and the crystallinity of the perovskite $Cs_{0.05}(MA_{0.17}FA_{0.83})_{0.95}Pb(I_{0.83}Br_{0.17})$ were also investigated. First, contact-angle measurements were conducted using deionized water and glycerol (Figure 5-9). As the amount of PAA increased, the contact angle decreased, indicating an

increase in the surface energy (up to 63.6 mJ m^{-2}; Figure 5-11a and Table 5-1). The increased hydrophilicity of the ETL surface improved the wettability by the perovskite solution.[208,209] Meanwhile, the change in the surface energy was not accompanied by a large change in crystallinity of the perovskite, as shown in Figure 5-10, which indicates no difference in the X-ray diffraction (XRD) patterns.

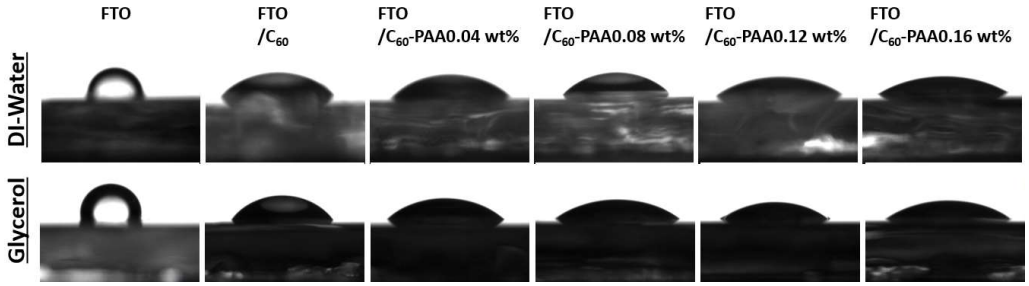

Figure 5-9 DI-water and glycerol contact angles of C_{60} and C_{60}-PAA (0.04, 0.08, 0.12, and 0.16 wt%) films on an FTO substrate.

Table 5-1 Summary of the contact angles and surface energy.

	FTO	FTO/C_{60}	FTO/C_{60}-PAA			
			0.04 wt%	0.08 wt%	0.12 wt%	0.16 wt%
DI-water (^{O})	82.1	53.8	44.4	42.8	37.2	29.7
Glycerol (^{O})	97.0	51.7	36.7	29.7	28.4	26.9
Surface Energy [mJ/m^2]	33.7	46.1	54.2	56.7	59.4	63.6

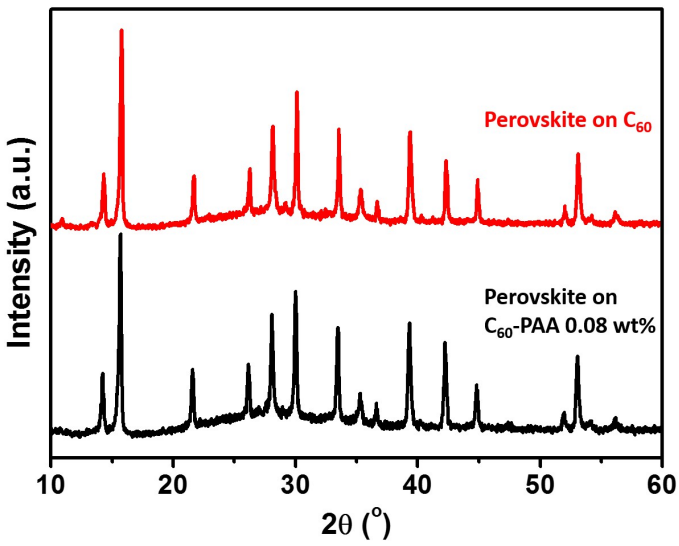

Figure 5-10 X-Ray diffraction (XRD) spectra of the triple cation perovskites prepared on the C_{60} and C_{60}-PAA 0.08wt% ETLs.

In addition to the surface properties, the electronic properties of the ETL were examined. To determine the electron mobility in the vertical direction, *i.e.*, the same direction as that of electron transport in solar-cell devices, the electron-transport properties of each layer were measured using the space-charge-limited current (SCLC) method (Figure 5-11b). Electron-only devices comprising FTO/C_{60}/PAA/perovskite/LiF/Al (PAA concentration = 0 wt%, 0.04 wt%, 0.08 wt%, 0.12 wt%, and 0.16 wt%) were fabricated. As the concentration of PAA solution used increased from 0 wt% to 0.08 wt%, the electron mobility of the ETL slightly decreased; however, it was similar to that of the neat C_{60} ETL (8.0×10^{-3} $cm^2\ V^{-1}\ s^{-1}$, 4.5×10^{-3} $cm^2\ V^{-1}\ s^{-1}$, and 3.8×10^{-3} $cm^2\ V^{-1}\ s^{-1}$). However, when the concentration of PAA was increased to 0.12 wt% and 0.16 wt%, the electron mobility decreased to 2.3×10^{-5} and 1.2×10^{-5} $cm^2\ V^{-1}\ s^{-1}$, respectively (Figure

5-12), which is consistent with the dilution of electron-transporting C_{60} with insulating PAA.

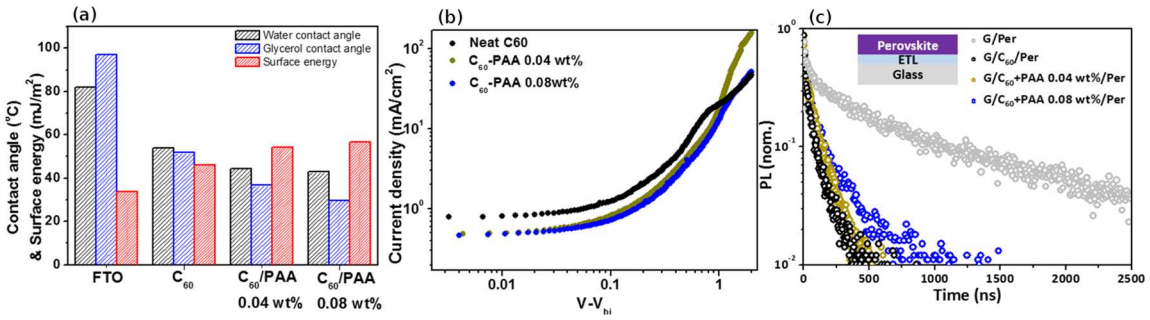

Figure 5-11. a) Deionized water and glycerol contact angles for bare FTO and C_{60} and C_{60}–PAA (0.04 and 0.08 wt%) films on FTO substrates and the calculated surface energies. b) Space-charge-limited current (SCLC) values of C_{60} and C_{60}–PAA (0.04 wt% and 0.08 wt% PAA) electron-only devices. c) Time-resolved photoluminescence (TRPL) decay of the perovskite on the bare glass, glass/C_{60}, and glass/C_{60}–PAA (0.04 wt% and 0.08 wt%) electron-transport layers (ETLs).

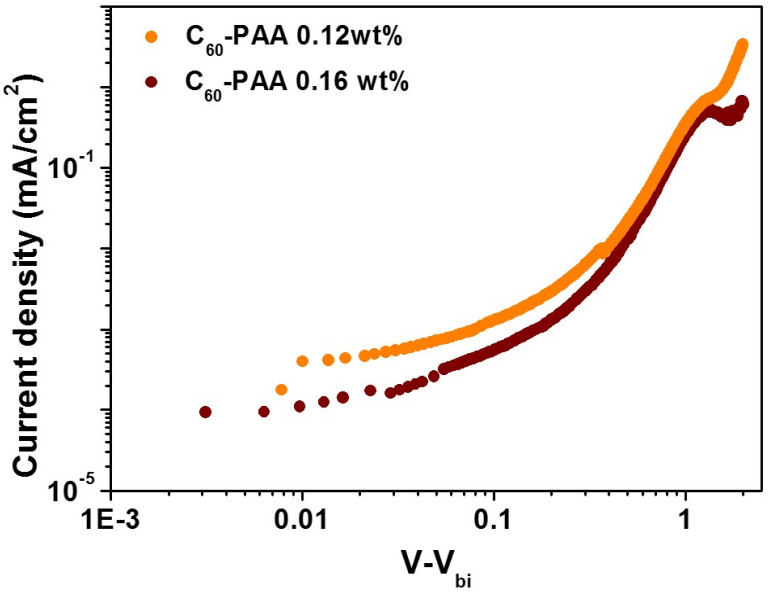

Figure 5-12 J-V characteristics of C_{60} and C_{60}-PAA (0.12, 0.16 wt%) electron only devices.

Time-resolved photoluminescence (TRPL) measurements of the C_{60}–PAA ETLs were performed to evaluate the electron extraction from the perovskite layer. Mixed-cation perovskites were deposited on bare glass/C_{60}–PAA and the perovskite side was illuminated with 474 nm light. The TRPL traces of all C_{60}–PAA ETLs are shown in Figure 5-13, and the decay lifetimes extracted from the data are listed in Table 5-2 and Table 5-3. Compared to the neat perovskite on the bare glass, the lifetimes of the samples with neat C_{60} and C_{60}–PAA (0.04 wt%) were significantly shorter for both fast and slow decay. In contrast, the lifetimes of C_{60}–PAA (0.08 wt%) were slightly increased (τ_1 = 17.0 ns and τ_2 = 162.0 ns) compared to the sample with neat C_{60}, indicating slower but still efficient electron extraction from the perovskite layer. When the PAA concentration was increased to 0.12 wt% and 0.16 wt%, the lifetimes significantly increased, indicating poor electron extraction from the perovskite layer (Figure 5-13).

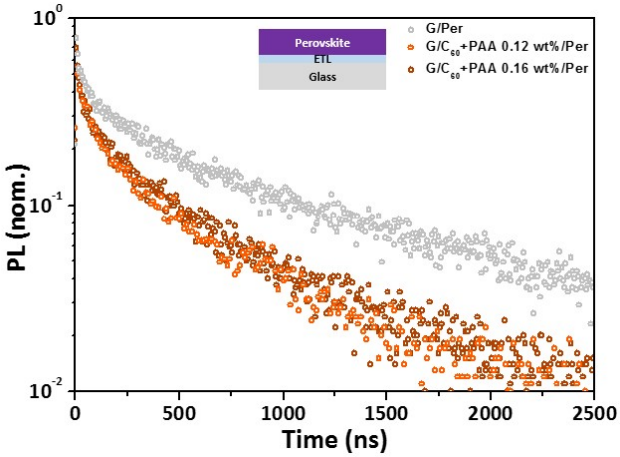

Figure 5-13 Time-resolved photoluminescence (TRPL) decay of perovskite on the bare glass, glass/C_{60}, and glass/C_{60}-PAA (0.12 and 0.16 wt%) ETLs.

Table 5-2. Lifetimes of perovskites on different substrates based on photoluminescence decay data.

	τ_1 [ns][a]	τ_2 [ns][b]
Glass/perovskite	26.6	637.0
Glass/C_{60}/perovskite	8.4	80.5
Glass/C_{60}–PAA (0.08 wt%)/perovskite	17.0	162.0

[a,b] Biexponential decay fits of $y = y_0 + A_1e^{-x/\tau 1} + A_2e^{-x/\tau 2}$ were used to extract the lifetimes.

Table 5-3 Lifetimes of perovskite on different substrate from photoluminescence decay.

	τ_1 [ns][a]	τ_2 [ns][b]
Glass /C_{60}+PAA 0.12 wt%/Perovskite	20.9	423.0
Glass /C_{60}+PAA 0.16 wt%/Perovskite	17.8	443.0

[a,b] Biexponential decay fits of $y = y_0 + A_1e^{-x/\tau 1} + A_2e^{-x/\tau 2}$ were used to extract the lifetimes

A flexible device on an ITO–PEN substrate using the C_{60}–PAA (0.08 wt%) ETL was fabricated and its performance was compared with the device fabricated with a neat C_{60} ETL (inset of Figure 5-15a). The mixed-cation perovskite was employed following a previously reported method.[208] The photovoltaic parameters are summarized in Table 5-4, and the current density (*J*)–voltage (*V*) curves are shown in Figure 5-14.

Table 5-4. Summary of the parameters of flexible perovskite solar cells obtained from the best devices employing C60 and C60–PAA (0.08 wt%) as ETLs. Measurements are performed under AM 1.5 solar illumination. The scan rate is 0.06 V s−1.

	J_{SC} (mA/cm^2)	V_{OC} (V)	FF (%)	PCE (%)
C_{60}–PAA (0.08 wt%) reverse	20.7	1.04	70.5	15.2
C_{60}–PAA (0.08 wt%) forward	20.7	1.04	70.5	15.2
C_{60} reverse	14.6	1.00	66.8	9.8
C_{60} forward	14.7	0.99	64.4	9.4

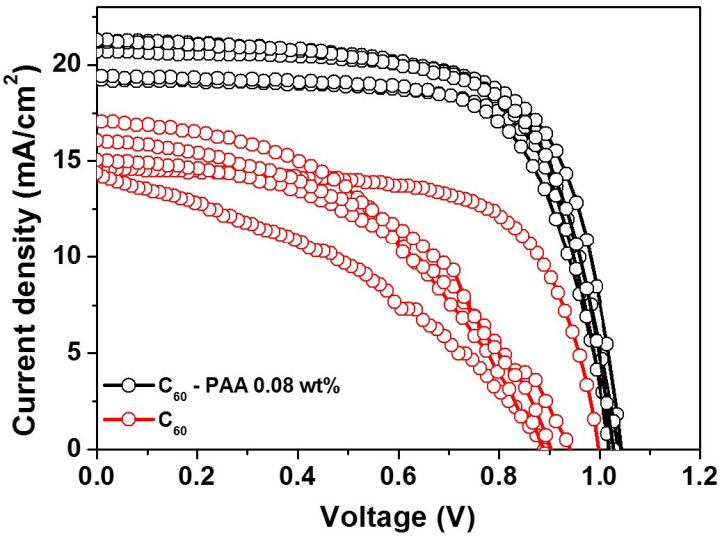

Figure 5-14 Current density−voltage (*J-V*) curves of the flexible devices employing C_{60} and C_{60}-PAA 0.08 wt% ETLs.

Due to the high solvent resistance and adhesion of the C_{60}–PAA layer, the device with the C_{60}–PAA (0.08 wt%) ETL exhibited higher and more reproducible efficiency than the device with the C_{60} ETL. Meanwhile, the low solvent resistance and weak adhesion of C_{60} on the flexible substrate may have provided pathways for recombination and hindered efficient electron extraction from the perovskite to the cathode. Consequently, the short-circuit current (J_{SC}), V_{OC}, and fill factor (FF) of the device with the C_{60}–PAA (0.08 wt%) ETL were dramatically improved compared to those of the device with the C_{60} ETL. In particular, the increased V_{OC} value can be attributed to the PAA-induced shift in the WF and the improved electron extraction. As shown in Figure 5-15a, the best flexible device employing the C_{60}–PAA (0.08 wt%) ETL exhibited a PCE of 15.2% without hysteresis and a maximum power output (MPP) efficiency of 15.1% (Figure 5-15b). These values were considerably greater than those obtained from the

flexible device employing the C_{60} ETL (PCE = 9.8% and 9.4% for the reverse and forward scans, respectively; MPP efficiency = 9.6%).

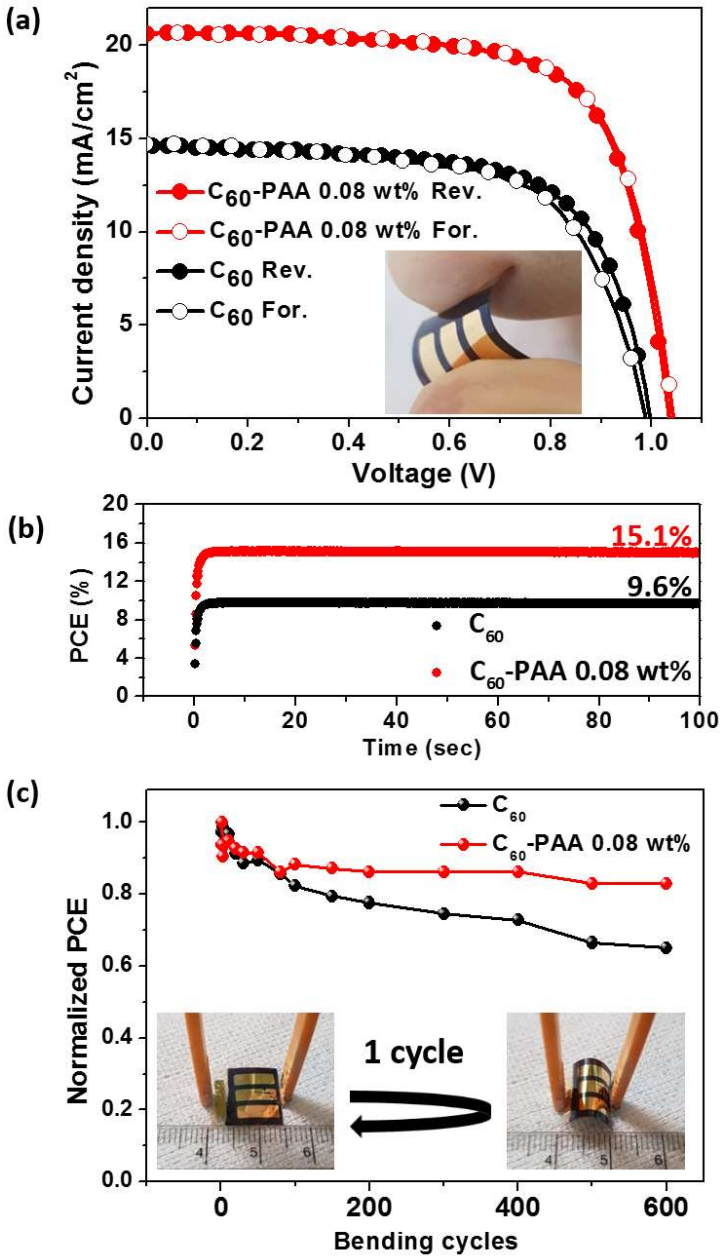

Figure 5-15. a) Forward and reverse current density (*J*)–voltage (*V*) curves of the best flexible device employing the C_{60}–PAA (0.08 wt%) ETL. b) Stabilized maximum power output (MPP) measurement of the best flexible device. c) Normalized power conversion efficiencies (PCEs) of flexible devices employing C_{60} and C_{60}–PAA (0.08 wt%) ETLs as functions of bending cycle (radius of bending = 10 mm).

The mechanical flexibility of the device under bending stress was evaluated using a bend test, as shown in Figure 5-15c. The flexible device was bent with a curvature of 10 mm in one bending cycle (insets of Figure 5-15c). The device retained 83% of its original efficiency after 600 binding cycles compared to 65% retention for the device with the C_{60} ETL.

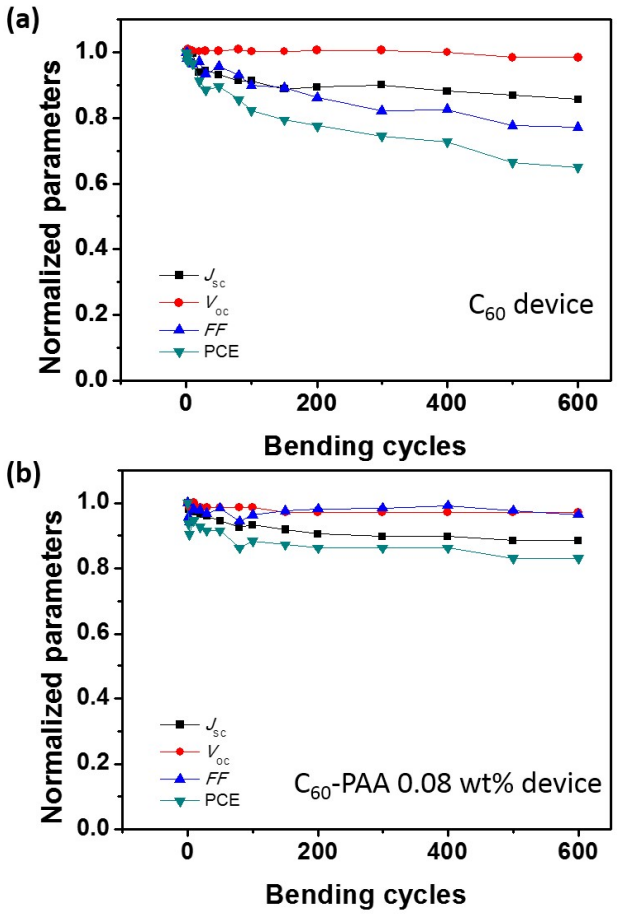

Figure 5-16 Normalized devices parameters of C_{60} and C_{60}-PAA 0.08 wt% flexible device as a function of bending cycles at a radius of 10 mm.

The decrease in PCE for the C_{60}-based device is due to significant decreases in both J_{SC} and FF values (Figure 5-16) and indicate that the C_{60} ETL is unstable to bending. On the other hand, the device employing C_{60}–PAA showed less significant decreases in J_{SC}

and FF upon bending. The J_{SC} value remained above 96% after 600 cycles of bending, indicating that the C_{60}–PAA ETL provided a high degree of stability and flexibility.

Planar devices were also fabricated with FTO substrates to determine the device reproducibility and efficiency (Figure 5-17). Although the best efficiency obtained by the device employing a C_{60} ETL was similar to that of the device employing a C_{60}–PAA ETL, the C_{60}-based devices exhibited wide ranges of the J_{SC}, V_{OC}, FF, and PCE values, which were attributed to the low solvent resistance of the bare C_{60} layer. However, the devices with C_{60}–PAA ETLs exhibited a more reproducible PCE due to greatly improved J_{SC}, *FF*, and V_{OC} values.

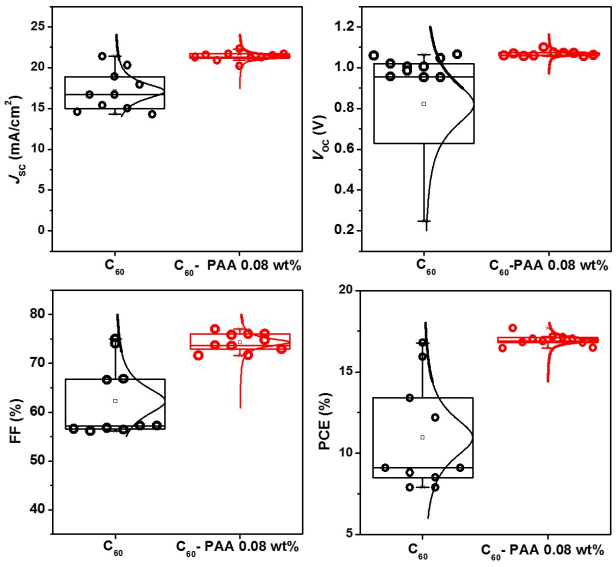

Figure 5-17. Histogram of the parameters of planar FTO-based devices with C_{60} and C_{60}–PAA (0.08 wt%) ETLs.

Figure 5-18 shows the *J*–*V* curves of the best cell (external quantum efficiency measurement of the device in Figure 5-19). This cell showed a J_{SC} value of 21.5 mA cm^{-2}, a V_{OC} value of 1.07 V, and an FF value of 77.0%, yielding a PCE of 17.7% with an

MPP efficiency of 15.7%. This device also exhibited long-term stability, maintaining more than 90% of its initial efficiency for over 1600 h (Figure 5-20).

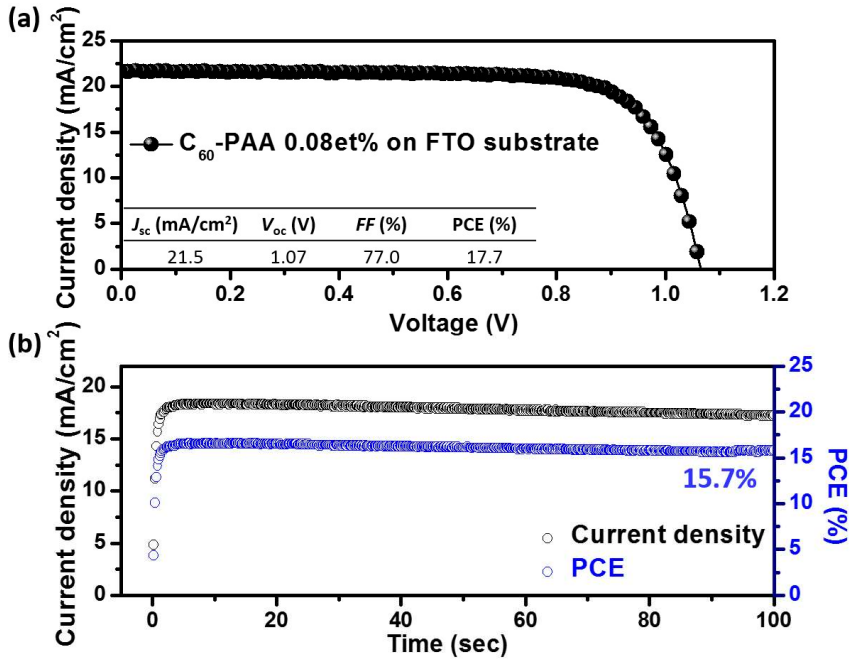

Figure 5-18 Current density−voltage (*J-V*) curves of the best device employing C_{60}-PAA 0.08 wt% ETLs on FTO substrate. b) Stabilized maximum power output (MPP) measurement of the best device.

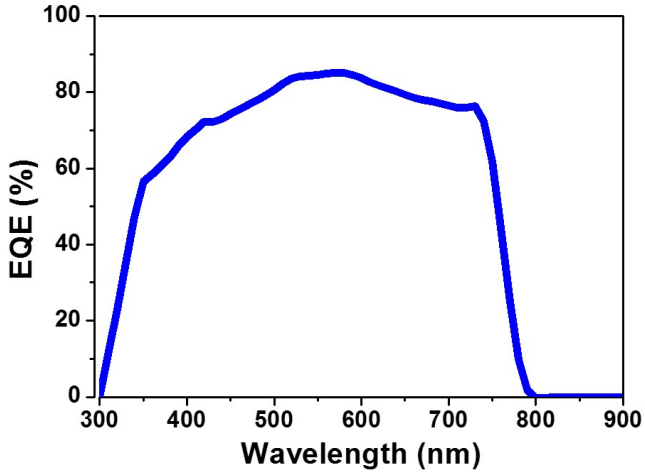

Figure 5-19 External quantum efficiency (EQE) of the planar perovskite device employing C_{60}-PAA 0.08 wt%.

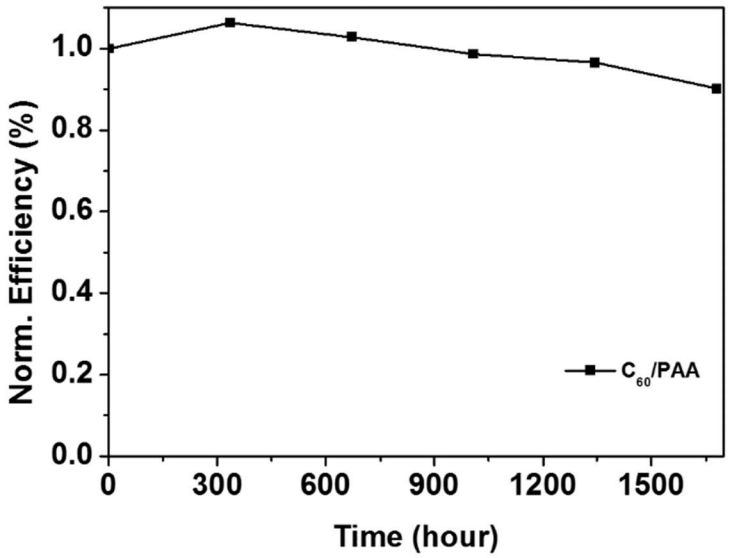

Figure 5-20 Long term stability measurement of the C_{60}-PAA 0.08 wt% device.

To investigate the reason for this, the transient photocurrent of conventional TiO_2 and C_{60}-PAA 0.08 wt% devices was measured (Figure 5-21). Upon illumination, the conventional TiO_2 device took almost 200 μs to stabilize, while the device employing a C_{60}-PAA ETL took less than 30 μs to stabilize. In addition, after illumination terminated, the current of the C_{60}/PAA 0.08 wt% ETL decreased abruptly compared to that of conventional TiO_2, which was indicative of superior electron-extraction and -collection ability of the C_{60}-PAA ETL.

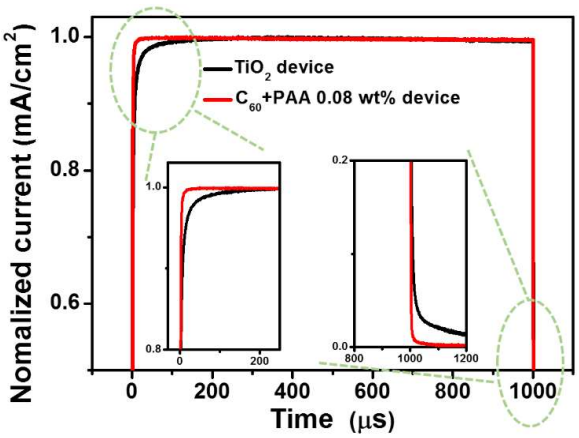

Figure 5-21. Transient photocurrent measurement of the perovskite device employing TiO_2 and the C_{60}–PAA (0.08 wt%) ETL.

5.2.3 Conclusions

Low-temperature-processed C_{60}–PAA ETLs for use in flexible perovskite solar cells have been successfully developed and demonstrated. The composition of these ETLs was optimized by varying the concentration of PAA in the casting solution. After processing, the C_{60}–PAA film exhibited excellent solvent resistance and C_{60} adhesion while maintaining the electrical properties of C_{60}. The introduction of PAA reduced the WF by ca. 1 eV [from 4.6 eV ± 0.1 eV for FTO/C_{60} to 3.7–3.9 eV ± 0.1 eV for FTO/C_{60}/PAA], and XPS analysis showed binding energies to be consistent with covalent bond formation. On the flexible substrate, the resulting ETL yielded a PCE of 15.2% and an MPP efficiency of 15.1% without hysteresis, making this ETL one of the best reported to date for flexible planar perovskite solar cells. In addition, the flexible device exhibited high stability during bending cycles. After 600 cycles of bending, the device retained over 83% of its original efficiency and the J_{SC} value remained above 96%. The optimized C_{60}–PAA ETL also exhibited excellent solvent resistance and adhesion with good

electrical properties, resulting in superior device reproducibility. The results of this study provide insights into the design strategies for efficient charge extraction layers for use in flexible perovskite devices.

5.3 Phosphonic Acid Surface Modification of ALD-Deposited Tin Oxide Electrodes

5.3.1 Introduction

Surface modification of metal oxide ETLs has been extensively explored, with surface modifiers first used in perovskite solar cells in 2014, when Ogomi *et al*. modified the surface of TiO_2 using HI salts of glycine, beta-alanine, and gamma-amino butyric acid (GABA) containing carboxylic acid binding groups.[210] The highest PCE was observed for GABA-HI, which had the longest alkyl chain. Several other groups continued to examine the use of amino acids and their derivatives on TiO_2 or ZnO.[211–214] Li *et al*. examined *p*-aminobenzoic acid (PABA) on TiO_2,[215] which was later compared directly to GABA by Zhang *et al*., with PABA exhibiting an increase in J_{SC} relative to GABA.[216] The authors ascribed the J_{SC} increase to the increased rigidity of the modifier and how this may guide perovskite crystallization, but their results could also indicate that a conjugated surface modifier may allow for better charge collection.

Using carboxy-alkyl-thiols or carboxy-phenyl-thiol at the TiO_2/perovskite interface, Cao *et al*. observed an increase in J_{SC} and a slight increase in V_{OC} with the phenyl group relative to no modification, while the J_{SC} and V_{OC} remained constant or

decreased for modification using carboxy-alkyl-thiols of varied alkyl chain lengths.[90] Kim *et al*. investigated various carboxylic acid derivatives and saw striking differences in perovskite film morphology depending on the end group of the surface modifier utilized.[217] Wojciechowski *et al*. used a carboxylic acid-bound fullerene surface modifier and observed significant decreases in hysteresis.[85] The modifier's structure and how it affects surface energy, crystal nucleation and electron transfer (tunneling vs. conjugation) will affect device performance.

The binding group of the modifier has its own effect. Liu *et al*. and later Yang *et al*. experimented with the use of silane-alkyl amines on ZrO_2 or TiO_2 and SnO_2, respectively.[192,218] Silane-based surface modification is attractive due to the ability to form stable, robust monolayers suitable for a wide variety of applications. However, silane monolayer formation can be very irreproducible, as homocondensation products can form in the presence of an excess of water, resulting in a polymeric multilayer instead of the desired monolayer.[164] Yang *et al*. observed that the treatment time of a silane SAM had a large effect on the perovskite solar cell PCE obtained, relative to no modification, with large improvements in V_{OC} seen after 3 h of treatment, but decreases in J_{SC} seen after 15 h of treatment. They hypothesized that the silane modification improved the perovskite film quality and the interfacial contact, but that extended modification made the silane layer become insulating.

Mutin *et al*. assert that organosilicon compounds are best suited for silicon-containing supports, while organophosphorus compounds appear to be better adapted to metals or transition metals and their oxides.[167] Phosphonic acids as surface modifiers for perovskite solar cells may provide advantages over carboxylic acids in terms of binding

strength and stability, and over silane-based modifiers in terms of reproducible and controlled monolayer formation. Phosphonic acids have been extensively studied as surface modifiers for various metal oxides,[170] including studies on ITO[219–221] and TiO_2.[222,223] In perovskite solar cells, Guerra *et al*. utilized a phosphonic acid modifier on a TiO_2 ETL.[224] Relative to no modification, a slight increase in PCE was seen from a decrease in V_{OC} and an increase in J_{SC}.

Phosphonic acids may be of interest to study on tin oxide ETLs. Tin oxide was used as an ETL in perovskite solar cells following the original report of Baena *et al*. on the use of an ALD-deposited SnO_2 layer,[102] and spin-coated tin oxide ETLs have also been developed.[103] ALD-deposited tin oxide ETLs improve PCE compared to TiO_2, and have the advantage of being able to be processed at lower temperatures (below 150 °C). Baena *et al*. had hypothesized that the work function of ALD-deposited SnO_2 may be responsible for the improved performance seen relative to TiO_2.[102] ALD-deposited tin oxide ETLs also exhibit enhanced stability in dry air, but degradation of performance after exposure to inert atmosphere.

Degradation of performance after exposure to inert atmosphere may indicate sensitivity of the SnO_2 surface to molecular oxygen. Various metal oxides are known to experience changes in their surface properties with changes in the partial pressure of oxygen, hypothesized to be due to the filling of interstitial vacancies at the oxide surface. Phosphonic acid surface modifiers have been used in organic solar cells for the modification of ITO or ZnO to impart increased stability,[225] improved open circuit voltage,[226] and suppressed surface recombination.[227] For ZnO, Cowan *et al*. presented evidence that the increase in stability in organic solar cells is due to passivating the ZnO

surface to molecular oxygen adsorption.[228] Phosphonic acid modification of ALD-deposited SnO_2 may increase device performance and stability, and can afford insight into the effects of this modification upon properties such as work function, surface energy, and perovskite morphology.

5.3.2 Results and discussion

Initially, the fluorinated phosphonic acids pentafluorobenzyl phosphonic acid (PFBPA) and (4-(trifluoromethyl)benzyl)phosphonic acid (*p*CF3-BPA) used previously for surface studies were tested for this system (Figure 5-22).

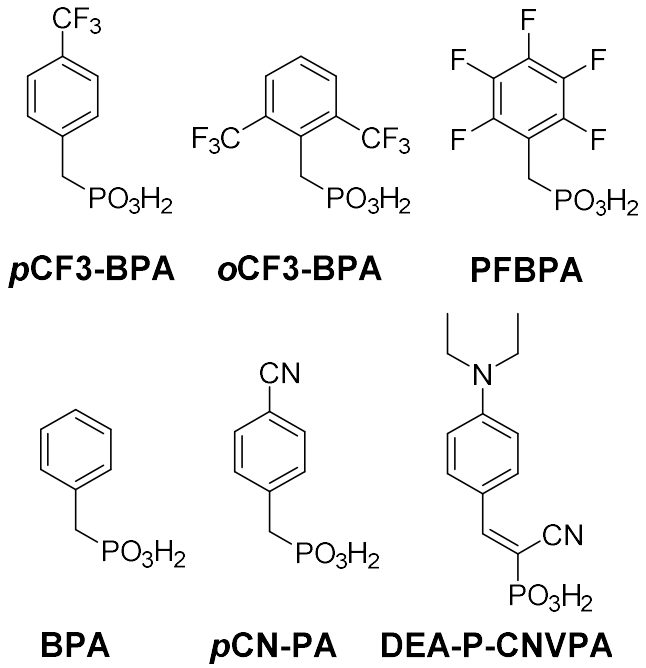

Figure 5-22. Phosphonic acid modifiers investigated for SnO_2 treatment.

Surface modification conditions were explored to determine the extent of modification optimal in perovskite solar cell devices. The modification conditions of 0.05 mM phosphonic acid in ethanol with a dipping time of 3 h were selected after examining the effect of dipping time on device efficiency (

Figure 5-23).

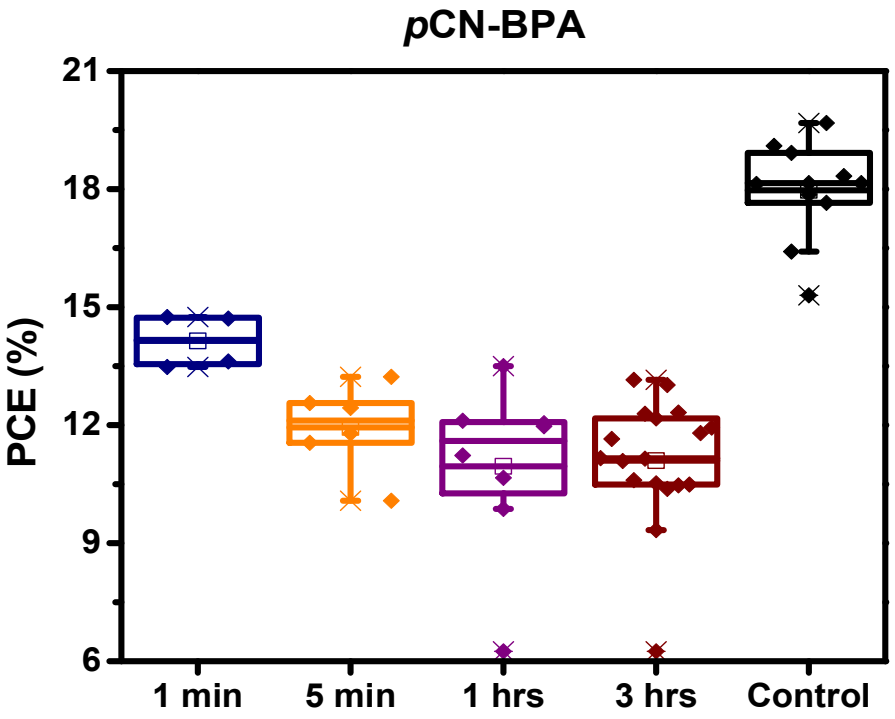

Figure 5-23. Power conversion efficiency as a function of dipping time for *p*CN-BPA.

Visual differences in film formation were seen, with extensive dewetting seen when the modifiers employing fluorine or trifluoromethylene in the *para* position were

utilized. The surface modifiers benzyl phosphonic acid (BPA), (4-cyanobenzyl)phosphonic acid (*p*CN-BPA), and (*E*)-(1-cyano-2-(4-(diethylamino)phenyl)vinyl)phosphonic acid (DEA-P-CNVPA) in Figure 5-22 were chosen for further studies as they exhibited similar film formation as the control devices and were expected to shift work function in varying ways based on their molecular dipoles.

The contact angle of the modified substrates was examined and the surface energy calculated using the Fowkes theory.[229] The largest difference seen between the substrates was in the contact angle of water and the corresponding polar component of the surface energy. The contact angle of water and the corresponding polar component of the surface energy correlates well with the trends in open circuit voltage and PCE. These results potentially point to using the polar component of the surface energy as an indication of suitability of a surface modifier for use in perovskite solar cells.

Table 5-5. Surface modified tin oxide contact angles using water and diiodomethane, with the calculated dispersive, polar, and total surface energy. The control sample was UV-Ozone treated prior to measurement. The surface energy error was propagated from the contact angle measurements, and does not include error from literature values.

	Control	**BPA**	***p*CN-BPA**	**DEA-P-CNVPA**
θ_{water}	5.4 ± 2.9	27.7 ± 5.3	37.8 ± 3.4	47.9 ± 2.1
$\theta_{diiodomethane}$	29.6 ± 3.8	25.9 ± 3.4	20.3 ± 3.4	21.4 ± 3.4
$\boldsymbol{\gamma_{polar}}$	31.8 ± 1.1	24.7 ± 2.3	19.0 ± 1.8	14.0 ± 1.2
$\boldsymbol{\gamma_{disp}}$	44.4 ± 1.6	45.8 ± 1.2	47.7 ± 1.0	47.4 ± 1.1
$\boldsymbol{\gamma_{total}}$	76.2 ± 1.9	70.5 ± 2.6	66.7 ± 2.1	61.3 ± 1.6

The morphology of the perovskite on top of the modified tin oxide was examined via atomic force microscopy (AFM)[230,231] and scanning electron microscopy (SEM)[232–234] for changes in morphology and roughness (Figure 5-24). The surface of the samples was fairly consistent, and it is hypothesized that changes in the surface energy may affect the interface, but not necessarily the bulk perovskite.

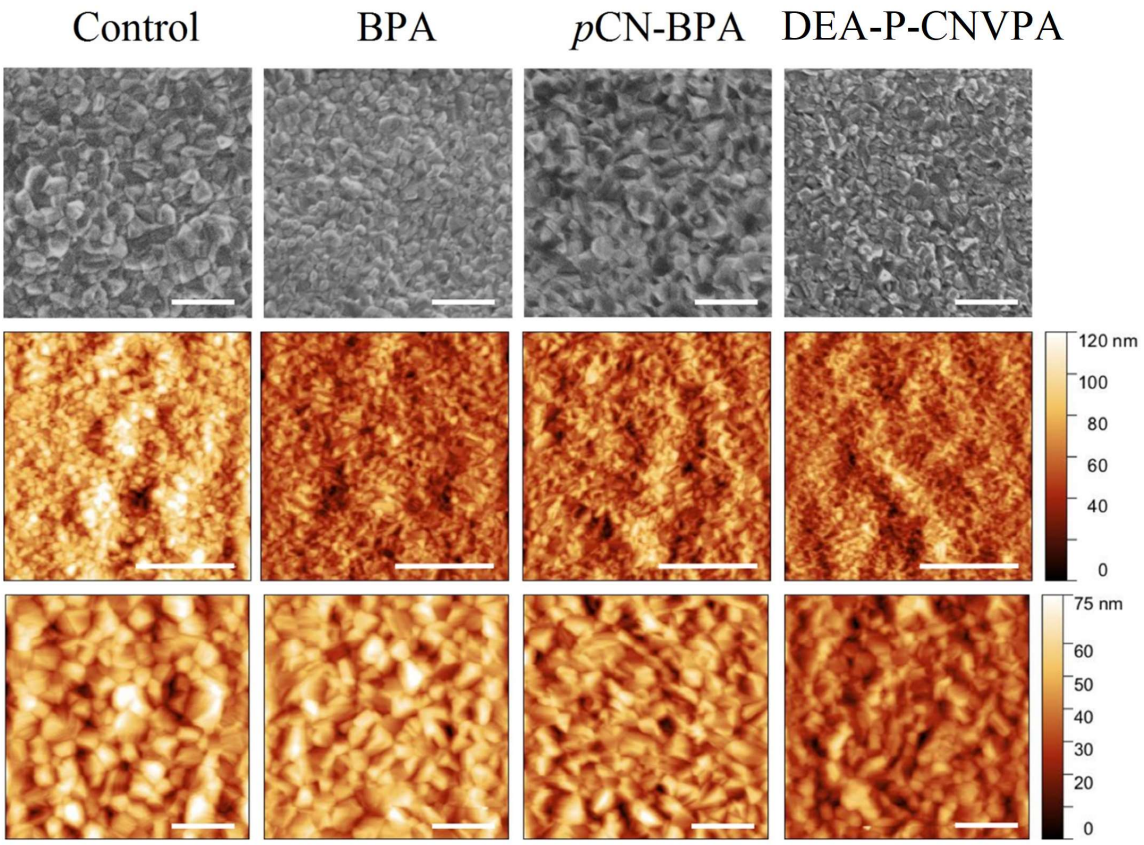

Figure 5-24. SEM and AFM of control and phosphonic acid modified substrates. Prior to device fabrication, the control was treated with UV-Ozone for 15 min, while the tin oxide was modified with 0.05 mM of phosphonic acid in ethanol for 3 h.

The secondary electron edge of the control and phosphonic acid-modified tin oxide substrates was measured by ultraviolet photoelectron spectroscopy to extract the work function values (Figure 5-25). As expected, surface modification with (4-cyanobenzyl)phosphonic acid (*p*CN-BPA), with its electron-withdrawing cyano group, exhibited the largest work function of the modified substrates at 4.5 ± 0.1 eV. Surface modification with benzyl phosphonic acid (BPA) produced an intermediate work function change (4.3 ± 0.1 eV), while modification by (*E*)-(1-cyano-2-(4-(diethylamino)phenyl)vinyl)phosphonic acid (DEA-P-CNVPA), with its electron-

donating amine, attained the lowest work function at 4.1 ± 0.1 eV. Based on these changes of 0.2-0.4 eV in the work function of the modified substrates (Figure 5-7), one could expect noticeable changes in the device V_{OC} if this modified potential is retained upon deposition of the perovskite.

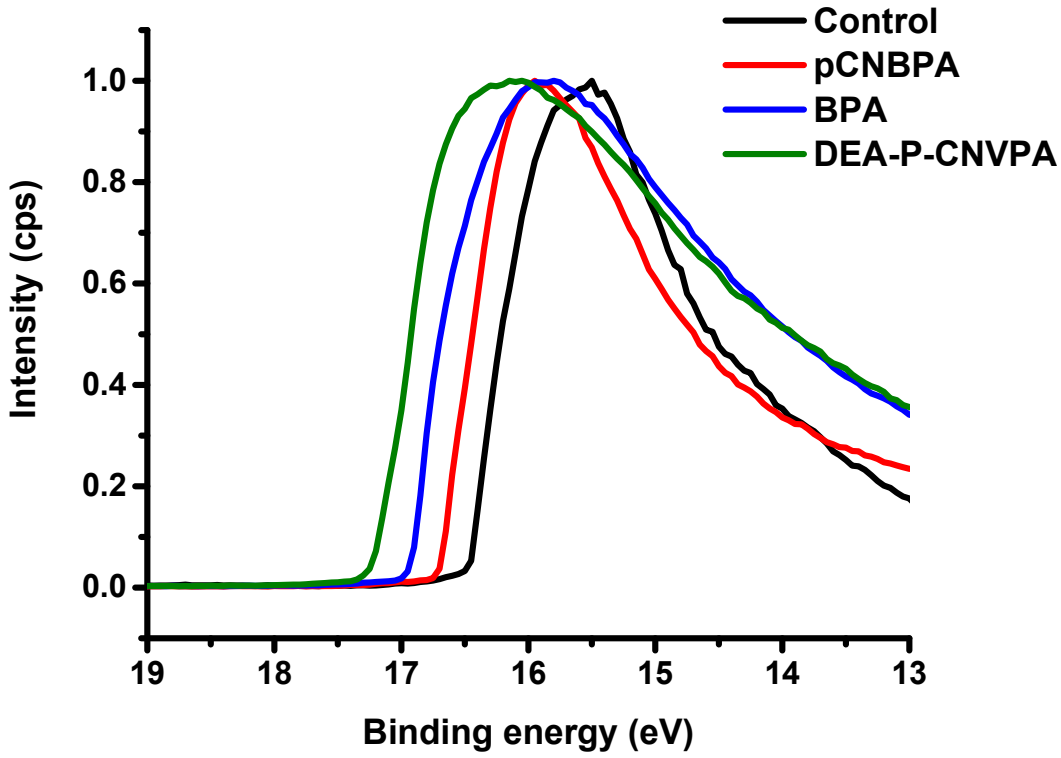

Figure 5-25. Secondary electron edge onset for control and phosphonic acid-modified tin oxide substrates. Prior to measurement, the control was treated with UV-Ozone for 15 min, while the tin oxide was modified with 0.05 mM of phosphonic acid in ethanol for 3 h.

Table 5-6. Work function in eV for control and phosphonic acid modified substrates. Prior to measurement, the control was treated with UV-Ozone for 15 min, while the tin oxide was modified with 0.05 mM of phosphonic acid in ethanol for 3 h.

	φ [eV]
Control	4.8 ± 0.1
***p*CN-BPA**	4.5 ± 0.1
BPA	4.3 ± 0.1
DEA-P-CNVPA	4.1 ± 0.1

Device results indicated that all phosphonic acid surface modifications resulted in decreased overall performance, including V_{OC}, relative to the control. Examining the average V_{OC} for each modifier, there are only slight differences, with the V_{OC} of DEA-P-CNVPA incrementally higher on average than that of the BPA. The *p*CN-BPA does exhibit the lowest V_{OC} of the series, as expected, but the differences between the average V_{OC} values seen is not very large. Differences in average J_{SC} were also very slight, with the modifier BPA exhibiting a small improvement relative to the other modifiers. The results also showed the BPA-modified devices maintaining the highest FF and overall PCE.

The differences in V_{OC} are not clear, and are not of the same magnitude as with similar studies done for the modification of ZnO for organic solar cells. This indicates that for this system the work function alone does not determine the V_{OC} obtained. It is possible and quite likely that in the absence of a full monolayer of phosphonic acid, the

surface properties after deposition of the perovskite may radically change. One could suppose that a full monolayer of modifier would be ideal for maintaining the desired work function and surface passivation. However, in this system, when increased concentrations of phosphonic acid and longer dipping times were employed, further decreases in overall performance were observed, potentially due to saturation of phosphonic acid binding on the surface, which could act as an insulating layer.

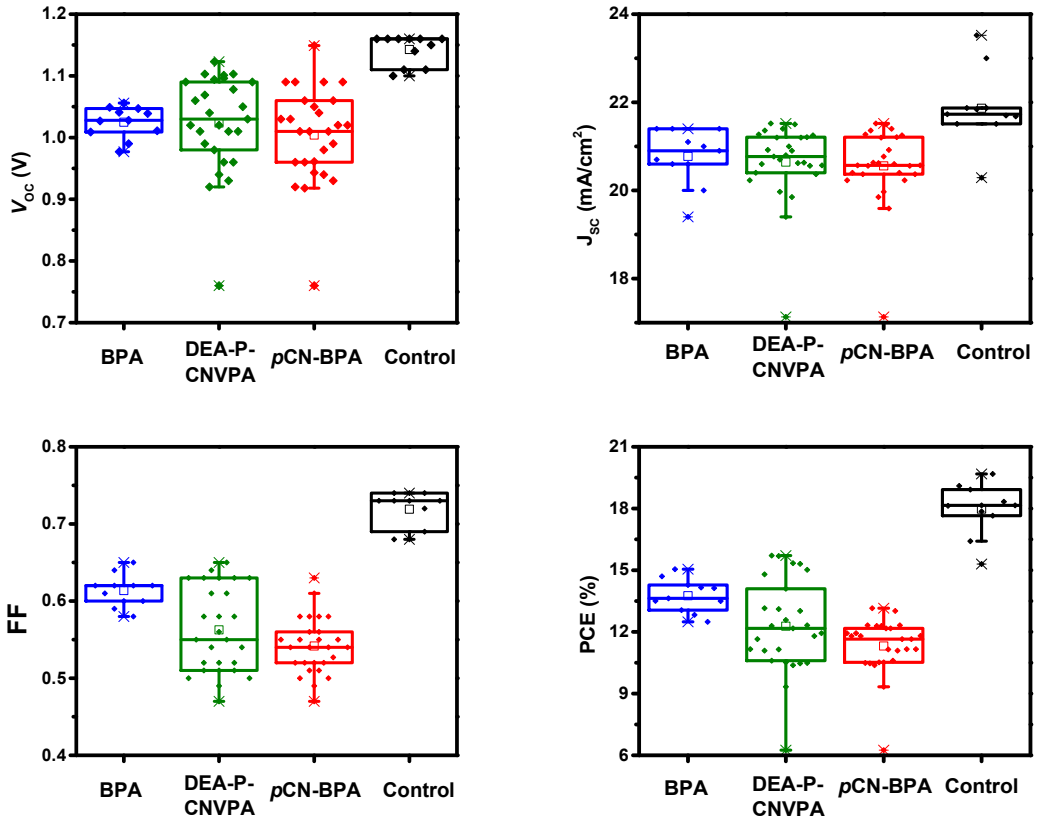

Figure 5-26. Distribution of photovoltaic results for tin oxide modified with 0.05 mM phosphonic acid in ethanol for 3 h.

As noted previously, a degradation of photovoltaic performance has been seen for perovskite solar cells with an ALD-deposited SnO_2 ETL kept under inert atmosphere. Based on surface passivation by phosphonic acids in organic solar cells, it was hypothesized that phosphonic acid modification would promote a stabilization of the photovoltaic performance for ALD-deposited SnO_2 ETL devices kept under inert atmosphere. Upon testing (Figure 5-27), the control sample showed a marked increase in hysteresis and decreased to 65% of the original PCE after 19 h. The phosphonic acid modified sample, however, maintained similar hysteresis and decreased to 86% of the original PCE after 19 h (Figure 5-28), ending at an efficiency higher than that of the control. This shows the importance and promise of phosphonic acid surface modification of ALD-deposited SnO_2 ETLs for perovskite solar cell stability under inert or low oxygen environments customary in commercial encapsulation of photovoltaic modules.

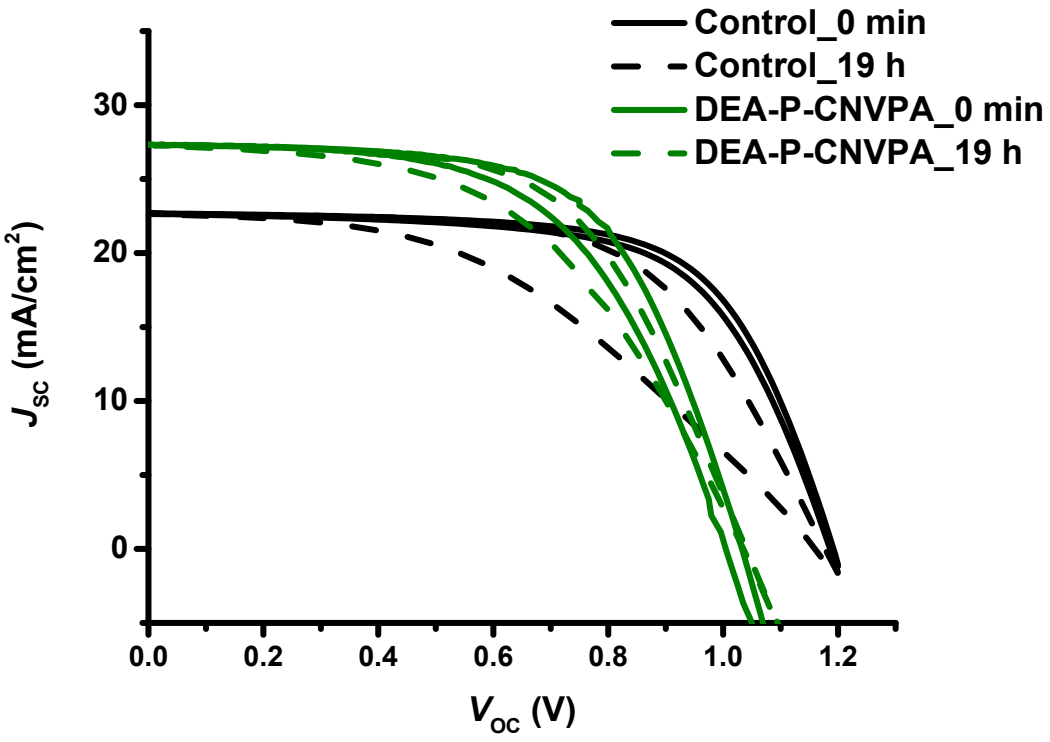

Figure 5-27. Forward and reverse J-V curves of control and modified devices before and after resting in inert atmosphere for 19 h. Prior to device fabrication, the control was treated with UV-Ozone for 15 min, while the tin oxide was modified with 0.05 mM DEA-P-CNVPA in ethanol for 1 h.

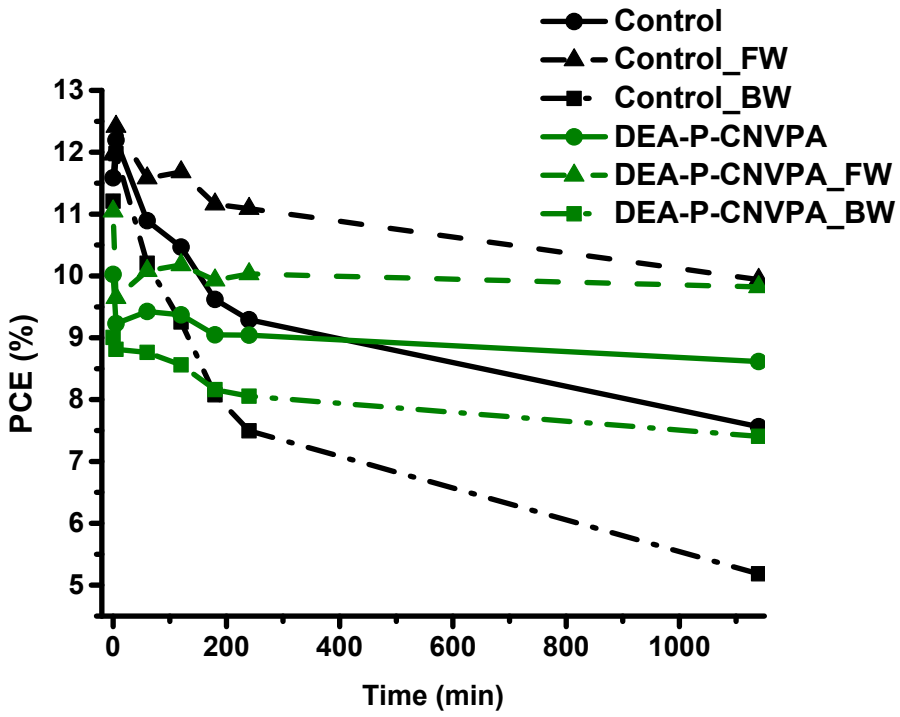

Figure 5-28. Control and modified devices as a function of time resting in inert atmosphere. Prior to device fabrication, the control was treated with UV-Ozone for 15 min, while the tin oxide was modified with 0.05 mM DEA-P-CNVPA in ethanol for 1 h.

5.3.3 Conclusions

In summary, phosphonic acid modification promotes stabilization of the photovoltaic performance for ALD-deposited SnO_2 ETL devices kept under inert atmosphere. The phosphonic acid modified sample, maintained similar hysteresis and decreased to only 86% of the original PCE after 19 h, compared to the control which showed an increase in hysteresis and decreased to 65% of the original PCE after 19 h. The effect of phosphonic acids on the work function and surface energy of ALD-deposited SnO_2 ETLs for perovskite solar cells was quantified, with the work function having an extremely minor influence on the V_{OC}, if at all. For surface energy, an increase

in the polar component of the surface energy correlated well with improved overall device performance. The phosphonic acid modifiers tested all had a lower polar component of surface energy than the unmodified substrate, so future modifiers could be developed to matech the surface energy of the unmodified substrate. Differences in surface energy may affect crystallization and grain boundaries near the SnO_2-perovskite interface, though AFM and SEM illustrate that the bulk perovskite morphology remains relatively unaffected. Device stability in inert atmosphere was greatly improved for the phosphonic acid-modified substrate, leading to greater PCE in the modified substrate than in the control substrate after 19 h in inert atmosphere. Phosphonic acids are a promising way to passivate the SnO_2 surface, and further studies could explore the use of phosphonic acids with end groups providing surface energy closer to that of unmodified SnO_2.

5.4 Experimental Methods

5.4.1 Material

Zinc powder, titanium isopropoxide (TTIP), lead (II) iodide (PbI_2), lead(II) bromide ($PbBr_2$), 4-*tert*-butylpyridine (tBP), bis(trifluoromethane)sulfonimide lithium salt (Li-TFSI), hydrochloric acid (HCl), ethanol (EtOH), acetone (Ace) isopropanol (IPA), chlorobenzene (CB), dimethyl sulfoxide (DMSO), dimethylformamide (DMF), 1.2-dichlorobenzene (DCB), 2-methoxy ethanol, fullerene (C_{60}, 99.5 % purity) and poly(allylamine) (PAA) were purchased from Sigma-Aldrich; formamidinium iodide (FAI), methylammonium bromide (MABr) and cesium iodide (CsI) were purchased from Dyesol; 2,2′,7,7′-tetrakis(*N,N′*-di-*p*-methoxyphenylamine)-9,9′-spirobifluorene (Spiro-

OMeTAD) was purchased from Merck; and fluorine-doped SnO_2 (FTO) glass was purchased from Solaronix SA.

5.4.2 Solar cell fabrication

Devices were fabricated on fluorine-doped SnO_2 (FTO) conducting glass (Pilkington TEC 8, 8 Ω/□). Some parts of FTO were treated with 2 M HCl solution containing zinc powder to make insulating regions. The resulting FTO was washed using detergent, acetone, ethanol, and IPA; oxygen plasma cleaning was then done to remove the organic residues. For the conventional TiO_2 ETL, a solution of 0.5 mM titanium isopropoxide (TTIP) in ethanol and 40 mM HCl solution in ethanol were slowly mixed together. The mixed solution was dropped onto the substrate and spin-coated at 2000 rpm for 1 min. The TiO_2-coated substrates were heated at 500 °C for 30 min. For the C_{60}-PAA ETLs, a solution of C_{60} (10 mg mL^{-1} in 1,2-dichlorobenzene) was spin-coated on top of the FTO at 1000 rpm for 1 min followed by drying at 60 °C for 2 min. After cooling down the substrate, the solution of PAA (20 wt% in water PAA solution was used and diluted using 2-methoxy ethanol to 0.04, 0.08, 0.12, and 0.16 wt% PAA) was spin-coated on the FTO/C_{60} substrate at 5000 rpm for 1 min followed by drying at 60 °C for 2 min. Then the substrates were transferred in a nitrogen atmosphere glovebox and annealed at 150 °C for 1 min. The substrates were then transferred to the drybox (< 25% humidity) and the triple mixed-cation perovskite ($Cs_{0.05}(MA_{0.17}FA_{0.83})_{0.95}Pb(I_{0.83}Br_{0.17})$) precursor solution was prepared from solutions containing FAI (1 M), PbI_2 (1.1 M), MABr (0.2 M), $PbBr_2$ (0.2 M) in anhydrous DMF:DMSO=4:1 (v:v). Then CsI (1.5 M) stock solution was added to the mixed perovskite solution in 5:95 vol. ratio. The perovskite solution was spin-coated at 1000 and 6000 rpm for 10 and 20 sec and CB was added 5 s prior to the

end of the program. The crystallization of the perovskite was finished by annealing at 100 °C for 1 h. Spiro-OMeTAD in chlorobenzene (180 mg in 1 mL) solution with Li-TFSI and tBP (molar ratio of 0.5 and 3.3, respectively, compared to Spiro-OMeTAD) was spin-coated on the perovskite layer. Finally, a 100 nm silver electrode was vacuum-deposited on the spiro-OMeTAD overlayer.

5.4.3 Device characterization

Keithley 2400 SMU and an Oriel xenon lamp (450 W) with an AM1.5 filter were used to obtain a *J-V* and MPP efficiency of solar cell (in air under AM 1.5G illumination of 100 mW cm^{-2} (Oriel 1 kW solar simulator)). AM 1.5G illumination was calibrated with a KG5 filter certified by NREL. For the *J-V* measurement, light soaking for 2000 ms, 0.06 V s^{-1} of scan rate with 100 ms voltage settling time were used. The active area of the devices was 0.09 cm^2. A mask was used to define the active area.

5.4.4 UV-vis measurements

UV-Vis. spectra were obtained using an OPTIZEN POP. For the measuring of solvent resistance, solvents (DMF, DMSO, and CB) were dropped on the substrate and spin-coated and then the UV-vis measurements were conducted.

5.4.5 SEM measurement

Field emission scanning electron microscope (FE-SEM, Hitachi S 4800) was employed to observe the surface of the various substrates.

5.4.6 SCLC measurement

The electron mobility (μ_e) was calculated by using the Mott-Gurney equation.

$$J = \frac{9}{8}\varepsilon_0\varepsilon_r\mu_e\frac{V^2}{L^3}$$

5.4.7 Transient photocurrent

Paios 2.0 (Fluxim) was employed to measure the transient photocurrent.

5.4.8 EQE measurement

Constant 100 W Xenon lamp source with an automated monochromator filters (5-position filter wheel) and 0.76 mm x 1.0 mm rectangular spot size was used for external quantum efficiency (EQE) spectra. The measurements were conducted in the wavelength range from 350 to 1100 nm, chopped at 4 Hz for high signal-to-noise (IQE-200B model).

5.4.9 Time resolved photoluminescence measurements

Time resolved photoluminescence (TRPL) measurements were performed using time correlated single photon counting (TCSPC) system (HAMAMATSU/C11367-31). Excitation wavelength of 474 nm and an emission wavelength of 770 nm were used for measurement. The samples were excited from the glass side under ambient conditions.

5.4.10 Contact angle measurement

Contact angle images were measured under white LED module (Surface and electro-optics 300A). Di-water and glycerol were applied to calculate surface energy and the drop volume was controlled precisely by 0.1µl of each. The surface energy was calculated by the Wu-harmonic mean method.

Values of the polar surface tension used were 50.7 mJ m^{-2} for DI-water and 1.8 mJ m^{-2} for glycerol, and of the dispersion surface tension were 22.1 mJ m^{-2} for DI-water and 49 mJ m^{-2} for glycerol were used.

5.4.11 TEM measurement

High-resolution transmission electron microscopy (TEM) images were obtained by a JEM-2200F electron microscope with an accelerating voltage of 200 kV. Cross-sectional TEM samples were prepared by focused ion beam method, and amorphous carbon paste was coated on the ETL for electron energy loss spectroscopy (EELS) analyses.

5.4.12 UPS and XPS

Measurements were conducted in a combined XPS-UPS Kratos Axis Ultra with a normal base pressure of 10^{-8}-10^{-9} Torr. UPS spectra were acquired prior to the acquisition of XPS spectra for all samples. UPS spectra were obtained with a 21.2 eV He (I) excitation and a pass energy of 5 eV using a 27 μm spot size. Each sample was examined in at least five spots to ensure consistency over the entire surface. XPS data were collected with a monochromatic Al Kα source (300 W) using a 400 μm spot size and a pass energy of 160 eV for survey acquisition and 20 eV for high resolution spectra. Exposure of the surfaces to X-rays was kept to a minimum (ca. 1 h), and survey spectra were acquired for at least three spots on each surface to ensure homogeneity of the sample. All characterizations were performed at normal takeoff angle (0°) and data analyzed using Vision Processing version 2.2.8. The energy-level diagram shown in Figure 5-8 was constructed using the WFs deduced from the secondary electron edge,

while the C_{60} valence-band maxima (VBM) were taken as the onset of the lowest binding energy peak seen in the valence spectra. In the case of the PAA-treated sample, the C_{60} VBM onset position is potentially complicated by the presence of low-IE amine species and so was estimated by assuming the lowest-energy peak corresponds to ionization of the C_{60} HOMO, and that the width of this feature is the same as in that of bare C_{60}. The conduction band minimum (CBM) position was deduced assuming the transport gap of C_{60} to be the same as that previously inferred from UPS/IPES measurements.

CHAPTER 6. CONCLUSION

This thesis has focused on the development and characterization of light-absorbing sensitizers and surface modified electron-selective layers for the next-generation photovoltaic systems of dye-sensitized and perovskite solar cells, respectively. In both dye-sensitized solar cells and perovskite solar cells, the broader effects of small structural modifications were observed. For dye-sensitized solar cells, molecular structures for panchromatic and bathochromically shifted absorption (Chapter 2) were developed, then in Chapter 3, the effects of these and additional modifications were examined, focusing on their effect upon aggregation. On rhodanine anchoring groups, strongly binding phosphonic acids were compared to carboxylic acids (Chapter 4), and the effects on not only dye desorption, but charge generation and prevention of recombination were examined. The solvent resistance of an interfacial layer in a lead organo-halide perovskite solar cell device was then modified using fullerene-amine reactivity, and the surface energy and work function were examined for their influence on the overall device (Chapter 5). Dipolar phosphonic acid surface modifiers were employed in ALD-deposited SnO_2 for use as an electron collecting electrode in perovskite solar cells, with interesting effects seen on device stability in an inert atmosphere. Optimization of interfaces is key to effective photovoltaic devices, and broader effects of small structural modifications were examined.

6.1 Results and Insights

Chapter 2 developed squaraine sensitizers with bathochromically shifted absorption maxima into the near-infrared and panchromatic absorption across the high-

energy part of the visible spectrum. The direct comparison of benzo[*e*]indole, benzo[*g*]indole, and bis(4-butoxyphenyl)amino-indole functionalities and comparison of π-bridges such as thiophene, cyclopentadithiophene, benzothiadiazole-cyclopentadithiophene, and cyclopentadithiophene-benzothiadiazole-cyclopentadithiophene gave a broad picture of various ways the absorption profile can be tuned and the broader effects seen in the device. The effects seen for each modification are summarized in Table 6-1. Promising photocurrent response in the 800-850 nm wavelength range was seen through the use of various functionalities including bis(4-butoxyphenyl)amino-indole and BTD. The benzo[*e*]indole and CPDT groups provided sensitizers with above average J_{SC} and the highest overall PCEs, at 6.2% for benzo[*e*]indole- and CPDT-substituted sensitizer **2.4** and at 6.4% for sensitizer **2.6**. Sensitizer **2.3** exhibited promising J_{SC}, but additional investigation into the cause of low V_{OC} and FF values is needed. The low performance of sensitizers **2.5** and **2.8** was shown to be related to the high TiO_2-electrolyte recombination for these sensitizers.

Table 6-1. Chapter 2 structural modifications and general results seen.

Structural modification	Result
Benzo[*e*]indole	Relative to indole, red-shifted absorption by 18 nm, improved J_{SC}, V_{OC}, and FF, higher τ_e
Benzo[*g*]indole	Relative to benzo[*e*]indole, red-shifted absorption by 5 nm, decreased J_{SC} and V_{OC}, lower τ_e
bis(4-butoxyphenyl)amino-indole	Relative to indole, red-shifted absorption by 47 nm for an IPCE onset of >850 nm, with a slightly decreased V_{OC} and τ_e, a decreased IPCE % and increased J_{SC}
CPDT	Relative to thiophene, increase in absorption near 300 and 500 nm, increase in J_{SC}, slight decrease in V_{OC}, FF, τ_e, and in IPCE % in at maximum absorption
BTD-CPDT	Relative to CPDT, sharp decrease in J_{SC} and slight decrease in τ_e, slight decrease in V_{OC} and FF, possibly due to lack of electron density on anchor upon excitation
Benzo[*e*]indole CPDT-BTD-CPDT	IPCE response tailing to 840 nm, increase in J_{SC} relative to BTD-CPDT with similar J_{SC} as CPDT, but a decrease in V_{OC} and τ_e relative to both CPDT and BTD-CPDT

In chapter 3, the effect of out-of-plane substituents on aggregation were examined on a series of squaraine dyes. Out-of-plane substituents on different regions of the

squaraine structure can have very different effects on both dye-dye and dye-electrolyte interactions. While the work focused on dye-dye interactions and aggregate formation, it became clear that a competing effect was recombination. For example, although the simple indole control with a thiophene π-bridge (sensitizer **2.1**) exhibited evidence of aggregation, it also exhibited low recombination as exhibited in its relatively high electron lifetime when compared to sensitizer **2.5** with linear chains on the CPDT π-bridge. Another interesting effect is that a modification resulted in a different magnitude of effect depending on what other functionalities are present. For example, a terminal mesityl will have less of an effect on J_{SC} and FF if a bulky CPDT π-bridge is also present. Interestingly, sensitizers **3.2**-**3.3** with out-of-plane groups in the terminal region I and without out-of-plane groups in region III on the π-bridge exhibited the highest electron lifetimes.

Table 6-2. Chapter 3 structural modifications and general results seen.

Structural modification	Result
Mesityl group in combination with small π-bridge	improved J_{SC}, V_{OC}, and FF, gave similar τ_e relative to indole- and thiophene- substituted control
Mesityl group in combination with bulky π-bridge	nearly identical τ_e & J_{SC} relative to benzo[*e*]indole- and CPDT- substituted comparison
Dibutyl-substituted indole	increased τ_e & increased J_{SC} and V_{OC} relative to indole- and thiophene- substituted control
CPDT with gem-di-n-hexyl alkyl chains	increase in J_{SC} relative to thiophene, but a decrease in V_{OC} and τ_e relative to benzo[*e*]indole- and thiophene-substituted control
CPDT with gem-di-2-ethylhexyl alkyl chains	decrease in J_{SC} and increase in V_{OC} relative to *n*-hexyl-based CPDT; increase in J_{SC} relative to thiophene
DTS with gem-di-2-ethylhexyl alkyl chains	decrease in J_{SC} and increase in V_{OC} relative to 2-ethylhexyl-based CPDT; increase in J_{SC} relative to thiophene

Chapter 4 examined whether the use of phosphonic acids in conjunction with rhodanine anchoring groups could promote efficient electron injection and strong and

stable binding. The comparison between rhodanine-3-methylphosphonic acid and rhodanaine-3-acetic acid on two donor-π-acceptor sensitizers incorporating dibutylaminothiophene or indoline-benzothiadiazole functionalities showed that J_{SC} decreased by approximately 50% with the use of phosphonic acids, but stability of the dyes on the TiO_2 surface increased dramatically. It is possible that the phosphonic acid sensitizers favored a binding configuration that did not allow the rhodanine to interact with the surface, inhibiting efficient electron injection. Lower V_{OC} values were seen for the phosphonic acid-substituted sensitizers **4.2** and **4.4** vs. the carboxylic acid-substituted sensitizers **4.1** & **4.3**, which was due to higher TiO_2-electrolyte recombination seen by the lower electron lifetimes for the phosphonic acid-substituted sensitizers.

In Chapter 5, the development of low-temperature-processed C_{60}–PAA ETLs for use in flexible perovskite solar cells was based on the concept that rather than synthesizing and purifying fullerene derivatives capable of cross-linking, the fullerene could be insolubilized *in situ*. In the end, the film not only exhibited excellent solvent resistance, but had optimized work function, improved surface energy, maintained electrical properties of C_{60}, high reproducibility, and high stability during bending cycles on a flexible substrate. In the second part of Chapter 5, phosphonic acids were used to modify the work function and surface energy of ALD-deposited SnO_2 ETLs for perovskite solar cells. The change in work function resulted in a negligible influence on the V_{OC} in these devices, while an increase in the polar component of the surface energy correlated well with improved overall device performance. Device stability in inert atmosphere was greatly improved for the phosphonic acid modified substrate, showing

promise for the strategic use of phosphonic acids to passivate the SnO_2 surface and increase stability under inert atmosphere.

6.2 Future Work

In relation to the donors examined in Chapter 2, further studies could examine similar functionalities to that of sensitizer **2.3** in conjuction with modifications to the squaraine termination that could facilitate proper interaction with cobalt or copper electrolytes. As previously discussed, to achieve a PCE of 20% in DSSCs, a loss-in-potential of 0.4 eV is needed for both electron injection and regeneration of the sensitizer. Depending on the sensitizer, the iodine/triiodide redox couple can require an overpotential of up to 0.5 eV for sensitizer regeneration, while cobalt complexes such as $Co(bpy)_3^{2+/3+}$ and $Co(phen)_3^{2+/3+}$ and copper complexes such as $[Cu(dmp)_2]^{1+/2+}$, $[Cu(tmpy)_2]^{2+/1+}$, and $[Cu(dmpy)_2]^{2+/1+}$ require lower overpotentials. In donor-π-acceptor sensitizers such as LEG4 (Figure 4-1), the use of out-of-plane alkoxy groups relative to no alkoxy groups has been shown to improve photovoltaic performance when using cobalt and copper complex redox couples. Figure 6-1 proposes a structural modification of squaraine sensitizer **2.3** to prevent close interaction of the squaraine core with cobalt or copper redox couples.

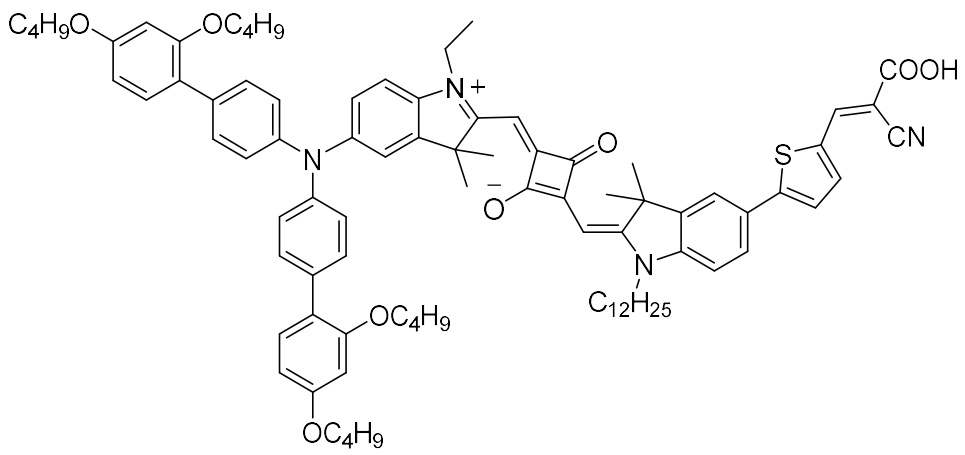

Figure 6-1. Proposed structural modification incorporating a "LEG4" end group on sensitizer **2.3**.

Building directly upon the work on aggregation in Chapter 3, a future study could examine the effect of chain length simultaneously on the squaraine end, center, and π-bridge, as shown in Figure 6-2. Makowsi *et al*. employed 2-ethylhexyl groups on the nitrogen of the indole to slow crystallization of a squaraine melt,[235] and the effect of branched chains in this position could also be of interest for further prevention of squaraine aggregation in DSSCs.

To modify the squaraine structure for better performance with cobalt and copper electrolytes, out-of-plane alkoxy groups could be used in place of methyls on the mesityl group to aid both in preventing aggregation and to facilitate use with cobalt or copper electrolytes. The triphenyl amine donor used in LEG4 could also be explored as an electron-donating group for a sensitizer similar to the sensitizer **2.3** developed in Chapter 2.

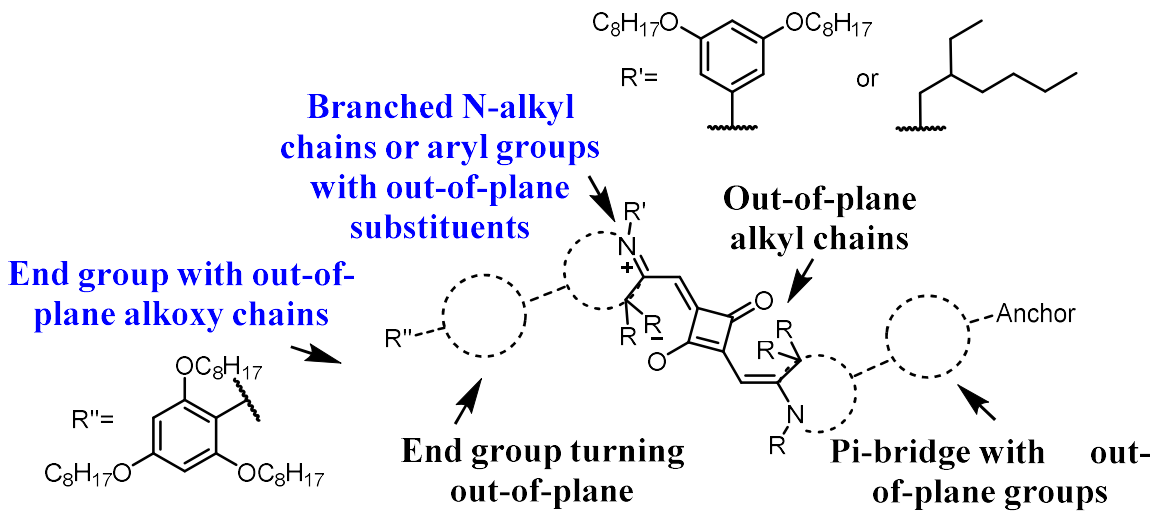

Figure 6-2. Potential groups to prevent aggregation and improve photovoltaic performance in squaraine-based DSSCs.

In biological applications, rotaxanes encircling the squaraine core (Figure 6-3) are used to prevent solid-state aggregation and impart increased stability,[236,237] and could be of interest for DSSC applications. Rotaxanes can be "clipped" on after synthesis of the squaraine sensitizer, or the squaric acid condensation can be performed while threading through a preformed rotaxane.

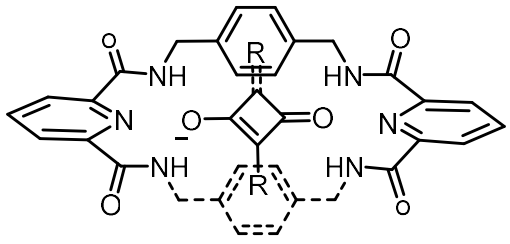

Figure 6-3. Rotaxane developed by Arunkumar by *et al*. and used to "clip" around synthesized squaraine.[236]

The use of dendrimeric substituents could also be investigated for the ability to prevent aggregation in squaraine sensitizers for DSSCs. Branched dendrons were used by Scarpaci *et al*. for decreasing aggregation in cyanine dyes for non-linear optics applications (Figure 6-4).[238]

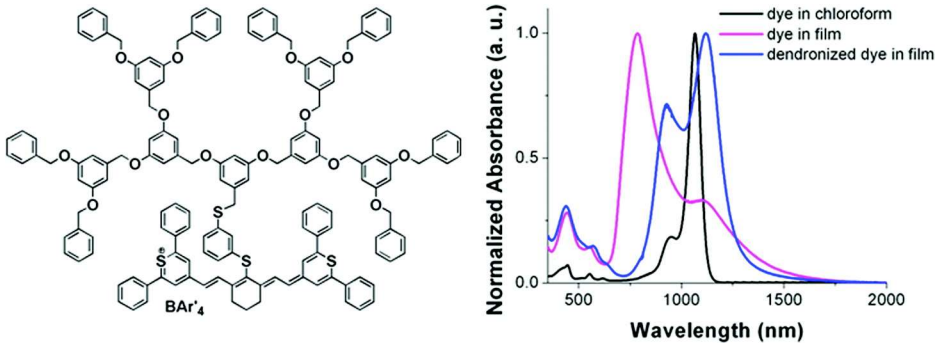

Figure 6-4. Cyanine structure with branched dendron incorporated and corresponding decrease in blue-shifted aggregate peaks in the film absorption.[238]

Cosensitization using two dyes with relatively different structures may also be a route for preventing aggregation between dyes at the surface of the TiO_2 film.[239] Cosensitization can also provide complementary absorption,[122] and enable the use of strongly near-IR absorbing squaraine dyes alongside sensitizers that absorb mainly in the high-energy visible region of the solar spectrum. Cosensitization could also be of interest for phosphonic acid-bound sensitizers. Further studies could computationally and experimentally examine the binding modes of the rhodanine-3-methlyphosphonic acid anchoring group on TiO_2 to understand how to modify this system for improved IPCE %.

Alternate electron acceptors where ancilliary phosphonic acids could be incorporated could also be explored.

For the surface modification of C_{60} electron transport layers discussed in Chapter 5, future work could combine the approach with n-doping the C_{60} for improved film conductivity. PAA itself is not conductive, and an amine-substituted conjugated polymer could also be explored with potentially beneficial effects on electron mobility and overall device performance. For the phosphonic acid surface modification of SnO_2, further studies could explore the effects seen on the stability of spin-coated, rather than ALD-deposited, SnO_2. Optimization of the polar component of surface energy of the modified surface could also be explored using various surface modifier end groups. End groups such as formamidinium could be investigated to template perovskite growth from the modified surface. The effect of conjugated vs. nonconjugated phosphonic acids could also be investigated, as conjugation of phosphonic acid surface modifiers has been seen to influence photovoltaic performance in organic solar cells.[240]

APPENDIX A. SUPPORTING DATA

Table A-1. Photovoltaic performance of the squaraine-based DSSCs under uniform conditions using no coadsorbent. [a,b,c]

	V_{OC} [mV]	J_{SC} [mA/cm^2]	FF [%]	PCE [%]
2.1, 3.1[a]	638	9.64	65.1	4.00
2.2, 3.4	633 ± 16	9.17 ± 0.62	62.2 ± 8.6	3.61 ± 0.47
2.3	607 ± 6	8.38 ± 0.06	59.3 ± 4.3	3.01 ± 0.16
2.4, 3.6	635 ± 17	9.20 ± 0.52	69.7 ± 4.7	4.08 ± 0.53
2.5	603 ± 6	6.92 ± 0.66	71.5 ± 0.8	2.98 ± 0.30
2.6, 3.7	630 ± 10	9.31 ± 1.93	70.2 ± 2.3	4.14 ± 1.05
2.7	625 ± 1	7.30 ± 0.98	70.7 ± 1.3	3.22 ± 0.37
2.8	604 ± 4	8.47 ± 0.35	64.6 ± 3.3	3.31 ± 0.33
3.2	661 ± 1	8.94 ± 0.10	74.9 ± 0.6	4.43 ± 0.02
3.3	653 ± 1	10.83 ± 0.47	73.0 ± 0.6	5.16 ± 0.26
3.5	587 ± 5	8.45 ± 0.08	67.3 ± 0.4	3.34 ± 0.04
3.8	626 ± 1	8.09 ± 0.99	72.9 ± 1.0	3.70 ± 0.49

[a]Based on measurements of 2-4 devices for all dyes except **2.1**,**3.1** (1 device only) with the standard deviation shown. [b]The photovoltaic measurements were conducted using a mask to restrict the cell active area to 0.16 cm^2. The dye solutions were 0.05 mM dye (no CDCA) in ethanol with a dipping time of 4 h, except compound for compound 2.8 which was dipped in 1:4 chloroform:ethanol. [c]YR6 was also tested at optimal literature conditions with 10 mM CDCA to yield the following: V_{OC}=654 ± 4 mV, J_{SC}=11.30 ± 0.16 mA/cm^2, FF=67.9 ± 1.4 (%), PCE=5.02 ± 0.1 %.

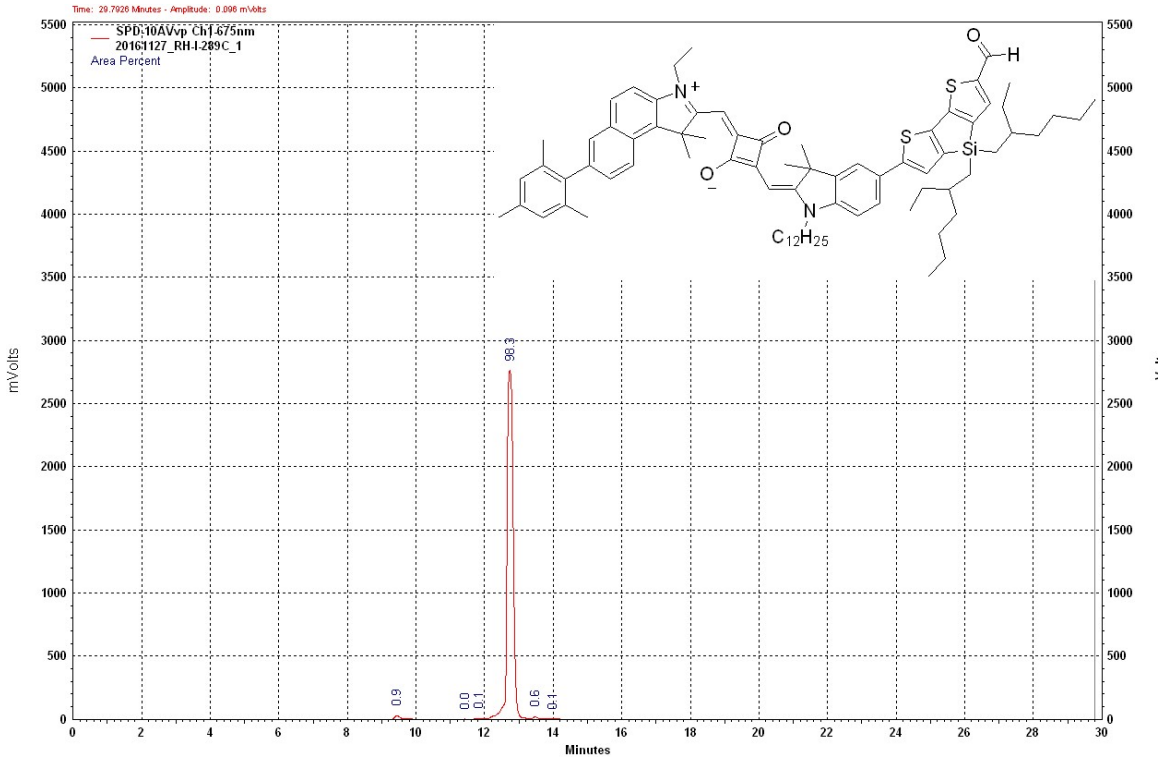

Figure A-1. HPLC of (*E*)-2-((*E*)-(5-(4,4-bis(2-ethylhexyl)-6-formyl-4*H*-silolo[3,2-*b*:4,5-*b'*]dithiophen-2-yl)-1-dodecyl-3,3-dimethylindolin-2-ylidene)methyl)-4-((3-ethyl-7-mesityl-1,1-dimethyl-1*H*-benzo[*e*]indol-3-ium-2-yl)methylene)-3-oxocyclobut-1-enolate (section 3.9.4.2).

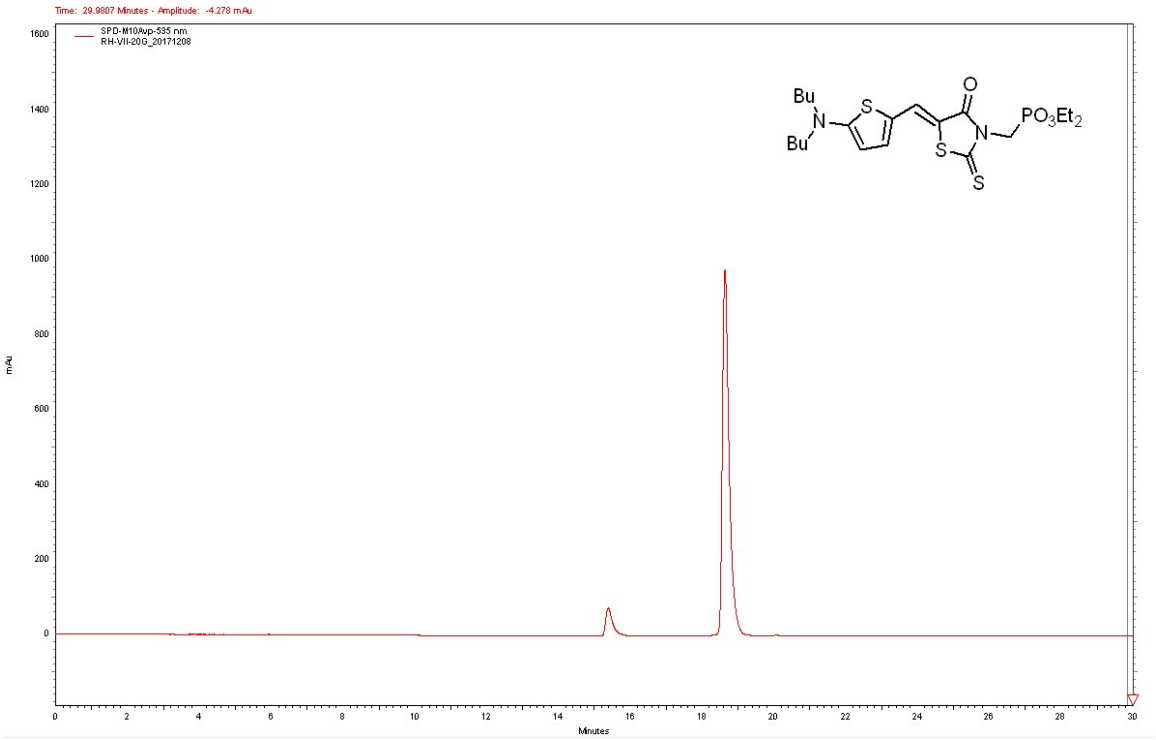

Figure A-2. HPLC of (*Z*)-5-((5-(dibutylamino)thiophen-2-yl)methylene)-3-(((diethyl- λ^3-oxidaneyl)(λ^1-oxidaneyl)phosphoryl)methyl)-2-thioxothiazolidin-4-one (section 4.10.2.3).

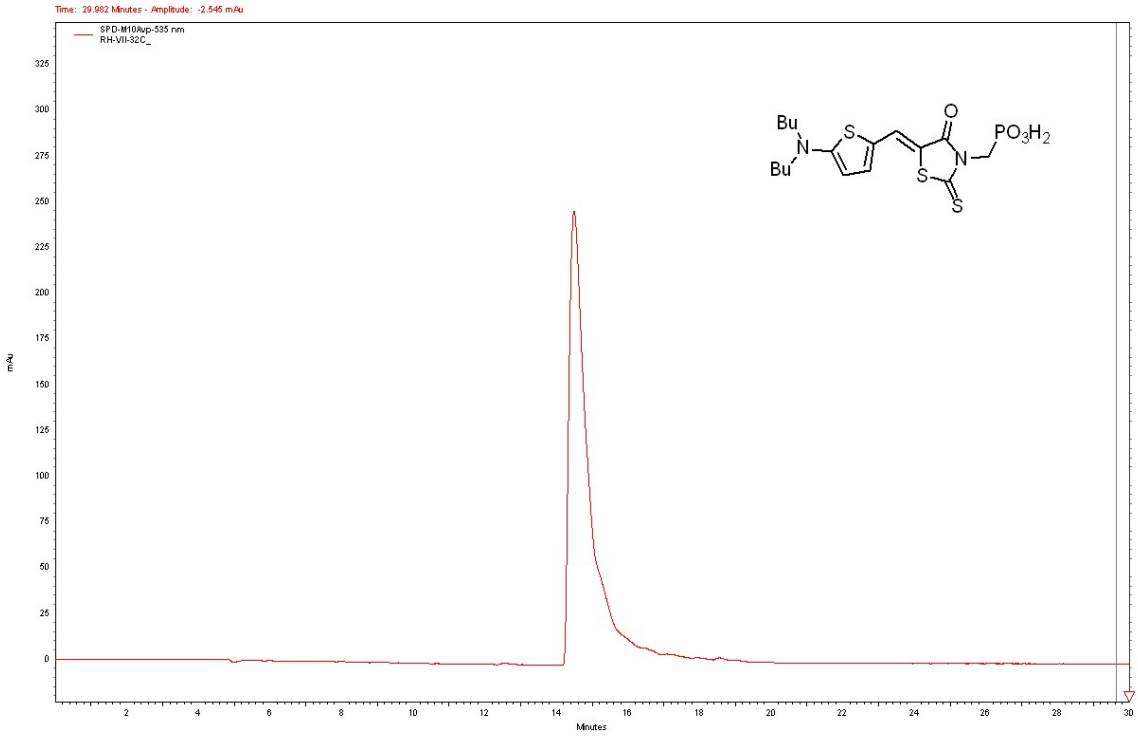

Figure A-3. HPLC of sensitizer **4.2**, (*Z*)-((5-((5-(dibutylamino)thiophen-2-yl)methylene)-4-oxo-2-thioxothiazolidin-3-yl)methyl)phosphonic acid.

A.1.1 Fabrication of dye-sensitized solar cells

Typical preparation of the counter electrode includes cleaning by sonication in a mildly acid solution and an organic solvent, then storage in a mildly acidic solution. Platinization is accomplished by dropping a solution of H_2PtCl_6 onto the conducting oxide surface, then heating at 450 °C for 15 min.

The working electrode preparation involves sintering the working electrode containing the TiO_2 film in air at 500 °C, then cooling to near 80 °C, immersion in the dye solution in which it is soaked at room temperature. The soaking time required varies according to the sensitizer's structure; for some ruthenium complexes an appropriate

soaking time is 12 h, while for certain organic sensitizers 4 h has been shown to be sufficient. The electrode is then rinsed with a selected solvent, such as acetonitrile or the solvent used in the dye solution, and the cell is assembled.

The dye solutions may be prepared in a variety of solvents, including ethanol, *tert*-butyl alcohol, acetonitrile, DMF, and DMSO. Commonly used solution concentrations for ruthenium sensitizers are in the range of 0.3 mM, while for dyes such as squaraines, optimal concentrations are seen in the range of 0.05-0.1 mM. Chenodeoxycholic acid (Figure A-4) is commonly used in the dye solution to disrupt dye aggregation.

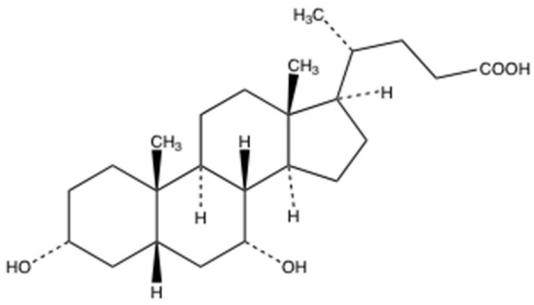

Figure A-4. Structure of chenodeoxycholic acid (CDCA).

Electrolytes used are tailored to the sensitizer and the optimization of its performance. The composition of a standard electrolyte used is noted below. Additives such as LiI are used to lower the Fermi level (E_F) of TiO_2, while tBP and CDCA raise E_F. tBP and GNCS have been shown to reduce dye desorption and recombination to I_3^-.

- Electrolyte "Z960"
    - 1,3-dimethylimidazolium iodide (DMII) 1.0M
    - I_2 0.03M

- Lithium iodide (LiI) 0.05 M
- 4-*tert*-butyl pyridine (4TBP) 0.5 M
- Guanidinium thiocynate (GNCS) 0.1 M
- Solvent: acetonitrile : valeronitrile = 85 : 15 (v/v)

A.1.2 Surface characterization

Various techniques can reveal information about surface structure.[241] The techniques employed must be sensitive enough to reveal information about extremely thin layers on a surface, and the appropriate techniques will depend on the nature of the modification itself and the desired information. Selected properties and techniques of interest are detailed below.

A.1.2.1 Chemical composition and bonding

The chemical composition of a surface before and after modification can be probed using X-ray photoelectron spectroscopy (XPS). XPS is an ultra-high vacuum technique that utilizes an x-ray source to ionize atoms at a sample surface, causing inner shell electrons to be ejected from the atoms at the surface to be analysed based on their kinetic energies. The energy of the emitted electrons will depend on both the atom and the shell the electron was emitted from, and the number of emitted electrons at each energy will depend on the number of atoms on the surface up to the detection limit (approximately 10 nm).[206] The energy of the electrons will also shift depending on how

the atom is bound in a molecule. For example, the C 1s peak will shift from 284.9 eV for a C-H or C-C bond to 286.6 eV for a C-O bond at the surface of aluminum.[242]

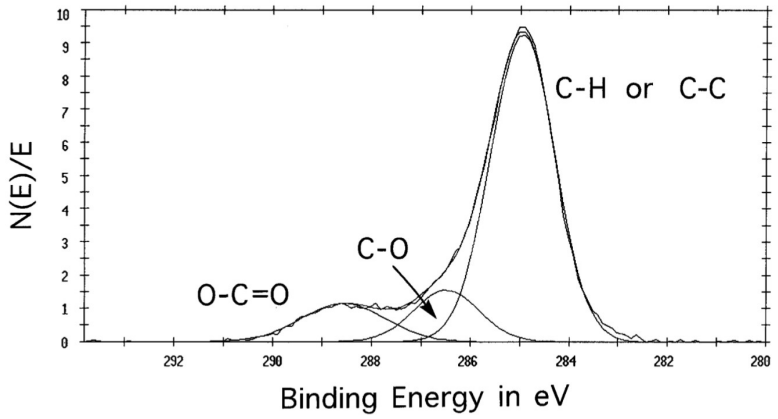

Figure A-5. The XPS C 1s region of an as-received aluminum sample. Reproduced from McCafferty and Wightman[242] with permission from John Wiley & Sons, Ltd.

A.1.2.2 Energy level alignment

Energy levels of interest include the following, as illustrated in Figure 1-13.

- Conduction band minimum (CBM) and valence band maximum (VBM): the electron and hole single-particle transport levels, respectively.
- Fermi level (E_F) is the boundary between occupied and unoccupied states in a continuum of states.
- Work function (ϕ_{WF}) is the energy needed to remove an electron from E_F to rest at a distance where it no longer experiences the effect of the surface, which is referred to as the vacuum level (E_{VAC}).

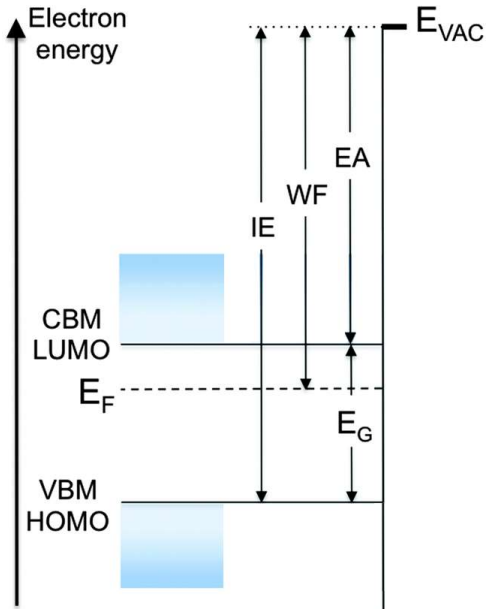

Figure A-6. Reproduced with modification from Kahn *et al.*[243] with permission from The Royal Society of Chemistry.

Work function can be measured by an absolute method, such as ultraviolet photoelectron spectroscopy (UPS), or by a relative method, such as Kelvin probe.

UPS is a technique used to measure the ionization energies of valence states, allowing identification of valence band states and the work function of the material. In UPS, a helium discharge source is used (normally tuned to He I at 21.22 eV), in order to examine the low binding energy valence electrons, rather than the core electrons examined in XPS. In UPS, secondary electrons, or electrons that have inelastically collided and lost varying amounts of energy, create a large spectral feature that allows one to determine the work function of the substrate, the secondary electron edge (SEE). The spectral features and values that can be derived therefrom are shown in Figure A-6.

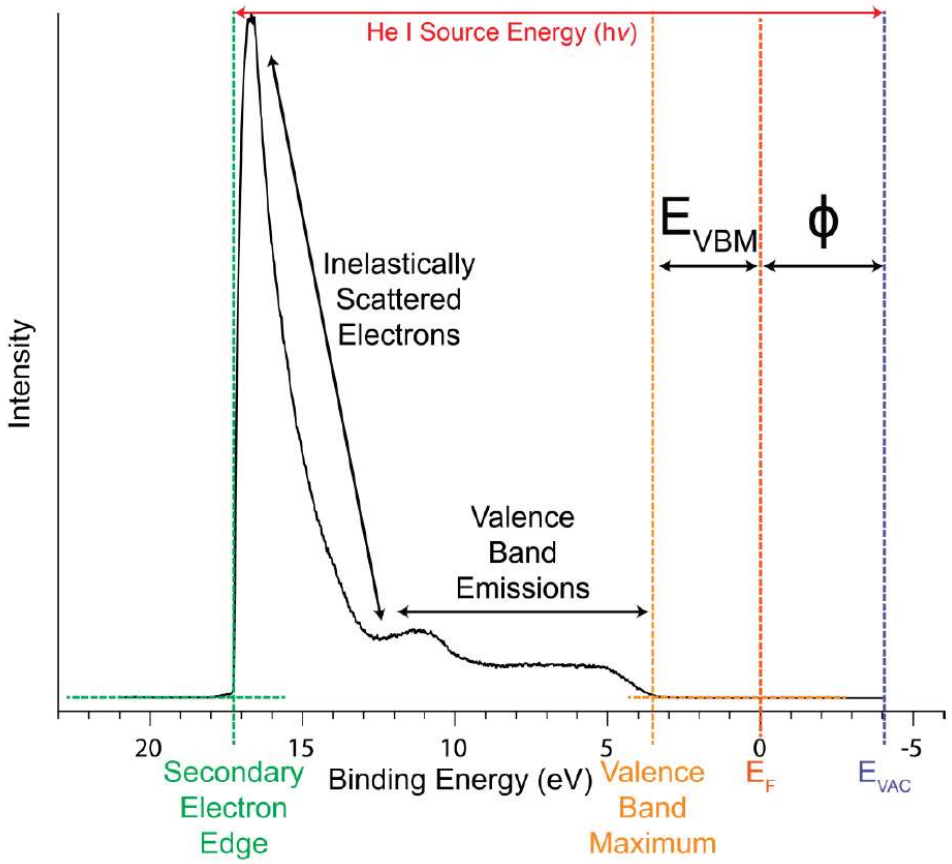

Figure A-7. Example spectra of bare ZnO obtained from UPS analysis. The work function (ϕ) and valence band maximum (E_{VBM}) are directly determined from the spectra; ϕ = (He I Source Energy) – SEE and E_{VBM} = (Valence Band Maximum) - E_F. The intensity of the SEE comes from inelastically scattered electrons that have escaped to vacuum, but lost energy in the process. Reproduced from Giordano.[244]

Kelvin probe is a realative technique to measure work function that is based on force microscopy principles and techniques. Kelvin probe measures the contact potential difference between an oscillating probe and a surface by bringing the probe into close proximity with the surface.[245,246] If the probe and surface are close enough for electron tunnelling, the system will reach an equilibrium state where the Fermi levels are aligned. To bring the system back to its original state, an external potential can then be applied.

This potential applied is measured to determine the work function difference between the probe and the substrate surface. Kelvin probe measurements are normally calibrated to highly oriented pyrolytic graphite, as its surface is chemically inert, and layers can be peeled off to produce a fresh surface prior to measurement. Kelvin probe may also be done in an inert atmosphere to avoid variability from humidity and atmospheric contamination of the probe. Work function values from Kelvin probe and UPS can be similar in magnitude, depending on a variety of factors.[247]

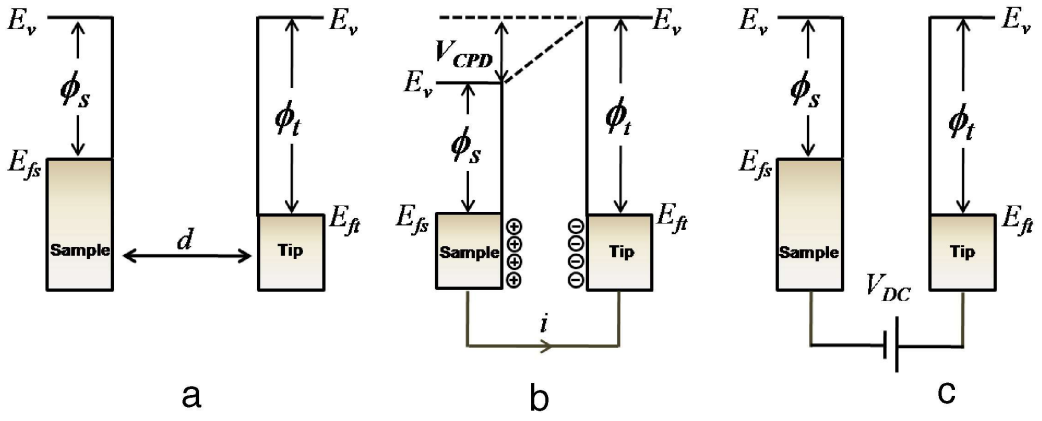

Figure A-8. Electronic energy levels of the sample and Kelvin probe tip for cases where: (a) the tip and sample are separated by a distance with no electrical contact, (b) the tip and sample are in electrical contact, and (c) an external bias is applied between the tip and sample to nullify the contact difference potential and, therefore, the tip–sample electrical force. E_v is the vacuum level, and E_{fs} and E_{ft} are the Fermi levels of the sample and tip, respectively. Reproduced from Melitz *et al*.[31] with permission from Elsevier.

REFERENCES

(1) Shi, J.; Xu, X.; Li, D.; Meng, Q. *Small* **2015**, *11* (21), 2472–2486.

(2) Fan, R.; Huang, Y.; Wang, L.; Li, L.; Zheng, G.; Zhou, H. *Adv. Energy Mater.* **2016**, *6* (17), 1600460.

(3) Niu, G.; Li, W.; Li, J.; Wang, L. *Sci. China Mater.* **2016**, *59* (9), 728–742.

(4) Mishra, A.; Fischer, M. K. R.; Bäuerle, P. *Angew. Chem. Int. Ed.* **2009**, *48* (14), 2474–2499.

(5) Snaith, H. J. *Adv. Funct. Mater.* **2010**, *20* (1), 13–19.

(6) Photovoltaic Research | NREL https://www.nrel.gov/pv/ (accessed Feb 17, 2017).

(7) Wojciechowski, K.; Leijtens, T.; Siprova, S.; Schlueter, C.; Hörantner, M. T.; Wang, J. T.-W.; Li, C.-Z.; Jen, A. K.-Y.; Lee, T.-L.; Snaith, H. J. *J. Phys. Chem. Lett.* **2015**, 2399–2405.

(8) Hewlett, C. W. Method of making a photoelectric cell. US2189580 A, February 6, 1940.

(9) Brattain, W. H. Light-sensitive electric device. US2537256 A, January 9, 1951.

(10) Green, M. A. *Semicond. Sci. Technol.* **1993**, *8* (1), 1.

(11) Chopra, K. L.; Paulson, P. D.; Dutta, V. *Prog. Photovolt. Res. Appl.* **2004**, *12* (2–3), 69–92.

(12) Green, M. A.; Hishikawa, Y.; Warta, W.; Dunlop, E. D.; Levi, D. H.; Hohl-Ebinger, J.; Ho-Baillie, A. W. H. *Prog. Photovolt. Res. Appl.* **2017**, *25* (7), 668–676.

(13) O'Regan, B.; Gratzel, M. *Nature* **1991**, *353* (6346), 737–740.

(14) Hahn, H.; Logas, J.; Averback, R. S. *J. Mater. Res.* **1990**, *5* (3), 609–614.

(15) Höfler, H. J.; Averback, R. S. *Scr. Metall. Mater.* **1990**, *24* (12), 2401–2406.

(16) Matsumura, M.; Nomura, Y.; Tsubomura, H. *Bull. Chem. Soc. Jpn.* **1977**, *50* (10), 2533–2537.

(17) Matsumura, M.; Mitsuda, K.; Yoshizawa, N.; Tsubomura, H. *Bull. Chem. Soc. Jpn.* **1981**, *54* (3), 692–695.

(18) V, N. A.; Beley, M.; Chartier, P.; Ern, V. *Rev. Phys. Appliquée* **1981**, *16* (1), 5–10.

(19) Willig, F.; Eichberger, R.; Sundaresan, N. S.; Parkinson, B. A. *J. Am. Chem. Soc.* **1990**, *112* (7), 2702–2707.

(20) Yella, A.; Lee, H.-W.; Tsao, H. N.; Yi, C.; Chandiran, A. K.; Nazeeruddin, M. K.; Diau, E. W.-G.; Yeh, C.-Y.; Zakeeruddin, S. M.; Grätzel, M. *Science* **2011**, *334* (6056), 629–634.

(21) Mathew, S.; Yella, A.; Gao, P.; Humphry-Baker, R.; Curchod, B. F. E.; Ashari-Astani, N.; Tavernelli, I.; Rothlisberger, U.; Nazeeruddin, M. K.; Grätzel, M. *Nat. Chem.* **2014**, *6* (3), 242–247.

(22) Kakiage, K.; Aoyama, Y.; Yano, T.; Otsuka, T.; Kyomen, T.; Unno, M.; Hanaya, M. *Chem. Commun.* **2014**, *50* (48), 6379–6381.

(23) Kakiage, K.; Aoyama, Y.; Yano, T.; Oya, K.; Fujisawa, J.; Hanaya, M. *Chem. Commun.* **2015**, *51* (88), 15894–15897.

(24) Lee, M. M.; Teuscher, J.; Miyasaka, T.; Murakami, T. N.; Snaith, H. J. *Science* **2012**, *338* (6107), 643–647.

(25) Mitzi, D. B.; Feild, C. A.; Harrison, W. T. A.; Guloy, A. M. *Nature* **1994**, *369* (6480), 467.

(26) Chondroudis, K.; Mitzi, D. B. *Chem. Mater.* **1999**, *11* (11), 3028–3030.

(27) Kojima, A.; Teshima, K.; Shirai, Y.; Miyasaka, T. *J. Am. Chem. Soc.* **2009**, *131* (17), 6050–6051.

(28) Im, J.-H.; Lee, C.-R.; Lee, J.-W.; Park, S.-W.; Park, N.-G. *Nanoscale* **2011**, *3* (10), 4088–4093.

(29) Bush, K. A.; Palmstrom, A. F.; Yu, Z. J.; Boccard, M.; Cheacharoen, R.; Mailoa, J. P.; McMeekin, D. P.; Hoye, R. L. Z.; Bailie, C. D.; Leijtens, T.; Peters, I. M.; Minichetti, M. C.; Rolston, N.; Prasanna, R.; Sofia, S.; Harwood, D.; Ma, W.; Moghadam, F.; Snaith, H. J.; Buonassisi, T.; Holman, Z. C.; Bent, S. F.; McGehee, M. D. *Nat. Energy* **2017**, *2* (4), 17009.

(30) Saygili, Y.; Söderberg, M.; Pellet, N.; Giordano, F.; Cao, Y.; Muñoz-García, A. B.; Zakeeruddin, S. M.; Vlachopoulos, N.; Pavone, M.; Boschloo, G.; Kavan, L.; Moser, J.-E.; Grätzel, M.; Hagfeldt, A.; Freitag, M. *J. Am. Chem. Soc.* **2016**, *138* (45), 15087–15096.

(31) Hardin, B. E.; Snaith, H. J.; McGehee, M. D. *Nat. Photonics* **2012**, *6* (3), 162.

(32) Hagfeldt, A.; Boschloo, G.; Sun, L.; Kloo, L.; Pettersson, H. *Chem. Rev.* **2010**, *110* (11), 6595–6663.

(33) Kalyanasundaram, K. *Dye-Sensitized Solar Cells*, 1st ed.; EPFL Press, 2010.

(34) Otsuka, A.; Funabiki, K.; Sugiyama, N.; Yoshida, T.; Minoura, H.; Matsui, M. *Chem. Lett.* **2006**, *35* (6), 666–667.

(35) Quintana, M.; Edvinsson, T.; Hagfeldt, A.; Boschloo, G. *J. Phys. Chem. C* **2007**, *111* (2), 1035–1041.

(36) Venditti, I.; Barbero, N.; Russo, M. V.; Carlo, A. D.; Decker, F.; Fratoddi, I.; Claudia Barolo; Dini, D. *Mater. Res. Express* **2014**, *1* (1), 015040.

(37) Shang, G.; Wu, J.; Huang, M.; Lin, J.; Lan, Z.; Huang, Y.; Fan, L. *J. Phys. Chem. C* **2012**, *116* (38), 20140–20145.

(38) Kay, A.; Grätzel, M. *Chem. Mater.* **2002**, *14* (7), 2930–2935.

(39) Ferrere, S.; Zaban, A.; Gregg, B. A. *J. Phys. Chem. B* **1997**, *101* (23), 4490–4493.

(40) Wang, M.; Grätzel, C.; M. Zakeeruddin, S.; Grätzel, M. *Energy Environ. Sci.* **2012**, *5* (11), 9394–9405.

(41) Cao, Y.; Saygili, Y.; Ummadisingu, A.; Teuscher, J.; Luo, J.; Pellet, N.; Giordano, F.; Zakeeruddin, S. M.; Moser, J.-E.; Freitag, M.; Hagfeldt, A.; Grätzel, M. *Nat. Commun.* **2017**, *8*, ncomms15390.

(42) Freitag, M.; Giordano, F.; Yang, W.; Pazoki, M.; Hao, Y.; Zietz, B.; Grätzel, M.; Hagfeldt, A.; Boschloo, G. *J. Phys. Chem. C* **2016**, *120* (18), 9595–9603.

(43) Bai, Y.; Yu, Q.; Cai, N.; Wang, Y.; Zhang, M.; Wang, P. *Chem. Commun.* **2011**, *47* (15), 4376–4378.

(44) Tsao, H. N.; Yi, C.; Moehl, T.; Yum, J.-H.; Zakeeruddin, S. M.; Nazeeruddin, M. K.; Grätzel, M. *ChemSusChem* **2011**, *4* (5), 591–594.

(45) Yum, J.-H.; Baranoff, E.; Kessler, F.; Moehl, T.; Ahmad, S.; Bessho, T.; Marchioro, A.; Ghadiri, E.; Moser, J.-E.; Yi, C.; Nazeeruddin, M. K.; Grätzel, M. *Nat. Commun.* **2012**, *3*, 631.

(46) Feldt, S. M.; Gibson, E. A.; Gabrielsson, E.; Sun, L.; Boschloo, G.; Hagfeldt, A. *J. Am. Chem. Soc.* **2010**, *132* (46), 16714–16724.

(47) Feldt, S. M.; Lohse, P. W.; Kessler, F.; Nazeeruddin, M. K.; Grätzel, M.; Boschloo, G.; Hagfeldt, A. *Phys. Chem. Chem. Phys.* **2013**, *15* (19), 7087–7097.

(48) Giribabu, L.; Bolligarla, R.; Panigrahi, M. *Chem. Rec.* **2015**, *15* (4), 760–788.

(49) Hamann, T. W. *Dalton Trans.* **2012**, *41* (11), 3111–3115.

(50) Wang, M.; Chamberland, N.; Breau, L.; Moser, J.-E.; Humphry-Baker, R.; Marsan, B.; Zakeeruddin, S. M.; Grätzel, M. *Nat. Chem.* **2010**, *2* (5), 385.

(51) Zhang, Z.; Chen, P.; Murakami, T. N.; Zakeeruddin, S. M.; Grätzel, M. *Adv. Funct. Mater.* **2008**, *18* (2), 341–346.

(52) Bach, U.; Lupo, D.; Comte, P.; Moser, J. E.; Weissortel, F.; Salbeck, J.; Spreitzer, H.; Gratzel, M. *Nature* **1998**, *395* (6702), 583–585.

(53) Hsu, C.-Y.; Chen, Y.-C.; Lin, R. Y.-Y.; Ho, K.-C.; Lin, J. T. *Phys. Chem. Chem. Phys.* **2012**, *14* (41), 14099–14109.

(54) Shockley, W.; Queisser, H. J. *J. Appl. Phys.* **1961**, *32* (3), 510–519.

(55) Durrant, J. R. *Philos. Trans. R. Soc. Math. Phys. Eng. Sci.* **2013**, *371* (1996).

(56) Nazeeruddin, M. K.; Péchy, P.; Renouard, T.; Zakeeruddin, S. M.; Humphry-Baker, R.; Comte, P.; Liska, P.; Cevey, L.; Costa, E.; Shklover, V.; Spiccia, L.; Deacon, G. B.; Bignozzi, C. A.; Grätzel, M. *J. Am. Chem. Soc.* **2001**, *123* (8), 1613–1624.

(57) Gabrielsson, E.; Ellis, H.; Feldt, S.; Tian, H.; Boschloo, G.; Hagfeldt, A.; Sun, L. *Adv. Energy Mater.* **2013**, *3* (12), 1647–1656.

(58) Liu, Y.; Jennings, J. R.; Wang, X.; Wang, Q. *Phys. Chem. Chem. Phys.* **2013**, *15* (17), 6170–6174.

(59) Cho, C.-P.; Chu, C.-C.; Chen, W.-T.; Huang, T.-C.; Tao, Y.-T. *J. Mater. Chem.* **2012**, *22* (7), 2915–2921.

(60) Grätzel, M. *J. Photochem. Photobiol. C Photochem. Rev.* **2003**, *4* (2), 145–153.

(61) Jradi, F. M.; Kang, X.; O'Neil, D.; Pajares, G.; Getmanenko, Y. A.; Szymanski, P.; Parker, T. C.; El-Sayed, M. A.; Marder, S. R. *Chem. Mater.* **2015**, *27* (7), 2480–2487.

(62) Jradi, F. M. Organic light-harvesting materials for power generation. Ph.D. Dissertation, Georgia Institute of Technology: Atlanta, GA, 2016.

(63) Hamann, T. W.; Ondersma, J. W. *Energy Environ. Sci.* **2011**, *4* (2), 370–381.

(64) Wang, Q.; Ito, S.; Grätzel, M.; Fabregat-Santiago, F.; Mora-Seró, I.; Bisquert, J.; Bessho, T.; Imai, H. *J. Phys. Chem. B* **2006**, *110* (50), 25210–25221.

(65) Boschloo, G.; Häggman, L.; Hagfeldt, A. *J. Phys. Chem. B* **2006**, *110* (26), 13144–13150.

(66) De Roo, J.; Ibáñez, M.; Geiregat, P.; Nedelcu, G.; Walravens, W.; Maes, J.; Martins, J. C.; Van Driessche, I.; Kovalenko, M. V.; Hens, Z. *ACS Nano* **2016**, *10* (2), 2071–2081.

(67) Park, N.-G. *Mater. Today* **2015**, *18* (2), 65–72.

(68) Xie, F. X.; Zhang, D.; Su, H.; Ren, X.; Wong, K. S.; Grätzel, M.; Choy, W. C. H. *ACS Nano* **2015**, *9* (1), 639–646.

(69) Lv, F.; Gao, C.; Zhou, H.-A.; Zhang, P.; Mi, K.; Liu, X. *ACS Appl. Mater. Interfaces* **2016**, *8* (29), 18985–18990.

(70) Liu, S.; Zheng, F.; Koocher, N. Z.; Takenaka, H.; Wang, F.; Rappe, A. M. *J. Phys. Chem. Lett.* **2015**, *6* (4), 693–699.

(71) Stranks, S. D.; Eperon, G. E.; Grancini, G.; Menelaou, C.; Alcocer, M. J. P.; Leijtens, T.; Herz, L. M.; Petrozza, A.; Snaith, H. J. *Science* **2013**, *342* (6156), 341–344.

(72) Miyata, A.; Mitioglu, A.; Plochocka, P.; Portugall, O.; Wang, J. T.-W.; Stranks, S. D.; Snaith, H. J.; Nicholas, R. J. *Nat. Phys.* **2015**, *11* (7), 582–587.

(73) Galkowski, K.; Mitioglu, A.; Miyata, A.; Plochocka, P.; Portugall, O.; Eperon, G. E.; Wang, J. T.-W.; Stergiopoulos, T.; Stranks, S. D.; Snaith, H. J.; Nicholas, R. J. *Energy Environ. Sci.* **2016**, *9* (3), 962–970.

(74) Kim, H.-S.; Lee, C.-R.; Im, J.-H.; Lee, K.-B.; Moehl, T.; Marchioro, A.; Moon, S.-J.; Humphry-Baker, R.; Yum, J.-H.; Moser, J. E.; Grätzel, M.; Park, N.-G. *Sci. Rep.* **2012**, *2*, 591.

(75) Burschka, J.; Pellet, N.; Moon, S.-J.; Humphry-Baker, R.; Gao, P.; Nazeeruddin, M. K.; Grätzel, M. *Nature* **2013**, *499* (7458), 316–319.

(76) Eperon, G. E.; Stranks, S. D.; Menelaou, C.; Johnston, M. B.; Herz, L. M.; Snaith, H. J. *Energy Environ. Sci.* **2014**, *7* (3), 982–988.

(77) Heo, Y.-J.; Kim, J.-E.; Weerasinghe, H.; Angmo, D.; Qin, T.; Sears, K.; Hwang, K.; Jung, Y.-S.; Subbiah, J.; Jones, D. J.; Gao, M.; Kim, D.-Y.; Vak, D. *Nano Energy* **2017**, *41* (Supplement C), 443–451.

(78) Yang, W. S.; Noh, J. H.; Jeon, N. J.; Kim, Y. C.; Ryu, S.; Seo, J.; Seok, S. I. *Science* **2015**, *348* (6240), 1234–1237.

(79) Zheng, L.; Zhang, D.; Ma, Y.; Lu, Z.; Chen, Z.; Wang, S.; Xiao, L.; Gong, Q. *Dalton Trans.* **2015**, *44* (23), 10582–10593.

(80) Bai, S.; Wu, Z.; Wu, X.; Jin, Y.; Zhao, N.; Chen, Z.; Mei, Q.; Wang, X.; Ye, Z.; Song, T.; Liu, R.; Lee, S.; Sun, B. *Nano Res.* **2014**, *7* (12), 1749–1758.

(81) Manspeaker, C.; Venkatesan, S.; Zakhidov, A.; Martirosyan, K. S. *Curr. Opin. Chem. Eng.* **2017**, *15*, 1–7.

(82) Snaith, H. J.; Abate, A.; Ball, J. M.; Eperon, G. E.; Leijtens, T.; Noel, N. K.; Stranks, S. D.; Wang, J. T.-W.; Wojciechowski, K.; Zhang, W. *J. Phys. Chem. Lett.* **2014**, *5* (9), 1511–1515.

(83) Green, M. A.; Emery, K.; Hishikawa, Y.; Warta, W.; Dunlop, E. D. *Prog. Photovolt. Res. Appl.* **2016**, *24* (7), 905–913.

(84) Kim, H.-S.; Park, N.-G. *J. Phys. Chem. Lett.* **2014**, *5* (17), 2927–2934.

(85) Wojciechowski, K.; Stranks, S. D.; Abate, A.; Sadoughi, G.; Sadhanala, A.; Kopidakis, N.; Rumbles, G.; Li, C.-Z.; Friend, R. H.; Jen, A. K.-Y.; Snaith, H. J. *ACS Nano* **2014**, *8* (12), 12701–12709.

(86) Shao, Y.; Xiao, Z.; Bi, C.; Yuan, Y.; Huang, J. *Nat. Commun.* **2014**, *5*, 5784.

(87) van Reenen, S.; Kemerink, M.; Snaith, H. J. *J. Phys. Chem. Lett.* **2015**, *6* (19), 3808–3814.

(88) Kim, H.-S.; Seo, J.-Y.; Park, N.-G. *ChemSusChem* **2016**, *9* (18), 2528–2540.

(89) Kaltenbrunner, M.; Adam, G.; Głowacki, E. D.; Drack, M.; Schwödiauer, R.; Leonat, L.; Apaydin, D. H.; Groiss, H.; Scharber, M. C.; White, M. S.; Sariciftci, N. S.; Bauer, S. *Nat. Mater.* **2015**, *14* (10), 1032–1039.

(90) Cao, J.; Yin, J.; Yuan, S.; Zhao, Y.; Li, J.; Zheng, N. *Nanoscale* **2015**, *7* (21), 9443–9447.

(91) Rong, Y.; Liu, L.; Mei, A.; Li, X.; Han, H. *Adv. Energy Mater.* **2015**, *5* (20).

(92) Sessolo, M.; Bolink, H. J. *Nat. Mater.* **2015**, *14* (10), 964–966.

(93) Li, Y.; Meng, L.; Yang, Y. (Michael); Xu, G.; Hong, Z.; Chen, Q.; You, J.; Li, G.; Yang, Y.; Li, Y. *Nat. Commun.* **2016**, *7*.

(94) Ha, J.; Kim, H.; Lee, H.; Lim, K.-G.; Lee, T.-W.; Yoo, S. *Sol. Energy Mater. Sol. Cells* **2017**, *161* (Supplement C), 338–346.

(95) Yao, K.; Wang, X.; Xu, Y.; Li, F. *Nano Energy* **2015**, *18*, 165–175.

(96) Shin, S. S.; Yang, W. S.; Noh, J. H.; Suk, J. H.; Jeon, N. J.; Park, J. H.; Kim, J. S.; Seong, W. M.; Seok, S. I. *Nat. Commun.* **2015**, *6*, ncomms8410.

(97) Hyuck Heo, J.; Ho Lee, M.; Ji Han, H.; Rudragouda Patil, B.; Su Yu, J.; Hyuk Im, S. *J. Mater. Chem. A* **2016**, *4* (5), 1572–1578.

(98) Hyuck Heo, J.; Ji Han, H.; Kim, D.; Kyu Ahn, T.; Hyuk Im, S. *Energy Environ. Sci.* **2015**, *8* (5), 1602–1608.

(99) Gheno, A.; Vedraine, S.; Ratier, B.; Bouclé, J. *Metals* **2016**, *6* (1), 21.

(100) Zardetto, V.; L. Williams, B.; Perrotta, A.; Giacomo, F. D.; A. Verheijen, M.; Andriessen, R.; M. Kessels, W. M.; Creatore, M. *Sustain. Energy Fuels* **2017**, *1* (1), 30–55.

(101) Halvani Anaraki, E.; Kermanpur, A.; Steier, L.; Domanski, K.; Matsui, T.; Tress, W.; Saliba, M.; Abate, A.; Grätzel, M.; Hagfeldt, A.; Correa-Baena, J.-P. *Energy Environ. Sci.* **2016**, *9* (10), 3128–3134.

(102) Baena, J. P. C.; Steier, L.; Tress, W.; Saliba, M.; Neutzner, S.; Matsui, T.; Giordano, F.; Jacobsson, T. J.; Kandada, A. R. S.; Zakeeruddin, S. M.; Petrozza, A.; Abate, A.; Nazeeruddin, M. K.; Grätzel, M.; Hagfeldt, A. *Energy Environ. Sci.* **2015**, *8* (10), 2928–2934.

(103) Zhu, Z.; Bai, Y.; Liu, X.; Chueh, C.-C.; Yang, S.; Jen, A. K.-Y. *Adv. Mater.* **2016**, *28* (30), 6478–6484.

(104) Yang, J.; Siempelkamp, B. D.; Mosconi, E.; De Angelis, F.; Kelly, T. L. *Chem. Mater.* **2015**, *27* (12), 4229–4236.

(105) Seo, J.; Park, S.; Kim, Y. C.; Joong Jeon, N.; Hong Noh, J.; Cheol Yoon, S.; Il Seok, S. *Energy Environ. Sci.* **2014**, *7* (8), 2642–2646.

(106) Jeng, J.-Y.; Chen, K.-C.; Chiang, T.-Y.; Lin, P.-Y.; Tsai, T.-D.; Chang, Y.-C.; Guo, T.-F.; Chen, P.; Wen, T.-C.; Hsu, Y.-J. *Adv. Mater.* **2014**, *26* (24), 4107–4113.

(107) Lo, M.-F.; Guan, Z.-Q.; Ng, T.-W.; Chan, C.-Y.; Lee, C.-S. *Adv. Funct. Mater.* **2015**, *25* (8), 1213–1218.

(108) Qiu, W.; P. Bastos, J.; Dasgupta, S.; Merckx, T.; Cardinaletti, I.; C. Jenart, M. V.; B. Nielsen, C.; Gehlhaar, R.; Poortmans, J.; Heremans, P.; McCulloch, I.; Cheyns, D. *J. Mater. Chem. A* **2017**, *5* (6), 2466–2472.

(109) Bai, Y.; Dong, Q.; Shao, Y.; Deng, Y.; Wang, Q.; Shen, L.; Wang, D.; Wei, W.; Huang, J. *Nat. Commun.* **2016**, *7*, ncomms12806.

(110) Li, M.; Chao, Y.-H.; Kang, T.; Wang, Z.-K.; Yang, Y.-G.; Feng, S.-L.; Hu, Y.; Gao, X.-Y.; Liao, L.-S.; Hsu, C.-S. *J. Mater. Chem. A* **2016**, *4* (39), 15088–15094.

(111) Wojciechowski, K.; Ramirez, I.; Gorisse, T.; Dautel, O.; Dasari, R.; Sakai, N.; Hardigree, J. M.; Song, S.; Marder, S.; Riede, M.; Wantz, G.; Snaith, H. J. *ACS Energy Lett.* **2016**, *1* (4), 648–653.

(112) Tatay, S.; Haque, S. A.; O'Regan, B.; Durrant, J. R.; Verhees, W. J. H.; Kroon, J. M.; Vidal-Ferran, A.; Gavina, P.; Palomares, E. *J. Mater. Chem.* **2007**, *17* (29), 3037–3044.

(113) de Miguel, G.; Marchena, M.; Ziółek, M.; Pandey, S. S.; Hayase, S.; Douhal, A. *J. Phys. Chem. C* **2012**, *116* (22), 12137–12148.

(114) Ito, S.; Nazeeruddin, M. K.; Liska, P.; Comte, P.; Charvet, R.; Péchy, P.; Jirousek, M.; Kay, A.; Zakeeruddin, S. M.; Grätzel, M. *Prog. Photovolt. Res. Appl.* **2006**, *14* (7), 589–601.

(115) Chung, I.; Lee, B.; He, J.; Chang, R. P. H.; Kanatzidis, M. G. *Nature* **2012**, *485* (7399), 486–489.

(116) Liu, L.; Chen, J.; Ku, Z.; Li, X.; Han, H. *Dyes Pigments* **2014**, *106*, 128–135.

(117) Magistris, C.; Martiniani, S.; Barbero, N.; Park, J.; Benzi, C.; Anderson, A.; Law, C.; Barolo, C.; O'Regan, B. *Renew. Energy* **2013**, *60*, 672–678.

(118) Paek, S.; Choi, H.; Kim, C.; Cho, N.; So, S.; Song, K.; Nazeeruddin, M. K.; Ko, J. *Chem. Commun.* **2011**, *47* (10), 2874.

(119) Choi, H.; Kim, J.-J.; Song, K.; Ko, J.; Nazeeruddin, M. K.; Grätzel, M. *J. Mater. Chem.* **2010**, *20* (16), 3280.

(120) Zhu, W.; Wu, Y.; Wang, S.; Li, W.; Li, X.; Chen, J.; Wang, Z.; Tian, H. *Adv. Funct. Mater.* **2011**, *21* (4), 756–763.

(121) Kang, X.; Zhang, J.; O'Neil, D.; Rojas, A. J.; Chen, W.; Szymanski, P.; Marder, S. R.; El-Sayed, M. A. *Chem. Mater.* **2014**, *26* (15), 4486–4493.

(122) Zhang, W.; Wu, Y.; Zhu, H.; Chai, Q.; Liu, J.; Li, H.; Song, X.; Zhu, W.-H. *ACS Appl. Mater. Interfaces* **2015**, *7* (48), 26802–26810.

(123) Shi, Y.; Hill, R. B. M.; Yum, J.-H.; Dualeh, A.; Barlow, S.; Grätzel, M.; Marder, S. R.; Nazeeruddin, M. K. *Angew. Chem. Int. Ed.* **2011**, *50* (29), 6619–6621.

(124) Terpetschnig, E.; Lakowicz, J. R. *Dyes Pigments* **1993**, *21* (3), 227–234.

(125) Fischer, E.; Jourdan, F. *Berichte Dtsch. Chem. Ges.* **1883**, *16* (2), 2241–2245.

(126) Davydenko, I.; Barlow, S.; Sharma, R.; Benis, S.; Simon, J.; Allen, T. G.; Cooper, M. W.; Khrustalev, V.; Jucov, E. V.; Castañeda, R.; Ordonez, C.; Li, Z.; Chi, S.-H.; Jang, S.-H.; Parker, T. C.; Timofeeva, T. V.; Perry, J. W.; Jen, A. K.-Y.; Hagan, D. J.; Van Stryland, E. W.; Marder, S. R. *J. Am. Chem. Soc.* **2016**, *138* (32), 10112–10115.

(127) Völker, S. F.; Renz, M.; Kaupp, M.; Lambert, C. *Chem. – Eur. J.* **2011**, *17* (50), 14147–14163.

(128) Scherer, D.; Dörfler, R.; Feldner, A.; Vogtmann, T.; Schwoerer, M.; Lawrentz, U.; Grahn, W.; Lambert, C. *Chem. Phys.* **2002**, *279* (2–3), 179–207.

(129) Coppo, P.; Cupertino, D. C.; Yeates, S. G.; Turner, M. L. *Macromolecules* **2003**, *36* (8), 2705–2711.

(130) Getmanenko, Y. A.; Tongwa, P.; Timofeeva, T. V.; Marder, S. R. *Org. Lett.* **2010**, *12* (9), 2136–2139.

(131) Cai, N.; Moon, S.-J.; Cevey-Ha, L.; Moehl, T.; Humphry-Baker, R.; Wang, P.; Zakeeruddin, S. M.; Grätzel, M. *Nano Lett.* **2011**, *11* (4), 1452–1456.

(132) Zhang, J.; Chen, W.; Rojas, A. J.; Jucov, E. V.; Timofeeva, T. V.; Parker, T. C.; Barlow, S.; Marder, S. R. *J. Am. Chem. Soc.* **2013**, *135* (44), 16376–16379.

(133) Geiger, T.; Kuster, S.; Yum, J.-H.; Moon, S.-J.; Nazeeruddin, M. K.; Grätzel, M.; Nüesch, F. *Adv. Funct. Mater.* **2009**, *19* (17), 2720–2727.

(134) Liang, M.; Chen, J. *Chem. Soc. Rev.* **2013**, *42* (8), 3453–3488.

(135) Heimer, T. A.; D'Arcangelis, S. T.; Farzad, F.; Stipkala, J. M.; Meyer, G. J. *Inorg. Chem.* **1996**, *35* (18), 5319–5324.

(136) Wang, Q.; Zakeeruddin, S. M.; Cremer, J.; Bäuerle, P.; Humphry-Baker, R.; Grätzel, M. *J. Am. Chem. Soc.* **2005**, *127* (15), 5706–5713.

(137) Pavlishchuk, V. V.; Addison, A. W. *Inorganica Chim. Acta* **2000**, *298* (1), 97–102.

(138) Boschloo, G.; Hagfeldt, A. *Acc. Chem. Res.* **2009**, *42* (11), 1819–1826.

(139) Delcamp, J. H.; Shi, Y.; Yum, J.-H.; Sajoto, T.; Dell'Orto, E.; Barlow, S.; Nazeeruddin, M. K.; Marder, S. R.; Grätzel, M. *Chem. – Eur. J.* **2013**, *19* (5), 1819–1827.

(140) M. J. Frisch, G. W. Trucks, H. B. Schlegel, G. E.; Scuseria, M. A. Robb, J. R. Cheeseman, G. Scalmani, V. Barone, B. Mennucci, G. A.; Petersson, H. Nakatsuji, M. Caricato, X. Li, H. P. Hratchian, A. F. Izmaylov, J. Bloino,; G. Zheng, J. L. Sonnenberg, M. Hada, M. Ehara, K. Toyota, R. Fukuda, J.; Hasegawa, M. Ishida, T. Nakajima, Y. Honda, O. Kitao, H. Nakai, T. Vreven, J. A.; Montgomery, Jr., J. E. Peralta, F. Ogliaro, M. Bearpark, J. J. Heyd, E. Brothers, K. N.; Kudin, V. N. Staroverov, R. Kobayashi, J. Normand, K. Raghavachari, A. Rendell, J.; C. Burant, S. S. Iyengar, J. Tomasi, M. Cossi, N. Rega, J. M. Millam, M. Klene, J. E.; Knox, J. B. Cross, V. Bakken, C. Adamo, J. Jaramillo, R. Gomperts, R. E. Stratmann,; O. Yazyev, A. J. Austin, R. Cammi, C. Pomelli, J. W. Ochterski, R. L. Martin, K.; Morokuma, V. G. Zakrzewski, G. A. Voth, P. Salvador, J. J. Dannenberg, S.; Dapprich, A. D. Daniels, Ö. Farkas, J. B. Foresman, J. V. Ortiz, J. Cioslowski, and D.; J. Fox,. Gaussian, Inc., Wallingford, CT 2009.

(141) Cancès, E.; Mennucci, B.; Tomasi, J. *J. Chem. Phys.* **1997**, *107* (8), 3032–3041.

(142) Zhao, Y.; Truhlar, D. G. *Theor. Chem. Acc.* **2008**, *120* (1–3), 215–241.

(143) Alberto, M. E.; Mazzone, G.; Quartarolo, A. D.; Sousa, F. F. R.; Sicilia, E.; Russo, N. *J. Comput. Chem.* **2014**, *35* (29), 2107–2113.

(144) Eichkorn, K.; Weigend, F.; Treutler, O.; Ahlrichs, R. *Theor. Chem. Acc.* **1997**, *97* (1–4), 119–124.

(145) Weigend, F.; Ahlrichs, R. *Phys. Chem. Chem. Phys.* **2005**, *7* (18), 3297–3305.

(146) Xu, J.; Zhang, H.; Wang, L.; Liang, G.; Wang, L.; Shen, X.; Xu, W. *Monatshefte Für Chem. - Chem. Mon.* **2010**, *141* (5), 549–555.

(147) Rocca, D.; Gebauer, R.; De Angelis, F.; Nazeeruddin, M. K.; Baroni, S. *Chem. Phys. Lett.* **2009**, *475* (1–3), 49–53.

(148) Tsai, H.-H. G.; Tan, C.-J.; Tseng, W.-H. *J. Phys. Chem. C* **2015**, *119* (9), 4431–4443.

(149) Nazeeruddin, M. K.; Péchy, P.; Renouard, T.; Zakeeruddin, S. M.; Humphry-Baker, R.; Comte, P.; Liska, P.; Cevey, L.; Costa, E.; Shklover, V.; Spiccia, L.; Deacon, G. B.; Bignozzi, C. A.; Grätzel, M. *J. Am. Chem. Soc.* **2001**, *123* (8), 1613–1624.

(150) Nazeeruddin, M. K.; De Angelis, F.; Fantacci, S.; Selloni, A.; Viscardi, G.; Liska, P.; Ito, S.; Takeru, B.; Grätzel, M. *J. Am. Chem. Soc.* **2005**, *127* (48), 16835–16847.

(151) Park, J.; Barbero, N.; Yoon, J.; Dell'Orto, E.; Galliano, S.; Borrelli, R.; Yum, J.-H.; Censo, D. D.; Grätzel, M.; Nazeeruddin, M. K.; Barolo, C.; Viscardi, G. *Phys. Chem. Chem. Phys.* **2014**, *16* (44), 24173–24177.

(152) Park, J.; Barolo, C.; Sauvage, F.; Barbero, N.; Benzi, C.; Quagliotto, P.; Coluccia, S.; Censo, D. D.; Grätzel, M.; Nazeeruddin, M. K.; Viscardi, G. *Chem. Commun.* **2012**, *48* (22), 2782–2784.

(153) Reddington, M. V. *Bioconjug. Chem.* **2007**, *18* (6), 2178–2190.

(154) Podrugina, T. A.; Temnov, V. V.; Doroshenko, I. A.; Kuzmin, V. A.; Nekipelova, T. D.; Proskurnina, M. V.; Zefirov, N. S. *Russ. Chem. Bull.* **2016**, *65* (11), 2722–2728.

(155) Hirata, T.; Kogiso, H.; Morimoto, K.; Miyamoto, S.; Taue, H.; Sano, S.; Muguruma, N.; Ito, S.; Nagao, Y. *Bioorg. Med. Chem.* **1998**, *6* (11), 2179–2184.

(156) He, J.; Benkö, G.; Korodi, F.; Polívka, T.; Lomoth, R.; Åkermark, B.; Sun, L.; Hagfeldt, A.; Sundström, V. *J. Am. Chem. Soc.* **2002**, *124* (17), 4922–4932.

(157) He, J.; Hagfeldt, A.; Lindquist, S.-E.; Grennberg, H.; Korodi, F.; Sun, L.; Åkermark, B. *Langmuir* **2001**, *17* (9), 2743–2747.

(158) Reddy, P. Y.; Giribabu, L.; Lyness, C.; Snaith, H. J.; Vijaykumar, C.; Chandrasekharam, M.; Lakshmikantam, M.; Yum, J.-H.; Kalyanasundaram, K.; Grätzel, M.; Nazeeruddin, M. K. *Angew. Chem.* **2007**, *119* (3), 377–380.

(159) Cid, J.-J.; García-Iglesias, M.; Yum, J.-H.; Forneli, A.; Albero, J.; Martínez-Ferrero, E.; Vázquez, P.; Grätzel, M.; Nazeeruddin, M. K.; Palomares, E.; Torres, T. *Chem. – Eur. J.* **2009**, *15* (20), 5130–5137.

(160) Bessho, T.; Zakeeruddin, S. M.; Yeh, C.-Y.; Diau, E. W.-G.; Grätzel, M. *Angew. Chem. Int. Ed.* **2010**, *49* (37), 6646–6649.

(161) Bisht, R.; Mk, M. F.; Singh, A. K.; Nithyanandhan, J. *J. Org. Chem.* **2017**.

(162) Petrenko. *Zhurnal Organicheskoĭ Khimii* **1978**, *14* (7), 1386.

(163) Funabiki, K.; Mase, H.; Hibino, A.; Tanaka, N.; Mizuhata, N.; Sakuragi, Y.; Nakashima, A.; Yoshida, T.; Kubota, Y.; Matsui, M. *Energy Environ. Sci.* **2011**, *4* (6), 2186–2192.

(164) Ulman, A. *Chem. Rev.* **1996**, *96* (4), 1533–1554.

(165) Sobuś, J.; Gierczyk, B.; Burdziński, G.; Jancelewicz, M.; Polanski, E.; Hagfeldt, A.; Ziółek, M. *Chem. – Eur. J.* **2016**, *22* (44), 15807–15818.

(166) Vioux, A.; Bideau, J. L.; Mutin, P. H.; Leclercq, D. In *New Aspects in Phosphorus Chemistry IV*; Majoral, J.-P., Ed.; Topics in Current Chemistry; Springer Berlin Heidelberg, 2004; pp 145–174.

(167) Hubert Mutin, P.; Guerrero, G.; Vioux, A. *J. Mater. Chem.* **2005**, *15* (35–36), 3761–3768.

(168) Vercelli, B.; Zotti, G.; Schiavon, G.; Zecchin, S.; Berlin, A. *Langmuir* **2003**, *19* (22), 9351–9356.

(169) Smith, O. L. Design and use of surface modifiers as tools for understanding and controlling interfaces in organic electronics. Ph.D. Dissertation, Georgia Institute of Technology: Atlanta, GA, 2014.

(170) Paniagua, S. A.; Giordano, A. J.; Smith, O. L.; Barlow, S.; Li, H.; Armstrong, N. R.; Pemberton, J. E.; Brédas, J.-L.; Ginger, D.; Marder, S. R. *Chem. Rev.* **2016**, *116* (12), 7117–7158.

(171) Guerrero, G.; Alauzun, J. G.; Granier, M.; Laurencin, D.; Mutin, P. H. *Dalton Trans.* **2013**, *42* (35), 12569–12585.

(172) Zhang, L.; Cole, J. M. *ACS Appl. Mater. Interfaces* **2015**, *7* (6), 3427–3455.

(173) Horiuchi, T.; Miura, H.; Uchida, S. *Chem. Commun.* **2003**, No. 24, 3036–3037.

(174) Horiuchi, T.; Miura, H.; Sumioka, K.; Uchida, S. *J. Am. Chem. Soc.* **2004**, *126* (39), 12218–12219.

(175) Horiuchi, T.; Miura, H.; Kodera, T. Organic Dye, Photoelectric Transducing Material, Semiconductor Electrode, and Photoelectric Transducing Device. EP1526159 (A1), April 27, 2005.

(176) Marinado, T.; Hagberg, D. P.; Hedlund, M.; Edvinsson, T.; Johansson, E. M. J.; Boschloo, G.; Rensmo, H.; Brinck, T.; Sun, L.; Hagfeldt, A. *Phys. Chem. Chem. Phys.* **2008**, *11* (1), 133–141.

(177) Abbotto, A.; Manfredi, N.; Marinzi, C.; Angelis, F. D.; Mosconi, E.; Yum, J.-H.; Xianxi, Z.; Nazeeruddin, M. K.; Grätzel, M. *Energy Environ. Sci.* **2009**, *2* (10), 1094–1101.

(178) Wiberg, J.; Marinado, T.; Hagberg, D. P.; Sun, L.; Hagfeldt, A.; Albinsson, B. *J. Phys. Chem. C* **2009**, *113* (9), 3881–3886.

(179) Matsui, M.; Fujita, T.; Kubota, Y.; Funabiki, K.; Jin, J.; Yoshida, T.; Miura, H. *Dyes Pigments* **2010**, *86* (2), 143–148.

(180) Kobayashi, K.; Kimura, K.; Susuki, T.; Satou, H.; Tani, Y. Dye, Photoelectric Conversion Element Using the Same, Photoelectrochemical Cell, and Method of Producing Dye. US2011213144 (A1), September 1, 2011.

(181) Matsui, M.; Shiota, T.; Kubota, Y.; Funabiki, K.; Jin, J.; Yoshida, T.; Higashijima, S.; Miura, H. *Tetrahedron* **2012**, *68* (22), 4286–4291.

(182) Echeverry, C. A.; Herranz, M. Á.; Ortiz, A.; Insuasty, B.; Martín, N. *New J. Chem.* **2014**, *38* (12), 5801–5807.

(183) Wu, G.; Kong, F.; Zhang, Y.; Zhang, X.; Li, J.; Chen, W.; Zhang, C.; Dai, S. *Dyes Pigments* **2014**, *105*, 1–6.

(184) Kazuyuki, S.; Makoto, O.; Norimasa, Y.; Sawa, I. Sensitizing Dye for Photoelectric Conversion, Photoelectric Conversion Element Using the Same, and Dye-Sensitized Solar Cell. JP20130033020 20130222.

(185) Qian, X.; Chang, W.-Y.; Zhu, Y.-Z.; Wang, S.-S.; Pan, B.; Lu, L.; Zheng, J.-Y. *RSC Adv.* **2015**, *5* (59), 47422–47428.

(186) Horiuchi, T.; Yashiro, T.; Kawamura, R.; Uchida, S.; Segawa, H. *Chem. Lett.* **2016**, *45* (5), 517–519.

(187) Mee, J. D. Method of synthesizing dyes and precursor compounds therefor. US5679795 A, October 21, 1997.

(188) Chen, J.; Chen, X.; Cho, A.; Chong, L.; Fardis, M.; Kirschberg, T.; Krawczyk, S.; Pyun, H.-J.; Watkins, W. Phosphonate Analogs for Treating Metabolic Diseases. WO2004096237 (A2), November 11, 2004.

(189) Sevov, C. S.; Fisher, S. L.; Thompson, L. T.; Sanford, M. S. *J. Am. Chem. Soc.* **2016**, *138* (47), 15378–15384.

(190) Xu, Y.; Flavin, M. T.; Xu, Z.-Q. *J. Org. Chem.* **1996**, *61* (22), 7697–7701.

(191) Da, P.; Zheng, G. *Nano Res.* **2017**, 1–27.

(192) Yang, G.; Wang, C.; Lei, H.; Zheng, X.; Qin, P.; Xiong, L.; Zhao, X.; Yan, Y.; Fang, G. *J. Mater. Chem. A* **2017**, *5* (4), 1658–1666.

(193) Schulz, P.; Edri, E.; Kirmayer, S.; Hodes, G.; Cahen, D.; Kahn, A. *Energy Environ. Sci.* **2014**, *7* (4), 1377–1381.

(194) Schulz, P.; Whittaker-Brooks, L. L.; MacLeod, B. A.; Olson, D. C.; Loo, Y.-L.; Kahn, A. *Adv. Mater. Interfaces* **2015**, *2* (7).

(195) Ball, J. M.; Lee, M. M.; Hey, A.; Snaith, H. J. *Energy Environ. Sci.* **2013**, *6* (6), 1739–1743.

(196) Giacomo, F. D.; Fakharuddin, A.; Jose, R.; M. Brown, T. *Energy Environ. Sci.* **2016**, *9* (10), 3007–3035.

(197) Zardetto, V.; Mincuzzi, G.; De Rossi, F.; Di Giacomo, F.; Reale, A.; Di Carlo, A.; Brown, T. M. *Appl. Energy* **2014**, *113* (Supplement C), 1155–1161.

(198) Fang, Y.; Bi, C.; Wang, D.; Huang, J. *ACS Energy Lett.* **2017**, *2* (4), 782–794.

(199) Wang, Q.; Shao, Y.; Dong, Q.; Xiao, Z.; Yuan, Y.; Huang, J. *Energy Environ. Sci.* **2014**, *7* (7), 2359–2365.

(200) Xu, J.; Buin, A.; Ip, A. H.; Li, W.; Voznyy, O.; Comin, R.; Yuan, M.; Jeon, S.; Ning, Z.; McDowell, J. J.; Kanjanaboos, P.; Sun, J.-P.; Lan, X.; Quan, L. N.; Kim, D. H.; Hill, I. G.; Maksymovych, P.; Sargent, E. H. *Nat. Commun.* **2015**, *6*, 7081.

(201) Zhou, Y.; Fuentes-Hernandez, C.; Shim, J.; Meyer, J.; Giordano, A. J.; Li, H.; Winget, P.; Papadopoulos, T.; Cheun, H.; Kim, J.; Fenoll, M.; Dindar, A.; Haske, W.; Najafabadi, E.; Khan, T. M.; Sojoudi, H.; Barlow, S.; Graham, S.; Brédas, J.-L.; Marder, S. R.; Kahn, A.; Kippelen, B. *Science* **2012**, *336* (6079), 327–332.

(202) Fabiano, S.; Braun, S.; Liu, X.; Weverberghs, E.; Gerbaux, P.; Fahlman, M.; Berggren, M.; Crispin, X. *Adv. Mater.* **2014**, *26* (34), 6000–6006.

(203) Russ, B.; J. Robb, M.; C. Popere, B.; E. Perry, E.; Mai, C.-K.; L. Fronk, S.; N. Patel, S.; E. Mates, T.; C. Bazan, G.; J. Urban, J.; L. Chabinyc, M.; J. Hawker, C.; A. Segalman, R. *Chem. Sci.* **2016**, *7* (3), 1914–1919.

(204) Hirsch, A.; Brettreich, M. In *Fullerenes*; Wiley-VCH Verlag GmbH & Co. KGaA, 2004; pp 73–99.

(205) Graf, N.; Yegen, E.; Gross, T.; Lippitz, A.; Weigel, W.; Krakert, S.; Terfort, A.; Unger, W. E. S. *Surf. Sci.* **2009**, *603* (18), 2849–2860.

(206) Moulder, J. F.; Stickle, W. F.; Sobol, P. E.; Bomben, K. D. *Handbook of x-ray photoelectron spectroscopy: a reference book of standard spectra for identification and interpretation of XPS data*; Chastain, J., King, R. C., Eds.; Physical Electronics: Eden Prairie, Minn., 1995.

(207) Sun, Y.; Cao, C.; Huang, P.; Yang, S.; Song, W. *RSC Adv.* **2015**, *5* (105), 86082–86087.

(208) Saliba, M.; Matsui, T.; Seo, J.-Y.; Domanski, K.; Correa-Baena, J.-P.; Khaja Nazeeruddin, M.; M. Zakeeruddin, S.; Tress, W.; Abate, A.; Hagfeldt, A.; Grätzel, M. *Energy Environ. Sci.* **2016**, *9* (6), 1989–1997.

(209) Almora, O.; Zarazua, I.; Mas-Marza, E.; Mora-Sero, I.; Bisquert, J.; Garcia-Belmonte, G. *J. Phys. Chem. Lett.* **2015**, *6* (9), 1645–1652.

(210) Ogomi, Y.; Morita, A.; Tsukamoto, S.; Saitho, T.; Shen, Q.; Toyoda, T.; Yoshino, K.; Pandey, S. S.; Ma, T.; Hayase, S. *J. Phys. Chem. C* **2014**, *118* (30), 16651–16659.

(211) Mei, A.; Li, X.; Liu, L.; Ku, Z.; Liu, T.; Rong, Y.; Xu, M.; Hu, M.; Chen, J.; Yang, Y.; Grätzel, M.; Han, H. *Science* **2014**, *345* (6194), 295–298.

(212) C. Shih, Y.; Y. Wang, L.; C. Hsieh, H.; F. Lin, K. *J. Mater. Chem. A* **2015**, *3* (17), 9133–9136.

(213) Zuo, L.; Gu, Z.; Ye, T.; Fu, W.; Wu, G.; Li, H.; Chen, H. *J. Am. Chem. Soc.* **2015**, *137* (7), 2674–2679.

(214) Dong, X.; Fang, X.; Lv, M.; Lin, B.; Zhang, S.; Wang, Y.; Yuan, N.; Ding, J. *Sci. Bull.* **2016**, *61* (3), 236–244.

(215) Li, B.; Chen, Y.; Liang, Z.; Gao, D.; Huang, W. *RSC Adv.* **2015**, *5* (114), 94290–94295.

(216) Zhang, C.; Zhang, S.; Miao, X.; Hu, Y.; Staaden, L.; Jia, G. *Part. Part. Syst. Charact.* **2017**, *34* (4).

(217) Kim, H. B.; Im, I.; Yoon, Y.; Sung, S. D.; Kim, E.; Kim, J.; Lee, W. I. *J. Mater. Chem. A* **2015**, *3* (17), 9264–9270.

(218) Liu, L.; Mei, A.; Liu, T.; Jiang, P.; Sheng, Y.; Zhang, L.; Han, H. *J. Am. Chem. Soc.* **2015**, *137* (5), 1790–1793.

(219) Paniagua, S. A.; Hotchkiss, P. J.; Jones, S. C.; Marder, S. R.; Mudalige, A.; Marrikar, F. S.; Pemberton, J. E.; Armstrong, N. R. *J. Phys. Chem. C* **2008**, *112* (21), 7809–7817.

(220) Hotchkiss, P. J.; Li, H.; Paramonov, P. B.; Paniagua, S. A.; Jones, S. C.; Armstrong, N. R.; Brédas, J.; Marder, S. R. *Adv. Mater.* **2009**, *21* (44), 4496–4501.

(221) Hotchkiss, P. J.; Jones, S. C.; Paniagua, S. A.; Sharma, A.; Kippelen, B.; Armstrong, N. R.; Marder, S. R. *Acc. Chem. Res.* **2012**, *45* (3), 337–346.

(222) Randon, J.; Blanc, P.; Paterson, R. *J. Membr. Sci.* **1995**, *98* (1), 119–129.

(223) Silverman, B. M.; Wieghaus, K. A.; Schwartz, J. *Langmuir* **2005**, *21* (1), 225–228.

(224) Guerra, V. L. P.; Altamura, D.; Trifiletti, V.; Colella, S.; Listorti, A.; Giannuzzi, R.; Pellegrino, G.; Condorelli, G. G.; Giannini, C.; Gigli, G.; Rizzo, A. *J. Mater. Chem. A* **2015**, *3* (41), 20811–20818.

(225) A. MacLeod, B.; Villers, B. J. T. de; Schulz, P.; F. Ndione, P.; Kim, H.; J. Giordano, A.; Zhu, K.; R. Marder, S.; Graham, S.; J. Berry, J.; Kahn, A.; C. Olson, D. *Energy Environ. Sci.* **2015**, *8* (2), 592–601.

(226) Ratcliff, E. L.; Garcia, A.; Paniagua, S. A.; Cowan, S. R.; Giordano, A. J.; Ginley, D. S.; Marder, S. R.; Berry, J. J.; Olson, D. C. *Adv. Energy Mater.* **2013**, *3* (5), 647–656.

(227) Knesting, K. M.; Ju, H.; Schlenker, C. W.; Giordano, A. J.; Garcia, A.; Smith, O. L.; Olson, D. C.; Marder, S. R.; Ginger, D. S. *J. Phys. Chem. Lett.* **2013**, *4* (23), 4038–4044.

(228) Cowan, S. R.; Schulz, P.; Giordano, A. J.; Garcia, A.; MacLeod, B. A.; Marder, S. R.; Kahn, A.; Ginley, D. S.; Ratcliff, E. L.; Olson, D. C. *Adv. Funct. Mater.* **2014**, *24* (29), 4671–4680.

(229) Fowkes, F. M. In *Contact Angle, Wettability, and Adhesion*; Advances in Chemistry; American Chemical Society, 1964; Vol. 43, pp 99–111.

(230) Binnig, G.; Quate, C. F.; Gerber, C. *Phys. Rev. Lett.* **1986**, *56* (9), 930–933.

(231) Yao, N.; Wang, Z. L. *Handbook of Microscopy for Nanotechnology*; 2005.

(232) Stintzing, D. H. *Tube Invest. Dep. Tech. Inf. Transl.* **1927**, No. 1666.

(233) Reichelt, R. In *Science of Microscopy*; Springer, New York, NY, 2007; pp 133–272.

(234) Goldstein, J. I.; Newbury, D. E.; Michael, J. R.; Ritchie, N. W. M.; Scott, J. H. J.; Joy, D. C. *Scanning Electron Microscopy and X-Ray Microanalysis*; Springer, 2017.

(235) Makowski, B. T.; Valle, B.; Singer, K. D.; Weder, C. *J. Mater. Chem.* **2012**, *22* (7), 2848–2850.

(236) Arunkumar, E.; Forbes, C. C.; Noll, B. C.; Smith, B. D. *J. Am. Chem. Soc.* **2005**, *127* (10), 3288–3289.

(237) Johnson, J. R.; Fu, N.; Arunkumar, E.; Leevy, W. M.; Gammon, S. T.; Piwnica-Worms, D.; Smith, B. D. *Angew. Chem. Int. Ed.* **2007**, *46* (29), 5528–5531.

(238) Scarpaci, A.; Nantalaksakul, A.; Hales, J. M.; Matichak, J. D.; Barlow, S.; Rumi, M.; Perry, J. W.; Marder, S. R. *Chem. Mater.* **2012**, *24* (9), 1606–1618.

(239) Su, J.; Zhu, S.; Chen, R.; An, Z.; Chen, X.; Chen, P. *J. Mater. Sci. Mater. Electron.* **2016**, 1–8.

(240) Braid, J. L.; Koldemir, U.; Sellinger, A.; Collins, R. T.; Furtak, T. E.; Olson, D. C. *ACS Appl. Mater. Interfaces* **2014**, *6* (21), 19229–19234.

(241) O'Connor, J.; Sexton, B.; Smart, R. S. C. *Surface Analysis Methods in Materials Science*; Springer, 2003.

(242) McCafferty, E.; Wightman, J. P. *Surf. Interface Anal.* **1998**, *26* (8), 549–564.

(243) Kahn, A. *Mater. Horiz.* **2015**, *3* (1), 7–10.

(244) Giordano, A. J. Altering the work function of surfaces: The influential role of surface modifiers for tuning properties of metals and transparent conducting oxides. Ph.D. Dissertation, Georgia Institute of Technology: Atlanta, GA, 2014.

(245) Nonnenmacher, M.; O'Boyle, M. P.; Wickramasinghe, H. K. *Appl. Phys. Lett.* **1991**, *58* (25), 2921–2923.

(246) Melitz, W.; Shen, J.; Kummel, A. C.; Lee, S. *Surf. Sci. Rep.* **2011**, *66* (1), 1–27.

(247) Beerbom, M. M.; Lägel, B.; Cascio, A. J.; Doran, B. V.; Schlaf, R. *J. Electron Spectrosc. Relat. Phenom.* **2006**, *152* (1), 12–17.